
COMPLEX MECHANISMS OF ORGANIC MOLECULES: FROM GROUND STATE REACTION TO EXCITED STATE DYNAMICS

Franziska Schüppel

München 2022

Dissertation zur Erlangung des Doktorgrades
der Fakultät für Chemie und Pharmazie
der Ludwig-Maximilians-Universität München

**Complex mechanisms of organic molecules: from ground
state reaction to excited state dynamics**

Franziska Schüppel
aus
Ebersberg, Deutschland

2022

Erklärung

Diese Dissertation wurde im Sinne von § 7 der Promotionsordnung vom 28. November 2011 von Frau Prof. Dr. Regina de Vivie-Riedle betreut.

Eidesstattliche Versicherung

Diese Dissertation wurde eigenständig und ohne unerlaubte Hilfe erarbeitet.

München, 12.04.2022
Franziska Schüppel

Dissertation eingereicht am:

12.04.2022

1. Gutachterin:

Prof. Dr. Regina de Vivie-Riedle

2. Gutachter:

Prof. Dr. Christian Ochsenfeld

Mündliche Prüfung am:

25.05.2022

CONTENTS

Abstract	v
List of Publications	vii
Introduction	1
1 Mechanistic studies of ground and excited state reactions	5
1.1 Oxidative ring contraction - a ground state reaction	5
1.2 Twisted intramolecular charge transfer - an excited state reaction	25
2 Dynamics of excited state reactions: quantum and semi-classical	39
2.1 Rotation of a molecular motor	40
2.2 Dissociation reaction of diphenylmethyl bromide	49
3 Control in the vicinity of a conical intersection	63
4 Summary	81
A Supporting Information to chapter 1.1	85
B OpenMolcas input-files for non-equilibrium PCM calculations	91
C Supporting Information to chapter 2.1	97
D Modifications of the program code in GAMESS and NewtonX	119
Bibliography	123
List of abbreviations	133
Danksagung	135

ABSTRACT

The significance of computational chemistry for a broad field of applications, as for example investigations of mechanisms or dynamics of chemical reactions, is rising. In this thesis various state-of-the-art computational chemistry methods are applied to different topics. This covers complex ground state reactions, excited state dynamics of molecular machines and detailed quantum dynamical studies at conical intersections (CoIns), decisive features for ultrafast reactions.

The complex mechanism of triplet oxygen with specifically substituted cyclobutene derivatives with a conjugated π system leading to an oxidative ring contraction under kinetic conditions and an oxidative ring opening reaction under thermodynamic conditions is revealed. The resulting barriers are in agreement with the experimentally observed product distribution under different conditions and the occurrence of a stable intermediate can be explained.

Further, the mechanism of the solvent dependent twisted intramolecular charge transfer (TICT) formation of certain hemithioindigo-stilbene (HTI) photoswitches is investigated. The necessary molecular conditions for a possible TICT formation as competing pathway next to the well-known $Z \rightarrow E$ isomerization are identified. With theoretical IR spectra at essential geometries along the reaction pathway the dynamics of a marker band observable in the experimental transient IR spectra of TICT formation is explained.

After this, the dynamics of the first photochemical step of a HTI based molecular motor is investigated. The significantly different reaction time of two related derivatives only differing in two substituents on the stilbene part is explained by comparing the electronic structure. These findings are strengthened by calculations of a related hypothetical motor with different electron distribution on the stilbene part. The dynamics of the faster derivative is simulated with semi-classical trajectories and by analyzing the molecular motion significant coordinates for the rotational step can be revealed.

Thereafter, the dynamics of the photodissociation of $\text{Ph}_2\text{CH}-\text{Br}$ with two competing pathways is simulated with grid-based wave packet quantum dynamics on two-dimensional ab-initio potential energy surface with specially adapted reactive coordinates and with full-dimensional ab-initio semi-classical trajectories with surface hopping. Both approaches can be tuned to reproduce the sequential appearance of the two different product pairs obtained by homolytic and heterolytic bond cleavage, respectively. An analysis of the wave packet motion explains the fluctuation in the experimental transient absorption signal only observable for the $\text{Ph}_2\text{CH}-\text{X}$ compound with bromine as leaving group.

The last part deals with the waveform control of a reaction in the vicinity of a conical intersection with a few cycle carrier-envelope phase (CEP) laser pulse. The phase-dependent control efficiency is analyzed varying several different pulse parameters (FWHM, t_0 , ω_0 , E_{max}) beside the CEP. Two different underlying control mechanisms are revealed determining the total control efficiency and the influence of the pulse parameters on the underlying mechanism is evaluated. First, the control scheme is applied to a dissociative model system identifying the general features for a possible

CEP control. Then the procedure is successfully adopted to the nucleobase uracil and the underlying control mechanism is discussed in detail.

LIST OF PUBLICATIONS

This thesis is based on the following five publications listed in chronological order. They are reprinted in chapter 1 (**1**, **4**), chapter 2 (**2**) and chapter 3 (**3**).

- **1** A. N. Baumann, F. Schüppel, M. Eisold, A. Kreppel, R. de Vivie-Riedle and D. Didier, “Oxidative Ring Contraction of Cyclobutenes: General Approach to Cyclopropylketones including Mechanistic Insights”, *J. Org. Chem.*, **83**, 4905–4921 (2018).
DOI: [10.1021/acs.joc.8b00297](https://doi.org/10.1021/acs.joc.8b00297)
Contributions by F. Schüppel: performing all theoretical calculations and their analysis, writing of the theoretical part.
- **2** F. Schüppel, M. K. Roos and R. de Vivie-Riedle, “Ultrafast non-adiabatic dynamics of excited diphenylmethyl bromide elucidated by quantum dynamics and semi-classical on-the-fly dynamics”, *Phys. Chem. Chem. Phys.*, **20**, 22753 (2018).
DOI: [10.1039/c8cp03257b](https://doi.org/10.1039/c8cp03257b)
Contributions by F. Schüppel: performing all calculations and analysis, writing of the manuscript.
- **3** F. Schüppel, T. Schnappinger, L. Bäuml and R. de Vivie-Riedle, “Waveform control of molecular dynamics close to a conical intersection”, *J. Chem. Phys.*, **153**, 224307 (2020).
DOI: [10.1063/5.0031398](https://doi.org/10.1063/5.0031398)
Contributions by F. Schüppel: performing the calculations of section III and their analysis, writing of the manuscript.
- **4** K. Stallhofer, M. Nuber, F. Schüppel, S. Thumser, H. Iglev, R. de Vivie-Riedle, W. Zinth and H. Dube, “Electronic and Geometric Characterization of TICT Formation in Hemithioindigo Photoswitches by Picosecond Infrared Spectroscopy”, *J. Phys. Chem. A*, **125**, 4390–4400 (2021).
DOI: [10.1021/acs.jpca.1c02646](https://doi.org/10.1021/acs.jpca.1c02646)
Contributions by F. Schüppel: performing all theoretical calculations and their analysis, writing of the theoretical part.

Additional publication:

- **5** J. Skotnitzki, A. Kremsmair, D. Keefer, F. Schüppel, B. Le Cacher de Bonneville, R. de Vivie-Riedle and P. Knochel, “Regio- and diastereoselective reactions of chiral secondary alkylcopper reagents with propargylic phosphates: preparation of chiral allenes”, *Chem. Sci.*, **11**, 5328–5332, (2020).
DOI: [10.1039/C9SC05982B](https://doi.org/10.1039/C9SC05982B)

INTRODUCTION

In nature, many biological processes are regulated by photochemical reactions. Investigating the dynamics of these reactions is necessary for understanding the unique mechanisms determined by the specific properties of the molecules formed by nature. For example, the DNA, the code of life, is built by the photostable nucleobases that have ultrafast radiationless relaxation channels to be stable against irradiation with sun light [1–3]. In contrast, the retinal, the most famous photoswitch in nature, used in the process of vision undergoes a wanted configurational change after photo excitation [4, 5].

To experimentally detect such ultrafast processes occurring in the femtosecond regime the generation of ultrashort laser pulses is required. The developments in laser technology allow to measure the dynamics of such reactions with high resolution using pump-probe spectroscopy [6, 7]. Hereby, the molecule is excited with the pump-pulse and a second pulse, the probe-pulse, is shifted in time and detects the time-dependent molecular response. With computational chemistry these processes can be simulated by various approaches [8–10]. The theoretical studies have the advantage to directly detect geometrical changes during the reactions and to reveal structures of transition states and intermediates. Precisely in combination with experimental studies quantum chemical calculations are a very powerful tool to disclose the underlying mechanism of reactions [11].

The main effort in the setup of a theoretical study is the right choice of method as various different approaches are available. High accuracy is accompanied by high computational costs and especially for large molecules restrictions in the accuracy are necessary for a feasible calculation. This is particularly difficult for investigations of open-shell systems and excited state reactions [12–14]. Here, conical intersections (CoIns) [15, 16], ubiquitous points where two states approach to intersect, emerge on the potential energy landscape. For such investigations, the use of approximations to reduce the computational time has to be treated with caution as most of those methods lack the potential to describe all relevant points of the reaction adequately. For a theoretical study this means, that the use of approximate methods has to be verified by a meaningful benchmark towards high-level methods for a relevant prediction [13, 17, 18].

Going one step further, to simulate the dynamics of those ultrafast excited state processes, additional approximations are necessary. In the vicinity of CoIns the Born-Oppenheimer approximation breaks as the motion of electron and nuclei can no longer be separated [8, 9]. One possibility is to calculate the system fully quantum and to set up a grid-based wave packet quantum dynamic (QD) simulation on ab-initio potential energy surface (PES) but in a reduced coordinate space [8, 19]. For this a precise knowledge of the ongoing reaction is required as few representative reactive coordinates need to be selected to describe the dynamics adequately. In an other approach, a swarm of independent trajectories moves classically on the ab-initio calculated PES and the quantum transitions are approximated by sudden hops between the electronic

states [10, 20–22]. An advantage of this approach is that a full-dimensional simulation of the dynamics is possible which is interesting if several different coordinates are important for the reaction [23–25].

This thesis deals with the computational description of extensive reaction mechanisms of medium sized molecules and the dynamics of ultrafast excited state processes with state-of-the-art methods. A major point hereby is the discussion of the right choice of theoretical method to establish a simulation with feasible calculation time.

In the first part of chapter 1 the complex mechanism of particularly substituted cyclobutene derivatives with a conjugated π -system with triplet oxygen is revealed in a combined experimental and theoretical study. From the theoretical side, the main attention herein lies within the selection of a feasible method. Through the appearance of biradical intermediates and the triplet-singlet transfer a multi-reference method is necessary to describe the present mechanism appropriately.

The second part of chapter 1 reveals the mechanism of a synthetic photoswitch with quantum chemical calculations. Several photoswitches with a similar mechanism to the natural photoswitch retinal have been developed so far [26–28] and are embedded in various different fields ranging from material science [29–31] to photopharmacology [32, 33]. An emerging group of these photoswitches build the hemithioindigo-stilbenes (HTIs) [34–36]. Their reactivity can be influenced by changing the polarity of the solvent and variously substituted derivatives show significantly different dynamics [35–38]. The peculiar characteristic of the investigated HTIs is the newly found competing reaction pathway occurring only in specific substituted derivatives next to the well-known $Z \rightarrow E$ double bond isomerization (DBI) [37, 38]. Depending on the solvent polarity the second pathway defined by a single bond twist (SBT) forming a twisted intramolecular charge transfer (TICT) state [37, 38] is available or solely the DBI is accessible. The section 1.2 discusses the twisted intramolecular charge transfer (TICT) formation in detail in a combined experimental and theoretical study.

In chapter 2, the thesis continues with the dynamics of an artificial molecular motor that is based on HTI like the previously mentioned photoswitches. In nature, molecular machines exist in several different areas. The probably most famous example is the adenosine triphosphate (ATP) synthase [39, 40], generating ATP, the molecule ensuring the energy delivery in the metabolism of living cells. In 2016 the Nobel-Prize in Chemistry was awarded to Bernard L. Feringa [33], Jean-Pierre Sauvage [41] and Sir J. Fraser Stoddart [42] “for the design and synthesis of molecular machines”. The here investigated HTI based molecular motor [43–45] has a similar four-step mechanism like the stilbene based Feringa-typ motors [33, 46, 47], with two photochemical steps via a DBI and two thermal steps via a helix conversion [48]. In section 2.1, the dynamics of the first photochemical step is simulated with full-dimensional semi-classical trajectories.

The second section of the chapter (2.2) deals with the dynamics of the ultrafast photodissociation of diphenylmethyl bromide ($\text{Ph}_2\text{CH} - \text{Br}$) with the bromide as leaving group. By the photoinduced bond cleavage of the C – Br bond carbocations and carboradicals are generated, both important intermediates for building blocks in organic synthesis [49–51]. In the study, the two mentioned approaches for dynamics simulations, wave packet quantum dynamics and semi-classical trajectory surface hopping, are applied and compared.

The thesis concludes with the control of reactions that is a key subject in chemistry. Beside by varying the conventional parameters, as temperature, concentration or catalyst, a chemical reaction can also be influenced by a light source. With the application of specifically shaped laser pulses a coherent control of the reaction can be achieved [52–54]. Strong field laser pulses are used to distort the PES via the Stark shift [55, 56] to generate so-called light-induced CoIns [57–59]. In a different approach, a coherent control in the vicinity of a CoIn can be accomplished by a resonant short

time few cycle carrier-envelope phase (CEP) laser pulse generating a phase-dependent superposition at the CoIn [60, 61]. By varying the carrier-envelope phase (CEP) the transfer through the CoIn is influenced and it is even possible to reverse the transfer rate. Chapter 3 analyses the control mechanism of an excited state reaction in the vicinity of a CoIn with a CEP laser pulse on the basis of a dissociative model system and expands the control scheme to the nucleobase uracil.

MECHANISTIC STUDIES OF GROUND AND EXCITED STATE REACTIONS

Clearing up mechanisms of chemical reactions is a key subject of quantum chemistry. The knowledge of the mechanism is useful for understanding the regioselectivity and stereoselectivity of reactions in organic synthesis [11, 62–64]. Identifying the key step helps to optimize the yield of reactions by changing parameters as temperature, concentration, catalyst or solvent to feature thermodynamic or kinetic conditions. Elucidating transition state structures is essential for the development of similar reactions or new catalysts [11, 62, 64, 65].

With the calculation of complex reactions of large molecules the chemical accuracy is accompanied by high computational costs. An intuitive chemical approach is necessary to find a feasible methodology to describe the required mechanism adequately. Through appearance of biradical intermediates, as for example in publication “Oxidative Ring Contraction of Cyclobutenes: General Approach to Cyclopropylketones including Mechanistic Insights” (chapter 1.1), the usage of a multi-reference method is necessary for the investigation of a ground state reaction mechanism.

Investigating excited state reactions is much more demanding. When for example molecules with large π -systems are of interest the fast and common method time-dependent density functional theory (TDDFT) reaches its limits [12, 66]. In such molecules charge-transfer states often play a crucial role but those states are known to be poorly described compared to other states with TDDFT [67–69]. Thus, when those states are of interest, it is necessary to apply a more accurate method which can be a challenge for large molecules [12]. In publication “Electronic and Geometric Characterization of TICT Formation in Hemithioindigo Photoswitches by Picosecond Infrared Spectroscopy” (chapter 1.2), where an excited state reaction path with a charge-transfer state is investigated, this is the crucial task.

1.1 Oxidative ring contraction - a ground state reaction

The synthesis of molecules with a cyclopropyl group, the smallest carbocyclic ring, is of great importance as many bioactive substances have those common motives [70–72]. The here investigated, easily accessible cyclobutene compounds **1** (fig. 1.1) are discovered to form a cyclopropyl group via ring contraction. This reaction of cyclobutene **1** was first observed at room temperature under atmospheric conditions. A specific analysis of the decomposition products revealed two different molecules, cyclopropane ketone (CPK) **2** and diketone (DK) **3** (fig. 1.1), both resulting from reaction of the cyclobutene compound with triplet oxygen ($^3\text{O}_2$). With further investigations the yields of the two products could be improved by varying the reaction conditions for several different compounds showing the cyclobutene center pictured in fig. 1.1. As a part of this work, a theoretical study revealed the reaction paths of both products also explaining the different yields under different reaction conditions.

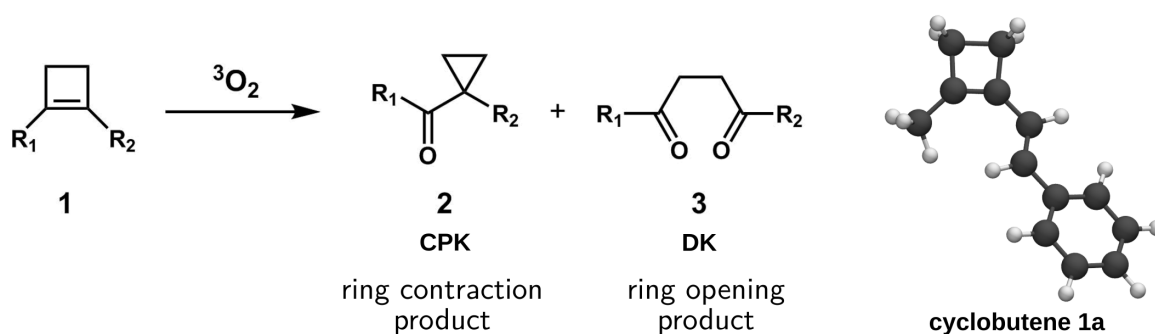


Figure 1.1: Reaction of cyclobutene compound **1** with triplet oxygen to the ring contraction product cyclopropane ketone (CPK) and the ring opening product diketone (DK). Cyclobutene **1a** is used as model for the calculation of the mechanism.

As $^3\text{O}_2$ is formally a diradical the ground state has multi-reference character and a method as complete active space self-consistent field (CASSCF) is necessary to describe the reaction path appropriately that moves from a triplet to a singlet state. An active space of 14 electrons in 13 orbitals is found suitable for the reaction path (see appendix A). $^3\text{O}_2$ is hereby included with an active space (8,6), which is the valence space with four lone pair orbitals and the σ/σ^* orbitals. Cyclobutene **1a** is identified as the best model for the calculations. The active space includes the π and corresponding π^* orbitals of the cyclic C-C double bond, the subsequent C-C double bond and the phenyl ring. The inclusion of π orbitals of the phenyl ring and the second C-C double bond is necessary because the aromatic system is essential for an emerging oxidative ring contraction. In cyclobutenes without this specific aromatic system next to the cyclic double bond no ring contraction is observed without further activation. For the oxidative ring opening reaction, in contrast, only the subsequent C-C double bond is required. The residue labeled R_1 in 1.1 is not important for the reaction, so it is substituted with a methyl group to accelerate the calculation time. It is challenging to find a stable and feasible active space including the same orbitals during the complete reaction path when several bonds are cleaved or rather newly formed. Therefore, the active space is adapted for the calculation of each single barrier, to include the corresponding σ and σ^* orbitals of the formed or cleaved bonds, respectively. This shortcoming can be compensated with the incorporation of dynamic electron correlation with complete active space perturbation theory to the second order (CASPT2) single-point calculations and the respective active space [73]. The geometries are optimized with ground state density functional theory (DFT) calculations to save calculation time. Finding a suitable and feasible method to describe the investigated reaction mechanism was the key challenge for the theory in this project.

The main points of article “Oxidative Ring Contraction of Cyclobutenes: General Approach to Cyclopropylketones including Mechanistic Insights” with emphasis on the theoretical study are:

- The investigated cyclobutene compounds **1** decompose under air by reaction with $^3\text{O}_2$ to build CPK or DK compounds. Both mechanisms are investigated theoretically using DFT (B3LYP) for geometry optimizations and CASPT2 with an active space of (14,13) to calculate the barriers. The methodology is benchmarked and found suitable to describe the decomposition of the smallest synthetically used compound **1a** showing both products (fig. 1.1).
- CPKs, the ring-contraction products, are preferred under kinetic conditions (high temperature and short reaction time). The calculated barriers and stabilization energies are in good agreement with the experiment. Further, it is possible to

experimentally detect a stable intermediate (an epoxide), confirming the reaction pathway found by theory.

- DKs, the ring-opening products, are preferred under thermodynamic conditions (room temperature and long reaction time) because the final products are more stable compared to the CPKs. The reaction barrier for the deciding step is slightly larger (around 4 kcal mol^{-1}) than the corresponding step to build CPKs. No intermediates can be detected along this path, because they are not stable.
- Both mechanisms exhibit the same initial step, the addition of $^3\text{O}_2$ to the cyclic C-C double bond. Under pure oxygen atmosphere DKs are preferentially formed. The deciding step to form CPKs is a two molecule transition state, so, when the first step is accelerated by adding more oxygen to the reaction, the second cyclobutene is missing to form the transition state.

The article “Oxidative Ring Contraction of Cyclobutenes: General Approach to Cyclopropylketones including Mechanistic Insights” published in *The Journal of Organic Chemistry* is reprinted hereafter with permission of *J. Org. Chem.*, **83**, 4905–4921 (2018). Copyright 2018 American Chemical Society.

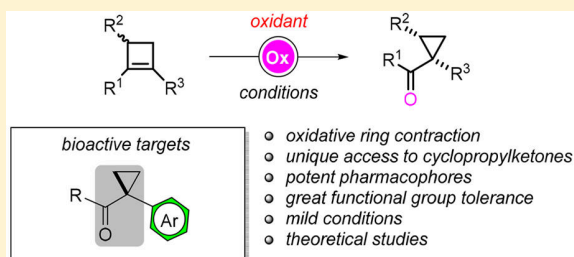
Oxidative Ring Contraction of Cyclobutenes: General Approach to Cyclopropylketones including Mechanistic Insights

Andreas N. Baumann, Franziska Schüppel, Michael Eisold,^{1b} Andrea Kreppel, Regina de Vivie-Riedle,^{1b} and Dorian Didier^{1b}

Department of Chemistry and Pharmacy, Ludwig-Maximilians-University, Butenandtstraße 5-13, 81377 Munich, Germany

Supporting Information

ABSTRACT: An original oxidative ring contraction of easily accessible cyclobutene derivatives for the selective formation of cyclopropylketones (CPKs) under atmospheric conditions is reported. Comprehensive mechanistic studies are proposed to support this novel, yet unusual, rearrangement. Insights into the mechanism ultimately led to simplification and generalization of the ring contraction of cyclobutenes using *m*CPBA as an oxidant. This unique and functional group tolerant transformation proceeds under mild conditions at room temperature, providing access to a new library of polyfunctionalized motifs. With CPKs being attractive and privileged pharmacophores, the elaboration of such a simple and straightforward strategy represents a highly valuable tool for drug discovery and medicinal chemistry. Additionally, the described method was employed to generate a pool of bioactive substances and key precursors in a minimum number of steps.



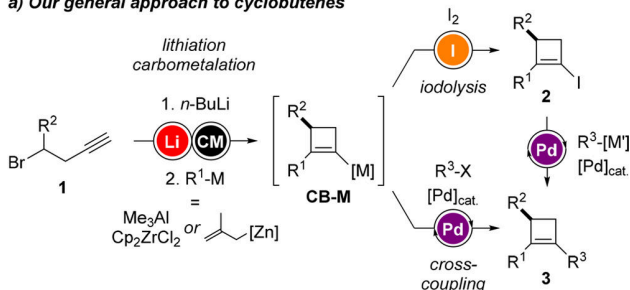
INTRODUCTION

Four-membered carbocyclic architectures, especially cyclobutenes, have recently become a source of inspiration for dependable synthetic methodologies because of their inherent ring strain.¹

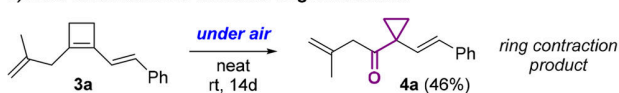
While most documented strategies are based on [2 + 2]-cycloadditions and transition-metal-catalyzed processes,² we have described an efficient, general, and regioselective route to cyclobutenes via the intermediate formation of an easily accessible cyclobutenylmetal species **CB-M** (Scheme 1a) from bromobutynes **1**.³ This one-pot generated **CB-M** was then

Scheme 1. Our Access Path to Cyclobutenes (a) and the First Observation of Oxidative Ring Contraction (b)

a) Our general approach to cyclobutenes



b) First observation of oxidative ring contraction



engaged either in a direct cross-coupling reaction with aryl halides or in a relayed sequence involving intermediate formation of iodocyclobutenes **2**. The synthetic approach to functionalized cyclobutenes **3** was studied in depth, leading to a unique library of diversified aryl-, heteroaryl-, alkynyl- and vinylcyclobutenes. While **CB-M** could be used in one-pot sequences to form challenging alkylidenecyclobutenes,⁴ vinylcyclobutenes were transformed into strained fused ring systems.⁵ Interestingly, when vinylcyclobutene **3a** was left under atmospheric conditions (Scheme 1b) a formal oxidative ring contraction was observed and cyclopropylketone (CPK) **4a** was isolated in 46% yield.

Notably, CPK-based pharmacophores can be found in a number of bioactive substances (Figure 1, A–F)⁶ by exalting crucial hydrophobic interactions.⁷ Efficient strategies that allow for a rapid and selective construction of these strained pharmacophores represent valuable tools for drug discovery and high throughput screenings.

Surprisingly, only a few methods are described concerning the synthesis of such structures possessing aromatic, hetero-aromatic, or vinylic substituents, and those require in most cases a large number of steps with low functional group tolerance. So far, formation of *gem*-disubstituted cyclopropanes has been achieved by employing preformed carbonylated cyclopropanes,⁸ double alkylations with dihaloethanes,⁹ Corey–Chaykovsky cyclopropanations,¹⁰ or α -arylation of cyclopropyl nitriles¹¹ or, more recently, via transition-metal-catalyzed oxidative cyclopropanations of alkynes.¹² Intrigued by

Received: February 1, 2018

Published: April 11, 2018

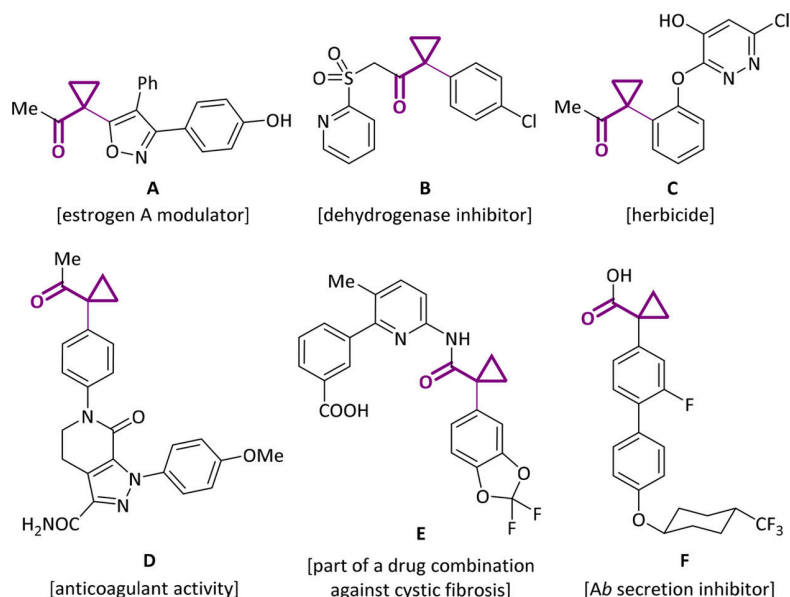
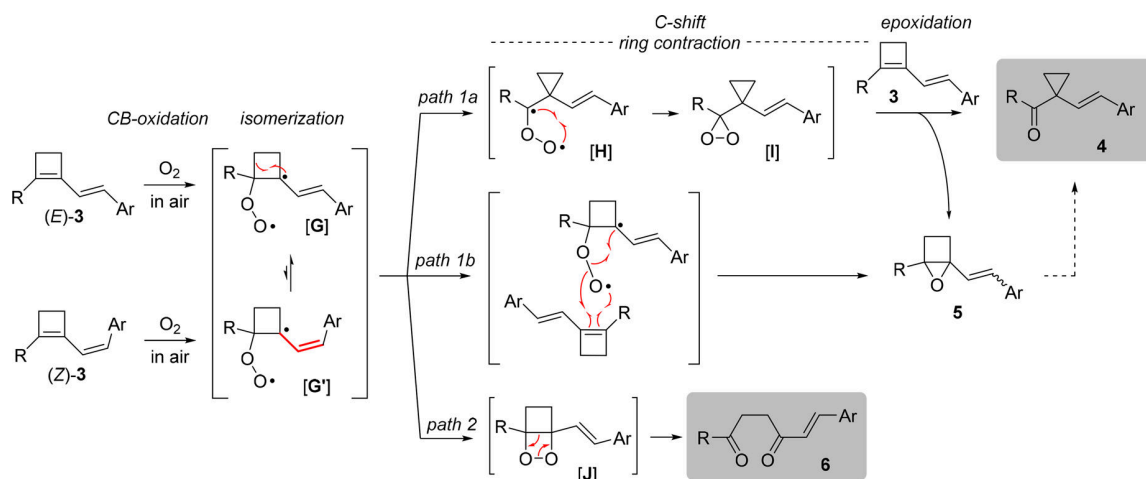


Figure 1. CPK-containing bioactive substances.⁶

Scheme 2. Proposed Mechanism for the Oxidative Ring Contraction of Cyclobutenes (Path 1) and Oxidative Ring Opening (Path 2)



the simplicity of our innovative sequence, when compared to functional group sensitive reported processes, we took on the challenge of generalizing the access to these important modules.

RESULTS AND DISCUSSION

On the Mechanism of the Oxidative Ring Contraction with O_2 . After the first observation of ring contraction of cyclobutenes under air, we became interested in the generalization and application of such an uncommon reaction.¹³ We thus started investigating the mechanism of the transformation to understand, and ultimately optimize, the synthesis of CPKs from cyclobutenes. Here we propose a mechanism for the oxidative addition of O_2 onto cyclobutenes, inspired by the early findings of Priesnitz et al.^{13a} Fundamental mechanistic assumptions were addressed both experimentally and by quantum-chemical calculations, the details of which can be found in the [Supporting Information](#). We describe and compare

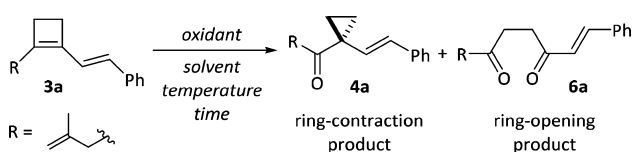
two alternative routes that can be envisioned for the formation of CPKs.

As the reaction readily occurs under air, we propose that cyclobutene (*E*)-3 is first oxidized by the presence of triplet O_2 , giving the biradical species [G] (Scheme 2). Importantly, we noticed that starting from either (*E*)-3 or (*Z*)-3 derivatives led to the same (*E*)-4 isomer. First, the consideration of this allows for explanation of the double-bond isomerization through an intermediate π -allyl radical species, the equilibrium being displaced toward the thermodynamic *E* product [G]. Two paths can then be described: in path 1a, a ring contraction takes place resulting in [H], which leads to formation of the dioxirane [I]. As dioxiranes are very reactive species, we assumed that a fast epoxidation occurs, consuming an equimolar amount of the starting material 3. However, a second route (path 1b) can be described, where G reacts in a concerted radical epoxidation with a molecule of the cyclobutene substrate 3, giving the same intermediate 5 as path 1a. In parallel, path 2 can be followed in which a 1,2-dioxetane [J] is formed as the product of a formal

[2 + 2]-cycloaddition. A subsequent ring-opening reaction undergoes the formation of 1,4-diketone **6**.

Formation of CPKs vs 1,4-Diketones under Atmospheric Conditions. Taking into account that a carbon shift of substituted epoxides can be triggered by addition of a Lewis acid or under thermal conditions (Meinwald rearrangement),^{13,14} optimizations were undertaken to favor the exclusive formation of the oxidative ring contraction product **4** (Table 1). Particular observations of such cyclobutene oxide rearrangements have been reported in the past but in most cases with low efficiency and versatility.¹⁵

Table 1. Condition Optimizations



entry	oxidant	solvent	temp (°C)	time (h)	conv (%)	4a/6a ^a
1	air	neat	rt	24	50	87:13
2	O ₂	neat	rt	2	98	30:70
3	O ₂	H ₂ O	rt	2	92	38:62
4	air	EtOAc	rt	48	>99	77:23
5	- ^b	neat	rt	20	0	
6	air ^c	EtOAc	rt	20	0	
7	air ^d	EtOAc	rt	20	0	
8	air	neat	100	3	89	>99:1

^aConversion of the starting material and ratios determined by GC.

^bUnder N₂. ^cTEMPO (1 equiv) was added. ^dBHT (1 equiv) was added.

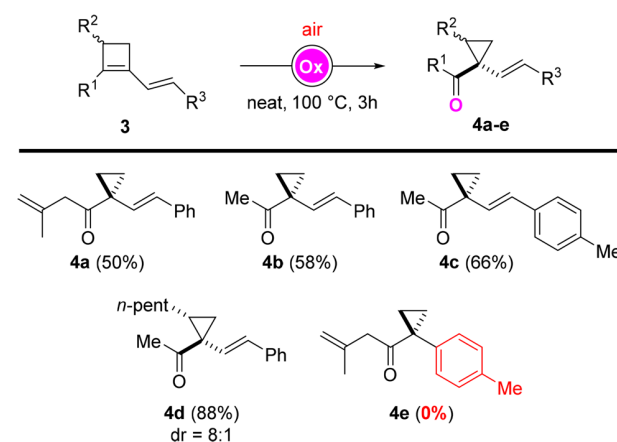
Performing the reaction neat in air led to incomplete conversion, while pure oxygen favored the formation of 1,4-diketone **6a** (entries 1 and 2), as recently exemplified by Loh and co-workers.¹⁶ Similar ratios were observed when H₂O was used as a solvent in the presence of O₂ (entry 3), and prolonged reaction times were noted when substrates were solubilized in EtOAc (entry 4). In the absence of air (nitrogen atmosphere), no oxidation was observed, leaving the starting material unreacted (entry 5). Addition of TEMPO or BHT to the solution prevented the reaction, supporting the assumption of an initial radical addition of O₂ to the unsaturated system (entries 6 and 7), and the starting material was recovered. Taking the reaction under air up to 100 °C afforded full conversion of the starting cyclobutene in 3 h, furnishing exclusively the mono-oxidized compound **4a**, supporting the intermediate formation of cyclobutene oxide **5**, undergoing a dyotropic rearrangement at higher temperatures (entry 8).

Through a favored path 1 under thermal conditions (see Scheme 2), the exclusive formation of the desired product is the result of two converging and complementary reactions: (1) the consumption of the dioxirane [I] giving the ketone **4** along with the epoxide **5** and (2) the Meinwald rearrangement of the latter epoxide under thermal conditions.

With optimized conditions in hand for air-promoted oxidative ring contraction, cyclobutenes **3a–c** led to CPKs **4a–c** in good yields up to 66%. When chiral cyclobutene **3d** was used, **4d** was isolated with a good diastereoisomeric ratio (dr = 8:1 determined by ¹³C NMR, Scheme 3).

Surprisingly, when arylcyclobutene (**3e**) was subjected to similar conditions, none of the corresponding CPK **4e** could be

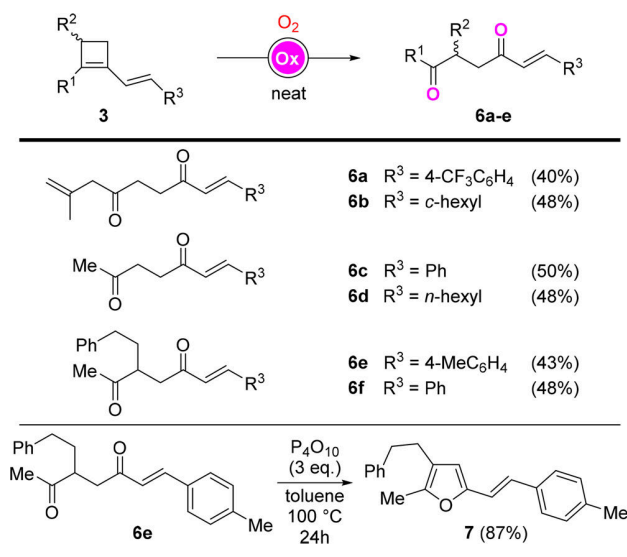
Scheme 3. Representative Examples of Air-Promoted Oxidative Ring Contraction



detected, even after prolonged reaction time (further optimizations will be disclosed later).

As depicted in Table 1, the use of pure oxygen favored a formal [2 + 2]-cycloaddition, giving a majority of 1,4-diketone **6**. The scope of this transformation was briefly explored, as such motifs present synthetic applications in organic chemistry.¹⁶ Vinylcyclobutenes **3** were submitted to an atmosphere of dioxygen, furnishing diketones **6a–f** in moderate yields (Scheme 4). Moreover, **6e** was employed in a Paal–Knorr condensation to undergo the formation of trisubstituted furan **7** in 87% yield.

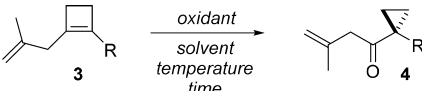
Scheme 4. Synthetic Scope of 1,4-Diketone Formation



Selective Formation of CPKs with Oxidants. Overcoming the limitation of the ring contraction to styryl systems required developing additional optimizations. Diverse oxidizing reagents were tested for the transformation of **3a** and **3e** into **4a** and **4e**, respectively (Table 2).

Even though DMDO afforded full conversion of **3a** at room temperature (entry 1, Table 2), many overoxidized side products were observed. When *m*CPBA was used (entries 2 and 3), complete consumption of the starting material was observed, giving the desired ring-contracted product independ-

Table 2. Condition Optimizations



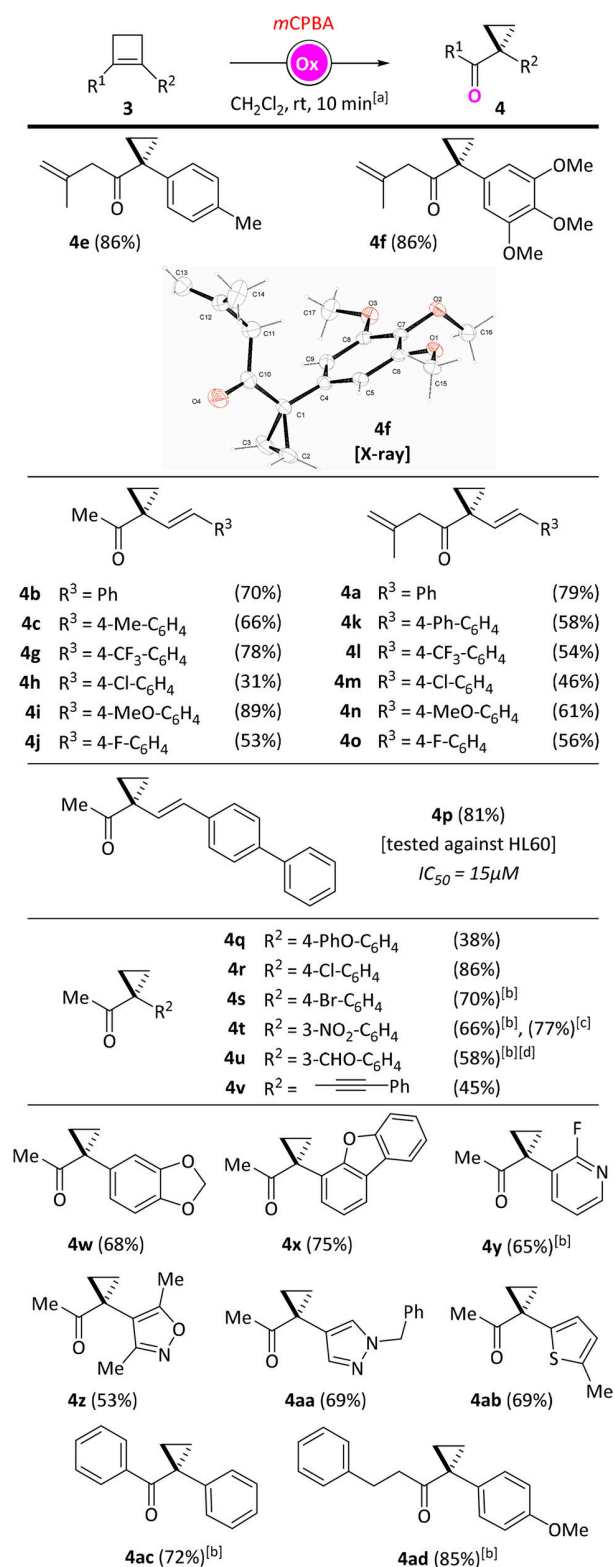
entry	R	oxidant	temp. (°C)	t	conv. (%) ^[a]
1	Ph	DMDO ^[b]	rt	3h	>99 ^[c]
2	Ph	<i>m</i> CPBA ^[d]	0	10min	>99
3	Ph	<i>m</i> CPBA ^[d]	rt	10min	>99
4	<i>p</i> -Tol	<i>m</i> CPBA ^[d]	rt	10min	>99
5	<i>p</i> -Tol	<i>m</i> CPBA ^[e]	rt	18h	75 ^[f]
6	<i>p</i> -Tol	<i>t</i> -BuOOH ^[d]	rt	18h	traces
7	<i>p</i> -Tol	AcOOH ^[d]	rt	18h	33
8	<i>p</i> -Tol	H ₂ O ₂ ^[g]	rt	18h	traces
9	<i>p</i> -Tol	NaOCl ^[h]	rt	18h	70 ^[h]

^aConversion of the starting material and proportions determined by GC/NMR. ^bAcetone from the in situ generation of DMDO. ^cMany side products observed. ^d1 equiv, in CH₂Cl₂. ^eNaHCO₃ (2 equiv) was added to the reaction. ^f75% conversion of the starting material, but in a 50:50 ratio of epoxidation product and desired product 4; see the SI. ^g5 equiv, NaOH (0.1 equiv), in MeOH. ^h(*R,R*)-Jacobsen's catalyst (5 mol %): 70% conversion of the starting material, but in a 30:70 ratio of epoxidation product and desired product 4; see the SI.

ently from the temperature.¹⁷ Interestingly, only the most activated double bond (cyclobutene) reacted during the reaction, leaving both allyl and vinyl groups untouched. Moreover, the air-stable substrate 3e furnished the rearranged product 4e under these optimized and mild conditions. We assumed that the Meinwald rearrangement was assisted by the presence of *m*-chlorobenzoic acid, released by the epoxidation reaction. To test this hypothesis, a similar experiment (entry 5) was conducted in the presence of NaHCO₃. If 75% conversion were observed, the ring contraction was partially inhibited by the presence of the base, as the cyclobutene oxide was observed in a 50:50 ratio with the desired cyclopropylketone, thus supporting the intermediary epoxide formation as well as the assistance of the acid in the ring-contraction process. Furthermore, the scope of oxidants was evaluated. While alkyl peroxide or hydrogen peroxide did not promote any oxidation, leaving the starting material unreacted (entries 6 and 8), peracetic acid afforded 33% conversion after 18h (entry 7). At last, Jacobsen's catalyst was employed in the presence of sodium hypochlorite (entry 9) and could convert 70% of the starting cyclobutene 3e in 18 h. However, the uncontracted cyclobutene oxide was detected in a 30:70 ratio with the desired product 4, supporting the need for acidic conditions in the Meinwald rearrangement.

To establish the scope of the transformation, a range of cyclobutenes was engaged in the oxidative ring contraction under reoptimized conditions. First, 3e, which remained unaffected under an atmospheric environment, furnished the desired CPK 4e in 86% yield (Scheme 5). Likewise, an electroenriched substrate led to the expected ring-contracted product 4f in similar yield, and a crystal structure was obtained to confirm the presence of the cyclopropylketone scaffold.¹⁸

Vinylcyclobutenes, the oxidative ring contraction of which was established with air, underwent smooth conversion to CPKs 4a–c and 4g–o with peracids in similar to high yields (up to 89%).

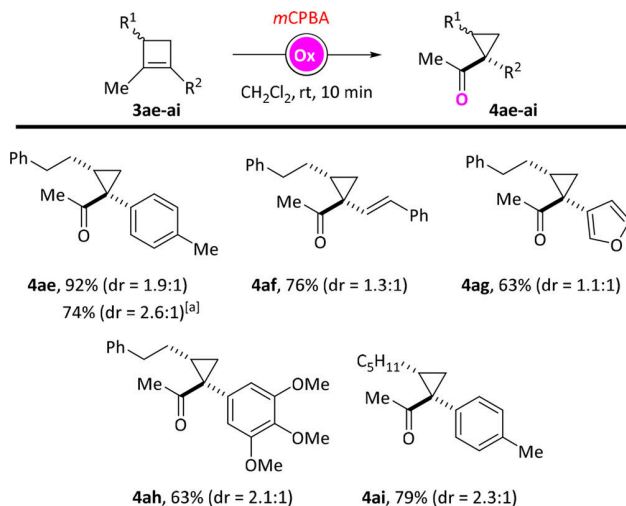
Scheme 5. Representative Examples of *m*CPBA-Promoted Oxidative Ring Contraction

^a*m*CPBA (1 equiv). ^bBF₃·OEt₂ (1 equiv) was added to the reaction mixture. ^cThe product was obtained from the corresponding 3-NH₂C₆H₄ derivative. ^dThe aldehyde was obtained after hydrolysis, starting from the corresponding 1,3-dioxolane (see the Supporting Information).

Noteworthy, the very simple CPK-containing skeleton **4p** was found to possess a moderate activity against tumor cells HL60 ($IC_{50} = 15 \mu M$; see the SI). In all cases, only the internal strained alkene reacted with the oxidant, leaving additional double bonds intact. In a second instance, aryl-substituted cyclobutenes were subjected to oxidation, yielding the corresponding adducts **4q–u** and **4w**. While electron-donor substituents underwent a direct ring contraction (**4q,r, 4w**), the addition of a Lewis acid ($BF_3 \cdot OEt_2$) was needed to drive the reaction to completion with electron-withdrawing groups (**4s–u**). Although an alkynyl derivative also furnished the desired product, a lower yield was obtained (**4v**, 45%). Finally, we pushed the methodology further to test the versatility of the process when using heteroaryl-substituted cyclobutenes. Dibenzofuryl, fluoropyridyl, dimethyloxazolyl, and benzylpyrazolyl substituents were tolerated, and the corresponding compounds **4w–z** were isolated in good yields up to 75%. Interestingly, the presence of a sulfur atom in the aromatic core (thiophene-yl) did not affect the course of the transformation, giving the derivative **4ab** in good yield (69%), the aromatic ring remaining unoxidized. Finally, different approaches were employed to introduce phenyl and ethylphenyl moieties on the starting cyclobutene.^{19,20} Their oxidation in the presence of *m*CPBA led to diversely substituted cyclopropylketones **4ac** and **4ad**, thus extending the scope of the oxidative ring contraction to aryl and alkyl groups.

Next, we investigated the oxidative ring contraction of chiral cyclobutenes (Scheme 6).

Scheme 6. Representative Examples of *m*CPBA-Promoted Oxidative Ring Contraction



^a–40 °C to rt, 3 h.

Employing similar oxidative conditions, cyclobutenes **3ae–ai** underwent rapid ring contraction, providing CPKs **4ae–ai** in good to excellent yields (up to 92%, **4ae**). The diastereoselectivity of the transformation seems to depend on the nature of the substrate. Only moderate to low diastereomeric ratios were observed (dr up to 2.3:1). We attributed the deficiency in stereoselectivity to a fast epoxidation, the shielding effect of the R^1 chain playing only a minor role in the stereodifferentiation of the double bond. Decreasing the temperature to –40 °C slightly improved the diastereoselectivity for the ring contraction to 2.6:1 dr (**4ae**).

Synthesis of Bioactive Targets. To further explore the synthetic utility of our methodology, we set out to access bioactive substances or their related precursors (Scheme 7). A common starting material (4-bromobutene) was utilized to begin these syntheses. Cyclobutene iodides were formed in a one-pot process through lithiation/carboalumination/iodolysis and, after simple extraction, reacted using a palladium-catalyzed Negishi or Suzuki cross-coupling reaction to afford the corresponding arylated cyclobutenes. Further oxidation with *m*CPBA was performed on crude materials, giving CPKs **4r, 4w**, and **4aj** in good yields (68–86%). At first, postderivatization was achieved on the methylketone moiety of **4r** by enolization/electrophilic trapping employing 2-pyridylsulfonylfluoride to provide the dehydrogenase inhibitor **B** in a single step. Second, modification of the methylketone was carried out through haloform reaction with CCl_4 , providing cyclopropylcarboxylic acids **8a,b** in quantitative yields. Importantly, **8b** stands as the precursor in the lumacaftor (**E**) synthesis (potent drug against cystic fibrosis in combination with ivacaftor).^{6g} Prederivatization was also envisioned and applied to the synthesis of an analogue structure of the herbicide **C** providing the deoxy-C herbicide in 43% yield over two steps. Initial Suzuki cross-coupling of previously iodinated **CB-M** (see Scheme 1) with (2-methoxyphenyl)boronic acid resulted in the corresponding cyclobutene **9** in 77%. Upon exposure of **9** to BBr_3 , followed by nucleophilic substitution on dichloropyridazine, **10** was obtained and directly employed in the final oxidative ring contraction without purification, completing the synthesis of deoxy-C **11** in 43% yield over two steps.

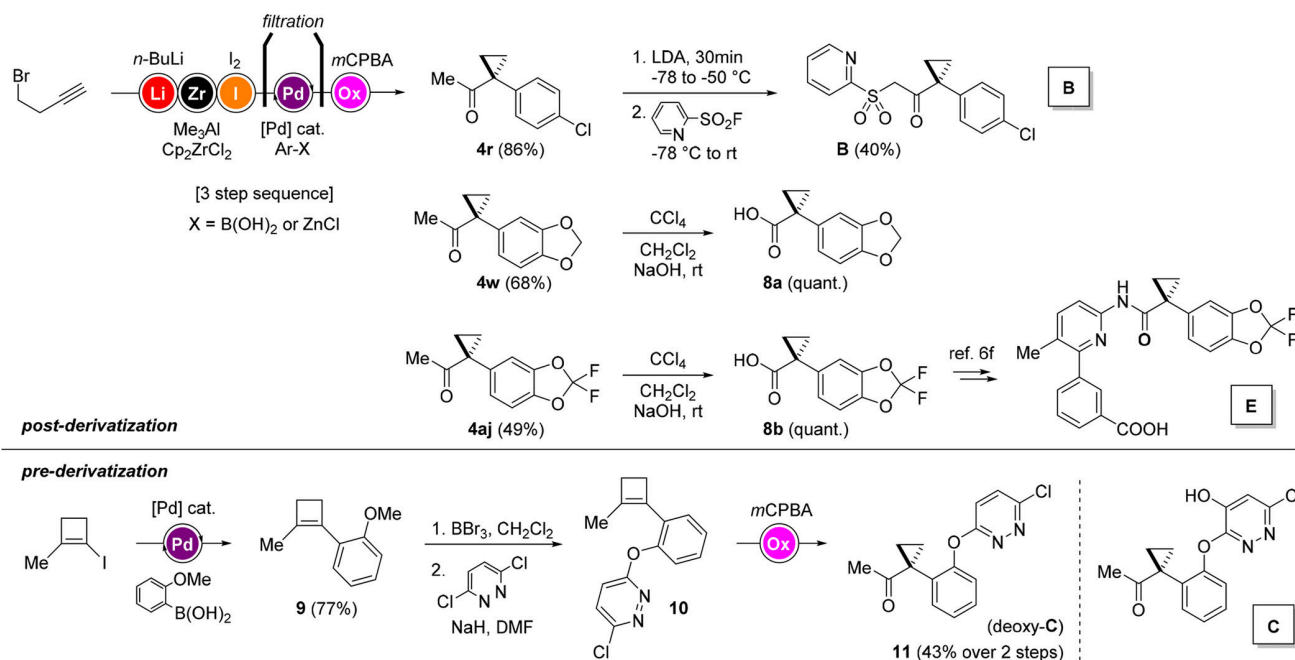
Sequence To Access Cyclopropyl Aldehydes. To ensure a broader applicability of the method, we finally assembled a sequence for the formation of cyclopropylaldehydes. To achieve that goal, commercially available cyclobutanone **12** was submitted to nucleophilic addition of an arylmetal species, and the resulting alcoholate was further acetylated. β -Elimination on **15** in the presence of lithium bromide after exchanging the solvent with dimethylformamide furnished arylated cyclobutene **16**. With a sufficient purity, **16** was further engaged without purification in the oxidative ring contraction in the presence of *m*CPBA, giving the desired rearranged compounds **13a–f** (Scheme 8). Employing diversely substituted aromatic structures showcases the efficient formation of a range of cyclopropyl aldehydes in six steps from commercial sources and with a sole purification step in moderate to good yields (34 to 69%).

COMPUTATIONAL ANALYSIS

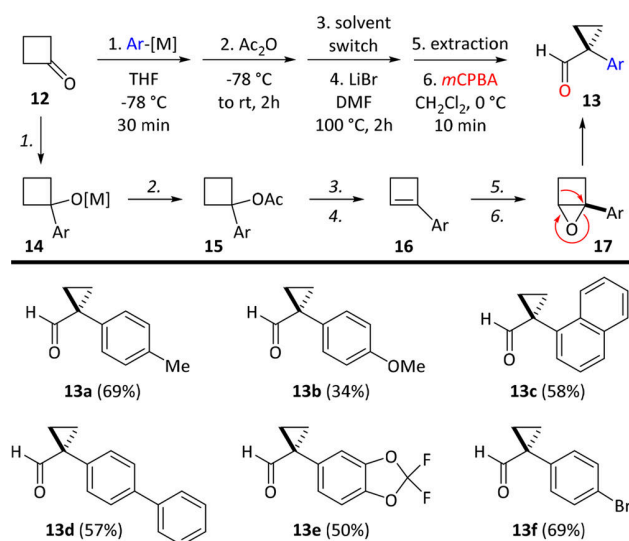
The proposed mechanism of the oxidative ring contraction of cyclobutene **3** (Scheme 2) was investigated theoretically for a better understanding. DFT with the B3LYP functional and the 6-31G(d) basis set of the program package Gaussian16²¹ was used generally for all geometry optimizations. Only geometry point TSDK1 was computed at the CASSCF/6-31G(d) level of theory with the program package Molpro2012²² for a correct description of the state.

The energies of the discussed reaction scheme were then obtained by applying the CASPT2 routine of the program package Molcas 8.2²³ with the ANO-L-VDZP basis set on the optimized structures. It is a common procedure to perform geometry optimizations on a low level of theory, as, e.g., DFT, and then correct the calculated energies using single-point calculations at a higher level of theory, as, e.g., the CASPT2, to include nondynamic and dynamic electron correlation.²⁴

Scheme 7. Straightforward Syntheses and Formal Synthesis of Bioactive Substances through Oxidative Ring Contraction

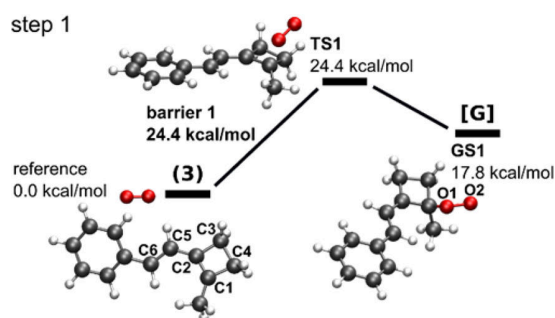


Scheme 8. Direct Access to Cyclopropyl Aldehydes from Commercially Available Cyclobutanone



Investigating the mechanism proposed in Scheme 2 computationally, we need to describe diradicalic structures. To do this correctly, we use the multireference method CASPT2. A more detailed description of the computational methods is given in the Supporting Information. Specific options for the CASPT2 calculations, as the chosen active space, are discussed there. For completeness, we also show the results at the B3LYP level of theory.

The first step of the mechanism (Scheme 9) is the same for both observed products, cyclopropane 4 and diketone 6. Triplet oxygen ($^3\text{O}_2$) adds to the C–C double bond of the cyclobutene ring forming a C–O bond between C1 and O1 to generate the diradical GS1. The barrier for this addition lies with 24.4 kcal/mol in the possible range for a slow reaction at room temperature. At GS1, the occupied T_1 state and the S_0 state

Scheme 9. Barrier for the Addition of Triplet Oxygen ($^3\text{O}_2$) to Cyclobutene 3 at the CASPT2/ANO-L-VDZP Level of Theory^a

^a[G] corresponds to the nomenclature used in Scheme 2. The given energies are referenced to the energy of the educts, cyclobutene 3, and $^3\text{O}_2$, separated at 10 Å. Additionally, the numbering of important atoms used in the following discussion is shown.

both have the equivalent electronic diradicalic character and lie energetically close with $\Delta E \approx 0.001$ eV. Figure 2 shows the two single occupied orbitals of the S_0 and T_1 state to confirm the diradicalic character. One electron is localized at the oxygen

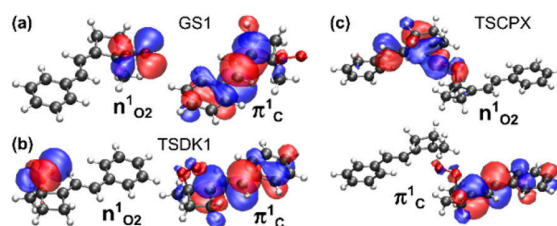
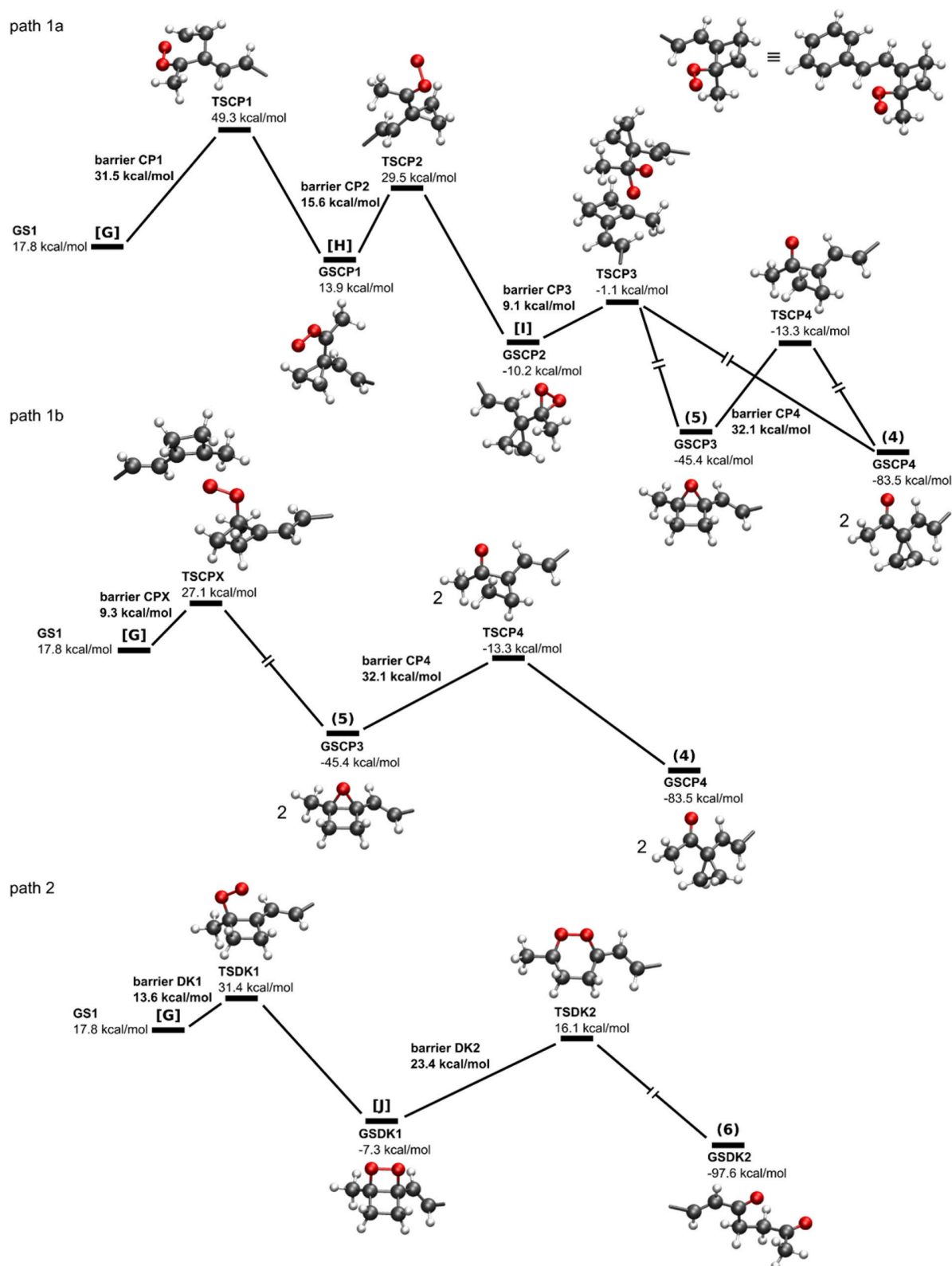


Figure 2. Single occupied orbitals of the S_0/T_1 state at (a) GS1, (b) TSDK1, and (c) TSCPX showing the diradicalic character at this geometry points.

Scheme 10. Reaction Scheme for Paths 1a, 1b, and 2 of the Oxidative Ring Contraction of Cyclobutene 3 at the CASPT2/ANO-L-VDZP Level of Theory^a^aThe labels in brackets correspond to the nomenclature used in Scheme 2. The structures are shown without the phenyl ring. The energies are referenced to the energy of the educts, cyclobutene 3, and ³O₂, separated at 10 Å.

atom O₂, and the second is delocalized over the allylic positions C2 and C6. The S₀ and T₁ states remain energetically close and keep their electronic character along the reaction path to the corresponding next transition state of each investigated pathway (Figure 2b,c). Calculations of the spin-orbit coupling suggest that intersystem crossing is possible in those regions. A detailed discussion and the calculated values are given in the Supporting Information. In the following discussion, we expect that intersystem crossing took place and all points are evaluated in the singlet ground state S₀.

Scheme 10 summarizes the results for the reaction pathways path 1a, path 1b, and path 2 discussed in Scheme 2. In path 1a, first proposed by Priesnitz,^{13a} the predicted dioxirane [I] (GSCP2) is reached in a stepwise process. First, the cyclobutene ring is rearranged to a cyclopropane ring to form GSCP1 [H]. The C–C bond between C1 and C4 is broken, and a bond between C2 and C4 is built in one step via TSCP1. This is followed by the formation of the second C–O bond between C1 and O2 via TSCP2 to form dioxirane [I]. For the next step, Priesnitz proposed that cyclobutene 3 is epoxidized by dioxirane [I]. This step via TSCP3 leads to the product CPK 4 (GSCP4) and the intermediate, epoxide 5 (GSCP3). Epoxide 5 can form another CPK 4 molecule via TSCP4, which corresponds to a Meinwald rearrangement.^{13,14} The first step of path 1a has a high barrier of 31.5 kcal/mol to TSCP1 accounting for a total barrier of 49.3 kcal/mol, which makes this pathway highly unlikely. Apparently, the rearrangement of the carbon bonds forming a cyclopropane ring from a cyclobutene ring is unfeasible at this point of the reaction path.

In Scheme 2 another mechanistic pathway to cyclobutene 3 was proposed (path 1b). Here, a direct epoxidation takes place after the addition of ³O₂ without formation of the cyclopropane ring. The diradical GS1 can epoxidize cyclobutene 3 via TSCPX to form two molecules of intermediate epoxide 5 (GSCP3). The next step of this pathway is the same as of path 1a. CPK 4 (GSCP4) is built via Meinwald rearrangement of epoxide 5. The barrier to TSCPX is with a value of 9.1 kcal/mol a lot of smaller than the barrier to TSCP1, which makes path 1b the favored pathway toward cyclobutene 4. The second transition state of this path (TSCP4) can be reached via a barrier of 32.1 kcal/mol, the largest barrier of this pathway. In the following, only the here proposed novel path 1b is discussed as reaction pathway leading to the product 4.

The reaction toward the second product, diketone 6, is described with path 2. Here, the first transition state (TSDK1) leads to a formation of a four-membered ring between the oxygen molecule and the two carbon atoms of the C–C double bond. This intermediate, dioxetane [G] (GSDK1), corresponds to a classical [2 + 2] cycloaddition product between ³O₂ and an alkene. The barrier for this step accounts for 13.6 kcal/mol. In the second step, the bonds of the four-membered dioxetane ring are rearranged via a six-membered transition state (TSDK2) to form diketone 6 (GSDK2). The corresponding barrier (23.4 kcal/mol) is of the same magnitude as the barrier for the first addition of ³O₂ to 3 (step 1).

Comparing both pathways (path 1b and path 2), first, confirms that the formation of both products is possible and, second, reveals a difference in 4.3 kcal/mol for the corresponding first barriers in favor of reaction path 1b. This also results in a difference of the same value in the total barriers of both pathways. Third, diketone 6 is the more stable product lying 14.1 kcal/mol lower than CPK 4.

In contrast to dioxetane [J], the intermediate epoxide 5 could be detected experimentally. This can be explained by the fact that 5 (GSCP3) is around 38.1 kcal/mol more stabilized than [J] (GSDK1). Furthermore, comparison of the corresponding barriers to each next step reveals that the barrier to TSCP4 is around 8.7 kcal/mol larger than the barrier to TSDK2. This means, the Meinwald rearrangement via TSCP4 to generate CPK 4 happens on a slower time-scale so that intermediate 5 can be detected under the given experimental conditions. The rearrangement toward 6 is expected to happen at the same time-scale than the initial attack of ³O₂ to 3 since the barriers are of the same height.

All computational results are in good agreement with the experimental product distributions under different reaction conditions. Using thermodynamical conditions with a low reaction temperature and a long reaction time leads preferentially to the more stable product diketone 6. In contrast, using kinetic conditions with a high reaction temperature and a short reaction time leads to CPK 4 whose pathway has the lower overall barrier. Furthermore, the observation of better yields of diketone 6 when the reaction is conducted under pure oxygen atmosphere (in contrast to the normal atmospheric conditions) can be explained by the theoretical results. The decisive transition state for the formation of CPK 4 (TSCPX) is a two-molecule transition-state between GS1 and educt cyclobutene 3. When more oxygen is available for the first reaction step, the addition of ³O₂ to 3, less reaction partner for GS1 is available to form epoxide 5 (GSCP2).

In summary, the proposed as well as observed intermediates are verified, and the complete proposed reaction mechanism is strongly supported by the theoretical study.

CONCLUSIONS

We have demonstrated a novel and efficient air-promoted oxidative ring contraction of easily generated vinyl cyclobutenes. Combining theoretical studies with experimental investigations finally led to proposing a new mechanistic path for the formation of α -substituted cyclopropylketones. These modules possessing interesting pharmacological properties, a general and selective sequence was designed starting from readily available substrates, allowing the synthesis of a wide variety of functionalized scaffolds. Such a straightforward approach undoubtedly opens an entire platform for high throughput screening in drug discovery processes.

EXPERIMENTAL SECTION

General Considerations. Commercially available starting materials were used without further purification unless otherwise stated. All reactions were carried out under N₂ atmosphere in flame-dried glassware. Syringes, which were used to transfer anhydrous solvents or reagents, were purged with nitrogen prior to use. CH₂Cl₂ was predried over CaCl₂ and distilled from CaH₂. THF was refluxed and distilled from sodium benzophenone ketyl under nitrogen. Et₂O was predried over CaCl₂ and passed through activated Al₂O₃ (the solvent purification system SPS-400-2 from Innovative Technologies, Inc.). Toluene was predried over CaCl₂ and distilled from, CaH₂. Chromatography purifications were performed using silica gel (SiO₂, 0.040–0.063 mm, 230–400 mesh ASTM) from Merck. The spots were visualized under UV (254 nm) or by staining the TLC with KMnO₄ solution (K₂CO₃, 10 g; KMnO₄, 1.5 g; H₂O, 150 mL; NaOH 10% in H₂O, 1.25 mL), PAA: *p*-anisaldehyde solution (concd H₂SO₄, 10 mL; EtOH, 200 mL; AcOH, 3 mL; *p*-anisaldehyde, 4 mL). Diastereoisomeric ratios were determined by ¹H NMR and ¹³C NMR.

^{13}C and ^1H NMR spectra were recorded on Varian Mercury 200, Bruker ARX 300, Varian VXR 400 S, and Bruker AMX 600 instruments. Chemical shifts are reported as δ values in ppm relative to residual solvent peak (^1H NMR) or solvent peak (^{13}C NMR) in deuterated chloroform (CDCl_3 ; δ 7.26 ppm for ^1H NMR and δ 77.16 ppm for ^{13}C NMR). Abbreviations for signal coupling are as follows: s (singlet), d (doublet), t (triplet), q (quartet), quint (quintet), m (multiplet) and br (broad). Reaction end points were determined by GC monitoring of the reactions. Gas chromatography was performed with machines of Agilent Technologies 7890, using a column of type HP 5 (Agilent 5% phenylmethylpolysiloxane; length: 15 m; diameter: 0.25 mm; film thickness: 0.25 μm) or Hewlett-Packard 6890 or 5890 series II, using a column of type HP 5 (Hewlett-Packard, 5% phenylmethylpolysiloxane; length: 15 m; diameter: 0.25 mm; film thickness: 0.25 μm). High-resolution mass spectra (HRMS) and low-resolution mass spectra (LRMS) were recorded on Finnigan MAT 95Q or Finnigan MAT 90 instrument or JEOL JMS-700. Infrared spectra were recorded on a Perkin 281 IR spectrometer and samples were measured neat (ATR, Smiths Detection DuraSample IR II Diamond ATR). The absorption bands were reported in wave numbers (cm^{-1}) and abbreviations for intensity are as follows: vs (very strong; maximum intensity), s (strong; above 75% of max. intensity), m (medium; from 50% to 75% of max. intensity), w (weak; below 50% of max. intensity) and br (broad). Melting points were determined on a Büchi B-540 apparatus and uncorrected. Single crystals were grown in small quench vials with a volume of 5.0 mL from slow evaporation of dichloromethane/hexanes mixtures at room temperature. Suitable single crystals were then introduced into perfluorinated oil and mounted on top of a thin glass wire. Data collection was performed at 100 K with a Bruker D8 Venture TXS equipped with a Spellman generator (50 kV, 40 mA) and a Kappa CCD detector operating with Mo $K\alpha$ radiation ($\lambda = 0.71071 \text{ \AA}$).

s-BuLi and *t*-BuLi were purchased as solutions in cyclohexane/hexanes mixtures from Rockwood Lithium GmbH. The commercially available Grignard reagents MeMgCl, PhMgCl, and *n*-BuMgCl were also purchased from Rockwood Lithium GmbH as solutions in THF.

The concentration of organometallic reagent from commercially purchased and synthesized reagents was determined either by titration of isopropyl alcohol using the indicator 4-(phenylazo)diphenylamine in THF for Grignard reagents or using the indicator *N*-benzylbenzamide in THF for organolithium reagents. [*s*-BuLi] = 1.31 M in cyclohexane (titration with isopropanol/1,10-phenanthroline), purchased from Rockwood Lithium GmbH. [*i*-PrMgCl-LiCl] = 1.1 M in THF (titration with iodine), purchased from Rockwood Lithium GmbH. [*n*-BuLi] = 2.44 M in cyclohexane (titration with isopropanol/1,10-phenanthroline), purchased from Rockwood Lithium GmbH.

General Procedure A for the Synthesis of Cyclobutenes 3.³ To cyclobutene iodides **2** in THF (0.2 M) were consecutively added Pd(dppf) $\text{Cl}_2 \cdot \text{CH}_2\text{Cl}_2$ (4 mol %), the appropriate organoboronic acid (1.0–2.0 equiv), and a 1 M solution of NaOH (3.0 equiv). The mixture was stirred at ambient temperature until TLC showed full consumption of the starting iodide **2** (20 min up to overnight). The reaction was quenched by addition of water, extracted with Et $_2$ O (3 \times 20 mL), and dried over MgSO $_4$. The crude product was concentrated under reduced pressure and finally filtrated through a short silica column to remove palladium salts. Crude materials were used without further purification.

General Procedure B for the Synthesis of Cyclopropylketones 4 and 11. To cyclobutenes **3** in CH_2Cl_2 (0.1 M) was added *m*CPBA in CH_2Cl_2 (0.3 M, 1.0 equiv) at 0 $^\circ\text{C}$. The reaction was checked after 10 min by TLC, and another portion of *m*CPBA (0.5 equiv) was added if the reaction was not complete. This step was repeated until full conversion of the substrates. The reaction was treated by addition of NaOH (1 M) and extracted with CH_2Cl_2 (3 \times 20 mL). Volatiles were removed under reduced pressure and the crude product purified by chromatography. **Procedure Ba.** The desired products **4** and **11** were obtained analytically pure. **Procedure Bb.** In the case of **4s,t,u,y,ac,ad,aj** the epoxide intermediate **5** was obtained after chromatography, as it did not undergo ring contraction. In such

cases, intermediates were dissolved in Et $_2$ O (0.3 M), and BF $_3 \cdot \text{OEt}_2$ (1.0 equiv) was added. As completion of the rearrangement was observed after 10 min, the final products could be purified by chromatography after extraction.

General Procedure C for the Synthesis of Cyclopropylaldehydes 13. To aryl halide (1.05 equiv) in THF (0.33 M) was added dropwise *n*-BuLi (1.1 eq, 2.44 M) at -78°C under inert atmosphere, and the mixture was stirred for 15 min at this temperature. Cyclobutanone **12** (1 equiv) in THF (1 M) was added at -78°C , and the reaction stirred for 30 min before warming to room temperature. Ac $_2$ O (2 equiv) was added at -78°C , and the reaction was allowed to warm to room temperature and stirred for 2 h. Volatiles were removed under vacuum, DMF (0.5 M) was added, followed by LiBr (10 equiv), and the mixture was heated to 100 $^\circ\text{C}$ and allowed to stir for 2 h. After completion of the transformation and monitoring by TLC, the mixture was allowed to cool to room temperature, washed with water and brine, and extracted with EtOAc. The organic phase was dried over MgSO $_4$ and the solvent removed under reduced pressure. To crude cyclobutenes **16** in CH_2Cl_2 (0.1 M) was added *m*CPBA in CH_2Cl_2 (1.0 equiv, 0.3 M) at 0 $^\circ\text{C}$. The reaction was checked after 10 min by TLC, and another portion of *m*CPBA (0.5 equiv) was added if the reaction was not complete. This was repeated once if need be. The reaction was quenched by addition of NaOH (1 M) and extracted with CH_2Cl_2 (3 \times 20 mL). The solvent was evaporated under reduced pressure and the crude product purified by chromatography.

Experimental Data. 1-Methoxy-4-(2-phenethylcyclobut-1-en-1-yl)benzene (3ad).¹⁹ To a solution of (C_5H_5) $_2\text{ZrCl}_2$ (1 equiv) in THF (0.2 M) was added EtMgBr (2 equiv) at -78°C . The reaction mixture was warmed to -40°C and stirred for 1 h. To the mixture was added (4-chlorobut-3-yn-1-yl)benzene (1 equiv) in THF (5 M) at -78°C . The mixture was stirred for 1 h at room temperature. After being cooled to -40°C , the reaction was quenched with iodide (2 equiv) and allowed to warm to room temperature. The mixture was poured onto an ice/1 M HCl solution, extracted with hexanes, dried with MgSO $_4$, and filtered. The solvent was removed under reduced pressure, and the crude mixture was purified over silica with hexanes as eluent ($R_f = 0.7$ (hexane, UV, KMnO $_4$, PAA)). (2-(2-Iodocyclobut-1-en-1-yl)ethyl)benzene was then used in the following cross-coupling reaction. Therefore, LiCl (1.1 equiv) and Mg (1.6 equiv) were dried under inert atmosphere followed by addition of THF (0.4 M) and one drop of dibromoethane. The mixture was heated once to reflux to activate the Grignard. After the mixture was cooled back to room temperature, B(Oi-Pr) $_3$ (1.5 equiv) was added. (2-(2-Iodocyclobut-1-en-1-yl)ethyl)benzene (0.5 M) was added dropwise to the reaction. After 2 h, a cloudy suspension was formed. To the suspension was then added Pd(dppf) Cl_2 dichloromethane adduct (4 mol %), 1-iodo-4-methoxybenzene (0.80 equiv), and an aqueous solution of sodium hydroxide (1.5 equiv, 1.00 M). The reaction mixture stirred overnight and then extracted with diethyl ether (3 \times 20 mL), washed with a saturated aqueous solution of sodium chloride (20 mL), dried with magnesium sulfate, filtered, concentrated, and purified via flash column chromatography to provide **3ad** (0.27 mmol, 72 mg, 55%) as a colorless oil. $R_f = 0.20$ (hexane, UV, KMnO $_4$, PAA). ^1H NMR (400 MHz, CDCl_3): δ 7.35–7.18 (m, 7H), 6.89–6.82 (m, 2H), 3.82 (s, 3H), 2.86 (dd, $J = 9.6, 6.4 \text{ Hz}$, 2H), 2.75–2.67 (m, 2H), 2.65–2.59 (m, 2H), 2.51–2.42 ppm (m, 2H). ^{13}C NMR (101 MHz, CDCl_3): δ 158.4, 142.2, 139.7, 137.3, 129.3, 128.5, 128.4, 126.9, 126.0, 113.9, 55.4, 33.7, 32.1, 27.7, 26.1 ppm. LRMS (DEP/EI-Orbitrap) m/z : 264.1 (30), 249.1 (40), 235.0 (5), 221.1 (5), 203.1 (2). HRMS (EI-Orbitrap) m/z : [$\text{M}]^+$ calcd for $\text{C}_{19}\text{H}_{20}\text{O}^+$ 264.1514, found 264.1507. IR (Diamond-ATR, neat) $\tilde{\nu}_{\text{max}}$: 3059 (w), 3024 (w), 1780 (w), 1726 (w), 1670 (s), 1614 (vw), 1597 (m), 1578 cm^{-1} (w).

(E)-3-Methyl-1-(1-styrylcyclopropyl)but-3-en-1-one (4a). Using 1-iodo-2-(2-methylallyl)cyclobut-1-ene (**2a**) and (E)-styrylboronic acid according to general procedures A and Ba provided **4a** (0.20 mmol, 45 mg, 79%) as a colorless oil. $R_f = 0.80$ (hexane/EtOAc 9:1, UV, KMnO $_4$, PAA). ^1H NMR (400 MHz, CDCl_3) δ 7.42–7.31 (m, 4H), 7.29–7.22 (m, 1H), 6.83 (d, $J = 15.8 \text{ Hz}$, 1H), 6.42 (d, $J = 15.8 \text{ Hz}$, 1H), 4.96–4.93 (m, 1H), 4.77–4.75 (m, 1H), 3.33 (s, 2H), 1.76 (t, $J = 1.1 \text{ Hz}$, 3H), 1.50 (dd, $J = 6.9, 3.7 \text{ Hz}$, 2H), 1.15 ppm (dd, $J = 7.1, 3.9$

Hz, 2H). ^{13}C NMR (101 MHz, CDCl_3) δ 207.8, 139.5, 136.9, 131.4, 128.8, 128.2, 127.8, 126.3, 114.8, 49.9, 33.8, 22.9, 19.8 ppm. LRMS (DEP/EI-Orbitrap) m/z : 226.2 (3), 211.2 (12), 184.1 (21), 141.1 (31), 128.1 (100). HRMS (EI-Orbitrap) m/z : $[\text{M}]^+$ calcd for $\text{C}_{16}\text{H}_{18}\text{O}^+$ 226.1358, found 226.1353. IR (Diamond-ATR, neat) $\tilde{\nu}_{\text{max}}$: 3080 (vw), 3027 (w), 2920 (w), 2852 (w), 1690 (s), 1646 (w), 1600 cm^{-1} (w).

(*E*)-1-(1-(*Styryl*cyclopropyl)ethanone (**4b**). Using 1-iodo-2-methylcyclobut-1-ene (**2b**) and (*E*)-styrylboronic acid according to general procedures A and Ba provided **4b** (0.35 mmol, 65 mg, 70%) as a colorless oil. Compound **4b** was also obtained by following procedure A and subjecting the cross-coupling product to air at 100 °C for 3 h (58%). R_f = 0.5 (hexane/EtOAc 9:1, UV, KMnO_4 , PAA). ^1H NMR (400 MHz, CDCl_3) δ 7.33–7.28 (m, 2H), 7.27–7.22 (m, 2H), 7.20–7.14 (m, 1H), 6.76 (d, J = 15.9 Hz, 1H), 6.31 (d, J = 15.9 Hz, 1H), 2.17 (s, 3H), 1.42 (dd, J = 6.6, 4.2 Hz, 1H), 1.09 ppm (dd, J = 7.3, 3.8 Hz, 1H). ^{13}C NMR (101 MHz, CDCl_3) δ 208.1, 136.9, 130.6, 128.8, 128.4, 127.8, 126.3, 33.9, 28.4, 19.6 ppm. LRMS (DEP/EI-Orbitrap) m/z : 186.1 (40), 171.1 (28), 157.1 (15), 143.1 (40), 128.1 (100). HRMS (EI-Orbitrap) m/z : $[\text{M}]^+$ calcd for $\text{C}_{13}\text{H}_{14}\text{O}^+$ 186.1045, found 186.1039. IR (Diamond-ATR, neat) $\tilde{\nu}_{\text{max}}$: 3082 (vw), 3058 (vw), 3026 (w), 3006 (w), 2926 (vw), 1688 (s), 1646 (w), 1600 cm^{-1} (w).

(*E*)-1-(1-(4-Methylstyryl)cyclopropyl)ethanone (**4c**). Using **2b** and (*E*)-(4-methylstyryl)boronic acid according to general procedures A and Ba provided **4c** (0.17 mmol, 33 mg, 66%) as a colorless oil. Compound **4c** was also obtained by following procedure A and subjecting the cross-coupling product to air at 100 °C for 3 h (66%). R_f = 0.5 (hexane/EtOAc 9:1, UV, KMnO_4 , PAA). ^1H NMR (400 MHz, CDCl_3) 7.30–7.26 (m, 2H), 7.18–7.10 (m, 2H), 6.77 (d, J = 15.8 Hz, 1H), 6.36 (d, J = 15.8 Hz, 1H), 2.34 (s, 3H), 2.25 (s, 3H), 1.48 (dd, J = 6.7, 4.0 Hz, 2H), 1.15 ppm (dd, J = 7.2, 3.6 Hz, 2H). ^{13}C NMR (101 MHz, CDCl_3) δ 208.4, 137.6, 134.1, 130.6, 129.5, 127.4, 126.2, 33.9, 28.5, 21.3, 19.5 ppm. LRMS (DEP/EI-Orbitrap) m/z : 200.1 (42), 185.1 (13), 157.1 (50), 142.1 (100). HRMS (EI-Orbitrap) m/z : $[\text{M}]^+$ calcd for $\text{C}_{14}\text{H}_{16}\text{O}^+$ 200.1201, found 200.1192. IR (Diamond-ATR, neat) $\tilde{\nu}_{\text{max}}$: 3088 (vw), 3022 (w), 2922 (w), 2864 (vw), 1690 (vs), 1650 (w), 1612 (w), 1572 (vw), 1560 (vw), 1540 (vw) cm^{-1} .

1-((1*R*,2*R*)-2-Pentyl-1-((*E*)-styryl)cyclopropyl)ethanone (**4d**). Using 1-iodo-2-methyl-3-pentylcyclobut-1-ene (**2c**) and (*E*)-styrylboronic acid according to general procedures A and Ba provided **4d** (0.35 mmol, 65 mg, 70%) as a colorless oil. Compound **4d** was also obtained by following procedure A and subjecting the cross-coupling product to air at 100 °C for 3 h (88%). R_f = 0.6 (hexane/EtOAc 9:1, UV, KMnO_4 , PAA). ^1H NMR (400 MHz, CDCl_3) δ 7.41–7.29 (m, 4H), 7.26–7.22 (m, 1H), 6.74 (d, J = 15.8 Hz, 1H), 6.39 (d, J = 15.8 Hz, 1H), 2.33 (s, 3H), 1.59 (dd, J = 6.8, 4.1 Hz, 1H), 1.49–1.24 (m, 9H), 1.21 (dd, J = 8.3, 4.2 Hz, 1H), 0.88 ppm (t, J = 6.6 Hz, 3H). ^{13}C NMR (101 MHz, CDCl_3) δ 206.3, 137.0, 130.6, 130.2, 128.8, 127.7, 126.3, 39.5, 35.0, 31.7, 30.6, 29.6, 27.1, 22.8, 21.0, 14.2 ppm. LRMS (DEP/EI-Orbitrap) m/z : 256.1 (8), 213.2 (15), 160.1 (50). HRMS (EI-Orbitrap) m/z : $[\text{M}]^+$ calcd for $\text{C}_{18}\text{H}_{24}\text{O}^+$ 256.1827, found 256.1823. IR (Diamond-ATR, neat) $\tilde{\nu}_{\text{max}}$: 3645 (m), 1738 (w), 1481 (w), 1467 (m), 1441 (s), 1429 (vs) cm^{-1} .

3-Methyl-1-(1-(*p*-tolyl)cyclopropyl)but-3-en-1-one (**4e**). Using **2a** and 4,4,5,5-tetramethyl-2-(*p*-tolyl)-1,3,2-dioxaborolane according to general procedures A and Ba provided **4e** (0.22 mmol, 46 mg, 86%) as a colorless oil. R_f = 0.45 (hexane/EtOAc 9:1, UV, KMnO_4 , PAA). ^1H NMR (400 MHz, CDCl_3) δ 7.28–7.24 (m, 2H), 7.15 (d, J = 7.8 Hz, 2H), 4.88–4.79 (m, 1H), 4.57–4.53 (m, 1H), 3.02 (s, 2H), 2.36 (s, 3H), 1.63 (s, 3H), 1.60 (dd, J = 7.1, 3.2 Hz, 2H), 1.15 ppm (dd, J = 7.2, 3.2 Hz, 2H). ^{13}C NMR (101 MHz, CDCl_3) δ 208.8, 139.7, 137.9, 137.3, 131.1, 129.4, 114.4, 50.1, 37.1, 22.8, 21.3, 19.2 ppm. LRMS (DEP/EI-Orbitrap) m/z : 214.1 (8), 159.1 (26), 131.1 (100). HRMS (EI-Orbitrap) m/z : $[\text{M}]^+$ calcd for $\text{C}_{15}\text{H}_{18}\text{O}^+$ 214.1358, found 214.1354. IR (Diamond-ATR, neat) $\tilde{\nu}_{\text{max}}$: 3080 (vw), 2974 (w), 2922 (w), 2252 (vw), 1776 (w), 1692 (s), 1650 (w) cm^{-1} .

3-Methyl-1-(1-(3,4,5-trimethoxyphenyl)cyclopropyl)but-3-en-1-one (**4f**). Using **2a** and (3,4,5-trimethoxyphenyl)boronic acid according to general procedures A and Ba provided **4f** (0.22 mmol,

62 mg, 86%) as colorless solid. R_f = 0.35 (hexane/EtOAc 8:2, UV, KMnO_4 , PAA). ^1H NMR (400 MHz, CDCl_3) δ 6.58 (s, 2H), 4.84 (t, J = 1.6 Hz, 1H), 4.59 (dq, J = 2.0, 1.0 Hz, 1H), 3.86 (s, 6H), 3.85 (s, 3H), 3.06 (s, 2H), 1.69–1.55 (m, 3H), 1.58 (dd, J = 6.7, 3.5 Hz, 2H), 1.17 ppm (dd, J = 7.0, 3.5 Hz, 2H). ^{13}C NMR (101 MHz, CDCl_3) δ 208.4, 153.2, 139.8, 137.5, 136.4, 114.4, 108.0, 61.1, 56.3, 49.7, 38.0, 22.9, 19.3 ppm. LRMS (DEP/EI-Orbitrap) m/z : 290.1 (67), 275.1 (45), 235.1 (10), 207.1 (100), 192.1 (29), 176.1 (84), 161.1 (50). HRMS (EI-Orbitrap) m/z : $[\text{M}]^+$ calcd for $\text{C}_{17}\text{H}_{22}\text{O}_4^+$ 290.1518, found 290.1514. IR (Diamond-ATR, neat) $\tilde{\nu}_{\text{max}}$: 2968 (w), 2940 (w), 2924 (w), 2832 (w), 1692 (m), 1586 (m) cm^{-1} . Mp (°C): 81–82.

(*E*)-1-(1-(4-(Trifluoromethyl)styryl)cyclopropyl)ethanone (**4g**). Using **2b** and (*E*)-(4-(trifluoromethyl)styryl)boronic acid according to general procedures A and Ba provided **4g** (0.19 mmol, 49 mg, 78%) as a colorless oil. R_f = 0.4 (hexane/EtOAc 9:1, UV, KMnO_4 , PAA). ^1H NMR (400 MHz, CDCl_3) δ 7.57 (d, J = 8.1 Hz, 1H), 7.47 (d, J = 8.3 Hz, 1H), 6.99 (d, J = 15.9 Hz, 0H), 6.38 (d, J = 15.9 Hz, 0H), 2.23 (s, 1H), 1.55 (dd, J = 7.0, 4.3 Hz, 1H), 1.21 ppm (dd, J = 6.6, 3.9 Hz, 1H). ^{13}C NMR (101 MHz, CDCl_3) δ 207.3, 140.4 (q, J = 1.3 Hz), 131.3, 129.3 (q, J = 32.6 Hz), 128.7, 126.5, 125.7 (q, J = 3.8 Hz), 122.9 (q, J = 271.7 Hz), 34.0, 27.9, 19.7 ppm. LRMS (DEP/EI-Orbitrap) m/z : 254.1 (46), 225.1 (23), 191.1 (22). HRMS (EI-Orbitrap) m/z : $[\text{M}]^+$ calcd for $\text{C}_{14}\text{H}_{13}\text{F}_3\text{O}^+$ 254.0918, found 254.0913. IR (Diamond-ATR, neat) $\tilde{\nu}_{\text{max}}$: 3044 (vw), 3012 (vw), 2932 (vw), 1692 (m), 1648 (w), 1616 (w) cm^{-1} .

(*E*)-1-(1-(4-Chlorostyryl)cyclopropyl)ethanone (**4h**). Using **2b** and (*E*)-(4-chlorostyryl)boronic acid according to general procedures A and Ba provided **4h** (0.08 mmol, 17 mg, 31%) as a colorless oil. R_f = 0.45 (hexane/EtOAc 9:1, UV, KMnO_4 , PAA). ^1H NMR (400 MHz, CDCl_3) δ 7.33–7.26 (m, 4H), 6.83 (d, J = 15.9 Hz, 1H), 6.32 (d, J = 15.9 Hz, 1H), 2.22 (s, 3H), 1.51 (dd, J = 7.2, 4.4 Hz, 2H), 1.17 ppm (dd, J = 7.4, 3.6 Hz, 2H). ^{13}C NMR (101 MHz, CDCl_3) δ 207.7, 135.4, 133.3, 129.2, 129.2, 128.9, 127.5, 33.9, 28.1, 19.5 ppm. LRMS (DEP/EI-Orbitrap) m/z : 220.0 (46), 191.0 (11), 177.0 (30), 162.0 (21), 142.1 (100). HRMS (EI-Orbitrap) m/z : $[\text{M}]^+$ calcd for $\text{C}_{13}\text{H}_{13}\text{ClO}^+$ 220.0655, found 220.0647. IR (Diamond-ATR, neat) $\tilde{\nu}_{\text{max}}$: 3022 (vw), 2926 (vw), 1690 (vs), 1646 (w) cm^{-1} .

(*E*)-1-(1-(4-Methoxystyryl)cyclopropyl)ethanone (**4i**). Using **2b** and (*E*)-(4-methoxystyryl)boronic acid according to general procedures A and Ba provided **4i** (0.22 mmol, 48 mg, 89%) as a colorless oil. R_f = 0.4 (hexane/EtOAc 9:1, UV, KMnO_4 , PAA). ^1H NMR (400 MHz, CDCl_3) δ 7.38–7.28 (m, 2H), 6.91–6.82 (m, 2H), 6.67 (d, J = 15.9 Hz, 1H), 6.34 (d, J = 15.8 Hz, 1H), 3.81 (s, 3H), 2.25 (s, 3H), 1.58 (s, 4H), 1.47 (dd, J = 6.9, 4.3 Hz, 3H), 1.14 ppm (dd, J = 7.5, 3.6 Hz, 3H). ^{13}C NMR (101 MHz, CDCl_3) δ 208.6, 159.4, 130.3, 129.7, 127.5, 126.2, 114.2, 55.5, 33.9, 28.6, 19.5 ppm. LRMS (DEP/EI-Orbitrap) m/z : 216.0 (95), 201.0 (22), 173.0 (81), 158.0 (100), 141.1 (35). HRMS (EI-Orbitrap) m/z : $[\text{M}]^+$ calcd for $\text{C}_{14}\text{H}_{16}\text{O}_2^+$ 216.1150, found 216.1153.

(*E*)-1-(1-(4-Fluorostyryl)cyclopropyl)ethanone (**4j**). Using **2b** and (*E*)-(4-fluorostyryl)boronic acid according to general procedures A and Ba provided **4j** (0.13 mmol, 27 mg, 53%) as a colorless oil. R_f = 0.45 (hexane/EtOAc 9:1, UV, KMnO_4 , PAA). ^1H NMR (400 MHz, CDCl_3) δ 7.40–7.28 (m, 2H), 7.06–6.96 (m, 2H), 6.75 (d, J = 15.9 Hz, 1H), 6.34 (d, J = 15.9 Hz, 1H), 2.23 (s, 3H), 1.49 (dd, J = 7.0, 3.6 Hz, 2H), 1.16 ppm (dd, J = 7.2, 3.7 Hz, 2H). ^{13}C NMR (101 MHz, CDCl_3) δ 208.0, 162.4 (d, J = 246.9 Hz), 133.1 (d, J = 3.4 Hz), 129.4, 128.2 (d, J = 2.3 Hz), 127.8 (d, J = 8.0 Hz), 115.7 (d, J = 21.6 Hz), 33.9, 28.2, 19.4 ppm. LRMS (DEP/EI-Orbitrap) m/z : 204.1 (34), 175.0 (11), 161.1 (39), 146.0 (100). HRMS (EI-Orbitrap) m/z : $[\text{M}]^+$ calcd for $\text{C}_{13}\text{H}_{13}\text{FO}^+$ 204.0950, found 204.0946. IR (Diamond-ATR, neat) $\tilde{\nu}_{\text{max}}$: 3040 (vw), 3008 (vw), 2926 (vw), 1690 (s), 1652 (w), 1602 (m) cm^{-1} .

(*E*)-1-(1-(2-([1,1'-Biphenyl]-4-yl)vinyl)cyclopropyl)-3-methylbut-3-en-1-one (**4k**). Using **2a** and (*E*)-(2-([1,1'-biphenyl]-4-yl)vinyl)boronic acid according to general procedures A and Ba provided **4k** (0.15 mmol, 44 mg, 58%) as a colorless oil. R_f = 0.5 (hexane/EtOAc 9:1, UV, KMnO_4 , PAA). ^1H NMR (400 MHz, CDCl_3) δ 7.66–7.55 (m, 4H), 7.50–7.41 (m, 4H), 7.38–7.32 (m, 1H), 6.88 (d, J = 15.8 Hz, 1H), 6.46 (d, J = 15.8 Hz, 1H), 4.99–4.93 (m, 1H), 4.82–4.76

(m, 1H), 3.35 (s, 2H), 1.78 (s, 3H), 1.53 (dd, $J = 7.0, 4.0$ Hz, 2H), 1.17 ppm (dd, $J = 7.0, 3.0$ Hz, 2H). ^{13}C NMR (101 MHz, CDCl_3) δ 207.7, 140.7, 140.6, 139.5, 135.9, 130.9, 128.9, 128.3, 127.5, 127.5, 127.0, 126.8, 114.8, 49.9, 33.9, 23.0, 19.8 ppm. LRMS (DEP/EI-Orbitrap) m/z : 302.1 (37), 287.1 (45), 260.1 (41), 247.1 (100), 233.1 (11), 219.1 (61), 204.1 (83), 191.0 (47), 178.1 (53). HRMS (EI-Orbitrap) m/z : $[\text{M}]^+$ calcd for $\text{C}_{22}\text{H}_{22}\text{O}^+$ 302.1671, found 302.1665. IR (Diamond-ATR, neat) $\tilde{\nu}_{\text{max}}$: 3078 (vw), 3056 (vw), 3028 (w), 2972 (vw), 2914 (vw), 1688 (s), 1646 (w), 1602 (w), 1582 (vw) cm^{-1} .

(E)-3-Methyl-1-(1-(4-(trifluoromethyl)styryl)cyclopropyl)but-3-en-1-one (4l). Using **2a** and (E)-(4-(trifluoromethyl)styryl)boronic acid according to general procedures A and Ba provided **4l** (0.14 mmol, 40 mg, 54%) as a colorless oil. $R_f = 0.5$ (hexane/EtOAc 9:1, UV, KMnO_4 , PAA). ^1H NMR (400 MHz, CDCl_3) δ 7.57 (d, $J = 8.2$ Hz, 2H), 7.46 (d, $J = 8.1$ Hz, 2H), 6.97 (d, $J = 15.9$ Hz, 1H), 6.42 (d, $J = 15.8$ Hz, 1H), 4.97–4.93 (m, 1H), 4.79–4.71 (m, 1H), 3.29 (s, 2H), 1.76 (s, 3H), 1.55 (dd, $J = 6.7, 3.4$ Hz, 2H), 1.18 ppm (dd, $J = 7.3, 3.5$ Hz, 2H). ^{13}C NMR (101 MHz, CDCl_3) δ 207.0, 140.4 (q, $J = 1.4$ Hz), 139.3, 131.1, 129.6, 129.5 (q, $J = 32.4$ Hz), 126.5, 125.8 (q, $J = 3.8$ Hz), 124.3 (q, $J = 271.5$ Hz), 114.9, 49.6, 33.9, 22.9, 19.9 ppm. LRMS (DEP/EI-Orbitrap) m/z : 294.1 (8), 279.1 (30), 252.2 (35), 239.2 (11), 211.1 (34), 191.1 (100). HRMS (EI-Orbitrap) m/z : $[\text{M}]^+$ calcd for $\text{C}_{17}\text{H}_{17}\text{F}_3\text{O}^+$ 294.1231, found 294.1225. IR (Diamond-ATR, neat) $\tilde{\nu}_{\text{max}}$: 3080 (vw), 2976 (vw), 2918 (vw), 1692 (m), 1648 (w) cm^{-1} .

(E)-1-(1-(4-Chlorostyryl)cyclopropyl)-3-methylbut-3-en-1-one (4m). Using **2a** and (E)-(4-chlorostyryl)boronic acid according to general procedures A and Ba provided **4m** (0.11 mmol, 29 mg, 46%) as a colorless oil. $R_f = 0.5$ (hexane/EtOAc 9:1, UV, KMnO_4 , PAA). ^1H NMR (400 MHz, CDCl_3) δ 7.29 (app s, 4H), 6.81 (d, $J = 15.8$ Hz, 1H), 6.35 (d, $J = 15.9$ Hz, 1H), 4.97–4.90 (m, 1H), 4.78–4.72 (m, 1H), 3.30 (s, 3H), 1.75 (s, 2H), 1.51 (dd, $J = 7.4, 3.9$ Hz, 2H), 1.14 ppm (dd, $J = 7.7, 3.2$ Hz, 2H). ^{13}C NMR (101 MHz, CDCl_3) δ 207.4, 139.4, 135.4, 133.4, 130.0, 128.9, 128.9, 127.5, 114.8, 49.7, 33.8, 22.9, 19.8 ppm. LRMS (DEP/EI-Orbitrap) m/z : 260.1 (5), 245.1 (14), 218.1 (33), 205.0 (12), 177.0 (22). HRMS (EI-Orbitrap) m/z : $[\text{M}]^+$ calcd for $\text{C}_{16}\text{H}_{17}\text{ClO}^+$ 260.0968, found 260.0966. IR (Diamond-ATR, neat) $\tilde{\nu}_{\text{max}}$: 3080 (vw), 3028 (vw), 3014 (vw), 2974 (w), 2942 (vw), 2916 (w), 1690 (vs), 1646 (m), 1592 (w) cm^{-1} .

(E)-1-(1-(4-Methoxystyryl)cyclopropyl)-3-methylbut-3-en-1-one (4n). Using **2a** and (E)-(4-methoxystyryl)boronic acid according to general procedures A and Ba provided **4n** (0.15 mmol, 39 mg, 61%) as a colorless oil. $R_f = 0.5$ (hexane/EtOAc 9:1, UV, KMnO_4 , PAA). ^1H NMR (400 MHz, CDCl_3) δ 7.34–7.29 (m, 2H), 6.90–6.84 (m, 2H), 6.66 (d, $J = 15.8$ Hz, 1H), 6.37 (d, $J = 15.9$ Hz, 1H), 4.97–4.91 (m, 1H), 4.77–4.72 (m, 1H), 3.82 (s, 3H), 3.33 (s, 2H), 1.75 (app t, 3H), 1.47 (dd, $J = 7.0, 4.0$ Hz, 2H), 1.11 ppm (dd, $J = 7.3, 3.4$ Hz, 2H). ^{13}C NMR (101 MHz, CDCl_3) δ 208.2, 159.4, 139.6, 131.1, 129.7, 127.5, 125.9, 114.7, 114.2, 55.5, 50.0, 33.8, 23.0, 19.7 ppm. LRMS (DEP/EI-Orbitrap) m/z : 256.1 (31), 241.1 (12), 214.1 (28), 201.1 (87), 173.1 (76), 158.1 (100), 141.1 (40), 128.1 (58), 115.1 (82), 102.0 (186.1 (40), 171.1 (10). HRMS (EI-Orbitrap) m/z : $[\text{M}]^+$ calcd for $\text{C}_{17}\text{H}_{20}\text{O}_2^+$ 256.1463, found 256.1465. IR (Diamond-ATR, neat) $\tilde{\nu}_{\text{max}}$: 2967 (w), 2944 (w), 2934 (w), 2916 (w), 1723 (w), 1690 (m), 1652 (w), 1606 (m), 1576 (w), 1528 (w), 1511 (vs) cm^{-1} .

(E)-1-(1-(4-Fluorostyryl)cyclopropyl)-3-methylbut-3-en-1-one (4o). Using **2a** and (E)-(4-fluorostyryl)boronic acid according to general procedures A and Ba provided **4o** (0.14 mmol, 34 mg, 56%) as a colorless oil. $R_f = 0.6$ (hexane/EtOAc 9:1, UV, KMnO_4 , PAA). ^1H NMR (400 MHz, CDCl_3) δ 7.37–7.30 (m, 2H), 7.07–6.97 (m, 2H), 6.74 (d, $J = 15.9$ Hz, 1H), 6.37 (d, $J = 15.8$ Hz, 1H), 4.97–4.92 (m, 1H), 4.79–4.73 (m, 1H), 3.31 (s, 3H), 1.75 (app t, 3H), 1.50 (dd, $J = 7.4, 3.8$ Hz, 2H), 1.13 ppm (dd, $J = 7.4, 3.3$ Hz, 2H). ^{13}C NMR (101 MHz, CDCl_3) δ 207.7, 162.5 (d, $J = 247.0$ Hz), 139.5, 133.1 (d, $J = 3.4$ Hz), 130.2, 128.0 (d, $J = 2.3$ Hz), 127.8 (d, $J = 7.9$ Hz), 115.7 (d, $J = 21.6$ Hz), 114.8, 49.8, 33.8, 22.9, 19.7 ppm. LRMS (DEP/EI-Orbitrap) m/z : 244.1 (100). HRMS (EI-Orbitrap) m/z : $[\text{M}]^+$ calcd for $\text{C}_{16}\text{H}_{17}\text{FO}^+$ 244.1263, found 244.1261. IR (Diamond-ATR, neat) $\tilde{\nu}_{\text{max}}$: 3078 (vw), 2992 (vw), 2936 (vw), 1692 (s), 1652 (w), 1602 (w) cm^{-1} .

(E)-1-(1-(2-([1,1'-Biphenyl]-4-yl)vinyl)cyclopropyl)ethanone (4p). Using **2b** and (E)-(2-([1,1'-biphenyl]-4-yl)vinyl)boronic acid according to general procedures A and Ba provided **4p** (0.20 mmol, 53 mg, 81%) as white solid. $R_f = 0.45$ (hexane/EtOAc 9:1, UV, KMnO_4 , PAA). ^1H NMR (400 MHz, CDCl_3) δ 7.68–7.54 (m, 4H), 7.50–7.39 (m, 4H), 7.38–7.32 (m, 1H), 6.90 (d, $J = 15.9$ Hz, 1H), 6.42 (d, $J = 15.9$ Hz, 1H), 2.27 (s, 3H), 1.52 (dd, $J = 7.0, 3.9$ Hz, 2H), 1.19 ppm (dd, $J = 7.5, 3.7$ Hz, 2H). ^{13}C NMR (101 MHz, CDCl_3) δ 208.1, 140.7, 140.5, 135.9, 130.1, 128.9, 128.6, 127.5, 127.5, 127.0, 126.8, 34.0, 28.4, 19.6 ppm. LRMS (DEP/EI-Orbitrap) m/z : 262.2 (100), 247.1 (5), 219.1 (80). HRMS (EI-Orbitrap) m/z : $[\text{M}]^+$ calcd for $\text{C}_{19}\text{H}_{18}\text{O}^+$ 262.1358, found 262.1352. IR (Diamond-ATR, neat) $\tilde{\nu}_{\text{max}}$: 3028 (w), 2924 (w), 2854 (vw), 1688 (s), 1644 (w), 1600 (w) cm^{-1} .

1-(1-(4-Phenoxyphenyl)cyclopropyl)ethanone (4q). Using **2b** and (4-phenoxyphenyl)boronic acid according to general procedures A and Ba provided **4q** (0.10 mmol, 24 mg, 38%) as a colorless oil. $R_f = 0.5$ (hexane/EtOAc 9:1, UV, KMnO_4 , PAA). ^1H NMR (400 MHz, CDCl_3) δ 7.39–7.33 (m, 2H), 7.33–7.30 (m, 2H), 7.17–7.08 (m, 1H), 7.05–7.01 (m, 2H), 7.00–6.95 (m, 2H), 2.03 (s, 3H), 1.60 (dd, $J = 6.5, 3.5$ Hz, 2H), 1.17 ppm (dd, $J = 6.9, 3.5$ Hz, 2H). ^{13}C NMR (101 MHz, CDCl_3) δ 209.3, 157.0, 156.8, 135.9, 132.2, 130.0, 123.7, 119.3, 118.8, 37.0, 29.6, 19.1 ppm. LRMS (DEP/EI-Orbitrap) m/z : 252.1 (100), 209.1 (35). HRMS (EI-Orbitrap) m/z : $[\text{M}]^+$ calcd for $\text{C}_{19}\text{H}_{18}\text{O}_2^+$ 252.1150, found 252.1145. IR (Diamond-ATR, neat) $\tilde{\nu}_{\text{max}}$: 3040 (w), 3010 (w), 1692 (s), 1590 (m) cm^{-1} .

1-(1-(4-Chlorophenyl)cyclopropyl)ethanone (4r). Using **2a** and (4-chlorophenyl)boronic acid according to general procedures A and Ba provided **4r** (0.22 mmol, 42 mg, 86%) as a colorless oil. $R_f = 0.5$ (hexane/EtOAc 9:1, UV, KMnO_4 , PAA). ^1H NMR (400 MHz, CDCl_3) δ 7.34–7.28 (m, 1H), 2.00 (s, 1H), 1.61 (dd, $J = 6.8, 3.9$ Hz, 1H), 1.15 ppm (dd, $J = 7.0, 3.5$ Hz, 1H). ^{13}C NMR (101 MHz, CDCl_3) δ 208.3, 139.7, 133.5, 132.2, 128.9, 37.1, 29.4, 18.9 ppm. HRMS (EI-Orbitrap) m/z : $[\text{M}]^+$ calcd for $\text{C}_{11}\text{H}_{11}\text{ClO}^+$ 194.0498, found 194.0496.

1-(1-(4-Bromophenyl)cyclopropyl)ethanone (4s). Using **2b** and (4-bromophenyl)boronic acid according to general procedures A and Bb provided **4s** (0.18 mmol, 42 mg, 70%) as a colorless oil. $R_f = 0.5$ (hexane/EtOAc 9:1, UV, KMnO_4 , PAA). ^1H NMR (400 MHz, CDCl_3) δ 7.50–7.46 (m, 2H), 7.26–7.22 (m, 2H), 2.00 (s, 3H), 1.61 (dd, $J = 6.5, 3.8$ Hz, 2H), 1.15 ppm (dd, $J = 7.0, 4.0$ Hz, 2H). ^{13}C NMR (101 MHz, CDCl_3) δ 208.4, 140.2, 132.6, 131.9, 121.6, 37.2, 29.4, 18.9 ppm. LRMS (DEP/EI-Orbitrap) m/z : 238.0 (38), 195.0 (13), 116.1 (100). HRMS (EI-Orbitrap) m/z : $[\text{M}]^+$ calcd for $\text{C}_{11}\text{H}_{11}^{79}\text{BrO}^+$ 237.9993, found IR (Diamond-ATR, neat) $\tilde{\nu}_{\text{max}}$: 237.9987, 2958 (m), 2918 (vs), 2850 (s), 2212 (m), 1740 (m) cm^{-1} .

1-Methyl-4-(3-nitrophenyl)-5-oxabicyclo[2.1.0]pentane (5t). Using **2b** and 4,4,5,5-tetramethyl-2-(3-nitrophenyl)-1,3,2-dioxaborolane according to general procedures A and B provided intermediate **5t** (0.17 mmol, 34 mg, 66%) as a colorless oil. $R_f = 0.8$ (hexane/EtOAc 9:1, UV, KMnO_4 , PAA). ^1H NMR (400 MHz, CDCl_3) δ 8.17 (t, $J = 1.9$ Hz, 1H), 8.13 (ddd, $J = 8.1, 2.3, 1.2$ Hz, 1H), 7.63 (dt, $J = 7.7, 1.4$ Hz, 1H), 7.53 (t, $J = 7.9$ Hz, 1H), 2.71–2.62 (m, 1H), 2.15–1.94 (m, 3H), 1.50 ppm (s, 3H). ^{13}C NMR (101 MHz, CDCl_3) δ 148.5, 137.3, 132.2, 129.4, 122.5, 121.4, 71.9, 68.5, 30.5, 27.3, 13.9 ppm. LRMS (DEP/EI-Orbitrap) m/z : 205.1 (40), 190.0 (100), 159.1 (20). HRMS (EI-Orbitrap) m/z : $[\text{M}]^+$ calcd for $\text{C}_{11}\text{H}_{11}\text{NO}_3^+$ 205.0739, found 205.0733.

1-(1-(3-Nitrophenyl)cyclopropyl)ethanone (4t). Treating **5t** with $\text{BF}_3 \cdot \text{OEt}_2$ (see general procedure Bb) resulted in ring contraction, yielding **4t** (0.17 mmol, 34 mg, quant) as slightly yellow solid. Using **2b** and 3-aminobenzenboronic acid hydrochloride according to general procedures A and Bb provided directly oxidized **4t** (0.19 mmol, 39 mg, 77%). $R_f = 0.5$ (hexane/EtOAc 9:1, UV, KMnO_4 , PAA). ^1H NMR (400 MHz, CDCl_3) δ 8.22 (t, $J = 2.0$ Hz, 1H), 8.17 (ddd, $J = 8.2, 2.3, 1.1$ Hz, 1H), 7.71 (ddd, $J = 7.6, 1.7, 1.1$ Hz, 1H), 7.55 (t, $J = 7.9$ Hz, 1H), 2.01 (s, 3H), 1.71 (dd, $J = 7.2, 3.6$ Hz, 2H), 1.25 (dd, $J = 7.2, 3.6$ Hz, 2H). ^{13}C NMR (101 MHz, CDCl_3) δ 206.7, 148.5, 143.1, 137.2, 129.8, 125.7, 122.8, 37.6, 28.8, 18.6 ppm. LRMS (DEP/EI-Orbitrap) m/z : 205.1 (85), 146.0 (10), 115.1 (100). HRMS (EI-Orbitrap) m/z : $[\text{M}]^+$ calcd for $\text{C}_{11}\text{H}_{11}\text{NO}_3^+$ 205.0739, found

205.0734. IR (Diamond-ATR, neat) $\tilde{\nu}_{\text{max}}$: 3096 (vw), 3008 (vw), 1700 (m), 1688 (m), 1534 (s) cm^{-1} . Mp ($^{\circ}\text{C}$): 106–107.

3-(1-Acetylcyclopropyl)benzaldehyde (4u). Using **2b** and 2-(3-(1,3-dioxolan-2-yl)phenyl)-4,4,5,5-tetramethyl-1,3,2-dioxaborolane according to general procedures A and Bb directly provided deprotected **4u** (0.15 mmol, 27 mg, 58%) as a colorless oil. R_f = 0.2 (hexane/EtOAc 9:1, UV, KMnO_4 , PAA). ^1H NMR (400 MHz, CDCl_3) δ 10.03 (s, 1H), 7.89 (t, J = 1.7 Hz, 1H), 7.82 (dt, J = 7.6, 1.5 Hz, 1H), 7.65 (ddd, J = 7.7, 1.9, 1.2 Hz, 1H), 7.54 (t, J = 7.6 Hz, 1H), 2.00 (s, 3H), 1.67 (dd, J = 6.8, 4.2 Hz, 2H), 1.22 ppm (dd, J = 7.1, 3.7 Hz, 2H). ^{13}C NMR (101 MHz, CDCl_3) δ 207.7, 192.2, 142.4, 137.1, 136.9, 131.5, 129.6, 129.4, 37.5, 29.2, 18.7 ppm. LRMS (DEP/EI-Orbitrap) m/z : 188.1 (100). HRMS (EI-Orbitrap) m/z : $[\text{M}]^+$ calcd for $\text{C}_{12}\text{H}_{12}\text{O}_2^+$ 188.0837, found 188.0831. IR (Diamond-ATR, neat) $\tilde{\nu}_{\text{max}}$: 3010 (w), 1758 (w), 1720 (m), 1692 (vs), 1604 (w), 1586 (w) cm^{-1} .

1-(1-(Phenylethynyl)cyclopropyl)ethanone (4v). ((2-Methylcyclobut-1-en-1-yl)ethynyl) according to general procedure Ba provided **4v** (0.11 mmol, 21 mg, 45%) as a colorless oil. R_f = 0.5 (hexane/EtOAc 9:1, UV, KMnO_4 , PAA). ^1H NMR (400 MHz, CDCl_3) δ 7.46–7.39 (m, 2H), 7.34–7.29 (m, 3H), 2.57 (s, 3H), 1.62 (dd, J = 8.2, 3.2 Hz, 2H), 1.39 ppm (dd, J = 8.1, 3.1 Hz, 2H). ^{13}C NMR (101 MHz, CDCl_3) δ 206.2, 131.7, 128.5, 128.3, 123.2, 90.4, 80.7, 29.7, 23.7, 23.4 ppm. LRMS (DEP/EI-Orbitrap) m/z : 184.1 (84), 141.1 (83). HRMS (EI-Orbitrap) m/z : $[\text{M}]^+$ calcd for $\text{C}_{13}\text{H}_{12}\text{O}^+$ 184.0888, found 184.0883. IR (Diamond-ATR, neat) $\tilde{\nu}_{\text{max}}$: 2958 (w), 2930 (w), 1706 (vs), 1598 (w) cm^{-1} .

1-(1-(Benzo[d][1,3]dioxol-5-yl)cyclopropyl)ethanone (4w). Using **2b** and benzo[d][1,3]dioxol-5-ylboronic acid according to general procedures A and Ba provided **4w** (0.17 mmol, 35 mg, 68%) as a colorless oil. R_f = 0.4 (hexane/EtOAc 9:1, UV, KMnO_4 , PAA). ^1H NMR (400 MHz, CDCl_3) δ 6.86–6.81 (m, 2H), 6.80–6.75 (m, 1H), 5.97 (s, 2H), 2.03 (s, 3H), 1.56 (dd, J = 7.0, 3.1 Hz, 2H), 1.13 ppm (dd, J = 6.9, 3.5 Hz, 2H). ^{13}C NMR (101 MHz, CDCl_3) 209.4, 147.8, 147.0, 135.1, 124.1, 111.2, 108.4, 101.3, 37.4, 29.5, 19.3 ppm. LRMS (DEP/EI-Orbitrap) m/z : 204.1 (70), 161.0 (30). HRMS (EI-Orbitrap) m/z : $[\text{M}]^+$ calcd for $\text{C}_{12}\text{H}_{12}\text{O}_3^+$ 204.0786, found 204.0774.

1-(1-(Dibenzo[b,d]furan-4-yl)cyclopropyl)ethanone (4x). Using **2b** and dibenzo[b,d]furan-4-ylboronic acid according to general procedures A and Ba provided **4x** (0.19 mmol, 50 mg, 75%) as a colorless oil. R_f = 0.5 (hexane/EtOAc 9:1, UV, KMnO_4 , PAA). ^1H NMR (400 MHz, CDCl_3) δ 7.98 (ddd, J = 7.7, 1.4, 0.7 Hz, 1H), 7.92 (dd, J = 7.6, 1.4 Hz, 1H), 7.62 (dt, J = 8.3, 0.9 Hz, 1H), 7.49 (ddd, J = 8.3, 7.3, 1.3 Hz, 1H), 7.41 (td, J = 7.2, 1.2 Hz, 1H), 7.36 (dd, J = 7.5, 1.0 Hz, 1H), 7.34 (t, J = 7.6 Hz, 1H), 2.03 (s, 3H), 1.80 (dd, J = 6.8, 3.9 Hz, 2H), 1.34 ppm (dd, J = 7.1, 3.7 Hz, 2H). ^{13}C NMR (101 MHz, CDCl_3) δ 208.5, 156.3, 155.9, 128.9, 127.5, 125.3, 124.6, 124.3, 123.1, 123.0, 120.9, 120.2, 112.1, 32.6, 29.2, 19.3 ppm. LRMS (DEP/EI-Orbitrap) m/z : 250.1 (100), 207.1 (97). HRMS (EI-Orbitrap) m/z : $[\text{M}]^+$ calcd for $\text{C}_{17}\text{H}_{14}\text{O}_2^+$ 250.0994, found 250.0995. IR (Diamond-ATR, neat) $\tilde{\nu}_{\text{max}}$: 3056 (vw), 3010 (w), 1692 (s), 1630 (vw), 1586 (w) cm^{-1} .

1-(1-(2-Fluoropyridin-3-yl)cyclopropyl)ethanone (4y). Using **2b** and 2-fluoro-3-(4,4,5,5-tetramethyl-1,3,2-dioxaborolan-2-yl)pyridine according to general procedures A and Bb provided **4y** (0.16 mmol, 29 mg, 65%) as a colorless oil. R_f = 0.2 (hexane/EtOAc 9:1, UV, KMnO_4 , PAA). ^1H NMR (400 MHz, CDCl_3) δ 8.18 (ddd, J = 4.9, 2.0, 1.1 Hz, 1H), 7.73 (ddd, J = 9.5, 7.4, 2.0 Hz, 1H), 7.20 (ddd, J = 7.4, 4.9, 1.7 Hz, 1H), 2.04 (s, 3H), 1.71 (dd, J = 7.1, 4.1 Hz, 2H), 1.19 ppm (dd, J = 7.4, 3.9 Hz, 2H). ^{13}C NMR (101 MHz, CDCl_3) δ 206.1, 163.1 (d, J = 240.8 Hz), 147.0 (d, J = 14.8 Hz), 142.4 (d, J = 4.8 Hz), 123.4 (d, J = 29.3 Hz), 121.8 (d, J = 4.4 Hz), 31.9 (d, J = 3.2 Hz), 28.2 (d, J = 1.3 Hz), 18.6 ppm. LRMS (DEP/EI-Orbitrap) m/z : 179.1 (100), 136.0 (88). HRMS (EI-Orbitrap) m/z : $[\text{M}]^+$ calcd for $\text{C}_{10}\text{H}_{10}\text{FNO}^+$ 179.0746, found 179.0741. IR (Diamond-ATR, neat) $\tilde{\nu}_{\text{max}}$: 3012 (vw), 1696 (s), 1636 (vw), 1606 (m), 1578 (w) cm^{-1} .

1-(1-(3,5-Dimethylisoxazol-4-yl)cyclopropyl)ethanone (4z). Using **2b** and (3,5-dimethylisoxazol-4-yl)boronic acid according to general procedures A and Ba provided **4z** (0.13 mmol, 24 mg, 53%) as a colorless oil. R_f = 0.25 (hexane/EtOAc 9:1, UV, KMnO_4 , PAA). ^1H NMR (400 MHz, CDCl_3) δ 2.37 (s, 3H), 2.24 (s, 3H), 2.04 (s, 3H),

1.65 (dd, J = 7.0, 3.0 Hz, 2H), 1.02 ppm (dd, J = 6.7, 3.4 Hz, 2H). ^{13}C NMR (101 MHz, CDCl_3) δ 207.6, 167.9, 160.6, 114.1, 28.8, 25.1, 18.8, 11.5, 10.5 ppm. LRMS (DEP/EI-Orbitrap) m/z : 179.1 (11), 136.1 (61). HRMS (EI-Orbitrap) m/z : $[\text{M} - \text{H}]^+$ calcd for $\text{C}_{10}\text{H}_{12}\text{NO}_2^+$ 178.0863, found 178.0859.

1-(1-(1-Benzyl-1H-pyrazol-4-yl)cyclopropyl)ethanone (4aa). Using **2b** and 1-benzyl-3-(4,4,5,5-tetramethyl-1,3,2-dioxaborolan-2-yl)-1H-pyrazole according to general procedures A and Ba provided **4aa** (0.17 mmol, 41 mg, 69%) as a colorless oil. R_f = 0.1 (hexane/EtOAc 9:1, UV, KMnO_4 , PAA). ^1H NMR (400 MHz, CDCl_3) δ 7.49 (d, J = 0.8 Hz, 1H), 7.39–7.31 (m, 4H), 7.24–7.20 (m, 2H), 5.28 (s, 2H), 2.08 (s, 3H), 1.53 (dd, J = 7.4, 3.7 Hz, 2H), 1.07 ppm (dd, J = 7.4, 3.7 Hz, 2H). ^{13}C NMR (101 MHz, CDCl_3) δ 208.9, 140.4, 136.4, 129.8, 129.0, 128.3, 127.8, 122.5, 56.3, 28.9, 27.5, 19.4 ppm. LRMS (DEP/EI-Orbitrap) m/z : 240.1 (38), 197.1 (22), 91.1 (100). HRMS (EI-Orbitrap) m/z : $[\text{M}]^+$ calcd for $\text{C}_{15}\text{H}_{16}\text{N}_2\text{O}^+$ 240.1263, found 240.1257. IR (Diamond-ATR, neat) $\tilde{\nu}_{\text{max}}$: 3090 (w), 3008 (w), 2940 (w), 1718 (m), 1690 (vs) cm^{-1} .

1-(1-(5-Methylthiophene-2-yl)cyclopropyl)ethanone (4ab). Using **2b** and (5-methylthiophene-2-yl)boronic acid according to general procedures A and Ba provided **4ab** (0.17 mmol, 31 mg, 69%) as a colorless oil. R_f = 0.6 (hexane/EtOAc 9:1, UV, KMnO_4 , PAA). ^1H NMR (400 MHz, CDCl_3) δ 6.77 (d, J = 3.4 Hz, 1H), 6.60 (dq, J = 3.4, 1.1 Hz, 1H), 2.46 (d, J = 1.1 Hz, 3H), 2.17 (s, 3H), 1.62 (dd, J = 7.2, 3.7 Hz, 2H), 1.26 ppm (dd, J = 7.2, 3.7 Hz, 2H). ^{13}C NMR (101 MHz, CDCl_3) δ 208.6, 142.7, 140.1, 128.0, 124.9, 31.8, 29.1, 21.1, 15.6 ppm. LRMS (DEP/EI-Orbitrap) m/z : 180.1 (90), 165.0 (81), 137.0 (100), 122.0 (23). HRMS (EI-Orbitrap) m/z : $[\text{M}]^+$ calcd for $\text{C}_{10}\text{H}_{12}\text{OS}^+$ 180.0609, found 180.0608. IR (Diamond-ATR, neat) $\tilde{\nu}_{\text{max}}$: 3010 (w), 2920 (w), 1698 (vs) cm^{-1} .

Phenyl(1-phenylcyclopropyl)methanone (4ac). 1,2-Diphenylcyclobut-1-ene (**3ac**) for the following rearrangement was synthesized according to the literature.²⁰ Using **3ac** according to general procedure Bc provided **4ac** (0.36 mmol, 80 mg, 72%) as yellowish oil. R_f = 0.5 (hexane/EtOAc 95:5, UV, KMnO_4 , PAA). ^1H NMR (400 MHz, CDCl_3) δ 7.91–7.84 (m, 2H), 7.53–7.23 (m, 8H), 1.79 (dd, J = 7.3, 4.1 Hz, 2H), 1.48 ppm (dd, J = 7.0, 3.9 Hz, 2H). ^{13}C NMR (101 MHz, CDCl_3) δ 200.5, 141.1, 137.1, 132.1, 129.5, 128.7, 128.1, 128.0, 126.7, 35.2, 16.4 ppm. LRMS (DEP/EI-Orbitrap) m/z : 222.1 (80), 193.1 (5), 165 (10), 105.0 (100). HRMS (EI-Orbitrap) m/z : $[\text{M}]^+$ calcd for $\text{C}_{16}\text{H}_{14}\text{O}^+$ 222.1045, found 222.1039.

1-(1-(4-Methoxyphenyl)cyclopropyl)-3-phenylpropan-1-one (4ad). Using **3ad** according to general procedure Bc provided **4ad** (0.16 mmol, 45 mg, 85%) as a colorless oil. R_f = 0.65 (hexane/EtOAc 8:2, UV, KMnO_4 , PAA). ^1H NMR (400 MHz, CDCl_3) δ 7.23 (tq, J = 6.7, 6.6, 3.4, 3.2 Hz, 4H), 7.18–7.13 (m, 1H), 7.09–7.04 (m, 2H), 6.87–6.83 (m, 2H), 3.81 (s, 3H), 2.78 (t, J = 7.6 Hz, 2H), 2.60 (t, J = 7.6 Hz, 2H), 1.57 (dd, J = 7.2, 3.5 Hz, 2H), 1.11 ppm (dd, J = 7.2, 3.5 Hz, 2H). ^{13}C NMR (101 MHz, CDCl_3) δ 210.5, 159.0, 141.5, 132.8, 132.1, 128.5, 128.5, 126.0, 114.1, 55.4, 43.5, 36.6, 30.3, 19.2 ppm. LRMS (DEP/EI-Orbitrap) m/z : 280.0 (60), 189.1 (30), 161.0 (70). HRMS (EI-Orbitrap) m/z : $[\text{M}]^+$ calcd for $\text{C}_{19}\text{H}_{20}\text{O}_2^+$ 280.1463, found 280.1458. IR (Diamond-ATR, neat) $\tilde{\nu}_{\text{max}}$: 3086 (vw), 3026 (w), 3003 (w), 2955 (w), 2952 (w), 2934 (w), 2931 (w), 2923 (vw), 2835 (vw), 1716 (w), 1689 (s), 1651 (vw), 1610 (m), 1579 cm^{-1} (w).

1-((1R*,2R*)-2-Phenethyl-1-(p-tolyl)cyclopropyl)ethanone ((R*)-4ae). Using (2-(3-iodo-2-methylcyclobut-2-en-1-yl)ethyl)benzene (**2d**) and 4,4,5,5-tetramethyl-2-(p-tolyl)-1,3,2-dioxaborolane according to general procedures A and Ba provided ((R*)-4ae) (0.15 mmol, 42 mg, 60%) as a colorless oil. R_f = 0.7 (hexane/EtOAc 9:1, UV, KMnO_4 , PAA). ^1H NMR (400 MHz, CDCl_3) δ 7.32–7.27 (m, 2H), 7.24–7.17 (m, 5H), 7.15–7.11 (m, 2H), 2.80–2.71 (m, 1H), 2.69–2.61 (m, 1H), 2.35 (s, 3H), 1.95 (s, 3H), 1.91–1.80 (m, 2H), 1.76–1.66 (m, 2H), 1.15–1.05 ppm (m, 1H). ^{13}C NMR (101 MHz, CDCl_3) δ 207.3, 141.8, 139.6, 137.2, 130.5, 129.4, 128.6, 128.5, 126.0, 42.6, 36.4, 32.1, 30.9, 28.5, 21.6, 21.2 ppm. LRMS (DEP/EI-Orbitrap) m/z : 278.1 (2), 187.1 (10), 173.1 (15), 148.1 (100). HRMS (EI-Orbitrap) m/z : $[\text{M}]^+$ calcd for $\text{C}_{20}\text{H}_{22}\text{O}^+$ 278.1671, found 278.1662. IR (Diamond-ATR, neat) $\tilde{\nu}_{\text{max}}$: 3086 (vw), 3062 (vw), 3026 (w), 3000 (w), 2922 (w), 2860 (w), 1688 (vs), 1654 (vw), 1604 (w) cm^{-1} .

1-((1*R,2*S**)-2-Phenethyl-1-(*p*-tolyl)cyclopropyl)ethanone ((*S**)-4ae).** Using **2d** and 4,4,5,5-tetramethyl-2-(*p*-tolyl)-1,3,2-dioxaborolane according to general procedures A and Ba provided (*S**)-4ae (0.08 mmol, 23 mg, 32%) as a colorless oil. $R_f = 0.6$ (hexane/EtOAc 9:1, UV, KMnO₄, PAA). ¹H NMR (400 MHz, CDCl₃) δ 7.25–7.20 (m, 2H), 7.15 (s, 5H), 7.09–7.06 (m, 2H), 2.77–2.58 (m, 2H), 2.35 (s, 3H), 1.99–1.92 (m, 1H), 1.97 (s, 3H), 1.79–1.67 (m, 1H), 1.60 (ddd, $J = 8.8, 3.6, 0.8$ Hz, 1H), 1.00 (dd, $J = 6.8, 3.6$ Hz, 1H), 0.91–0.79 ppm (m, 1H). ¹³C NMR (101 MHz, CDCl₃) δ 209.4, 142.0, 137.2, 135.0, 131.4, 129.4, 128.6, 128.4, 125.9, 42.2, 35.7, 33.0, 29.9, 29.7, 25.3, 21.3 ppm. LRMS (DEP/El-Orbitrap) m/z : 278.1 (100). HRMS (El-Orbitrap) m/z : [M]⁺ calcd for C₂₀H₂₂O⁺ 278.1671, found 278.1660. IR (Diamond-ATR, neat) $\tilde{\nu}_{\max}$: 3026 (w), 3000 (w), 2924 (w), 2858 (w), 1690 (w) cm⁻¹.

1-((1*R,2*R**)-2-Phenethyl-1-(*E*)-styryl)cyclopropyl)ethanone ((*R**)-4af).** Using **2d** and (*E*)-styrylboronic acid according to general procedures A and Ba provided (*R**)-4af (0.11 mmol, 31 mg, 43%) as a colorless oil. $R_f = 0.8$ (hexane/EtOAc 9:1, UV, KMnO₄, PAA). ¹H NMR (400 MHz, CDCl₃) δ 7.37–7.23 (m, 7H), 7.23–7.16 (m, 3H), 6.68 (d, $J = 15.8$ Hz, 1H), 6.35 (d, $J = 15.8$ Hz, 1H), 2.74–2.54 (m, 2H), 2.21 (s, 3H), 1.83–1.73 (m, 2H), 1.60 (dd, $J = 7.5, 4.1$ Hz, 1H), 1.52–1.41 (m, 1H), 1.22 ppm (dd, $J = 8.6, 4.1$ Hz, 1H). ¹³C NMR (101 MHz, CDCl₃) δ 206.3, 141.7, 136.9, 130.9, 129.9, 128.8, 128.8, 128.5, 127.8, 126.2, 126.1, 39.4, 36.1, 34.2, 30.6, 28.6, 21.1 ppm. LRMS (DEP/El-Orbitrap) m/z : 290.1 (5), 199.1 (10). HRMS (El-Orbitrap) m/z : [M]⁺ calcd for C₂₁H₂₂O⁺ 290.1671, found 290.1660. IR (Diamond-ATR, neat) $\tilde{\nu}_{\max}$: 3060 (w), 3026 (m), 3000 (w), 2920 (w), 1692 (vs), 1644 (w), 1602 (w) cm⁻¹.

1-((1*S,2*R**)-2-Phenethyl-1-(*E*)-styryl)cyclopropyl)ethanone ((*S**)-4af).** Using **2d** and (*E*)-styrylboronic acid according to general procedures A and Ba provided (*S**)-4af (0.08 mmol, 24 mg, 33%) as a colorless oil. $R_f = 0.7$ (hexane/EtOAc 9:1, UV, KMnO₄, PAA). ¹H NMR (400 MHz, CDCl₃) δ 7.36–7.25 (m, 7H), 7.24–7.18 (m, 1H), 7.15–7.09 (m, 2H), 6.39 (d, $J = 15.8$ Hz, 1H), 6.21 (d, $J = 15.8$ Hz, 1H), 2.77–2.59 (m, 2H), 2.16 (s, 3H), 1.77–1.62 (m, 2H), 1.62–1.53 (m, 2H), 1.03 ppm (dd, $J = 6.2, 3.6$ Hz, 1H). ¹³C NMR (101 MHz, CDCl₃) δ 208.4, 141.8, 136.8, 134.3, 128.8, 128.8, 128.5, 127.9, 126.4, 126.1, 125.6, 39.4, 36.1, 32.4, 30.6, 29.3, 21.9 ppm. LRMS (DEP/El-Orbitrap) m/z : 290.1 (4), 199.1 (53), 141.1 (10). HRMS (El-Orbitrap) m/z : [M]⁺ calcd for C₂₁H₂₂O⁺ 290.1671, found 290.1663. IR (Diamond-ATR, neat) $\tilde{\nu}_{\max}$: 3060 (w), 3025 (w), 2998 (w), 2926 (w), 2922 (w), 2919 (w), 2859 (w), 1729 (w), 1691 (vs), 1655 (w), 1643 (w), 1602 (w) cm⁻¹.

1-((1*R,2*R**)-1-(Furan-3-yl)-2-phenethylcyclopropyl)ethanone ((*R**)-4ag).** Using **2d** and furan-3-ylboronic acid according to general procedures A and Ba provided (*R**)-4ag (0.085 mmol, 21 mg, 33%) as a colorless oil. $R_f = 0.5$ (hexane/EtOAc 9:1, UV, KMnO₄, PAA). ¹H NMR (400 MHz, CDCl₃) δ 7.36 (dd, $J = 1.7$ Hz, 1H), 7.32–7.24 (m, 3H), 7.23–7.16 (m, 3H), 6.30 (dd, $J = 1.8, 0.9$ Hz, 1H), 2.74–2.56 (m, 2H), 2.06 (s, 3H), 1.92–1.72 (m, 2H), 1.63 (dd, $J = 7.3, 3.5$ Hz, 1H), 1.61–1.53 (m, 1H), 1.03 ppm (dd, $J = 8.2, 3.5$ Hz, 1H). ¹³C NMR (101 MHz, CDCl₃) δ 206.9, 143.2, 141.6, 141.4, 128.7, 128.5, 127.3, 126.1, 112.1, 36.2, 33.1, 32.2, 30.5, 28.2, 21.6 ppm. LRMS (DEP/El-Orbitrap) m/z : 254.1 (3), 163.0 (29). HRMS (El-Orbitrap) m/z : [M]⁺ calcd for C₁₇H₁₈O₂⁺ 254.1307, found 254.1299. IR (Diamond-ATR, neat) $\tilde{\nu}_{\max}$: 3026 (w), 3002 (w), 2924 (w), 2860 (w), 1770 (m), 1690 (s), 1602 (w) cm⁻¹.

1-((1*R,2*S**)-1-(Furan-3-yl)-2-phenethylcyclopropyl)ethanone ((*S**)-4ag).** Using **2d** and furan-3-ylboronic acid according to general procedures A and Ba provided (*S**)-4ag (0.08 mmol, 19 mg, 30%) as a colorless oil. $R_f = 0.4$ (hexane/EtOAc 9:1, UV, KMnO₄, PAA). ¹H NMR (400 MHz, CDCl₃) δ 7.42 (dd, $J = 1.7$ Hz, 1H), 7.30 (dd, $J = 1.5, 0.9$ Hz, 1H), 7.28–7.21 (m, 2H), 7.20–7.13 (m, 1H), 7.12–7.07 (m, 2H), 6.33 (dd, $J = 1.8, 0.9$ Hz, 1H), 2.75–2.59 (m, 2H), 2.11 (s, 3H), 1.94–1.81 (m, 1H), 1.68–1.58 (m, 2H), 1.28–1.17 (m, 1H), 0.93 ppm (dd, $J = 6.9, 3.6$ Hz, 1H). ¹³C NMR (101 MHz, CDCl₃) δ 208.6, 143.3, 142.6, 141.9, 128.5, 128.5, 126.0, 122.6, 112.9, 35.6, 33.1, 32.2, 29.8, 29.4, 25.0 ppm. LRMS (DEP/El-Orbitrap) m/z : 254.1 (29), 117.1 (17). HRMS (El-Orbitrap) m/z : [M]⁺ calcd for C₁₇H₁₈O₂⁺ 254.1307, found 254.1299. IR (Diamond-ATR, neat)

$\tilde{\nu}_{\max}$: 3025 (w), 2932 (w), 2926 (w), 2923 (w), 1758 (vs), 1688 (vs), 1635 (w), 1627 (w), 1602 (w) cm⁻¹.

1-((1*R,2*R**)-2-Phenethyl-1-(3,4,5-trimethoxyphenyl)cyclopropyl)ethanone ((*R**)-4ah).** Using **2d** and (3,4,5-trimethoxyphenyl)boronic acid according to general procedures A and Ba provided (*R**)-4ah (0.07 mmol, 26 mg, 43%) as a colorless oil. $R_f = 0.4$ (hexane/EtOAc 8:2, UV, KMnO₄, PAA). ¹H NMR (400 MHz, CDCl₃) δ 7.32–7.27 (m, 2H), 7.25–7.16 (m, 3H), 6.46 (s, 2H), 3.83 (s, 3H), 3.82 (s, 6H), 2.70 (t, $J = 7.3$ Hz, 2H), 1.98 (s, 3H), 1.93–1.80 (m, 2H), 1.77–1.67 (m, 2H), 1.10 ppm (dd, $J = 7.8, 2.9$ Hz, 1H). ¹³C NMR (101 MHz, CDCl₃) δ 207.1, 153.3, 141.6, 138.1, 137.3, 128.6, 128.6, 126.1, 107.4, 61.0, 56.3, 43.5, 36.2, 31.7, 30.6, 28.1, 21.7 ppm. LRMS (DEP/El-Orbitrap) m/z : 354.2 (26), 311.2 (17), 263.1 (10), 219.1 (919), 181.1 (100), 165.1 (24). HRMS (El-Orbitrap) m/z : [M]⁺ calcd for C₂₂H₂₆O₄⁺ 354.1831, found 354.1819. IR (Diamond-ATR, neat) $\tilde{\nu}_{\max}$: 2998 (w), 2936 (w), 2838 (vw), 1688 (m) cm⁻¹.

1-((1*R,2*S**)-2-Phenethyl-1-(3,4,5-trimethoxyphenyl)cyclopropyl)ethanone ((*S**)-4ah).** Using **2d** and (3,4,5-trimethoxyphenyl)boronic acid according to general procedures A and Ba provided (*S**)-4ah (0.03 mmol, 12 mg, 20%) as a colorless oil. $R_f = 0.3$ (hexane/EtOAc 8:2, UV, KMnO₄, PAA). ¹H NMR (400 MHz, CDCl₃) δ 7.29–7.20 (m, 2H), 7.19–7.13 (m, 1H), 7.12–7.07 (m, 2H), 6.47 (s, 2H), 3.86 (s, 3H), 3.85 (s, 6H), 2.79–2.61 (m, 2H), 2.02 (s, 3H), 2.01–1.93 (m, 1H), 1.81–1.69 (m, 1H), 1.57 (dd, $J = 9.0, 3.7$ Hz, 1H), 1.00 (dd, $J = 6.8, 3.7$ Hz, 1H), 0.98–0.88 ppm (m, 1H). ¹³C NMR (101 MHz, CDCl₃) δ 208.9, 153.3, 141.9, 137.4, 133.6, 128.5, 128.5, 126.0, 108.3, 61.1, 56.3, 43.1, 35.7, 33.0, 29.6, 29.5, 25.4 ppm. LRMS (DEP/El-Orbitrap) m/z : 354.2 (100), 339.2 (39), 207.1 (17), 189.1 (22). HRMS (El-Orbitrap) m/z : [M]⁺ calcd for C₂₂H₂₆O₄⁺ 354.1831, found 354.1822. IR (Diamond-ATR, neat) $\tilde{\nu}_{\max}$: 3000 (w), 2936 (w), 1688 (m) cm⁻¹.

1-((1*R,2*R**)-2-Pentyl-1-(*p*-tolyl)cyclopropyl)ethanone ((*R**)-4ai).** Using **2c** and 4,4,5,5-tetramethyl-2-(*p*-tolyl)-1,3,2-dioxaborolane according to general procedures A and Ba provided (*R**)-4ai (0.18 mmol, 21 mg, 55%) as a colorless oil. $R_f = 0.6$ (hexane/EtOAc 9:1, UV, KMnO₄, PAA). ¹H NMR (400 MHz, CDCl₃) δ 7.25–7.21 (m, 2H), 7.16–7.12 (m, 2H), 2.35 (s, 3H), 1.98 (s, 3H), 1.71–1.65 (m, 2H), 1.52–1.40 (m, 3H), 1.37–1.24 (m, 5H), 1.11–1.03 (m, 1H), 0.93–0.84 ppm (m, 3H). ¹³C NMR (101 MHz, CDCl₃) δ 207.4, 139.9, 137.1, 130.6, 129.4, 42.6, 32.8, 31.8, 30.8, 30.0, 26.8, 22.8, 21.6, 21.3, 14.2 ppm. LRMS (DEP/El-Orbitrap) m/z : 244.2 (56), 187.1 (10), 160.1 (14). HRMS (El-Orbitrap) m/z : [M]⁺ calcd for C₁₇H₂₄O⁺ 244.1827, found 244.1820. IR (Diamond-ATR, neat) $\tilde{\nu}_{\max}$: 3000 (w), 2956 (m), 2924 (m), 2858 (m), 1692 (vs) cm⁻¹.

1-((1*R,2*S**)-2-Pentyl-1-(*p*-tolyl)cyclopropyl)ethanone ((*S**)-4ai).** Using **2c** and 4,4,5,5-tetramethyl-2-(*p*-tolyl)-1,3,2-dioxaborolane according to general procedures A and Ba provided (*S**)-4ai (0.08 mmol, 9 mg, 24%) as a colorless oil. $R_f = 0.55$ (hexane/EtOAc 9:1, UV, KMnO₄, PAA). ¹H NMR (400 MHz, CDCl₃) δ 7.16 (s, 4H), 2.36 (s, 3H), 1.96 (s, 3H), 1.93–1.84 (m, 1H), 1.61 (ddd, $J = 8.8, 3.5, 0.7$ Hz, 1H), 1.49–1.31 (m, 3H), 1.27–1.16 (m, 4H), 1.01 (dd, $J = 6.9, 3.5$ Hz, 1H), 0.87–0.78 (m, 3H), 0.57–0.44 ppm (m, 1H). ¹³C NMR (101 MHz, CDCl₃) δ 209.7, 137.0, 135.3, 131.4, 129.3, 42.2, 31.7, 30.8, 30.3, 29.9, 29.1, 25.6, 22.7, 21.3, 14.2 ppm. LRMS (DEP/El-Orbitrap) m/z : 244.2 (100), 187.1 (12), 169.1 (12), 160.1 (20), 145.1 (43). HRMS (El-Orbitrap) m/z : [M]⁺ calcd for C₁₇H₂₄O⁺ 244.1827, found 244.1821. IR (Diamond-ATR, neat) $\tilde{\nu}_{\max}$: 3000 (w), 2956 (m), 2928 (m), 2858 (m), 1692 (vs) cm⁻¹.

(*E*)-8-Methyl-1-(4-(trifluoromethyl)phenyl)nona-1,8-diene-3,6-dione (6a). Using **2c** and (*E*)-(4-(trifluoromethyl)styryl)boronic acid according to general procedures A and C provided **6a** (0.10 mmol, 31 mg, 40%) as a colorless oil. $R_f = 0.28$ (hexane/EtOAc 9:1, UV, KMnO₄, PAA). ¹H NMR (400 MHz, CDCl₃) δ 7.64 (s, 4H), 7.58 (d, $J = 16.2$ Hz, 1H), 6.81 (d, $J = 16.2$ Hz, 1H), 4.97 (s, 1H), 4.86 (s, 1H), 3.20 (s, 2H), 2.98 (t, $J = 6.1$ Hz, 2H), 2.87 (t, $J = 6.1$ Hz, 2H), 1.77 ppm (s, 3H). ¹³C NMR (101 MHz, CDCl₃) δ 207.4, 198.3, 140.8, 139.3, 138.0, 132.0 (q, $J = 32.7$ Hz), 128.5, 128.1, 126.0 (q, $J = 3.8$ Hz), 123.9 (q, $J = 27.2$ Hz), 115.4, 52.4, 35.6, 34.7, 22.8 ppm. LRMS (DEP/El-Orbitrap) m/z : 310.2 (2), 255.1 (100), 227.1 (30), 199.1 (62). HRMS (El-Orbitrap) m/z : [M]⁺ calcd for C₁₇H₁₇F₃O₂⁺

310.1181, found 310.1168. IR (Diamond-ATR, neat) $\tilde{\nu}_{\text{max}}$: 2973 (vw), 2917 (vw), 2854 (vw), 1714 (m), 1694 (m), 1670 (m), 1616 (m) cm^{-1} .

(*E*)-1-Cyclohexyl-8-methylnona-1,8-diene-3,6-dione (**6b**). Using **2a** and (*E*)-(2-cyclohexylvinyl)boronic acid according to general procedures A and C provided **6b** (0.12 mmol, 29 mg, 48%) as slightly yellow oil. R_f = 0.50 (hexane/EtOAc 9:1, UV, KMnO_4 , PAA). ^1H NMR (400 MHz, CDCl_3) δ 6.80 (dd, J = 16.1, 6.8 Hz, 1H), 6.05 (dd, J = 16.1, 1.3 Hz, 1H), 4.95 (s, 1H), 4.84 (s, 1H), 3.18 (s, 2H), 2.85 (t, J = 6.3 Hz, 2H), 2.77 (t, J = 6.2 Hz, 2H), 2.23–2.07 (m, 1H), 1.76 (s, 3H), 1.83–1.60 (m, 4H), 1.34–1.05 ppm (m, 6H). ^{13}C NMR (101 MHz, CDCl_3) δ 207.6, 199.1, 152.7, 139.2, 127.5, 115.1, 52.3, 40.6, 35.3, 33.5, 31.7, 25.9, 25.7, 22.6 ppm. LRMS (DEP/EI-Orbitrap) m/z : 248.3 (2), 193.2 (23). HRMS (EI-Orbitrap) m/z : $[\text{M}]^+$ calcd for $\text{C}_{16}\text{H}_{24}\text{O}_2^+$ 248.1776, found 248.1772. IR (Diamond-ATR, neat) $\tilde{\nu}_{\text{max}}$: 2926 (vs), 2853 (m), 1717 (m), 1698 (m), 1674 (s), 1650 (w), 1628 (m) cm^{-1} .

(*E*)-7-Phenylhept-6-ene-2,5-dione (**6c**). Using **2b** and (*E*)-styrylboronic acid according to general procedures A and C provided **6c** (0.13 mmol, 25 mg, 50%) as a colorless oil. R_f = 0.10 (hexane/EtOAc 9:1, UV, KMnO_4 , PAA). ^1H NMR (400 MHz, CDCl_3) δ 7.59 (d, J = 16.2 Hz, 1H), 7.56–7.51 (m, 2H), 7.42–7.36 (m, 3H), 6.76 (d, J = 16.2 Hz, 1H), 2.98 (dd, J = 6.6, 5.5 Hz, 2H), 2.83 (dd, J = 6.9, 5.7 Hz, 2H), 2.24 ppm (s, 3H). ^{13}C NMR (101 MHz, CDCl_3) δ 207.5, 198.6, 143.0, 134.5, 130.7, 129.1, 128.4, 126.1, 37.2, 34.3, 30.2 ppm. LRMS (DEP/EI-Orbitrap) m/z : 202.1 (4), 144.1 (24), 131.1 (100). HRMS (EI-Orbitrap) m/z : $[\text{M} - \text{H}]^+$ calcd for $\text{C}_{13}\text{H}_{13}\text{O}_2^+$ 201.0910, found 201.0912. IR (Diamond-ATR, neat) $\tilde{\nu}_{\text{max}}$: 2908 (w), 1714 (vs), 1690 (s), 1664 (vs), 1614 (vs) cm^{-1} .

(*E*)-Tridec-6-ene-2,5-dione (**6d**). Using **2b** and (*E*)-oct-1-en-1-ylboronic acid according to general procedures A and C provided **6d** (0.12 mmol, 25 mg, 48%) as a colorless oil. R_f = 0.13 (hexane/EtOAc 9:1, UV, KMnO_4 , PAA). ^1H NMR (400 MHz, CDCl_3) δ 6.87 (dt, J = 15.9, 6.9 Hz, 1H), 6.10 (d, J = 15.9 Hz, 1H), 2.84 (t, J = 6.3 Hz, 2H), 2.75 (t, J = 6.3 Hz, 2H), 2.21 (dd, J = 13.6, 7.0 Hz, 2H), 2.21 (s, 3H), 1.52–1.38 (m, 2H), 1.37–1.21 (m, 6H), 0.88 ppm (t, J = 6.6 Hz, 3H). ^{13}C NMR (101 MHz, CDCl_3) δ 207.6, 198.8, 148.2, 130.1, 37.1, 33.6, 32.7, 31.7, 30.2, 29.0, 28.2, 22.7, 14.2 ppm. HRMS (ESI-quadrupole pos) m/z : $[\text{M}]^+$ calcd for $\text{C}_{13}\text{H}_{22}\text{O}_2^+$: 210.1620, found 210.1622. IR (Diamond-ATR, neat) $\tilde{\nu}_{\text{max}}$: 2956 (m), 2926 (s), 2871 (m), 2857 (m), 1718 (vs), 1700 (vs), 1675 (vs), 1630 (s) cm^{-1} .

(*E*)-3-Phenethyl-7-(*p*-tolyl)hept-6-ene-2,5-dione (**6e**). Using **2d** and (*E*)-(4-methylstyryl)boronic acid according to general procedures A and C provided **6e** (0.11 mmol, 34 mg, 43%) as a colorless oil. R_f = 0.3 (hexane/EtOAc 9:1, UV, KMnO_4 , PAA). ^1H NMR (400 MHz, CDCl_3) δ 7.53 (d, J = 16.2 Hz, 1H), 7.47–7.41 (m, 2H), 7.34–7.27 (m, 2H), 7.23–7.14 (m, 5H), 6.68 (d, J = 16.2 Hz, 1H), 3.29–3.14 (m, 2H), 2.84–2.71 (m, 1H), 2.68–2.54 (m, 2H), 2.38 (s, 3H), 2.29 (s, 3H), 2.03–1.90 (m, 1H), 1.84–1.69 ppm (m, 1H). ^{13}C NMR (101 MHz, CDCl_3) δ 211.4, 198.5, 143.1, 141.2, 141.1, 131.6, 129.7, 128.6, 128.4, 128.3, 126.2, 124.9, 46.6, 42.1, 33.4, 33.1, 30.0, 21.6 ppm. LRMS (DEP/EI-Orbitrap) m/z : 320.1 (2), 216.1 (26), 145.1 (100). HRMS (EI-Orbitrap) m/z : $[\text{M}]^+$ calcd for $\text{C}_{22}\text{H}_{24}\text{O}_2^+$ 320.1776, found 320.1768. IR (Diamond-ATR, neat) $\tilde{\nu}_{\text{max}}$: 3056 (w), 3026 (w), 2924 (w), 2860 (w), 1710 (vs), 1686 (s), 1656 (s), 1602 (vs) cm^{-1} .

(*E*)-3-Phenethyl-7-phenylhept-6-ene-2,5-dione (**6f**). Using **2d** and (*E*)-styrylboronic acid according to general procedures A and C provided **6f** (0.12 mmol, 37 mg, 48%) as a colorless oil. R_f = 0.3 (hexane/EtOAc 9:1, UV, KMnO_4 , PAA). ^1H NMR (400 MHz, CDCl_3) δ 7.60–7.51 (m, 3H), 7.43–7.37 (m, 3H), 7.33–7.27 (m, 2H), 7.25–7.15 (m, 3H), 6.72 (d, J = 16.3 Hz, 1H), 3.29–3.16 (m, 2H), 2.84–2.71 (m, 1H), 2.71–2.53 (m, 2H), 2.29 (s, 3H), 2.06–1.92 (m, 1H), 1.84–1.71 ppm (m, 1H). ^{13}C NMR (101 MHz, CDCl_3) δ 211.5, 198.6, 143.1, 141.3, 134.5, 130.7, 129.1, 128.7, 128.5, 128.4, 126.3, 125.9, 46.7, 42.2, 33.5, 33.2, 30.1 ppm. LRMS (DEP/EI-Orbitrap) m/z : 306.0 (2), 202.1 (40), 159.0 (10), 131.0 (100). HRMS (EI-Orbitrap) m/z : $[\text{M}]^+$ calcd for $\text{C}_{21}\text{H}_{22}\text{O}_2^+$ 306.1620, found 306.1620. IR (Diamond-ATR, neat) $\tilde{\nu}_{\text{max}}$: 3060 (w), 3026 (w), 2928 (w), 2860 (w), 1708 (s), 1688 (m), 1658 (s), 1610 (s) cm^{-1} .

1-(1-(4-Chlorophenyl)cyclopropyl)-2-(pyridin-2-ylsulfonyl)ethanone (**4r**). **4r** was transformed to **6a** according to a literature procedure.²⁵ Purification by chromatography afforded **B** (0.06 mmol, 20 mg, 40%) as a colorless oil. R_f = 0.5 (hexane/EtOAc 5:5, UV, KMnO_4 , PAA). ^1H NMR (400 MHz, CDCl_3) δ 8.70 (dt, J = 4.8, 1.2 Hz, 1H), 8.05 (dt, J = 7.9, 1.1 Hz, 1H), 7.97 (td, J = 7.7, 1.7 Hz, 1H), 7.55 (ddd, J = 7.6, 4.7, 1.2 Hz, 1H), 7.40–7.29 (m, 4H), 4.47 (s, 2H), 1.64 (dd, J = 7.3, 4.1 Hz, 2H), 1.27 ppm (dd, J = 7.1, 3.5 Hz, 2H). ^{13}C NMR (101 MHz, CDCl_3) δ 198.5, 157.1, 150.1, 138.3, 137.2, 134.5, 132.5, 129.5, 127.6, 122.3, 59.5, 38.0, 20.5 ppm. LRMS (DEP/EI-Orbitrap) m/z : 335.0 (3), 243.0 (13), 229.1 (11), 193.1 (43), 158.1 (21). HRMS (EI-Orbitrap) m/z : $[\text{M} - \text{H}]^+$ calcd for $\text{C}_{16}\text{H}_{13}\text{ClNO}_3\text{S}^+$ 334.0299, found 334.0288. IR (Diamond-ATR, neat) $\tilde{\nu}_{\text{max}}$: 2918 (w), 1696 (s), 1580 (w) cm^{-1} .

1-(Benzo[d][1,3]dioxol-5-yl)cyclopropanecarboxylic Acid (**8a**). To a solution of **4w** (0.1 mmol) in CCl_4 (0.2 mL) and CH_2Cl_2 (0.1 mL) was added benzyltriethylammonium chloride (6 mg) followed by a dropwise addition of a 50% solution of NaOH (0.15 mL). The mixture was then stirred for 16 h at rt. Water was added, and the mixture was extracted with EtOAc, concentrated under vacuum and purified on silica gel, providing **8a** (0.1 mmol, 26 mg, quant.) as white solid. R_f = 0.3 (hexane/EtOAc 6:4, UV, KMnO_4 , PAA). ^1H NMR (400 MHz, CDCl_3) δ 6.83 (d, J = 1.6 Hz, 1H), 6.80 (dd, J = 7.9, 1.7 Hz, 1H), 6.73 (dd, J = 6.4, 3.3 Hz, 1H), 5.94 (s, 2H), 1.62 (dd, J = 7.0, 4.1 Hz, 3H), 1.22 ppm (dd, J = 6.9, 3.6 Hz, 2H) (COOH not observed). ^{13}C NMR (101 MHz, CDCl_3) 181.2, 147.4, 147.0, 132.7, 123.8, 111.3, 108.1, 101.2, 28.7, 17.8 ppm. LRMS (DEP/EI-Orbitrap) m/z : 206.1 (100), 161.0 (61). HRMS (EI-Orbitrap) m/z : $[\text{M}]^+$ calcd for $\text{C}_{11}\text{H}_{10}\text{O}_4^+$: 206.0579, found 206.0570. IR (Diamond-ATR, neat) $\tilde{\nu}_{\text{max}}$: 3014 (w), 2894 (w), 2594 (w), 1684 (vs) cm^{-1} . Mp ($^{\circ}\text{C}$): 157–158.

2,2-Difluoro-5-(2-methylcyclobut-1-en-1-yl)benzo[d][1,3]dioxole (**12**). To a solution of 5-bromo-2,2-difluorobenzo[d][1,3]dioxole in THF (0.5 M) at -10°C was slowly added $i\text{PrMgCl}\cdot\text{LiCl}$ (1.1 M in THF) and stirred at aforesaid temperature for 60 min. The so obtained (2,2-difluorobenzo[d][1,3]dioxol-5-yl)magnesium bromide was subsequently transmetalated to zinc by addition of a zinc chloride solution (1.0 M in THF) and stirring for another 60 min at -10°C . The resulting zinc species was subjected to a Negishi cross-coupling³ with **2b** to obtain **12**.

1-(1-(2,2-Difluorobenzo[d][1,3]dioxol-5-yl)cyclopropyl)ethanone (**4aj**). Using **12** according to general procedure Bb provided **4aj** (0.49 mmol, 118 mg, 49%) as a colorless oil. R_f = 0.5 (hexane/EtOAc 9:1, UV, KMnO_4 , PAA). ^1H NMR (400 MHz, CDCl_3) δ 7.12–7.06 (m, 2H), 7.02 (dd, J = 7.9, 0.7 Hz, 1H), 2.01 (s, 3H), 1.61 (dd, J = 6.8, 3.9 Hz, 2H), 1.16 ppm (dd, J = 7.1, 3.9 Hz, 2H). ^{13}C NMR (101 MHz, CDCl_3) 208.0, 143.8, 143.1, 137.4, 131.8 (t, J = 255.5 Hz), 126.2, 112.1, 109.5, 37.6, 29.1, 19.1 ppm. LRMS (DEP/EI-Orbitrap) m/z : 240.0 (100), 197.0 (32), 131.0 (40), 103.1 (76). HRMS (EI-Orbitrap) m/z : $[\text{M}]^+$ calcd for $\text{C}_{12}\text{H}_{10}\text{F}_2\text{O}_3^+$ 240.0598, found 240.0581.

1-(2,2-Difluorobenzo[d][1,3]dioxol-5-yl)cyclopropanecarboxylic Acid (**8b**). To a solution of **4aj** (0.33 mmol) in CCl_4 (0.66 mL) and CH_2Cl_2 (0.33 mL) was added benzyltriethylammonium chloride (20 mg) followed by a dropwise addition of a 50% solution of NaOH (0.5 mL). The mixture was then stirred for 16 h at rt. Water was added, and the mixture was extracted with EtOAc, concentrated under vacuum, and purified on silica gel, providing **8b** (0.33 mmol, 80 mg, quant.) as white solid. R_f = 0.3 (hexane/EtOAc 6:4, UV, KMnO_4 , PAA). ^1H NMR (400 MHz, CDCl_3) δ 7.08–7.03 (m, 2H), 6.98 (d, J = 8.2 Hz, 1H), 1.69 (dd, J = 7.2, 4.3 Hz, 2H), 1.25 ppm (dd, J = 7.2, 3.8 Hz, 2H) (COOH not observed). ^{13}C NMR (101 MHz, CDCl_3) 180.7, 143.6, 143.1, 134.9, 131.8 (t, J = 253.2 Hz), 125.8, 112.2, 109.1, 28.8, 17.9 ppm. LRMS (DEP/EI-Orbitrap) m/z : 242.0 (68), 224.0 (16), 196.0 (35). HRMS (EI-Orbitrap) m/z : $[\text{M}]^+$ calcd for $\text{C}_{11}\text{H}_8\text{F}_2\text{O}_4^+$ 242.0391, found 242.0382. IR (Diamond-ATR, neat) $\tilde{\nu}_{\text{max}}$: 2886 (w), 2840 (w), 1678 (vs) cm^{-1} . Mp ($^{\circ}\text{C}$): 179–180.

3-Chloro-6-(2-(2-methylcyclobut-1-en-1-yl)phenoxy)pyridazine (**10**). Using **2b** and (2-methoxyphenyl)boronic acid according to general procedure A provided **9**. The product was dissolved in CH_2Cl_2 (1.0 M) and treated with a solution of BBr_3 in CH_2Cl_2 (1.0 equiv, 1.0 M) at 30°C . After 5 min, TLC indicated completion of the reaction.

The reaction mixture was slowly poured onto ice-cold water and subsequently extracted with CH_2Cl_2 (3×20 mL) and dried over magnesium sulfate. After evaporation of solvents and purification by chromatography, pure **13** was dissolved in DMF (1.0 M). To the solution were added NaH (1.1 equiv, 60% dispersion in mineral oil) and 3,6-dichloropyridazine. After the solution was stirred for 30 min at ambient temperature, TLC indicated full consumption of the starting materials. The reaction mixture was extracted with Et_2O (3×20 mL), washed with a saturated aqueous solution of LiCl (20 mL) and brine (20 mL). After the organic phase was dried over magnesium sulfate and solvents were evaporated, chromatography afforded pure **10** as a colorless oil. Most fractions contained impurities, a yield was therefore not determined. $R_f = 0.3$ (hexane/EtOAc 8:2, UV, KMnO_4 , PAA). ^1H NMR (400 MHz, CDCl_3) δ 7.35 (d, $J = 9.2$ Hz, 1H), 7.36–7.33 (m, 1H), 7.18–7.12 (m, 2H), 7.02–6.98 (m, 1H), 6.96 (d, $J = 9.1$ Hz, 1H), 2.46–2.41 (m, 2H), 2.24–2.20 (m, 2H), 1.80–1.77 ppm (m, 3H). ^{13}C NMR (101 MHz, CDCl_3) δ 165.5, 151.8, 149.6, 142.5, 133.9, 131.4, 129.0, 129.0, 128.0, 126.0, 122.4, 119.2, 31.0, 28.9, 16.6 ppm. HRMS (EI-Orbitrap) m/z : $[\text{M}]^+$ calcd for $\text{C}_{15}\text{H}_{13}\text{ClN}_2\text{O}^+$ 272.0716, found 272.0714.

1-(2-((6-Chloropyridazin-3-yl)oxy)phenyl)cyclopropyl-ethanone (11). Using **10** (also impure fractions) according to general procedure Ba provided **11** (1.00 mmol, 288 mg, 43% over two steps) as a colorless oil. $R_f = 0.1$ (hexane/EtOAc 8:2, UV, KMnO_4 , PAA). ^1H NMR (400 MHz, CDCl_3) δ 7.49 (d, $J = 9.1$ Hz, 1H), 7.45–7.36 (m, 2H), 7.29 (dd, $J = 7.5$, 1.3 Hz, 1H), 7.19 (dd, $J = 8.0$, 1.3 Hz, 1H), 7.18 (d, $J = 9.1$ Hz, 1H), 2.08 (s, 3H), 1.43 (dd, $J = 6.9$, 3.8 Hz, 2H), 1.08 ppm (dd, $J = 7.2$, 3.9 Hz, 2H). ^{13}C NMR (101 MHz, CDCl_3) δ 208.2, 164.8, 153.9, 152.4, 132.9, 131.8, 131.8, 129.3, 126.4, 122.5, 120.2, 33.5, 28.9, 18.1 ppm. LRMS (DEP/EI-Orbitrap) m/z : 272.1 (9), 237.1 (100), 222.1 (30), 209.1 (15), 194.1 (18), 183.0 (10), 165.0 (12). HRMS (EI-Orbitrap) m/z : $[\text{M}]^+$ calcd for $\text{C}_{15}\text{H}_{12}\text{ClN}_2\text{O}^+$ ($[\text{M} - \text{OH}]^+$) 271.0638, found 271.0635. IR (Diamond-ATR, neat) $\tilde{\nu}_{\text{max}}$: 3066 (w), 2972 (w), 1754 (w), 1692 (m), 1642 (w), 1614 (w), 1606 (w) cm^{-1} .

(E)-2-Methyl-5-(4-methylstyryl)-3-phenethylfuran (7). Compound **6e** was dissolved in toluene (0.1 M), and P_4O_{10} (3.0 equiv) was added. The reaction mixture was heated to 100 °C for 24 h in a pressure tube. After being cooled to room temperature, the reaction was quenched with water, extracted with Et_2O (3×20 mL), washed with brine (20 mL), and dried over magnesium sulfate. The organic phase was concentrated under reduced pressure and purified by column chromatography. **7** was obtained (0.10 mmol, 29 mg, 87%) as a colorless oil. $R_f = 0.2$ (hexane, UV, KMnO_4 , PAA). ^1H NMR (400 MHz, CDCl_3) δ 7.36–7.32 (m, 2H), 7.31–7.26 (m, 2H), 7.23–7.11 (m, 5H), 6.90 (d, $J = 16.2$ Hz, 1H), 6.75 (d, $J = 16.2$ Hz, 1H), 6.13 (s, 1H), 2.81 (dd, $J = 8.7$, 6.7 Hz, 2H), 2.62 (dd, $J = 8.7$, 6.7 Hz, 2H), 2.34 (s, 3H), 2.10 ppm (s, 3H). ^{13}C NMR (101 MHz, CDCl_3) 150.8, 147.9, 141.8, 137.2, 134.7, 129.5, 128.7, 128.4, 126.2, 126.1, 125.2, 120.6, 115.9, 110.9, 36.8, 27.1, 21.4, 11.6 ppm. LRMS (DEP/EI-Orbitrap) m/z : 302.1 (100), 211.1 (42), 169.1 (35). HRMS (EI-Orbitrap) m/z : $[\text{M}]^+$ calcd for $\text{C}_{22}\text{H}_{22}\text{O}^+$ 302.1671, found 302.1670.

1-(p-Tolyl)cyclopropane-1-carbaldehyde (13a). Using 1-bromo-4-methylbenzene and cyclobutanone according to general procedure C provided **13a** (8.4 mmol, 1.346 g, 69%) as a colorless oil. $R_f = 0.5$ (hexane/EtOAc 9:1, UV, KMnO_4 , PAA). ^1H NMR (400 MHz, CDCl_3) δ 9.28 (s, 1H), 7.26–7.13 (m, 4H), 2.38 (s, 3H), 1.57 (dd, $J = 3.9$ Hz, 2H), 1.40 ppm (dd, 2H). ^{13}C NMR (101 MHz, CDCl_3) δ 201.4, 137.5, 134.6, 130.0, 129.4, 37.2, 21.2, 16.2 ppm. LRMS (DEP/EI-Orbitrap-Orbitrap) m/z : 160.1 (100), 145.1 (20). HRMS (EI-Orbitrap) m/z : $[\text{M}]^+$ calcd for $\text{C}_{11}\text{H}_{12}\text{O}^+$ 160.0888, found 160.0882. IR (Diamond-ATR, neat) $\tilde{\nu}_{\text{max}}$: 3010 (w), 2923 (w), 2919 (w), 2822 (vw), 2818 (vw), 1705 (vs), 1517 (m) cm^{-1} .

1-(4-Methoxyphenyl)cyclopropane-1-carbaldehyde (13b). Using 1-bromo-4-methoxybenzene and cyclobutanone according to general procedure C provided **13b** (0.34 mmol, 60 mg, 34%) as a colorless oil. $R_f = 0.4$ (hexane/EtOAc 9:1, UV, KMnO_4 , PAA). ^1H NMR (400 MHz, CDCl_3) δ 9.22 (s, 1H), 7.25–7.20 (m, 2H), 6.93–6.87 (m, 2H), 3.81 (s, 3H), 1.54 (dd, $J = 3.9$ Hz, 2H), 1.37 ppm (dd, $J = 3.5$ Hz, 2H). ^{13}C NMR (101 MHz, CDCl_3) δ 201.5, 159.1, 131.4, 129.6, 114.1, 55.4,

37.0, 16.2 ppm. LRMS (DEP/EI-Orbitrap-Orbitrap) m/z : 176.1 (100), 161.1 (10), 147.1 (70), 132.1 (15). HRMS (EI-Orbitrap) m/z : $[\text{M}]^+$ calcd for $\text{C}_{11}\text{H}_{12}\text{O}_2^+$ 176.0837, found IR (Diamond-ATR, neat) $\tilde{\nu}_{\text{max}}$: 176.0831. 3003 (vw), 2958 (vw), 2836 (w), 2708 (vw), 1780 (vw), 1703 (s), 1611 (m), 1579 (w), 1514 (vs) cm^{-1} .

1-(Naphthalen-1-yl)cyclopropane-1-carbaldehyde (13c). Using 1-bromonaphthalene and cyclobutanone according to general procedure C provided **13c** (0.58 mmol, 114 mg, 58%) as a colorless oil. $R_f = 0.4$ (hexane/EtOAc 9:1, UV, KMnO_4 , PAA). ^1H NMR (400 MHz, CDCl_3) δ 9.42 (s, 1H), 8.04–7.97 (m, 1H), 7.94–7.81 (m, 2H), 7.58–7.45 (m, 4H), 1.88–1.78 (m, 2H), 1.54–1.47 ppm (m, 2H). ^{13}C NMR (101 MHz, CDCl_3) δ 201.7, 134.2, 134.0, 133.3, 129.0, 128.8, 128.5, 126.6, 126.1, 125.5, 124.4, 35.7, 17.2 ppm. LRMS (DEP/EI-Orbitrap-Orbitrap) m/z : 196.1 (90), 178.1 (10), 165.1 (100), 152.1 (90), 139.1 (20). HRMS (EI-Orbitrap) m/z : $[\text{M}]^+$ calcd for $\text{C}_{14}\text{H}_{12}\text{O}^+$ 196.0888, found 196.0883. IR (Diamond-ATR, neat) $\tilde{\nu}_{\text{max}}$: 3044 (w), 3007 (vw), 2819 (vw), 2732 (vw), 2702 (vw), 1780 (vw), 1702 (s), 1595 (w) cm^{-1} .

1-([1,1'-Biphenyl]-4-yl)cyclopropane-1-carbaldehyde (13d). Using 4-bromo-1,1'-biphenyl and cyclobutanone according to general procedure C provided **13d** (0.57 mmol, 133 mg, 57%) as a colorless oil. $R_f = 0.45$ (hexane/EtOAc 9:1, UV, KMnO_4 , PAA). ^1H NMR (400 MHz, CDCl_3) δ 9.29 (s, 1H), 7.64–7.57 (m, 4H), 7.51–7.35 (m, 5H), 1.63 (dd, $J = 4.1$ Hz, 2H), 1.47 ppm (dd, $J = 4.3$ Hz, 2H). ^{13}C NMR (101 MHz, CDCl_3) δ 201.0, 140.8, 140.7, 136.5, 130.6, 128.9, 127.5, 127.2, 37.3, 16.2 ppm. HRMS (EI-Orbitrap) m/z : $[\text{M}]^+$ calcd for $\text{C}_{16}\text{H}_{14}\text{O}^+$ 222.1045, found 222.1048. IR (Diamond-ATR, neat) $\tilde{\nu}_{\text{max}}$: 1677 (m), 1498 (m), 1440 (w), 1427 (w) cm^{-1} .

1-(2,2-Difluorobenzo[d][1,3]dioxol-5-yl)cyclopropane-1-carbaldehyde (13e). Using S-bromo-2,2-difluorobenzo[d][1,3]dioxole and cyclobutanone according to general procedure C provided **13e** (0.5 mmol, 105 mg, 50%) as a colorless oil. $R_f = 0.5$ (hexane/EtOAc 9:1, UV, KMnO_4 , PAA). ^1H NMR (400 MHz, CDCl_3) δ 9.07 (s, 1H), 7.09–6.89 (m, 3H), 1.59 (dd, $J = 4.1$ Hz, 2H), 1.41 ppm (dd, $J = 3.7$ Hz, 2H). ^{13}C NMR (101 MHz, CDCl_3) δ 200.0, 143.9, 143.4, 133.5, 131.81 (t, $J = 255.5$ Hz), 125.6, 111.8, 109.5 ppm. LRMS (DEP/EI-Orbitrap-Orbitrap) m/z : 226.1 (80), 207.0 (5), 197.1 (15), 182.0 (5), 170.9 (5). HRMS (EI-Orbitrap) m/z : $[\text{M}]^+$ calcd for $\text{C}_{11}\text{H}_8\text{F}_2\text{O}_3^+$ 226.0442, found 226.0435.

1-(4-Bromophenyl)cyclopropane-1-carbaldehyde (13f). Using 1-bromo-4-iodobenzene and cyclobutanone according to general procedure C provided **13f** (0.69 mmol, 155 mg, 69%) as a colorless oil. $R_f = 0.5$ (hexane/EtOAc 9:1, UV, KMnO_4 , PAA). ^1H NMR (400 MHz, CDCl_3) δ 9.14 (s, 1H), 7.51–7.47 (m, 2H), 7.20–7.16 (m, 2H), 1.58 (dd, $J = 6.9$, 5.0 Hz, 2H), 1.39 ppm (dd, $J = 7.8$, 4.1 Hz, 2H). ^{13}C NMR (101 MHz, CDCl_3) δ 200.3, 136.5, 131.9, 131.9, 131.8, 37.2, 15.9 ppm. LRMS (DEP/EI-Orbitrap-Orbitrap) m/z : 226.0 (30), 197.0 (5), 181.9 (5). HRMS (EI-Orbitrap) m/z : $[\text{M}]^+$ calcd for $\text{C}_{10}\text{H}_9\text{BrO}^+$ 223.9837, found 223.9830. IR (Diamond-ATR, neat) $\tilde{\nu}_{\text{max}}$: 1682 (vs), 1488 (m), 1429 (m), 1420 (m) cm^{-1} .

■ ASSOCIATED CONTENT

● Supporting Information

The Supporting Information is available free of charge on the ACS Publications website at DOI: 10.1021/acs.joc.8b00297.

^1H and ^{13}C NMR spectra for all new compounds and computational details (PDF)

X-ray crystallographic data of compound **4f** (CIF)

X-ray crystallographic data of compound **4t** (CIF)

■ AUTHOR INFORMATION

Corresponding Authors

*E-mail: dorian.didier@cup.uni-muenchen.de.

*E-mail: regina.de_vivie@cup.uni-muenchen.de.

ORCID

Michael Eisold: 0000-0002-2314-3990

Regina de Vivie-Riedle: 0000-0002-7877-5979

Dorian Didier: 0000-0002-6358-1485

Notes

The authors declare no competing financial interest.

ACKNOWLEDGMENTS

Generous support from the Fonds der Chemischen Industrie, the Deutsche Forschungsgemeinschaft (DFG Grant No. DI 2227/2-1), and the SFB749 is greatly acknowledged. We kindly thank Dr. Peter Mayer for X-ray measurements and Martina Stadler for bioassays.

REFERENCES

- (1) (a) Wang, X.-N.; Krenske, E. H.; Johnston, R. C.; Houk, K. N.; Hsung, R. P. *J. Am. Chem. Soc.* **2015**, *137*, 5596. (b) Frebault, F.; Luparia, M.; Oliveira, M. T.; Goddard, R.; Maulide, N. *Angew. Chem., Int. Ed.* **2010**, *49*, 5672.
- (2) (a) Lee-Ruff, E.; Mladenova, G. *Chem. Rev.* **2003**, *103*, 1449. (b) Namyslo, J. C.; Kaufmann, D. E. *Chem. Rev.* **2003**, *103*, 1485. (c) Xu, Y.; Conner, M. L.; Brown, M. K. *Angew. Chem., Int. Ed.* **2015**, *54*, 11918. (d) Misale, A.; Niyomchon, S.; Maulide, N. *Acc. Chem. Res.* **2016**, *49*, 2444.
- (3) Eisold, M.; Baumann, A. N.; Kiefl, G. M.; Emmerling, S. T.; Didier, D. *Chem. - Eur. J.* **2017**, *23*, 1634.
- (4) (a) Eisold, M.; Didier, D. *Org. Lett.* **2017**, *19*, 4046. (b) Eisold, M.; Kiefl, G. M.; Didier, D. *Org. Lett.* **2016**, *18*, 3022. (c) Eisold, M.; Didier, D. *Angew. Chem., Int. Ed.* **2015**, *54*, 15884.
- (5) Baumann, A. N.; Eisold, M.; Didier, D. *Org. Lett.* **2017**, *19*, 2114.
- (6) (a) Bailey, S.; Barrett, S. D.; Bratton, L. D.; Fakhoury, S. A.; Jennings, S. M.; Mitchell, L. H.; Raheja, R. K.; Shanmugasundaram, V. PCT Int. Appl. WO 2007072164 A2 20070628, 2007. (b) Tsukamoto, Y.; Komai, H.; Kadotani, J.; Koi, K.; Mio, S.; Takeshiba, H. PCT Int. Appl. WO 2003016286 A1 20030227, 2003. (c) Vicker, N.; Su, X.; Pradaux-Caggiano, F.; Potter, B. V. L. WO 2009106817 A2 20090903, 2009. (d) Qiao, J. X.; King, S. R.; He, K.; Wong, P. C.; Rendina, A. R.; Luetgten, J. M.; Xin, B.; Knabb, R. M.; Wexler, R. R.; Lam, P. Y. S. *Bioorg. Med. Chem. Lett.* **2009**, *19*, 462. (e) Shibayama, K.; Inagaki, J.; Saiki, Y.; Mitani, A.; Kuwahara, R.; Sato, M.; Nishimura, S.; Kuboki, M. PCT Int. Appl. WO 2011081174 A1 20110707, 2011. (f) Delany, C.; Kale, R. D.; Gabriel, S.; Bove, P. PCT Int. Appl. WO 2017151725 A1 20170908, 2017. (g) Wainwright, C. E.; Elborn, J. S.; Ramsey, B. W.; Marigowda, G.; Huang, X.; Cipolli, M.; Colombo, C.; Davies, J. C.; De Boeck, K.; Flume, P. A.; Konstan, M. W.; McColley, S. A.; McCoy, K.; McKone, E. F.; Munck, A.; Ratjen, F.; Rowe, S. M.; Waltz, D.; Boyle, M. P. N. *Engl. J. Med.* **2015**, *373*, 220. (h) Ries, U. J.; Pripke, H. W. M.; Huel, N. H.; Handschuh, S.; Mihm, G.; Stassen, J. M.; Wienen, W.; Nar, H. *Bioorg. Med. Chem. Lett.* **2003**, *13*, 2297. (i) Peretto, I.; Radaelli, S.; Parini, C.; Zandi, M.; Raveglia, L. F.; Dondio, G.; Fontanella, L.; Misiano, P.; Bigogno, C.; Rizzi, A.; Riccardi, B.; Biscailioli, M.; Marchetti, S.; Puccini, P.; Catinella, S.; Rondelli, I.; Cenacchi, V.; Bolzoni, P. T.; Caruso, P.; Villetti, G.; Facchinetti, F.; Del Giudice, E.; Moretto, N.; Imbimbo, B. P. *J. Med. Chem.* **2005**, *48*, 5705.
- (7) (a) Li, J.; Kennedy, L. J.; Wang, H.; Li, J. J.; Walker, S. J.; Hong, Z.; O'Connor, S. P.; Nayeem, A.; Camac, D. M.; Morin, P. E.; Sheriff, S.; Wang, M.; Harper, T.; Golla, R.; Seethala, R.; Harry, T.; Ponticello, R. P.; Morgan, N. N.; Taylor, J. R.; Zebo, R.; Gordon, D. A.; Robl, J. A. *ACS Med. Chem. Lett.* **2014**, *5*, 803. (b) Lerner, C.; Jakob-Roetne, R.; Buettelmann, B.; Ehler, A.; Rudolph, M.; Rodríguez Sarmiento, R. M. *J. Med. Chem.* **2016**, *59*, 10163. (c) Pieroni, M.; Annunziato, G.; Beato, C.; Wouters, R.; Benoni, R.; Campanini, B.; Pertinhez, T. A.; Bettati, S.; Mozzarelli, A.; Costantino, G. *J. Med. Chem.* **2016**, *59*, 2567. (d) Geldenhuys, W. J.; Caporoso, J.; Leeper, T. C.; Lee, Y.-K.; Lin, L.; Darvesh, A. S.; Sadana, P. *Bioorg. Med. Chem. Lett.* **2017**, *27*, 303.
- (8) (a) Zhang, Y.; Pan, L.; Xu, X.; Liu, Q. *RSC Adv.* **2012**, *2*, 5138. (b) Huang, A.; Moretto, A.; Janz, K.; Lowe, M.; Bedard, P. W.; Tam, S.; Di, L.; Clerin, V.; Sushkova, N.; Tchernychev, B.; Tsao, D. H. H.; Keith, J. C., Jr.; Shaw, G. D.; Schaub, R. G.; Wang, Q.; Kaila, N. *J. Med. Chem.* **2010**, *53*, 6003.
- (9) (a) Papahatjis, D. P.; Nikas, S.; Tsotinis, A.; Vlachou, M.; Makriyannis, A. *Chem. Lett.* **2001**, *30*, 192. (b) Arava, V. R.; Siripalli, U. B.; Dubey, P. K. *Tetrahedron Lett.* **2005**, *46*, 7247. (c) Barbasiewicz, M.; Marciniak, K.; Fedoryński, M. *Tetrahedron Lett.* **2006**, *47*, 3871. (d) Berger, M. D.; Hammerschmidt, F.; Qian, R.; Hahner, S.; Schirbel, A.; Stichelberger, M.; Schibli, R.; Yu, J.; Arion, V. B.; Woschek, A.; Öhler, E.; Zolle, I. M. *Mol. Pharmaceutics* **2013**, *10*, 1119.
- (10) (a) Aggarwal, V. K.; Winn, C. L. *Acc. Chem. Res.* **2004**, *37*, 611. (b) Clemens, J. J.; Asgian, J. L.; Busch, B. B.; Coon, T.; Ernst, J.; Kaljevic, L.; Krenitsky, P. J.; Neubert, T. D.; Schweiger, E. J.; Termin, A.; Stamos, D. J. *Org. Chem.* **2013**, *78*, 780. (c) Gololobov, Y. G.; Nesmeyanov, A. N.; Lysenko, V. P.; Boldeskul, I. E. *Tetrahedron* **1987**, *43*, 2609.
- (11) (a) Klapars, A.; Waldman, J. H.; Campos, K. R.; Jensen, M. S.; McLaughlin, M.; Chung, J. Y. L.; Cvetovich, R. J.; Chen, C. J. *Org. Chem.* **2005**, *70*, 10186. (b) Caron, S.; Vazquez, E.; Wojcik, J. M. *J. Am. Chem. Soc.* **2000**, *122*, 712. (c) McCabe Dunn, J. M.; Kuethe, J. T.; Orr, R. K.; Tudge, M.; Campeau, L.-C. *Org. Lett.* **2014**, *16*, 6314.
- (12) (a) Chen, H.; Zhang, L. *Angew. Chem., Int. Ed.* **2015**, *54*, 11775. (b) Liu, B.; Song, R.-J.; Ouyang, X.-H.; Li, Y.; Hu, M.; Li, J.-H. *Chem. Commun.* **2015**, *51*, 12819.
- (13) For early studies of cyclobutene oxide rearrangements, see: (a) Heine, H.-G.; Hartmann, W.; Knops, H.-J.; Priesnitz, U. *Tetrahedron Lett.* **1983**, *24*, 2635. (b) Conia, J. M. *Angew. Chem.* **1968**, *80*, 578. (c) Garin, D. L. *J. Org. Chem.* **1971**, *36*, 1697.
- (14) For seminal studies and recent examples, see: (a) Meinwald, J.; Labana, S. S.; Chadha, M. S. *J. Am. Chem. Soc.* **1963**, *85*, 582. (b) Rickborn, B. In *Comprehensive Organic Synthesis*; Trost, B. M., Fleming, I., Pattenden, G., Eds.; Pergamon: Oxford, 1991; Vol. 3, p 733. (c) Gorzynski Smith, J. *Synthesis* **1984**, 1984, 629. (d) Fraile, J. M. A.; Mayoral, J. A.; Salvatella, L. *J. Org. Chem.* **2014**, *79*, 5993. (e) Jung, M. E.; D'Amico, D. C. *J. Am. Chem. Soc.* **1995**, *117*, 7379. (f) Pace, V.; Castoldi, L.; Mazzeo, E.; Rui, M.; Langer, T.; Holzer, W. *Angew. Chem., Int. Ed.* **2017**, *56*, 12677.
- (15) (a) Criegee, R.; Noll, N. *Liebigs Ann. Chem.* **1959**, *627*, 1–14. (b) Shabarov, Y. S.; Blagodatskikh, S. A.; Levina, M. I.; Fedotov, A. N. *Z. Org. Khim.* **1975**, *11*, 1223. (c) Kurita, J.; Sakai, H.; Tsuchiya, T. *J. Chem. Soc., Chem. Commun.* **1985**, 1769–1770. (d) Wiberg, K. B.; Matturro, M. G.; Okarma, P. J.; Jason, M. E.; Dailey, W. P.; Burgmaier, G. J.; Bailey, W. F.; Warner, P. *Tetrahedron* **1986**, *42*, 1895–1902. (e) Kurita, J.; Sakai, H.; Tsuchiya, T. *Chem. Pharm. Bull.* **1988**, *36*, 2887–2896. (f) Mévellec, L.; Evers, M.; Huet, F. *Tetrahedron* **1996**, *52*, 15103–15116. (g) Lescop, C.; Huet, F. *Tetrahedron* **2000**, *56*, 2995–3003. (h) Ripoll, J.-L.; Conia, J.-M. *Bull. Soc. Chim. Fr.* **1965**, 2755. (i) de Mayo, P.; Wenska, G. *Tetrahedron* **1987**, *43*, 1661–1670.
- (16) A [4 + 2]-cycloaddition of the diene with O₂ is assumed to be responsible for the formation of 1,4-diketones. For a recent example, see: Shen, L.; Zhao, K.; Doitomi, K.; Ganguly, R.; Li, Y.-X.; Shen, Z.-L.; Hirao, H.; Loh, T.-P. *J. Am. Chem. Soc.* **2017**, *139*, 13570.
- (17) See the [Supporting Information](#).
- (18) CCDC 1580399 (4f) and CCDC 1580400 (4t) contain the crystallographic data for this paper.
- (19) Kasai, K.; Liu, Y.; Hara, R.; Takahashi, T. *Chem. Commun.* **1998**, *18*, 1989.
- (20) Toda, F.; Takehira, Y.; Kataoka, Y.; Mori, K.; Sato, T.; Segawa, M. *J. Chem. Soc., Chem. Commun.* **1984**, 1234.
- (21) *Gaussian 16*, Revision A.03: Frisch, M. J.; Trucks, G. W.; Schlegel, H. B.; Scuseria, G. E.; Robb, M. A.; Cheeseman, J. R.; Scalmani, G.; Barone, V.; Petersson, G. A.; Nakatsuji, H.; Li, X.; Caricato, M.; Marenich, A. V.; Bloino, J.; Janesko, B. G.; Gomperts, R.; Mennucci, B.; Hratchian, H. P.; Ortiz, J. V.; Izmaylov, A. F.; Sonnenberg, J. L.; Williams-Young, D.; Ding, F.; Lipparini, F.; Egidi, F.; Goings, J.; Peng, B.; Petrone, A.; Henderson, T.; Ranasinghe, D.; Zakrzewski, V. G.; Gao, J.; Rega, N.; Zheng, G.; Liang, W.; Hada, M.; Ehara, M.; Toyota, K.; Fukuda, R.; Hasegawa, J.; Ishida, M.; Nakajima, T.; Honda, Y.; Kitao, O.; Nakai, H.; Vreven, T.; Throssell, K.; Montgomery, J. A., Jr.; Peralta, J. E.; Ogliaro, F.; Bearpark, M. J.; Heyd,

J. J.; Brothers, E. N.; Kudin, K. N.; Staroverov, V. N.; Keith, T. A.; Kobayashi, R.; Normand, J.; Raghavachari, K.; Rendell, A. P.; Burant, J. C.; Iyengar, S. S.; Tomasi, J.; Cossi, M.; Millam, J. M.; Klene, M.; Adamo, C.; Cammi, R.; Ochterski, J. W.; Martin, R. L.; Morokuma, K.; Farkas, O.; Foresman, J. B.; Fox, D. J. Gaussian, Inc., Wallingford, CT, 2016.

(22) Werner, H.-J.; Knowles, P. J.; Knizia, G.; Manby, F. R.; Schütz, M.; Celani, P.; Korona, T.; Lindh, R.; Mitrushenkov, A.; Rauhut, G.; Shamasundar, K. R.; Adler, T. B.; Amos, R. D.; Bernhardsson, A.; Berning, A.; Cooper, D. L.; Deegan, M. J. O.; Dobbyn, A. J.; Eckert, F.; Goll, E.; Hampel, C.; Hesselmann, A.; Hetzer, G.; Hrenar, T.; Jansen, G.; Köppl, C.; Liu, Y.; Lloyd, A. W.; Mata, R. A.; May, A. J.; McNicholas, S. J.; Meyer, W.; Mura, M. E.; Nicklass, A.; O'Neill, D. P.; Palmieri, P.; Peng, D.; Pflüger, K.; Pitzer, R.; Reiher, M.; Shiozaki, T.; Stoll, H.; Stone, A. J.; Tarroni, R.; Thorsteinsson, T.; Wang, M. MOLPRO, version 2012.1, a package of ab initio programs, 2012.

(23) Molcas 8: Aquilante, F.; Autschbach, J.; Carlson, R. K.; Chibotaru, L. F.; Delcey, M. G.; De Vico, L.; Fdez. Galván, I.; Ferré, N.; Frutos, L. M.; Gagliardi, L.; Garavelli, M.; Giussani, A.; Hoyer, C. E.; Li Manni, G.; Lischka, H.; Ma, D.; Malmqvist, P. Å.; Müller, T.; Nenov, A.; Olivucci, M.; Pedersen, T. B.; Peng, D.; Plasser, F.; Pritchard, B.; Reiher, M.; Rivalta, I.; Schapiro, I.; Segarra-Martí, J.; Stenrup, M.; Truhlar, D. G.; Ungur, L.; Valentini, A.; Vancoillie, S.; Veryazov, V.; Vysotskiy, V. P.; Weingart, O.; Zapata, F.; Lindh, R. *J. Comput. Chem.* **2016**, 37, 506.

(24) Sevin, F.; McKee, M. L. *J. Am. Chem. Soc.* **2001**, 123, 4591.

(25) Hirsch, E.; Hünig, S.; Reißig, H.-U. *Chem. Ber.* **1982**, 115, 399.

1.2 Twisted intramolecular charge transfer - an excited state reaction

Photoswitches are a class of molecules undergoing configurational change by exciting them with light. They have a broad field of applications ranging from material science [29], e.g. as light-responsive polymers [30, 31] to photopharmacology, e.g. in cancer therapy [32]. Common photoswitches are for example azobenzenes and stilbenes, which have been extensively studied, both experimentally [26–28] and theoretically [74, 75]. A further group of photoswitches are HTIs which undergo $Z \rightarrow E$ isomerization by excitation with UV light [34–36], analog to azobenzenes and stilbenes. By integrating a chiral center in the molecule it can also be used as a molecular motor [44, 45] similar to the molecular motors developed by the group of Feringa [46, 47]. Chapter 2.1 is going into more detail concerning the case of molecular motors. The here investigated HTI derivative has next to the well-studied $Z \rightarrow E$ double bond isomerization (DBI) [34–36] (fig. 1.2 blue) a second competing pathway. A single bond twist (SBT) (fig. 1.2 orange) leads to a TICT state [37, 38]. This pathway is determined by the pre-twist of the C-C single bond in the ground state due to sterical hinderance of the methyl groups in ortho-position. The distribution of the competing pathways highly depends on the polarity of the solvent because the polar TICT state is very sensitive to the change of solvent. Thus, polar solvents reveal the SBT pathway whereas in unpolar solvents solely the DBI pathway is reachable. Both reaction pathways are confirmed with CASSCF/CASPT2 including the solvent environment via single point calculations. Important vibrations activated during the reaction are identified and related to experimental bands of transient infrared (IR)-spectra.

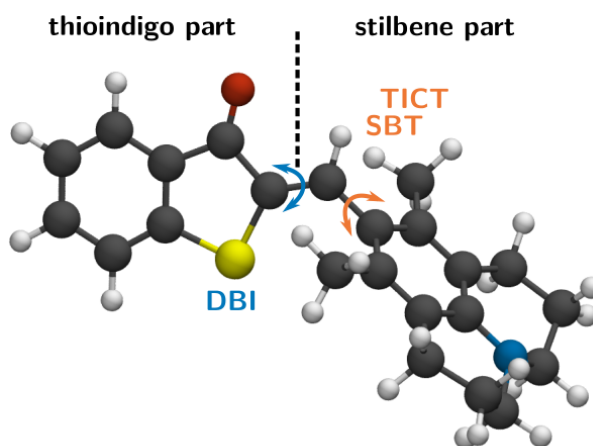


Figure 1.2: Pre-twisted ground state geometry of HTI derivative **Z-2** with the competing pathways highlighted in blue (DBI) and orange (SBT).

The solvent environment is described with the polarized continuum model (PCM). Here, a spherical cavity is built around the solute and the solvent is represented by a continuous dielectric medium around this cavity. For the solvent-solute interaction the solute is treated as a polarizable dipole [76, 77]. In a basic polarized continuum model (PCM) scheme, e.g. valid for minima, the solvent is always in complete equilibrium with the solute, dependent on the respective wavefunction (fig 1.3 (1)) [77, 78]. For the correct description of fast processes, such as vertical excitations, the response of the solvent to the solute is separated in a fast and slow part (fast and slow charges). The fast charges correspond to an electronic alignment of the solvent molecules, whereas the slow charges corresponds to a reorientation of the solvent molecules around the solute cavity [77, 79]. In the non-equilibrium scheme describing a vertical excitation process, only the fast part of the response is re-calculated for the new state and the

slow part of the response is taken from the original state (fig 1.3 (2)). The solute cavity is also assumed to remain constant during the fast process of electronic transition [77–79]. The vertical excitation energy for a $S_0 \rightarrow S_1$ excitation is hereby calculated according to eq 1.1. During the relaxation to the excited state minimum the solvent can completely equilibrate to the solute in the new state (fig 1.3 (3)). When the solute relaxes from the $S_{1\text{Min}}$ back to the ground state (vertical deexcitation process), again only the fast part of the solvent response is in equilibrium to the new state (fig 1.3 (4)). The vertical deexcitation energy ($S_1 \rightarrow S_0$) is calculated according to eq 1.2.

$$\Delta E_{\text{exc}} = E_{\text{noneq}}(S_1) - E_{\text{eq}}(S_0) \quad (1.1)$$

$$\Delta E_{\text{dex}} = E_{\text{noneq}}(S_0) - E_{\text{eq}}(S_1) \quad (1.2)$$

As the slow part of the solvent response can only be calculated as the difference of the

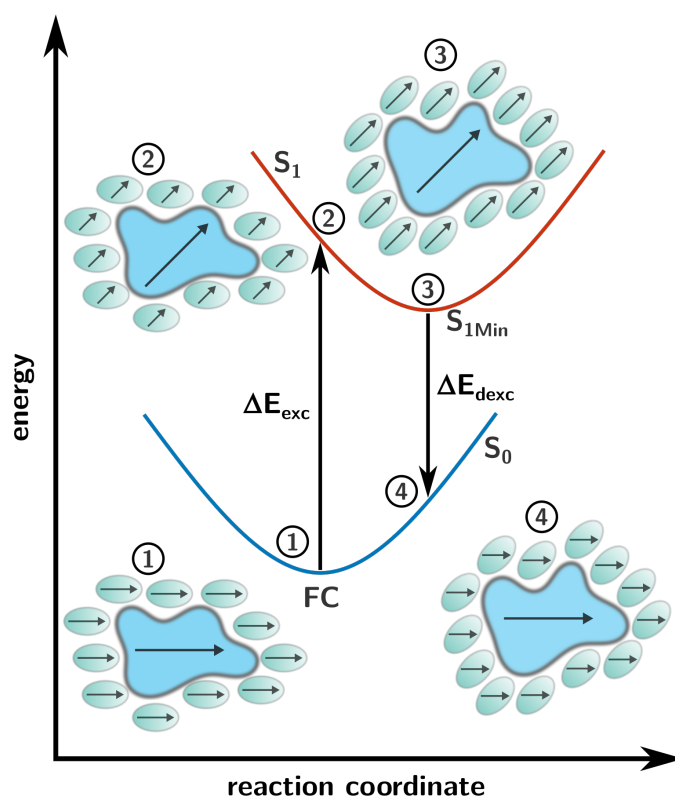


Figure 1.3: Response of the solvent in vertical excitation and deexcitation processes. The response of the solvent with the change of electronic state is separated in fast charges, namely the electronic rearrangement illustrated with arrows and the slow charges, namely the reorientation around the solute cavity illustrated by the ellipsoidal form. The solute cavity is assumed to not change during the fast electronic transition. **1** The solvent is in complete equilibrium at the Franck-Condon (FC) point. **2** After vertical excitation the solvent is in non-equilibrium with only the fast part of the response aligned to the solute. **3** With the relaxation to the $S_{1\text{Min}}$ also the slow part of the solvent response equilibrates to the new state. **4** After the vertical deexcitation process the solvent is in non-equilibrium in the ground state with the slow part of the response still oriented to the excited state.

total and the fast response, two consecutive single point calculations are necessary. In the first, the solvent is calculated in equilibrium to the original state. In the second calculation the solvent orientation (slow part) of the first calculation is used to calculate the solvent in non-equilibrium in the new state. In the appendix B the necessary

input-files for the calculation of the excited state relaxation process at the CASPT2 level of theory using PCM with OpenMolcas[80, 81] (fig. 4 of reference [82]) are listed (steps 1 to 4 from fig. 1.3).

The key points of the article “Electronic and Geometric Characterization of TICT Formation in Hemithioindigo Photoswitches by Picosecond Infrared Spectroscopy” with emphasis on the calculations are:

- The photo-chemistry of the discussed HTI derivatives **Z-1** and **Z-2** is determined by two competing pathways, the single bond twist (SBT) forming a long-living TICT state and the double bond isomerization (DBI) resulting in a $Z \rightarrow E$ isomerization. Hereby, the solvent environment is decisive for the preferred pathway. In polar solvents the SBT is preferred while in unpolar solvents only DBI is observed.
- The excited state reaction pathway of the HTI TICT formation is investigated at the CASSCF/CASPT2 level of theory including the solvent environment by using PCM. First, a S_1 minimum with $\pi \Rightarrow \pi^*$ character shows the same pre-twist along the C-C single bond as the FC point. Second, a S_2/S_1 CoIn and a S_1 minimum with charge transfer (CT) character are identified, both show an almost 90° twist of the single bond. With the found intermediates, the occurrence of a TICT state in polar solvents can be explained compared to the solely $Z \rightarrow E$ isomerization in unpolar solvents.
- The transient IR-spectra show specific bands appearing only in polar solvents. The dynamic of these bands is defined by a red-shift that fits the time-scale of TICT formation. Excited state IR-spectra are calculated for the key geometries with TDDFT. The marker bands for the TICT formation are identified, namely a C-O and a C-N stretch vibration shifting along the TICT formation. The first mentioned shows a red-shift comparable to the experimental observed red-shift.
- The C-O marker band shift can be associated with the change in charge distribution while forming the TICT. The electrostatic potential surfaces along the reaction path reveal the charge separation across the twisted C-C single bond. Negative charge is shifted from the electronrich stilbene to the thioindigo part which goes along with an elongation of the C-O double bond. Those effects are mostly pronounced at the TICT geometry and are reflected in the red-shift of the C-O marker band.

The article “Electronic and Geometric Characterization of TICT Formation in Hemithioindigo Photoswitches by Picosecond Infrared Spectroscopy” published in *The Journal of Physical Chemistry A* is reprinted with permission of *J. Phys. Chem. A*, **125**, 4390–4400 (2021). Copyright 2021 American Chemical Society.

Electronic and Geometric Characterization of TICT Formation in Hemithioindigo Photoswitches by Picosecond Infrared Spectroscopy

Klara Stallhofer, Matthias Nuber, Franziska Schüppel, Stefan Thumser, Hristo Iglev, Regina de Vivie-Riedle,* Wolfgang Zinth,* and Henry Dube*



Cite This: *J. Phys. Chem. A* 2021, 125, 4390–4400



Read Online

ACCESS |



Metrics & More

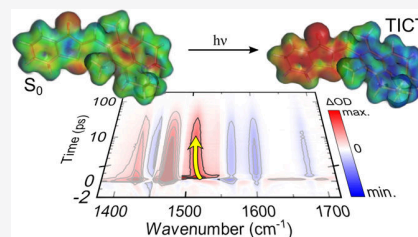


Article Recommendations



Supporting Information

ABSTRACT: Deciphering the exact electronic and geometric changes of photoexcited molecules is an important task not only to understand the fundamental atomistic mechanisms but also to rationally design molecular properties and functions. Here, we present a combined experimental and theoretical study of the twisted intramolecular charge transfer (TICT) process in hemithioindigo photoswitches. Using ultrafast transient IR spectroscopy as the main analytical method, a detailed understanding of the extent and direction of charge transfer within the excited molecule is obtained. At the same time, the geometrical distortion is monitored directly via changes of indicative vibrational modes over the time course of the photoreaction. These high-resolution data deliver a detailed molecular movie of the TICT process in this important class of chromophores with picosecond time resolution.



INTRODUCTION

Twisted intramolecular charge transfer (TICT) is a process in which electronically excited molecules assume strongly twisted geometries upon charge transfer from one molecular part to another.^{1–6} Because of this pronounced twist, the two molecular parts are electronically strongly decoupled and charge separation is typically not readily reversed. Additionally, the electronic decoupling and limited orbital overlap typically hamper direct radiative deexcitation pathways. Taken together, this leads to prolonged lifetimes of the TICT excited states, which is a hallmark for their presence in combination with strongly red-shifted, yet very weak emissions. Since TICT states can result in pronounced geometry changes after light irradiation, they can be used to achieve advanced responsive molecular functions and applications⁷ ranging from molecular rotors⁸ to viscosity or polarity sensors,^{9–11} organic light-emitting diodes¹² or solar cells.¹³ When TICT behavior is combined with photoswitching, interesting multidimensional control over molecular motions can be achieved,^{14–22} which is of great potential interest for applications in responsive materials or molecular machinery.^{23–25}

We have recently established TICT formation in hemithioindigo (HTI) chromophores (Figure 1)—an emerging class of photoswitches^{26,27}—and used this excited-state pathway for controlling the type of light-induced molecular motion by simply changing the solvent.²¹ A similar charge transfer behavior in the excited state was also suggested for *N,N*-diarylamine-substituted HTIs.²⁸ With the additional TICT state, it is possible to either favor double-bond isomerization (DBI) in apolar solvents or single-bond twisting (SBT) in strongly polar solvents using the same molecule

(Figure 1b). The reason for this behavior is the inherently most polar character of the TICT state as compared to other excited states (Figure 1c). Therefore, its associated energy can be altered much more effectively by the outside medium as compared to the other excited states. In apolar solvents, the TICT state is not stabilized enough to be accessible; however, polar environments favor its energy up to a point where it is the only populated excited state that directly connects back to the ground state (GS) (Figure 1b). To reveal, which bond is rotated upon TICT formation, the electron-donating amine group was fused into rings in the julolidine derivative **2**. In this way, only rotation around the single bond connecting the stilbene part with the central double bond can lead to an excited-state twisting of the molecular structure. As TICT formation is unperturbed by this structural restriction, the TICT rotation coordinate—i.e., the aforementioned single bond—was elucidated. In a subsequent study, we have delivered a comprehensive analysis of the structural prerequisites to achieve TICT formation in HTI photoswitches in general.²² It requires a strong pretwist along the TICT coordinate (the aforementioned single bond) in the ground state (see, for example, ref 29 for related pretwisting effects in

Received: March 24, 2021

Revised: April 29, 2021

Published: May 14, 2021

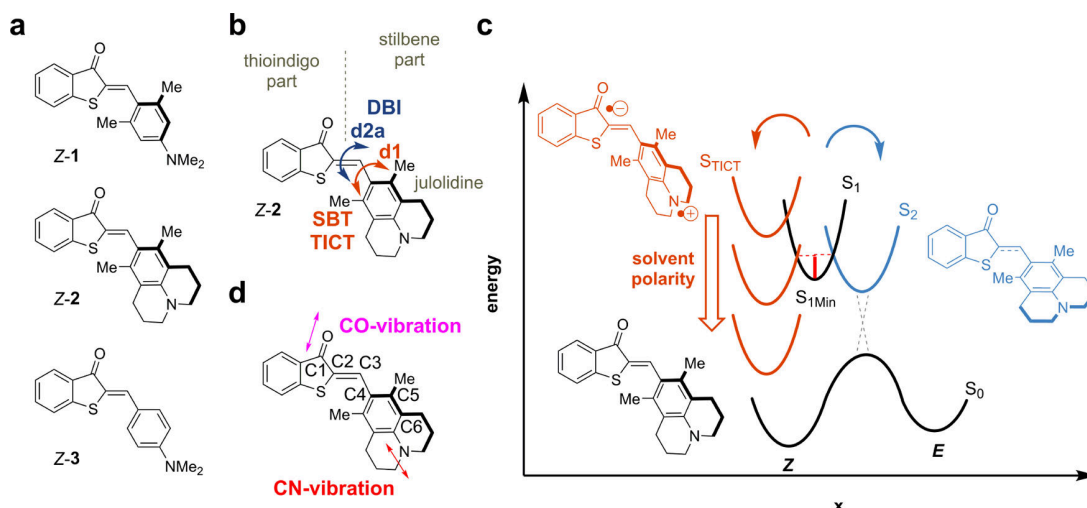


Figure 1. TICT formation in HTI photoswitches. (a) HTI derivatives Z-1–Z-3 used in the present study. (b) Double-bond isomerization (DBI) and TICT-induced single-bond twist (SBT) as accessible rotation processes within HTI Z-2. (c) General TICT formation mechanism in HTIs. (d) Important vibrations monitored in the present study.

TICT molecules) and a strong electron donor at the stilbene part.

Despite this progress in the general understanding of TICT processes, the short-lived excited state of HTI molecules renders a detailed mechanistic analysis difficult. So far, the excited-state behavior deduced from transient UV–vis absorption spectroscopy yields only limited insights into the exact structural and electronic changes that govern TICT formation. Such information is nevertheless crucial if TICT states shall be used as a rationally designable tool, whose properties can be determined by variation of the molecular structure as well as solvent polarity, especially in the context of light-powered molecular nanotechnology.

In this work, we present a combined experimental and theoretical study of transient infrared (IR)-spectroscopy (see refs 30, 31 for examples of transient infrared or Raman spectroscopy of TICT states in traditional TICT dyes) to gain a deeper understanding of the nature of TICT formation in HTI (see Figure 1d for important vibrations monitored). To this end, a series of three HTI derivatives 1–3 are analyzed in their Z configuration (Figure 1a). HTIs 1 and 2 differ in the relative electron richness of the stilbene part with 2 bearing the stronger julolidine-based donor. Both HTIs readily undergo TICT formation in polar solvents. HTI 3 serves as a control compound, which bears the same electron-rich stilbene part as 1, yet is not pretwisted in the ground state and thus does not undergo TICT formation in any solvent. The central questions that are addressed in this work are the extent of charge transfer in the TICT state as opposed to the other excited states and the nature of the structural changes that accompany the process.

MATERIALS AND METHODS

Infrared Spectroscopy. The HTI derivatives were dissolved in deuterated solvents [cyclohexane- d_{12} 99.5% (dCH), tetrahydrofuran- d_8 99.5% (dTHF), dichloromethane- d_2 99.96% (dDCM); all from deuterio GmbH], and dimethylsulfoxide- d_6 99.8% (dDMSO; Merck KGaA), at a concentration of 1.0–2.5 mg/ml in the sample cells. For the time-resolved experiments, HTI Z-1 was dissolved in dCH,

dDCM, and dDMSO; HTI Z-2 in dCH, dTHF; and dDCM; and HTI Z-3 in dCH, dDCM, and dDMSO.

Steady-state visible spectra were recorded on a Shimadzu UV1800 spectrophotometer, and infrared spectra were obtained using a Bruker IFS66v/s Fourier transform infrared (FTIR)-spectrometer. The infrared spectra shown in this article were corrected for the solvent background.

The setup for time-resolved infrared spectroscopy is based on a commercial Ti:sapphire CPA system (Coherent Libra, 130 fs, 800 nm, 1 kHz). One part of the pulse was used to seed a home-built two-stage noncollinear optical parametric amplifier (NOPA) to generate excitation pulses close to absorption maxima of the samples at 460–500 nm with a pulse energy of 1–2 μ J. A second part of the laser output generated mid-infrared pulses by a home-built two-stage optical parametric amplifier (OPA) with a subsequent difference frequency generation (DFG) stage, where the signal and idler pulses were used to generate the mid-IR probing pulses. After passing the excited part of the sample, the probe pulses were spectrally resolved in a polychromator (Chromex 250is, Bruker) and recorded on a 2×64 pixel HgCdTe infrared detector (InfraRed Associates) with a resolution of 4 cm^{-1} . Changes in the infrared absorption of the samples upon excitation are monitored as the change in the optical density, $\Delta OD = -\log_{10}(T/T_0)$, with T being the infrared transmission of the excited sample and T_0 being the reference signal with a blocked pump beam.

Probe beam and pump beam polarization were arranged in a magic angle (54.7°) configuration to avoid anisotropy effects. The samples were pumped through a thin (90 μm) flow cell with CaF_2 -windows in a closed cycle. Illuminating the reservoir with a cold light lamp (KL 2500 LCD, Schott) and using appropriate longpass glass filters (Schott) for selecting the appropriate wavelengths ensured that the molecules were photoisomerized to their Z-isomeric state before being excited by the pump pulse. We reduced the influence of atmospheric water vapor absorption by flushing with dry air the part of the experimental setup where the mid-IR pulses propagated. Fluctuations in the laser setup were corrected using a reference beam on the second detector row. As the spectra shown in this article are composed of two subsequent measurements with

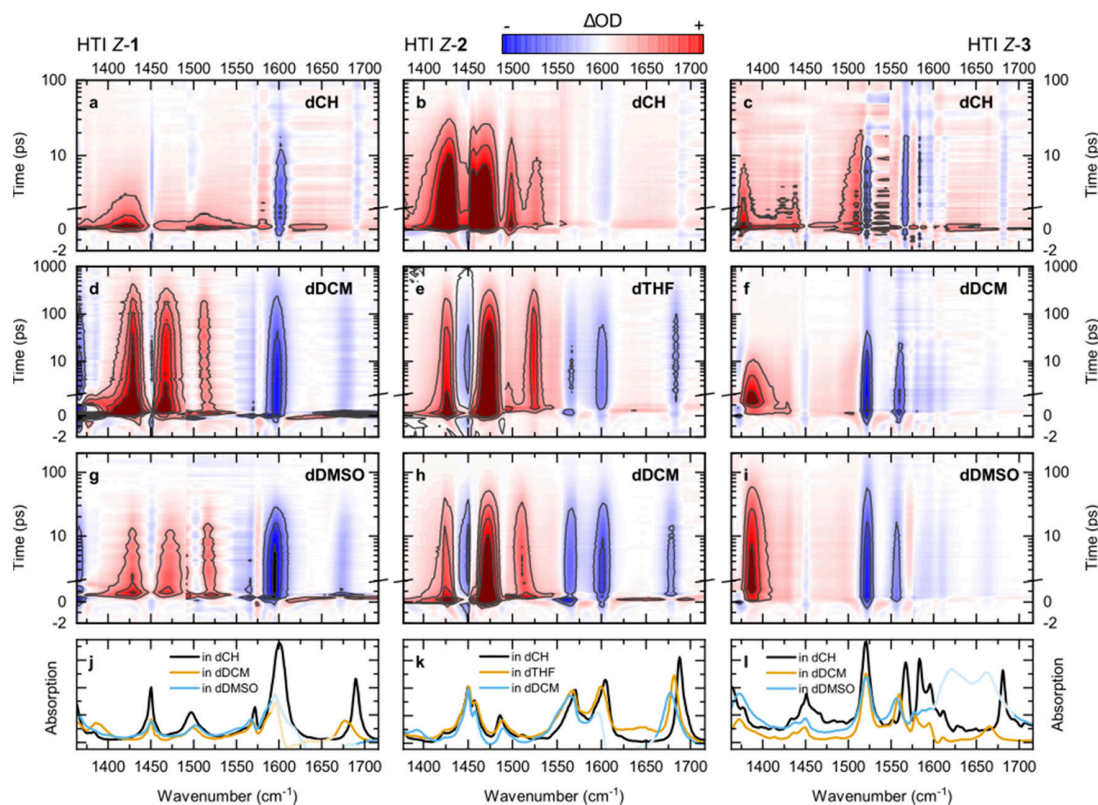


Figure 2. Transient absorption measurements on HTI Z-1 (left column), HTI Z-2 (middle column), and HTI Z-3 (right column) dissolved in different solvents with solvent polarity increasing from top to bottom. (j–l) Steady-state absorption of HTI (FTIR spectra) subtracted by pure solvent absorption. Spectral regions where solvent absorption could not be fully compensated by subtraction of the respective spectra are faded.

different probe frequency ranges, we normalized the data using the signals of overlapping spectral regions.

Computational Methods. The reaction mechanism of HTI derivative Z-2 and Z-3 was investigated using a complete active space self-consistent field (CASSCF) with an active space of 10 electrons in 9 orbitals (for more details, see Figure S10 and S11 in the Supporting Information (SI)) and the ANO-RCC-VDZP basis set.³² In a previous study, an active space of 12 electrons in 10 orbitals was used to describe HTI, additionally including the lone pair orbital of the oxygen atom.^{33,34} As the inclusion of lone pair orbitals is not necessary for the reaction pathway investigated here, they can be neglected resulting in the CAS(10,9) active space. In all calculations, the state average wave function over four singlet states was evaluated. To include dynamic correlation, single-state CASPT2 was performed at the CASSCF optimized geometries. As the investigated TICT formation is strongly solvent-dependent, we applied the polarized continuum method (PCM) considering the “fast” and “slow” response of the solvent in the calculations of the vertical excitation and emission energies.^{35,36}

As frequency analysis on the CASSCF level of theory is computationally very demanding, the IR spectra for ground and excited states were calculated using density functional theory (DFT). The ω B97X-D functional³⁷ was used with the Dunning triple- ζ basis cc-pVTZ.³⁸ The geometry optimizations were performed with PCM. For the excitation energies, 10 excited singlet states were calculated using time-dependent DFT (TDDFT).

All CASSCF/CASPT2 calculations were conducted using the OpenMolcas program package.³⁹ For all DFT and TDDFT calculations, the Gaussian16 program package was used.⁴⁰ More details on the methods can be found in the [Supporting Information](#).

Transient Picosecond Infrared Spectra. Figure 2 presents an overview of the time-resolved infrared measurements for the three HTI derivatives Z-1 (left column), Z-2 (middle), and Z-3 (right) in different solvents with solvent polarity increasing from top to bottom. In the bottom row, the FTIR spectra of the ground-state compounds in the different solvents used are presented. While the overall spectral profile is similar for the different solvents in the ground state, some bands display solvent-dependent shifts. In particular, the C=O vibration in the range of 1650–1700 cm^{-1} exhibits a distinct red-shift with increasing solvent polarity.

Time-resolved measurements of the electronically excited compounds show a number of absorption and bleaching bands. The latter represent a decrease of absorption upon excitation (negative ΔOD , blue) and correspond to bleaching of the ground-state spectrum as can be seen from a comparison with the FTIR spectra (see Figure 2, bottom). Positive bands (in red) correspond to increased absorption of the molecules in the excited state or in the product state, representing new bands. In apolar deuterated cyclohexane (dCH) ($\epsilon = 2.0$), only the S_1 state and no TICT state should be populated according to previous UV–vis measurements.²¹ Here, we observe the expected bleach at the position of strong ground-state absorption bands of Z-1. Around 1425 and 1520 cm^{-1} , there are bands of increased absorption, indicating vibrational modes

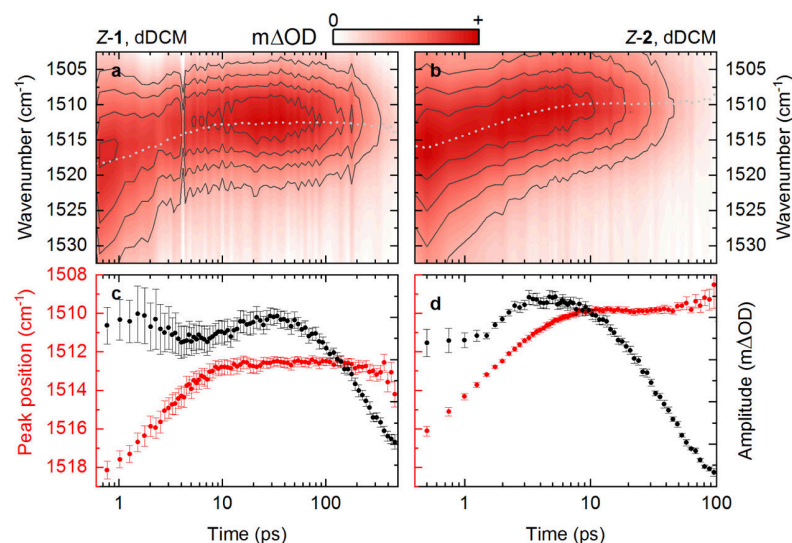


Figure 3. Dynamics of the C–O mode during TICT formation for HTI Z-1 (left column) and Z-2 (right column) in dDCM. (a, b) Absorption band attributed to C–O stretching vibration; details from Figure 2. (c, d) Peak position (red data points, left ordinate scale) and amplitude (black data points, right ordinate scale) of Gaussian fits the shifting mode.

in the excited electronic state. These absorption features decay rapidly on the time scale of a few picoseconds, close to the temporal resolution of our experiment. Subsequent dynamics up to the 10 ps time scale are observed in the red wing of ground-state bands and point to vibrational cooling^{41,42} following the rapid decay of the excited electronic state. For HTI Z-2, in dCH, several pronounced absorption bands are evident between 1400 and 1550 cm^{-1} , decaying over the course of few tens of picoseconds. The positive absorption bands are much stronger than the bleaching bands at 1600 and 1680 cm^{-1} . For Z-3, the more complex ground-state spectrum is reflected in the time-resolved spectrum by a number of clearly visible bleaching bands. These features decay on a time scale of 10 ps. A quantitative analysis of the absorption features of the three HTI compounds in dCH with a global biexponential fit yielded time constants comparable to the ones obtained in previous UV–vis measurements (see Table 2 as well as Table S1 and Figure S1 in the SI).

A first inspection of the transient absorption changes of Z-1 and Z-2 in polar solvents shows that the spectral characteristics of the two compounds are similar. However, since the lifetime of the excited electronic state of Z-2 in dCH (16 ps) is much longer than that of Z-1 (1.4 ps), we focus on Z-2, here, allowing for a better comparison between S_1 spectra in polar and apolar solvents. Within the lifetime of the excited electronic state, we observe bleaching bands at the position of the respective ground state in both polar solvents (dTHF, dDCM). Three pronounced absorption bands are found at 1425, 1475, and around 1525 cm^{-1} . Compared to the apolar dCH, the overall transient absorption appears to be blue-shifted for the spectral region between 1400 and 1500 cm^{-1} . Of special interest is the band at about 1520 cm^{-1} , which shows a solvent-dependent temporal spectral evolution (red-shift) on the time scale of few picoseconds. In the more polar dDCM, this band is significantly red-shifted compared to dTHF. The transient absorption changes in Z-1 exhibit very similar spectral features, including the spectral evolution of the 1520 cm^{-1} band.

Spectral and temporal evolution of the 1520 cm^{-1} band in Z-1 (a, c) and Z-2 (b, d) in dDCM is presented in detail in

Figure 3 (the respective dynamics for Z-1 in dDMSO and Z-2 in dTHF are shown in Figure S2 in the SI). The absorption changes presented in the upper panels are modeled by Gaussian spectra at each delay time, and the resulting peak positions and amplitudes of the Gaussians are given in the lower panels. For both molecules, the peak position shifts to lower wavenumbers by 5–6 cm^{-1} within the first 10 ps. The respective time constants are summarized in Table 2 and lie around 2–3 ps. At later delay times, peak positions remain unchanged. The peak amplitudes of Z-1 and Z-2 evolve toward a maximum reached within ~ 30 and 5 ps, respectively. Subsequently, decay of the TICT states back to the ground state is observed according to the time constants found in the global analysis of the respective compound, i.e., 210 ps for Z-1 and 32 ps for Z-2 in dDCM.

In the planar reference compound Z-3, the overall spectral features are comparable for polar and apolar solvents. The major difference lies in the decay time of the absorption changes, where the time constants increase moderately from 13 ps (dCH) to 44 ps for the most polar solvent dDMSO. No spectral evolution with time can be observed in the excited state for any one of the absorption bands. This precludes structural changes akin to TICT formation of the molecule Z-3 within the excited state, in accordance with previous observations employing UV–vis spectroscopy.

Summarizing our experimental observations for the electronically excited state, we find that Z-1 and Z-2 show no spectral evolution of the initial excited-state spectrum toward new excited-state species in the apolar solvent dCH. Instead, a simple decay back to the ground state was observed with concomitant formation of the corresponding E isomers as photoproducts. This behavior was also observed for the control compound Z-3 in all solvents tested.

Z-1 and Z-2 in polar solvents, on the other hand, do exhibit a more complex temporal evolution of the excited state. Here, the absorption spectra observed at later delay times differ significantly from the spectra in the apolar solvent dCH. In particular, Z-1 and Z-2 in polar solvents develop a pronounced absorption band around 1520 cm^{-1} , whose red-shift allows to follow the state evolution from the initial excited state to the

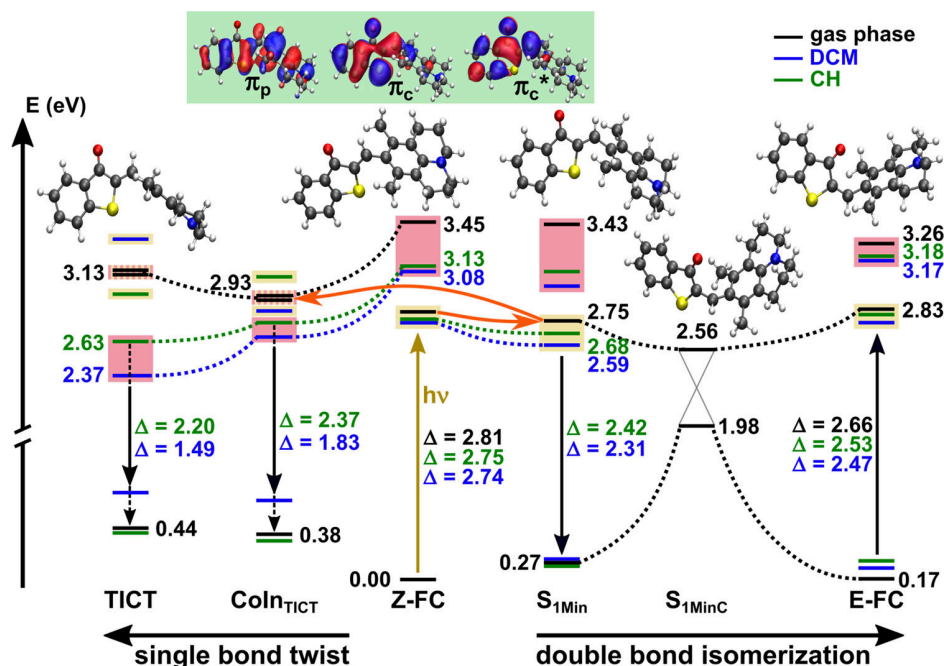


Figure 4. Vertical excitation and emission energies of HTI Z-2 along the reaction pathway at the CASSCF/CASPT2(10,9) level of theory. The energy levels of the excited states are shown in blue for the polar solvent DCM, in green for the nonpolar solvent CH and in black for the gas phase. The orange arrow connecting Z-FC and $S_{1\text{Min}}$ displays the direction of the gradient at the FC point in the gas phase. The second arrow between $S_{1\text{Min}}$ and $\text{CoIn}_{\text{TICT}}$ indicates the possible excited-state reaction path in the S_1 . The orbitals at the Z-FC are shown in the green area and describe the electronic character of the resulting excited states. States with $\pi_c \rightarrow \pi_c^*$ character are highlighted in yellow and with $\pi_p \rightarrow \pi_c^*$ character in red. A more detailed scheme with all energy levels is shown in Figure S4 of the SI.

new species with a time constant of 2–3 ps. This red-shifted absorption then decays with much larger time constants in the range of 30–210 ps (dDCM).

Calculation of the Electronically Excited States with CASPT2. The excited-state reaction pathway of HTI Z-2 and Z-3, respectively, was calculated with CASPT2 in two different solvents, DCM and CH. The corresponding active spaces are shown in the SI, Figures S10 and S11. We only focused on the Z-2 derivative as TICT forming species and neglected Z-1 in the calculations because both derivatives behave similarly as discussed in the previous section. The pathways of Z-2 for isomerization and TICT formation are shown in Figure 4. At the Franck–Condon (FC) point of the Z-isomer, the first two excited states have $\pi \rightarrow \pi^*$ character (see Figure 4, green area for assignments of the orbitals). The S_1 describes an excitation from the π orbital of the central C–C double bond to the corresponding antibonding π^* orbital ($\pi_c \rightarrow \pi_c^*$). The S_2 is a charge transfer state characterized by the excitation from a π orbital of the stilbene part (π_p) to the π_c^* orbital ($\pi_p \rightarrow \pi_c^*$). In the following, the development of these excited states is discussed taking into account the solvent effects. The excitation energies at the two FC points of the isomerization, Z-FC and E-FC, respectively, show almost no solvent dependence on the level of theory used. At Z-FC, they are nearly degenerate with values of 2.74 eV in DCM and 2.75 eV in CH. The experimentally observed absorption bands are 2.56 and 2.74 eV in DCM and CH, respectively.²² The red-shift in the more polar solvent is not reflected in the theory. A limitation in the used methodology is that only single-point calculations are possible when including the solvent environment. Optimizations in the solution were therefore not possible. This may explain the discrepancies in the relative

energies on the excited-state surfaces, in general. At E-FC, the solvent effect on the excitation energies is also minor with $\Delta E = 2.53$ eV in CH and $\Delta E = 2.47$ eV in DCM for the excitation to the S_1 state as compared to $\Delta E = 2.66$ eV in the gas phase.

The main geometry parameters for the DBI and the SBT are two distinguished dihedral angles. The dihedral angle along C5–C4–C3–C2 is named d1 and defines the twist along the central C3–C4 single bond. The dihedral angle along H–C3–C2–C1 is named d2a and describes the rotation of the central C2–C3 double bond. The angles d1 and d2a are indicated in Figure 1b and the atom numbering in Figure 1d.

Close to the Z-FC point, a minimum on the S_1 surface ($S_{1\text{Min}}$) with $\pi_c \rightarrow \pi_c^*$ character was optimized. The two dihedrals show only small changes compared to the ground state (GS) (see Table S12 in the SI). At the $S_{1\text{Min}}$, the solvent effect is again not significant because the dipole moment of the $\pi_c \rightarrow \pi_c^*$ state is comparable to the ground state (Figure S7 in the SI). A further minimum on the S_1 surface ($S_{1\text{MinC}}$) along the DBI pathway with π^2 character, the original GS configuration, leads to an S_1/S_0 conical intersection (CoIn) seam.³⁴ As the geometry is rather distorted, the original π^2 configuration obtains a diradical character. The dihedral d2a is twisted from -1.6 to 92.0° dissolving the C3–C2 double bond and the dihedral d1 is deformed from -71.1 to 0.6° . At the twisted $S_{1\text{MinC}}$, the solvent effects are insignificant, as well. In summary, this means that the solvent environment is not very significant for the Z/E-photoisomerization pathway.

The solvent dependence for the TICT formation is much more pronounced. Along this pathway, an S_2/S_1 CoIn ($\text{CoIn}_{\text{TICT}}$) between a CT state with $\pi_p \rightarrow \pi_c^*$ character and the $\pi_c \rightarrow \pi_c^*$ state is found. Here, the dihedral d1 is twisted to -90.3° and d2a is almost planar. When the solvent is included,

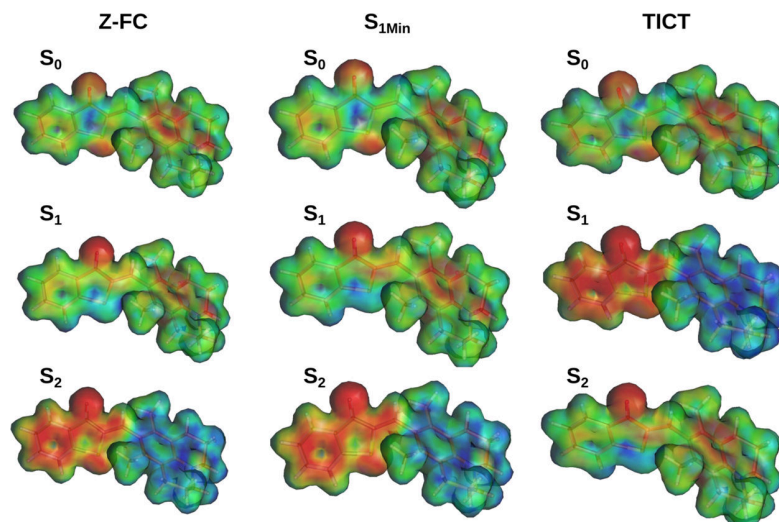


Figure 5. Electrostatic potential surfaces (ESPs) of HTI Z-2 at the CASSCF(10,9)/ANO-RCC-VDZP level of theory for the first three singlet states. At the FC and the $S_{1\text{Min}}$, the S_1 state has a small CT character within the indigo part from the sulfur atom to the oxygen atom. The S_2 state, in contrast, has a large CT character from the stilbene part to the indigo part. At the TICT geometry, those two states change in energy, and the CT state becomes the S_1 .

the gas-phase S_2/S_1 degeneracy at the CoIn is abrogated. Due to their different electronic characters, the states are now differently stabilized in solution. The search for a TICT minimum, however, proved to be challenging. It required lower convergence criteria for the optimization as detailed in the SI. The resulting TICT geometry is similar to the optimized CoIn_{TICT} showing the same distortion along d1 and d2a. The CT state with $\pi_p \rightarrow \pi_c^*$ character is now the S_1 state and is stabilized about 0.37 eV in DCM and only about 0.12 eV in CH compared to the S_1 at Z-FC. The stabilization can be explained by the increasing dipole moment of the $\pi_p \rightarrow \pi_c^*$ state, which is most pronounced for the more polar solvent DCM.

The TICT state is the preferred one in DCM, as the TICT lies about 0.22 eV lower in energy than the $S_{1\text{Min}}$. This agrees well with the experimental findings. In the less polar solvent CH, the TICT and $S_{1\text{Min}}$ have similar energies, suggesting that both states can be populated. In the experiment, a preference for Z/E photoisomerization is observed, which means the sole population of the $S_{1\text{Min}}$. This slight discrepancy may be explained by the limitation in our procedure relying on single-point calculations in the solvent with no re-optimization. In DCM, the calculated emission energies of 1.49 eV at the TICT geometry and of 2.31 eV at the $S_{1\text{Min}}$ lie in the range of the experimental fluorescence bands²² of 1.6 and 2.3 eV, respectively. In CH, the calculated emission energy of 2.42 eV at the $S_{1\text{Min}}$ also agrees well with the experimental fluorescence band of 2.4 eV.²² The presence of only one absorption band suggests that no TICT is formed in CH. In this regard, the gas-phase calculations reflect the experimentally observed behavior much better because, without a solvent environment, the TICT pathway is much higher in energy as compared to the photoisomerization pathway.

Insights obtained from the transient UV–vis absorption spectroscopy of a previous study suggest that in polar solvents the $S_{1\text{Min}}$ is populated in a first step before the TICT state is populated.²² Considering the gradient at the Z-FC pointing to the $S_{1\text{Min}}$ (see Figure S13 in the SI), this is consistent with the here discussed theoretical results. The possible excited-state

reaction path is highlighted with arrows for the gas phase in Figure 4.

For comparison, the derivative Z-3 was also calculated. It exhibits a completely planar structure at the FC points and at the minimum on the S_1 surface. Accordingly, the orbitals describing the S_1 and S_2 excitations are strongly delocalized and no CT state is found within the first two excited states. Furthermore, there is no pretwist at the FC point. Therefore, no CoIn_{TICT} or TICT geometry is found. Thus, in Z-3, only the Z/E -isomerization pathway is available, which is in good agreement with the experiment. A scheme showing the corresponding reaction pathways can be found in Figure S5 of the SI.

From the theoretical description, the associated charge redistributions are precisely quantified (Figure 5; also see the SI for a more detailed description and quantification). TICT formation leads to a significant charge separation across the twisted single bond that connects the stilbene part with the photoisomerizable double bond. Electron density is transferred from the electron-rich julolidine to the thioindigo part and strongly localizes at the (former) carbonyl oxygen atom. Significantly increased electron density is also established throughout the thioindigo part, while the electron deficiency is similarly delocalized throughout the julolidine. This charge transfer could directly be detected via the shifting of the carbonyl and amine stretching vibrations to lower energies in the transient IR spectra. The theoretical description provides additional quantification by, e.g., the dipole moment, which is tabulated in Tables 2 and S10 in the SI.

Calculated IR Spectra. To allow for a detailed interpretation of the experimental transient IR spectra, changes in the vibrational absorption bands between TICT and $S_{1\text{Min}}$ were examined on the basis of the calculated IR spectra. To obtain these spectra, re-optimization within the solvent proved essential. Thus, we moved to TDDFT methods for which these calculations are possible. Generally, both CASSCF and TDDFT methods have problems converging to a TICT minimum geometry. To obtain a converged TICT geometry, the dihedrals d1 and d2a have to be frozen as the PES is very

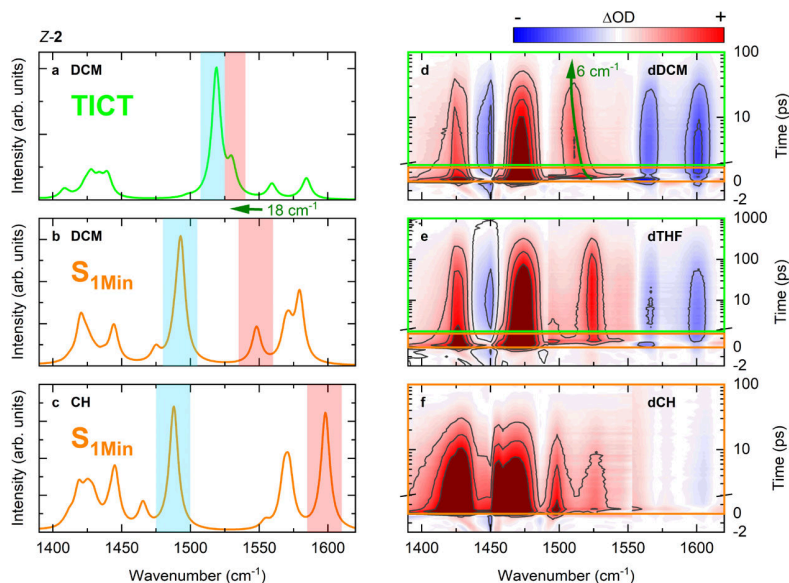


Figure 6. Selected spectral features associated with the $S_{1\text{Min}}$ geometry (orange traces and frames) and the TICT geometry (green traces and frames) in the excited electronic state. (a) Calculated IR spectrum for the TICT state in DCM. Calculated IR spectra in the $S_{1\text{Min}}$ state for Z-2 in (b) DCM and in (c) nonpolar CH. The absorption bands associated with the C–N mode and the C–O mode are highlighted in cyan and red, respectively. Time-resolved experimental spectra in (d) dDCM, (e) dTHF and (f) nonpolar dCH. The spectral red-shift of the absorption band assigned to the C–O mode between the $S_{1\text{Min}}$ and the TICT state is marked by the dark-green arrow.

flat along these coordinates. Thus, we conclude that the TICT state is not manifested by a pronounced minimum but rather corresponds to a flat area on the S_1 -surface (see the SI for more details on the calculation of the TICT state).

The calculated excited-state IR spectra of Z-2 (see Figures 6a–c and S14 (in the SI)) in CH and DCM show significant band shifts of the two IR marker-bands, C1–O and C6–N stretch, which are referred to as C–O (highlighted in red) and C–N bands (highlighted in cyan) hereafter. The spectra in THF are similar to the spectra in DCM (Table S14 in the SI showing the calculated normal modes) and we exemplarily discuss the findings for Z-2 in DCM. We observe band shifts along the excited-state reaction pathway, which reflect the change in the C–O and C–N bond lengths from the Z-FC geometry to the $S_{1\text{Min}}$ and the TICT geometry (see Table 1).

Table 1. C–O and C–N Bond Lengths (in Å) of Z-2 along the Reaction Pathways in DCM and CH Solutions Calculated at the $\omega\text{B97X-D/cc-pVTZ}$ Level of Theory

stretch vibration	Z-FC		$S_{1\text{Min}}$		TICT	
	DCM	CH	DCM	CH	DCM	CH
C–O	1.2135	1.2109	1.2438	1.2363	1.2567	1.2503
C–N	1.3929	1.3947	1.3537	1.3636	1.3340	1.3421

The C–O bond is elongated while the C–N bond is shortened most pronounced at the TICT geometry. Here, the CT character of the S_1 state shifts the electron density from the stilbene part with the electron-donating amino group to the indigo part bearing the electron-withdrawing carbonyl group. The C–N bond develops a double-bond character, while the C–O bond develops a single-bond character. These variations in the electronic structure are reflected in the IR band shifts. The C–O band is red-shifted about 18 cm^{-1} in DCM at the TICT geometry compared to the $S_{1\text{Min}}$. At the same time, the

C–N band shows a blue-shift by about 26 cm^{-1} . Regarding the solvent dependence of both band shifts at $S_{1\text{Min}}$, the C–N band barely varies ($\Delta = 5\text{ cm}^{-1}$). The C–O band, however, shifts significantly by about 50 cm^{-1} in the polar solvent DCM compared to the band position in CH.

Summarizing, the C–O band shifts to lower energies when more electron density is located at the oxygen atom, and the C–N band shifts more slightly to higher energies. These shifts occur most strongly at the TICT geometry and in a polar solvent.

Experimental Vibrational Signatures of the TICT State. On the basis of the calculated IR spectra, as depicted in Figures 6a–c and S14 (in the SI), we can now identify the distinct experimental IR absorption bands in the ground state and in the electronically excited state. While the spectral positions of the absorption bands of interest vary slightly depending on the HTI derivative and solvent polarity, our key findings regarding the formation of the TICT state apply to all TICT forming variants. Therefore, we focus on Z-2 in dDCM as an example in the following discussion.

The calculated absorption bands for the ground state correspond well to the experimentally observed spectral signatures (see Figure S14 in the SI). The C–N and the C–O modes, which have been identified as particularly suitable to monitor charge distribution within the molecule as described above, are assigned to the experimental ground-state absorption bands found at 1498 and 1678 cm^{-1} , respectively. The remaining bands between 1550 and 1620 cm^{-1} are identified as aromatic C–C stretch vibrations, while the bands between 1400 and 1470 cm^{-1} can be assigned to C–H bending vibrations.

While several positive absorption bands are observable in the time-resolved measurements in the range of the calculated C–N band between 1400 and 1500 cm^{-1} , the overall line shape does not directly match the calculated spectrum. Absorption bands associated with C–H bending vibrations, which are also

Table 2. Kinetic Data Describing the Excited-State Processes for HTIs Z-1, Z-2, and Z-3 in Different Solvents^a

HTI in solvent	Global bi-exponential fit to transient IR measurements		Initial shift of CO band (cm ⁻¹)	Theoretical dipole moment in S ₁ gas phase in Debye (state)
	τ_1 (ps)	τ_2 (ps)		
Z-1				
dCH	1.4	11.9	-	
dDCM	1.2	210.6	2.8	
dDMSO	3.9	17.8	1.9	
Z-2				
dCH	4.8	19.1	-	
dTHF	5.8	201.8	1.6	7.38 (Z-FC)
dDCM	1.5	32.1	1.9	7.96 (S _{1Min}) 22.36 (TICT)
Z-3				
dCH	0.8	13.2	-	
dDCM	6.0	17.4	-	
dDMSO	5.7	44.0	-	

^aTime constants assigned to the S₁ state are marked in red and TICT lifetimes are marked in blue.

expected to lie in this spectral region, as well as ground-state bleaching, impede a clear assignment of the C–N mode in the excited-state spectra. Furthermore, we assume that the calculated band is somewhat shifted compared to the experiment, which is also observed for the ground-state spectra. In contrast, the C–O absorption band remains a good marker band, also for the excited states, because it lies at higher frequencies and is not superimposed by ground-state bleaching. We assign the distinct positive signal in the time-resolved spectrum around 1515 cm⁻¹ to the C–O band. In the calculated spectrum of the TICT geometry, this band lies lower by 15 cm⁻¹ compared to the experiment. This deviation is comparable to the difference in band position between the experimental and theoretical ground-state spectra.

As described before, the calculations indicate that the spectral position of the C–O vibration can be used as an indicator of electron density on the thioindigo part of the HTI molecule. Electron density is shifted to the thioindigo part upon electronic excitation from the ground state. For the TICT geometry, the negative charge on this part of the molecule is highest (compare with Figure 5). The calculated spectra indicate that this change in charge distribution is accompanied by a red-shift in the frequency of the absorption band associated with the carbonyl group (see Figure 6a–c). Such a red-shift is indeed observed for the assigned C–O band in the transient spectra around 1515 cm⁻¹ taking place on time scales associated with the lifetime of the S₁ state and resulting in the TICT spectrum at later times (see Figure 6d,e). The red-shift amounts to ~6 cm⁻¹ for Z-2 in dDCM (see Figure 3d). Identification of the S₁ state in polar solvents is supported

by the similarity between the spectral shape for Z-2 in the polar solvents on short delay times (see Figure 6d,e) and the spectral features observed for Z-2 in the nonpolar solvent dCH (see Figure 6f), where no TICT state is formed and only the S₁ state is present. The subsequent occurrence of spectral characteristics associated with the S₁ state and the TICT state indicates a serial mechanism, where the decay of the S₁ state leads to the population of the TICT state. This is in line with the reaction path in the excited state inferred from the calculations above.

Based on the joint consideration of calculated and experimental spectra in the excited electronic state, the shift of the absorption band at 1515 cm⁻¹ in the experimental spectra with time can be interpreted as structural development toward the molecular geometry supporting the fully charge-separated TICT state. The temporal evolution of the C–O band of Z-2 in dDCM is characterized by a shift to lower frequencies with a time constant of around 2 ps. At later delay times, the peak position remains unchanged. The peak amplitude evolves toward a maximum reached within 5 ps. Subsequently, it decays with the same time constant of 32 ps as found for the lifetime of the TICT state in the global analysis. For Z-1, in dDCM (see Figure 3a,c), the C–O band shows a qualitatively similar behavior, with the time constant for the shift of ~5 cm⁻¹ lying at about 3 ps and the maximum amplitude reached after ~30 ps. The time constants for these shifts are comparable to those tentatively associated with structural rearrangement of the molecule subsequent to electronic changes during the formation of the TICT state from the S₁ minimum in the respective time-resolved UV–vis

spectra (see the SI of ref 21 and Table S1 in the SI). With the C–O band as an indicator of negative charge on the thioindigo part of the HTI molecule, the shift of the associated IR absorption band with a time constant of 2–3 ps can therefore be interpreted as the full structural and electronic formation of the TICT state resulting in an increased amount of electron density on the thioindigo part. This implies that after ~10 ps, when the red-shifting is finished (see Figure 3c,d), the structural reaction to the charge redistribution upon electronic excitation is also completed. A similar delay between the electronic formation of the excited state and the subsequent structural rearrangement has been reported before in another molecular switch.⁴³ Solvent relaxation induced by the significant change in the dipole of the molecule for the TICT state could also contribute to the spectral shift on the observed time scale of around 2 ps and might contribute to the stabilization of the excited state.⁴⁴

For HTI Z-1, the global picture is very similar but lessened in degree. In this case, identification of the C–O marker band was not corroborated by quantum chemical calculations and thus a full assignment of the spectral features in the transient measurements was not possible. However, we assume that similar spectral behavior emerges from the same marker bands as discussed for HTI Z-2.

The quantitative kinetic data are summarized in Table 2 to give a comprehensive overview of all of the different processes occurring upon excitation of HTIs Z-1, Z-2, and Z-3.

In summary, we addressed TICT formation via a combination of picosecond IR spectroscopy with quantum chemistry. Three HTI derivatives were studied in solvents of different polarities to realize conditions where the excited-state reaction proceeded exclusively without TICT formation or via a TICT state. In the transient IR experiment, the same reaction dynamics as found in a recent UV–vis study were observed. In addition, the IR experiment revealed characteristic spectral features associated with the formation of the TICT state. For compounds pretwisted around the single bond constituting the TICT coordinate, a distinct transient red-shift was observed in polar solvents for the absorption band around 1515 cm⁻¹. In dDCM, this shift occurs with a time constant of 2–3 ps. Comparison with the theoretical study allowed the assignment of the observed band to the C–O-mode in the excited electronic state and presented the molecular background of the reaction path upon TICT formation. Thus, we interpreted the C–O mode as a structural indicator of the charge distribution on the molecule, which allows us to observe the structural rearrangement of the HTI photoswitch upon charge redistribution in the TICT state. The combination of picosecond IR spectroscopy with quantum chemical calculation not only reconfirms TICT formation but also leads to a detailed and quantitative understanding of the photochemical processes in HTI photoswitches. As a result, a significantly refined picture of TICT formation and the associated charge redistribution in HTIs is established. It is shown directly that TICT formation leads to the strongest charge transfer from the stilbene to the thioindigo part of the molecule resulting in a dipole moment of 22.36 Debye according to the calculations (Tables 2 and S10 in the SI). Furthermore, the formation of the TICT state could be followed and the associated kinetics elucidated. A comprehensive and quantitative picture of the associated excited-state energy profile could be obtained explaining the strong influence of the surrounding medium on the different excited-state pathways.

■ ASSOCIATED CONTENT

SI Supporting Information

The Supporting Information is available free of charge at <https://pubs.acs.org/doi/10.1021/acs.jpca.1c02646>.

Time-resolved IR measurements: global fit results, dynamics of the C–O mode for Z-1 in dDMSO and for Z-2 in dTHF; computational analysis: TICT state optimization, CASSCF/CASPT2 calculations in solution, calculated IR spectra, charge transfer discussion for Z-2, reaction pathways, electrostatic potential and dipole moment of Z-2 and Z-3, development of selected dihedral angles and bond lengths along the reaction pathway, active space, gradient at the FC point, ground-state IR spectra, normal modes, and coordinates of relevant geometries (PDF)

■ AUTHOR INFORMATION

Corresponding Authors

Regina de Vivie-Riedle – Department für Chemie, Ludwig-Maximilians-Universität München, 81377 Munich, Germany; orcid.org/0000-0002-7877-5979; Email: rdvpc@cup.uni-muenchen.de

Wolfgang Zinth – Lehrstuhl für Biomolekulare Optik, Ludwig-Maximilians-Universität München, 80538 Munich, Germany; Email: wolfgang.zinth@physik.uni-muenchen.de

Henry Dube – Department of Chemistry and Pharmacy, Friedrich-Alexander-Universität Erlangen-Nürnberg, 91058 Erlangen, Germany; orcid.org/0000-0002-5055-9924; Email: henry.dube@fau.de

Authors

Klara Stallhofer – Physik-Department, Lehrstuhl für Laser- und Röntgenphysik, Technische Universität München, 85748 Garching, Germany; orcid.org/0000-0001-6314-0156

Matthias Nuber – Physik-Department, Lehrstuhl für Laser- und Röntgenphysik, Technische Universität München, 85748 Garching, Germany; orcid.org/0000-0002-4409-3590

Franziska Schüppel – Department für Chemie, Ludwig-Maximilians-Universität München, 81377 Munich, Germany

Stefan Thumser – Department für Chemie, Ludwig-Maximilians-Universität München, 81377 Munich, Germany

Hristo Iglev – Physik-Department, Lehrstuhl für Laser- und Röntgenphysik, Technische Universität München, 85748 Garching, Germany; orcid.org/0000-0001-9208-0068

Complete contact information is available at:

<https://pubs.acs.org/doi/10.1021/acs.jpca.1c02646>

Notes

The authors declare no competing financial interest.

■ ACKNOWLEDGMENTS

H.D. thanks the “Fonds der Chemischen Industrie” for a Liebig fellowship (Li 188/05) and the Deutsche Forschungsgemeinschaft (DFG) for an Emmy Noether fellowship (DU 1414/1-2). M.N. thanks the “Studienstiftung des deutschen Volkes” for a PhD-scholarship. The authors acknowledge the financial support from the Deutsche Forschungsgemeinschaft (SFB 749, A12) and the Clusters of Excellence “Center for Integrated Protein Science Munich” (CIPS^M), “Munich Centre of Advanced Photonics” (MAP) and “e-conversion” (EXC 2089/1-390776260).

REFERENCES

- (1) Grabowski, Z. R.; Rotkiewicz, K.; Rettig, W. Structural Changes Accompanying Intramolecular Electron Transfer: Focus on Twisted Intramolecular Charge-Transfer States and Structures. *Chem. Rev.* **2003**, *103*, 3899–4031.
- (2) Rotkiewicz, K.; Grellmann, K. H.; Grabowski, Z. R. Reinterpretation of the Anomalous Fluorescence of P-N,N-Dimethylamino-Benzotrile. *Chem. Phys. Lett.* **1973**, *19*, 315–318.
- (3) Rettig, W. Tict States and Beyond: Reaction Dimensionality and Application to Photosynthesis. *Proc. - Indian Acad. Sci., Chem. Sci.* **1992**, *104*, 89–104.
- (4) Letard, J.-F.; Lapouyade, R.; Rettig, W. Structure-Photophysics Correlations in a Series of 4-(Dialkylamino)Stilbenes: Intramolecular Charge Transfer in the Excited State as Related to the Twist around the Single Bonds. *J. Am. Chem. Soc.* **1993**, *115*, 2441–2447.
- (5) Maus, M.; Rettig, W.; Bonafoux, D.; Lapouyade, R. Photo-induced Intramolecular Charge Transfer in a Series of Differently Twisted Donor-Acceptor Biphenyls as Revealed by Fluorescence. *J. Phys. Chem. A* **1999**, *103*, 3388–3401.
- (6) Rettig, W. Charge Separation in Excited States of Decoupled Systems—Tict Compounds and Implications Regarding the Development of New Laser Dyes and the Primary Process of Vision and Photosynthesis. *Angew. Chem., Int. Ed.* **1986**, *25*, 971–988.
- (7) Sasaki, S.; Drummen, G. P. C.; Konishi, G.-i. Recent Advances in Twisted Intramolecular Charge Transfer (Tict) Fluorescence and Related Phenomena in Materials Chemistry. *J. Mater. Chem. C* **2016**, *4*, 2731–2743.
- (8) Kottas, G. S.; Clarke, L. I.; Horinek, D.; Michl, J. Artificial Molecular Rotors. *Chem. Rev.* **2005**, *105*, 1281–1376.
- (9) Haidekker, M. A.; Theodorakis, E. A. Environment-Sensitive Behavior of Fluorescent Molecular Rotors. *J. Biol. Eng.* **2010**, *4*, No. 11.
- (10) Haidekker, M. A.; Theodorakis, E. A. Molecular Rotors—Fluorescent Biosensors for Viscosity and Flow. *Org. Biomol. Chem.* **2007**, *5*, 1669–1678.
- (11) Dal Molin, M.; Verolet, Q.; Soleimanpour, S.; Matile, S. Mechanosensitive Membrane Probes. *Chem.—Eur. J.* **2015**, *21*, 6012–6021.
- (12) Hu, Y.; Liang, X.; Wu, D.; Yu, B.; Wang, Y.; Mi, Y.; Cao, Z.; Zhao, Z. Towards White-Light Emission of Fluorescent Polymeric Nanoparticles with a Single Luminogen Possessing Aie and Tict Properties. *J. Mater. Chem. C* **2020**, *8*, 734–741.
- (13) El-Zohry, A. M.; Karlsson, M. Gigantic Relevance of Twisted Intramolecular Charge Transfer for Organic Dyes Used in Solar Cells. *J. Phys. Chem. C* **2018**, *122*, 23998–24003.
- (14) Rurack, K.; Dekhtyar, M. L.; Bricks, J. L.; Resch-Genger, U.; Rettig, W. Quantum Yield Switching of Fluorescence by Selectively Bridging Single and Double Bonds in Chalcones: Involvement of Two Different Types of Conical Intersections. *J. Phys. Chem. A* **1999**, *103*, 9626–9635.
- (15) Pines, D.; Pines, E.; Rettig, W. Dual Fluorescence and Excited-State Structural Relaxations in Donor-Acceptor Stilbenes. *J. Phys. Chem. A* **2003**, *107*, 236–242.
- (16) Yang, J.-S.; Liao, K.-L.; Wang, C.-M.; Hwang, C.-Y. Substituent-Dependent Photoinduced Intramolecular Charge Transfer in N-Aryl-Substituted Trans-4-Aminostilbenes. *J. Am. Chem. Soc.* **2004**, *126*, 12325–12335.
- (17) Yang, J.-S.; Liao, K.-L.; Hwang, C.-Y.; Wang, C.-M. Photo-induced Single- Versus Double-Bond Torsion in Donor-Acceptor-Substituted Trans-Stilbenes. *J. Phys. Chem. A* **2006**, *110*, 8003–8010.
- (18) Yang, J.-S.; Liao, K.-L.; Li, C.-Y.; Chen, M.-Y. Meta Conjugation Effect on the Torsional Motion of Aminostilbenes in the Photoinduced Intramolecular Charge-Transfer State. *J. Am. Chem. Soc.* **2007**, *129*, 13183–13192.
- (19) Yang, J.-S.; Lin, C.-K.; Lahoti, A. M.; Tseng, C.-K.; Liu, Y.-H.; Lee, G.-H.; Peng, S.-M. Effect of Ground-State Twisting on the Trans to Cis Photoisomerization and Tict State Formation of Amino-stilbenes. *J. Phys. Chem. A* **2009**, *113*, 4868–4877.
- (20) Yang, S.; Han, K. Effects of Solvent Dielectric Constant and Viscosity on Two Rotational Relaxation Paths of Excited 9-(Dicyanovinyl) Julolidine. *J. Phys. Chem. A* **2016**, *120*, 4961–4965.
- (21) Wiedbrauk, S.; Maerz, B.; Samoylova, E.; Reiner, A.; Trommer, F.; Mayer, P.; Zinth, W.; Dube, H. Twisted Hemithioindigo Photoswitches: Solvent Polarity Determines the Type of Light-Induced Rotations. *J. Am. Chem. Soc.* **2016**, *138*, 12219–12227.
- (22) Wiedbrauk, S.; Maerz, B.; Samoylova, E.; Mayer, P.; Zinth, W.; Dube, H. Ingredients to Tict Formation in Donor Substituted Hemithioindigo. *J. Phys. Chem. Lett.* **2017**, *8*, 1585–1592.
- (23) Erbas-Cakmak, S.; Leigh, D. A.; McTernan, C. T.; Nussbaumer, A. L. Artificial Molecular Machines. *Chem. Rev.* **2015**, *115*, 10081–10206.
- (24) Kay, E. R.; Leigh, D. A.; Zerbetto, F. Synthetic Molecular Motors and Mechanical Machines. *Angew. Chem., Int. Ed.* **2007**, *46*, 72–191.
- (25) Arahamian, I. The Future of Molecular Machines. *ACS Cent. Sci.* **2020**, *6*, 347–358.
- (26) Wiedbrauk, S.; Dube, H. Hemithioindigo—an Emerging Photoswitch. *Tetrahedron Lett.* **2015**, *56*, 4266–4274.
- (27) Petermayer, C.; Dube, H. Indigoid Photoswitches: Visible Light Responsive Molecular Tools. *Acc. Chem. Res.* **2018**, *51*, 1153–1163.
- (28) Wang, J.; Rück-Braun, K. The Effect of Substituent-Dependent Photoinduced Intramolecular Charge Transfer on the Photochromism of Hemithioindigos. *ChemPhotoChem* **2017**, *1*, 493–498.
- (29) Ghosh, R.; Kushwaha, A.; Das, D. Conformational Control of Ultrafast Molecular Rotor Property: Tuning Viscosity Sensing Efficiency by Twist Angle Variation. *J. Phys. Chem. B* **2017**, *121*, 8786–8794.
- (30) Li, G.; Magana, D.; Dyer, R. B. Direct Observation and Control of Ultrafast Photoinduced Twisted Intramolecular Charge Transfer (Tict) in Triphenyl-Methane Dyes. *J. Phys. Chem. B* **2012**, *116*, 12590–12596.
- (31) Ishikawa, H.; Sugiyama, M.; Setaka, W.; Kira, M.; Mikami, N. Direct Observation of the Solvent Reorientation Dynamics in the “Twisted” Intramolecular Charge-Transfer Process of Cyanophenyl-disilane-Water Cluster by Transient Infrared Spectroscopy. *Phys. Chem. Chem. Phys.* **2007**, *9*, 117–126.
- (32) Roos, B. O.; Lindh, R.; Malmqvist, P.-Å.; Veryazov, V.; Widmark, P.-O. Main Group Atoms and Dimers Studied with a New Relativistic Basis Set. *J. Phys. Chem. A* **2004**, *108*, 2851–2858.
- (33) Wilcken, R.; Schildhauer, M.; Rott, F.; Huber, L. A.; Guentner, M.; Thumser, S.; Hoffmann, K.; Oesterling, S.; de Vivie-Riedle, R.; Riedle, E.; et al. Complete Mechanism of Hemithioindigo Motor Rotation. *J. Am. Chem. Soc.* **2018**, *140*, 5311–5318.
- (34) Nenov, A.; Cordes, T.; Herzog, T. T.; Zinth, W.; de Vivie-Riedle, R. Molecular Driving Forces for Z/E Isomerization Mediated by Heteroatoms: The Example Hemithioindigo. *J. Phys. Chem. A* **2010**, *114*, 13016–13030.
- (35) Corni, S.; Cammi, R.; Mennucci, B.; Tomasi, J. Electronic Excitation Energies of Molecules in Solution within Continuum Solvation Models: Investigating the Discrepancy between State-Specific and Linear-Response Methods. *J. Chem. Phys.* **2005**, *123*, No. 134512.
- (36) Cammi, R.; Corni, S.; Mennucci, B.; Tomasi, J. Electronic Excitation Energies of Molecules in Solution: State Specific and Linear Response Methods for Nonequilibrium Continuum Solvation Models. *J. Chem. Phys.* **2005**, *122*, No. 104513.
- (37) Chai, J. D.; Head-Gordon, M. Long-Range Corrected Hybrid Density Functionals with Damped Atom-Atom Dispersion Corrections. *Phys. Chem. Chem. Phys.* **2008**, *10*, 6615–6620.
- (38) Dunning, T. H., Jr. Gaussian Basis Sets for Use in Correlated Molecular Calculations. I. The Atoms Boron through Neon and Hydrogen. *J. Chem. Phys.* **1989**, *90*, 1007–1023.
- (39) Fdez. Galván, L.; Vacher, M.; Alavi, A.; Angeli, C.; Aquilante, F.; Autschbach, J.; Bao, J. J.; Bokarev, S. I.; Bogdanov, N. A.; Carlson, R. K.; et al. Openmolcas: From Source Code to Insight. *J. Chem. Theory Comput.* **2019**, *15*, 5925–5964.

(40) Frisch, M. J.; Trucks, G. W.; Schlegel, H. B.; Scuseria, G. E.; Robb, M. A.; Cheeseman, J. R.; Scalmani, G.; Barone, V.; Petersson, G. A.; Nakatsuji, H. et al. *Gaussian 16*, revision C.01; Gaussian, Inc.: Wallingford, CT, 2016.

(41) Hamm, P.; Ohline, S. M.; Zinth, W. Vibrational Cooling after Ultrafast Photoisomerization of Azobenzene Measured by Femtosecond Infrared Spectroscopy. *J. Chem. Phys.* **1997**, *106*, 519–529.

(42) Gottfried, N. H.; Seilmeier, A.; Kaiser, W. Transient Internal Temperature of Anthracene after Picosecond Infrared Excitation. *Chem. Phys. Lett.* **1984**, *111*, 326–332.

(43) Pontecorvo, E.; Ferrante, C.; Elles, C. G.; Scopigno, T. Structural Rearrangement Accompanying the Ultrafast Electrocyclization Reaction of a Photochromic Molecular Switch. *J. Phys. Chem. B* **2014**, *118*, 6915–6921.

(44) Hunger, J.; Stoppa, A.; Thoman, A.; Walther, M.; Buchner, R. Broadband Dielectric Response of Dichloromethane. *Chem. Phys. Lett.* **2009**, *471*, 85–91.

DYNAMICS OF EXCITED STATE REACTIONS: QUANTUM AND SEMI-CLASSICAL

Conical intersections (CoIns) play a key role for the excited states dynamics of many molecules [15, 16, 83]. Various biological molecules, as for example the nucleobases forming the DNA and RNA, have ultrafast radiationless decay channels to be stable against the irradiation of light [1–3]. Hereby, the dangerous potential energy obtained by the excitation is converted into heat (kinetic energy) by internal conversion, for example in form of ring puckering or elongation of a bond, without configurational change at the end of the reaction [84–86]. Other molecules, as for example the photoswitches discussed in chapter 1, experience a wanted configurational change after excitation. The probably most famous photoswitch in nature is the retinal in the process of vision [4, 5]. A photoswitch with more than two stable configurations, e.g. accomplished by including a chiral center [44, 45], can be used as molecular motor giving rise to a complete new field of applications. In section 2.1, the dynamics of the first step of a molecular motor based on HTI is investigated. In general, conical intersections can also act as branching point of competing reaction pathways which is the focus of section 2.2. Here, the photolysis of C – X bonds is investigated, that can generate carbocations and carboradicals, both key intermediates for organic synthesis [49–51].

In the dynamics of all mentioned excited state reactions CoIns and their vicinity are of central relevance. In the theoretical description of such regions the Born-Oppenheimer approximation breaks down, which means the electrons no longer adjust instantaneously with the motion of the nuclei and in principle both need to be considered quantum [8, 9]. Thus, classical dynamics is not sufficient for such investigations and further approximations are necessary. One way is to describe the system fully quantum (electron and nuclei) but in reduced dimension. A disadvantage of this approach is, that specific knowledge of the investigated reaction is necessary as the active coordinates have to be chosen in advance to calculate the complete potential energy surfaces (PES) before the simulation [8, 19]. Another possibility is to describe the system full-dimensional but in a semi-classical approach, meaning only the electrons are treated quantum and the nuclei move classically [10, 20]. The nonadiabatic transitions between the excited states can hereby be simulated with a surface-hopping algorithm [21, 22]. The dynamics of the HTI based motor is investigated using a semi-classical method because several degrees of freedom are important for the rotation. In publication “Ultrafast non-adiabatic dynamics of excited diphenylmethyl bromide elucidated by quantum dynamics and semi-classical on-the-fly dynamics” both approaches are applied to simulate the photodissociation of $\text{Ph}_2\text{CH} - \text{Br}$.

2.1 Rotation of a molecular motor

Molecular motors take a relevant place in biology. A well known example is the ATP synthase [39, 40], a molecular machine driven by a proton gradient producing ATP, the organic compound responsible for the energy delivery in the metabolism of living cells. Several smaller artificial molecular motors with different mechanism are known [47], for example the well known Feringa-type molecular motors [46, 47]. Hereby, the mechanism is determined by a rotation along a C-C double bond with two photochemical steps including a temporary double bond cleavage and two thermal steps with a helix inversion [48]. The chiral hemithioindigo-stilbene based motors developed in the group of Henry Dube [43–45] have a similar rotation mechanism. Up to now, several theoretical studies investigating the dynamics of the molecular rotation of Feringa-type motors are available [87–90]. The dynamics of a HTI based molecular motor has, to the best of our knowledge, not yet been investigated with theoretical methods. Here, we investigate the first photochemical step of *motor-1* and *motor-2* from reference [44] (fig. 2.1). Both molecules show the same stepwise rotation around the central C-C double bond, but with different reaction time and quantum yields for the single steps. While *motor-1* has a rather slow reaction time of 1.5 ps for the first photochemical step (**A** → **B**, fig. 2.2), *motor-2* relaxates a lot faster in the femtosecond regime with 330 fs. With only static comparison of single-point energies at the optimized geometries this fact can not be explained, as the relative energies between the geometry points of the ground state and the decisive CoIn are quit similar. Additionally, the first step of a hypothetical *motor-3* with electron withdrawing aldehyde groups at the stilbene part is calculated to confirm our theory concerning the different reaction time. To save calculation time, the semi-classical simulation for the **A** → **B** step is only set up for the "faster" *motor-2*.

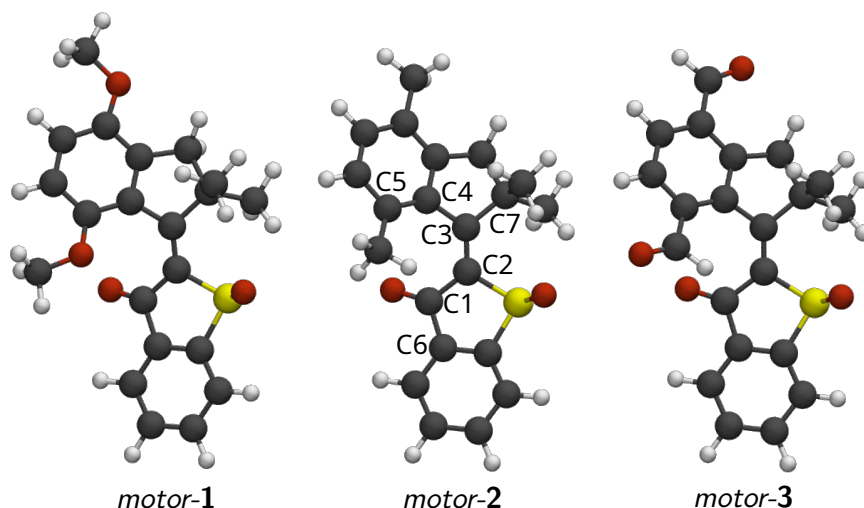


Figure 2.1: Ground state geometries of the *E*-(*S*)-(*P*) isomer of *motor-1*, *motor-2* and *motor-3*.

Computational Details

Spin-flip time-dependent density functional theory (SF-TDDFT) is found suitable to describe the photochemical **A** → **B** step. In this method, a triplet reference for the ground state is used and the excited states are calculated via $\alpha \rightarrow \beta$ spin-flip analog to standard TDDFT [91–93]. By that, the actual singlet ground state is the first excited state and it is possible to describe the CoIn between the S_1 and S_0 state (**CoIn**₁) crucial for the reaction pathway. In SF-TDDFT only four spin-adapted states can be calculated correctly, namely the ground state, the HOMO → LUMO and the doubly

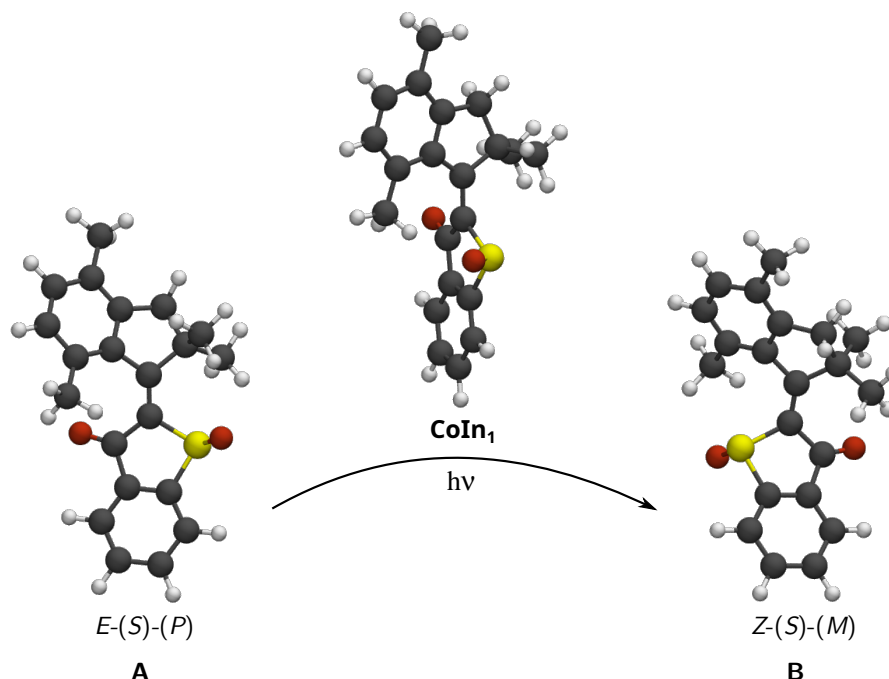


Figure 2.2: Reaction scheme for *motor-2* of the first photochemical step. The $E-(S)-(P)$ isomer (**A**) relaxates via CoIn_1 to the $Z-(S)-(M)$ isomer (**B**).

HOMO \rightarrow LUMO excitation and the triplet state [92, 94]. All other states are spin-contaminated because of the missing configurations due to the spin-flip and have to be treated with caution. As for the dynamics of the motor only the relaxation from the S_1 to the S_0 is important SF-TDDFT can be applied. For the dynamics simulation three states are calculated and the spin-adapted triplet state is removed by excluding the state with highest $\langle S^2 \rangle$ along each trajectory [94]. For the dynamics simulation SF-TDDFT has the great advantage that unlike in CASSCF no set up of an active space is necessary that can turn out to be difficult as the significant orbitals may change during the reaction. All attempts to set up a simulation with a feasible active space failed because of the instability of the active space along the trajectories. Further, the calculation time of energy and gradient is faster compared to CASSCF.

The BHHLYP functional in combination with the Pople 6-31G* basis set is used in all SF-TDDFT calculations. A detailed benchmark comparing this method to CASSCF and CASPT2 is available in the appendix C. ORCA-5.0 [95–98] is used for the geometry optimizations and the single point calculations.

A modified version of NewtonX 2.2 [99, 100] is used in combination with the quantum chemistry program GAMESS [101] for the gradient calculation to simulate the dynamics. 100 trajectories are set up with a Wigner distribution at a temperature of 293.15 K using the frequency analysis obtained at the optimized ground state geometry at the BHHLYP/6-31G* level of theory with ORCA-5.0 [95–98]. Thereof 52 trajectories run to the end of the simulation and are used for the evaluation in the following. The 48 discarded trajectories broke off due to convergence problem in the self-consistent field (SCF) cycle in the beginning of the simulation or because the energy conservation failed. The trajectories start in the S_1 state with a time step of 0.5 fs and the transitions are simulated with time-derivative couplings according to the Hammes-Schiffer–Tully model [22, 102]. The necessary modifications in the programs NewtonX and GAMESS are described in appendix D.

Quantum chemistry: Excited state surface

The vertical excitation energies of *motor-1* and *motor-2* at the optimized geometry of isomer **A** (*E*-(*S*)-(*P*)) obtained with SF-TDDFT of ORCA 5.0 are shown in table 2.1. Both show similar excited states and excitation energies. The first spin-flip state is the closed-shell ground state (π^2). The second is the spin-adapted triplet state ($\langle S^2 \rangle > 2.0$) with $\pi_c \Rightarrow \pi_c^*$ character that is excluded in the dynamics simulation (see appendix fig. C.10 and C.12 for the nomenclature of the orbitals). The third spin-flip state is the actual S_1 state which describes a $\pi_{st} \Rightarrow \pi_c^*$ excitation from the π_{st} orbital located at the stilbene part for *motor-1* and a $n \Rightarrow \pi_c^*$ excitation from the lone pair orbital of the oxygen at the sulfur for *motor-2*. The S_2 state lies close to the S_1 about 0.3 eV higher in energy for both derivatives. For *motor-1* this state has a $n \Rightarrow \pi_c^*$ character whereas for *motor-2* this state describes a $\pi_{st} \Rightarrow \pi_c^*$ excitation. Thus, the order of states is inverted for the both derivatives. Please note, that the order of states is benchmarked against CASPT2 for both derivatives (see appendix tab. C.1 and C.2). The third derivative, *motor-3* with the electron poor stilbene part, has the same order of states as *motor-2* and similar excitation energies (see appendix tab. C.3).

Table 2.1: Vertical excitation energies for *motor-1* and *motor-2* at the BHHLYP/6-31G* level of theory with SF-TDDFT of the program package ORCA 5.0 [95–98]. The relevant orbitals can be found in the appendix in fig. C.10 and C.12. The states are benchmarked according to CASPT2 (see appendix tab. C.1 and C.2).

state	ΔE (eV)	$\langle S^2 \rangle$	osc. str.	character	CI-coef
Motor 1 SF-TDDFT					
S_0	0.00	0.10	–	π^2	0.9846
T_1	3.12	2.10	0.00	$\pi_c \Rightarrow \pi_c^*$	-0.5797
S_1	3.53	0.91	0.07	$\pi_{st} \Rightarrow \pi_c^*$	0.8561
S_2	3.83	0.93	0.05	$n_1 \Rightarrow \pi_c^*$	-0.7798
S_3	4.23	0.63	0.49	$\pi_c \Rightarrow \pi_c^*$	0.7328
Motor 2 SF-TDDFT					
S_0	0.00	0.11	–	π^2	-0.9828
T_1	3.17	2.15	0.00	$\pi_c \Rightarrow \pi_c^*$	0.6007
S_1	3.74	0.84	0.06	$n_1 \Rightarrow \pi_c^*$	0.6073
S_2	4.03	1.06	0.04	$\pi_{st} \Rightarrow \pi_c^*$	-0.9022
S_3	4.16	0.64	0.47	$\pi_c \Rightarrow \pi_c^*$	0.7605

To explain the different reaction time for *motor-1* and *motor-2*, the relevant S_1/S_0 CoIn (**CoIn₁**) is (re)optimized with SF-TDDFT and its relative position is compared to the ground state geometries of isomer **A** and **B** in tab. 2.2. The **CoIn₁** lies lower in energy compared to the S_1 state at the FC point of isomer **A** for both derivatives with about 1.41 eV and 1.65 eV, respectively. Thus, the position of the CoIn alone is not explaining the different reaction times.

The easiest way to detect existing reaction barriers between different geometry points is to perform a linear interpolation between the points of interest. The results of the linear interpolation from isomer **A** to isomer **B** via **CoIn₁** are shown in fig. 2.3. A barrier of about 1.0 eV is inhibiting the direct path from the FC point to the **CoIn₁** in the S_1 state for *motor-1*. In contrast, no barrier exists on the direct path to the CoIn for *motor-2*, which explains the significant shorter reaction time. Comparing the geometries of the two derivatives no varying steric hindrance becomes obvious as the decisive parts are equal (fig. 2.3 (c)). The two methyl groups at the aliphatic carbon atom might be the reason for the barrier when solely looking at *motor-1* but it does not explain the missing barrier for *motor-2*.

Table 2.2: Development of the S_1 and S_0 state along the **A** \rightarrow **B** reaction path for *motor-1* and *motor-2* at the BHHLYP/6-31G* level of theory with ORCA 5.0 [95–98]. The energies are given in eV relative to the S_0 at the respective isomer **A**.

	A	CoIn₁	B
<i>motor-1</i>			
S_0	0.00	2.11	0.10
S_1	3.53	2.12	3.79
<i>motor-2</i>			
S_0	0.00	2.08	0.45
S_1	3.74	2.09	4.19

The difference might be explained by the varying electronic characters of the S_1 state at the FC of **A-1** and **A-2**, respectively. The spin-density difference between the S_1 and S_0 visualized on the right side of fig. 2.3 reveals this disparity. The electron donating methoxy groups at the stilbene part of *motor-1* lead to an electron distribution stabilizing an excitation on the stilbene part to be the first excited state (p_1 in fig. 2.3 (a) right). On the pathway towards **CoIn₁** a significant change in electronic configuration from $\pi_{st} \Rightarrow \pi_c^*$ to $\pi_c \rightarrow \pi_c^*$ has to take place. Thus, a barrier arises in the S_1 until the change is completed (p_2 in fig. 2.3 (a) right), as the $\pi_c \rightarrow \pi_c^*$ lies higher in energy at the FC and has to descend. From that point, the $\pi_c \rightarrow \pi_c^*$ state is stabilized towards **CoIn₁** (p_3 in fig. 2.3 (a) right), where the perpendicular position of the two aromatic rings induces a similar electronic structure in both derivatives giving the same relative energetic position. In the derivative **A-2**, the excitation from the stilbene part lies higher in energy and the first excited state is already described by an excitation taking place in the center of the molecule (spin density difference at p_1 in fig. 2.3 (b)). Thus, the character of the S_1 can change smoothly along the reaction path from the FC point to the CoIn where the $\pi_c \rightarrow \pi_c^*$ configuration is most stabilized (fig. 2.3 (b), spin density difference at p_2). Therefore no barrier exists for this derivative. The same is valid for *motor-3* (see appendix fig. C.1). Here, the electron poor stilbene part leads to a similar electron distribution as in *motor-2* and no barrier occurs, as well. The change in the electronic character and the spin density of all states along the interpolation towards **CoIn₁** are shown in the appendix C highlighting the different behavior of *motor-1* compared to *motor-2* and *motor-3*.

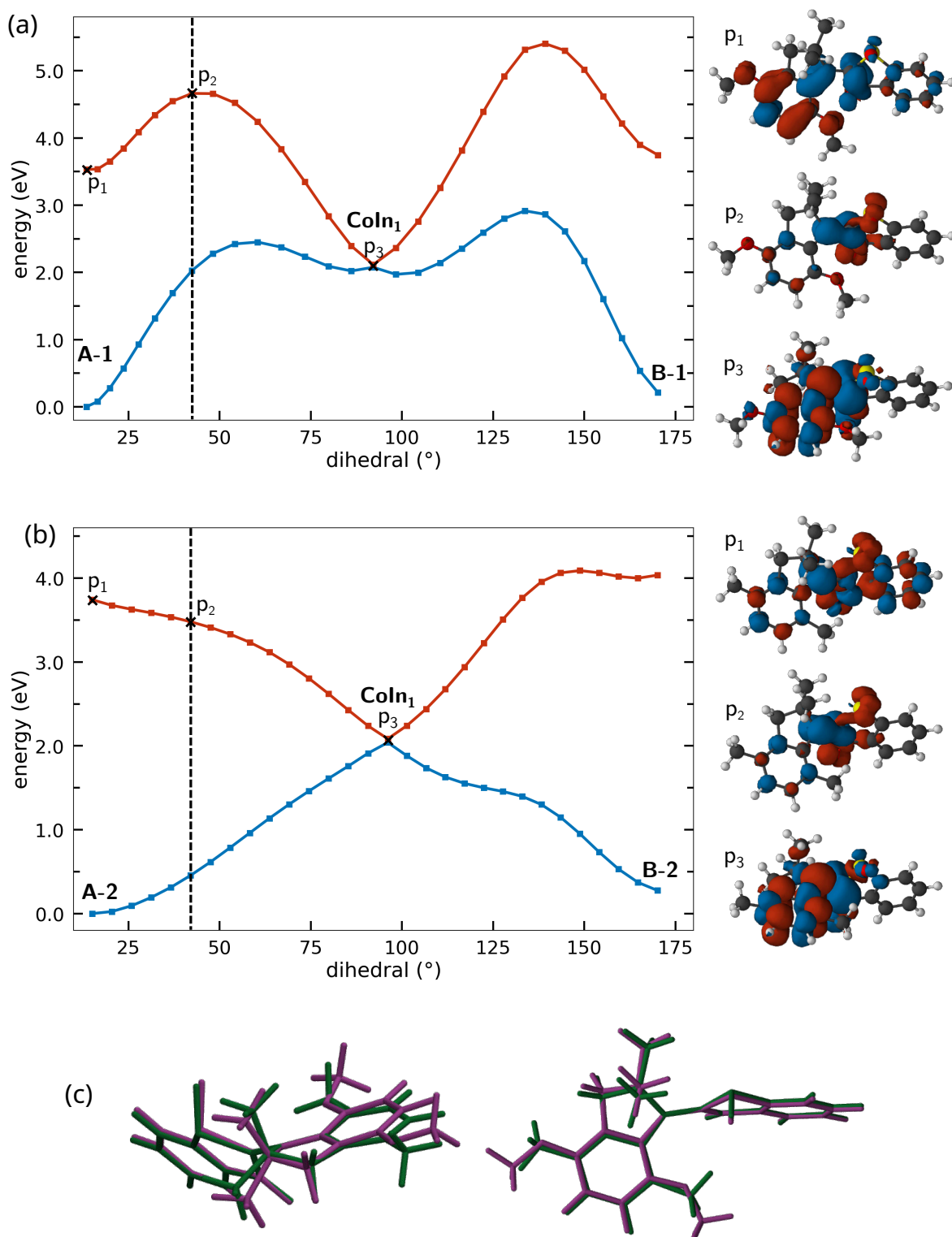


Figure 2.3: Linear interpolation of (a) *motor-1* and (b) *motor-2* between the isomers **A** and **B** via **Coln₁**. The S₀ is shown in blue and the S₁ in red. The dihedral angle C1-C2-C3-C4 (see fig. 2.1) is selected as reaction coordinate. The spin density difference between the S₀ and S₁ state is visualized on the right with an isovalue of ± 0.002 for the selected points p₁ to p₃. (c) shows the aligned geometries of both derivatives with the same dihedral angle taken at the maximum in the S₁ state of *motor-1* highlighted with the dashed lines in (a) and (b). *motor-1* is hereby shown in red and *motor-2* in green.

On-the-fly dynamics

The rotation of **A-2** \rightarrow **B-2** via the S_1/S_0 **CoIn**₁ is simulated with 52 semi-classical trajectories. The evolution of the state population is visualized in fig. 2.4 (red shows the population change in the S_1 and blue in the S_0). The first trajectories reach the **CoIn**₁ after about 200 fs. After around 330 fs more than 50 % of the trajectories passed through the CoIn which is in perfect agreement with the experimental reaction time. At a simulation time of about 470 fs the population transfer is completed and the remaining 10 % stay in the excited state until the end of the simulation. All of those trajectories staying in the S_1 state maintain the *E* configuration as they did not reach the CoIn.

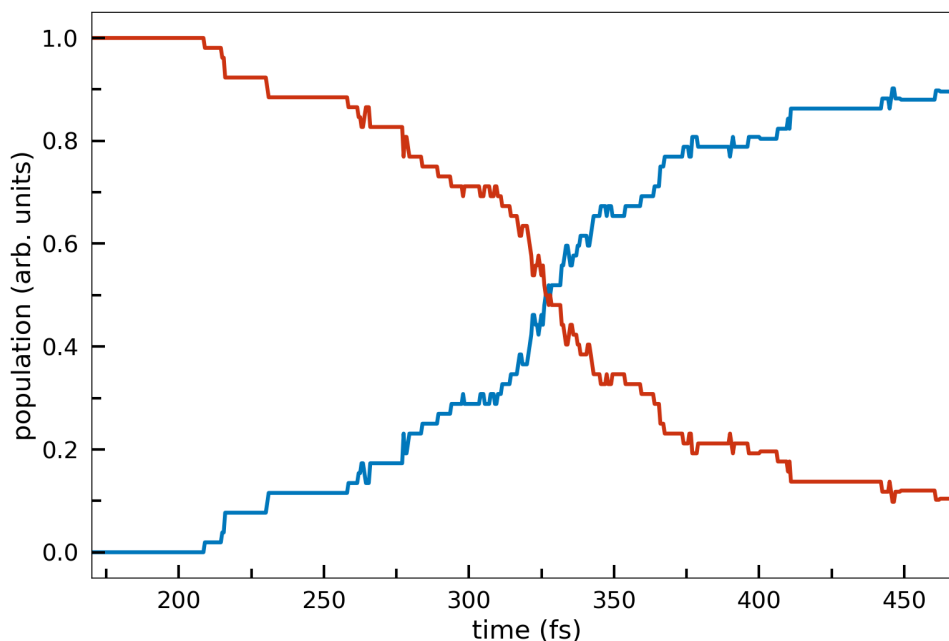


Figure 2.4: Evolution of the population after excitation to the S_1 state. The population in the S_0 is shown in blue and in the S_1 in red.

The energetic evolution of two typical trajectories, one remaining in the *E* configuration and one reaching the *Z* configuration, is visualized in the appendix (fig. C.5). The trajectories completing the isomerization directly pass through the CoIn region without stopping the rotation. The trajectories returning to the *E* isomer, in contrast, remain in the CoIn region for a longer time not able to surpass the dihedral angle of 90° towards the *Z* configuration. Analyzing the product distribution, 38 of the 52 suitable trajectories undergo a successful $E \rightarrow Z$ isomerization while the other 13 stay in the *E* configuration. With that a ratio of 73 % for the *Z* isomer is obtained. This is a lot larger than the experimentally observed isomerization ratio of 10 % [44]. A reason for that is, that in the simulation only the $S_1 \rightarrow S_0$ transfer via **CoIn**₁ is considered. Losses due to the known triplet channel via intersystem crossing are not described in our simulation. Further, our simulations are performed without consideration of solvent effects. However, our simulation is not set up to describe the product distribution quantitatively but to obtain a qualitative picture of the rotation mechanism. Several internal coordinates are found to be important for the rotation beside the obvious dihedral angle C1-C2-C3-C4 (see fig. 2.1) determining the $E \rightarrow Z$ isomerization. The temporal evolution of the dihedral from about 15° (*E*-(S)-(P)) to about 175° (*Z*-(S)-(M)) is shown in fig. 2.5. Within the first 80 fs the average dihedral rises from about 15° to 30° . After that further rotation stops and the molecule oscillates around the dihedral angle of 30° for the next 120 fs. During this time, a second internal coordinate, the ring puckering of the aliphatic carbon atom of the five membered ring of the stilbene part (fig. 2.6), becomes important. The aliphatic methyl groups are a sterical hinderance to the oxygen atom of

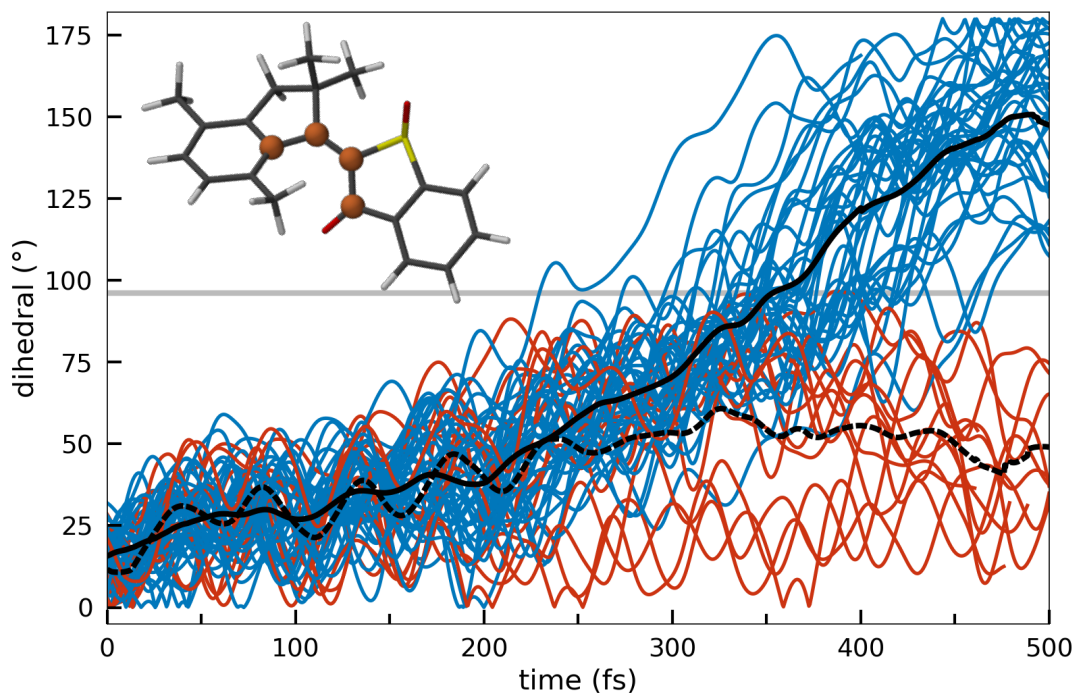


Figure 2.5: Temporal evolution of the dihedral angle C1-C2-C3-C4 during the simulation. Trajectories undergoing the $E \rightarrow Z$ isomerization are visualized in blue and trajectories staying in the E configuration are shown in red. The respective dihedral at **CoIn₁** is marked in gray. The black solid and dashed lines show the averaged angle over all trajectories ending in the Z or E configuration, respectively.

the sulfur blocking the further rotation that can only continue when the oxygen atom has passed the sterical obstruction. The hindrance of the methyl groups is removed by a planarization motion of the five membered ring. After around 180 fs the average angle (C3-C7)-(C3-C4-C5) (solid line) amounts to about -4° compared to previously -29° and the rotation along the double bond continues towards **CoIn₁** and further for the trajectories ending in the Z isomer. After a successful $E \rightarrow Z$ isomerization the angle (C3-C7)-(C3-C4-C5) is inverted for most trajectories (fig. 2.6, blue) while all trajectories ending in the E isomer (fig. 2.6, red) return to the original orientation. Considering the distortion of the five-membered ring at the beginning of the simulation it is conspicuous that the trajectories accomplishing the isomerization tend to be more twisted (-29°) compared to the trajectories returning to the original configuration (-26°). The trajectories leading to the Z or returning to the E configuration show a similar behavior until a simulation time of about 220 fs (compare solid and dashed line of fig. 2.5 and 2.6). After that only the Z trajectories with the larger momentum towards the **CoIn** continue the rotation mechanism while the E trajectories return to the starting point.

A further internal coordinate with distinct changes during the isomerization is the angle C1-C2-C3 (fig. 2.7). It decreases in average from about 127° to about 121° after 300 fs and thereafter increases again to its original value at 500 fs. Here no difference between trajectories ending in the Z or E isomer is observed. Comparing the angles at the critical points no significant difference can be observed (E : 126.9° ; **CoIn₁**: 127.9° ; Z : 127.0°). Thus this motion is not determined by a specific path but necessary to reach **CoIn₁** to avoid steric hindrance between the aliphatic methyl groups and the oxygen atom at the sulfur. The angle C2-C3-C4 shows a similar behavior for the same reasons but to a lesser extend and the evolution is visualized in the appendix (fig. C.7). The bond length of the C2-C3 double bond, in contrast, shows no distinct dynamics related to the rotation reaction but oscillates between 1.25 \AA to 1.65 \AA during the whole

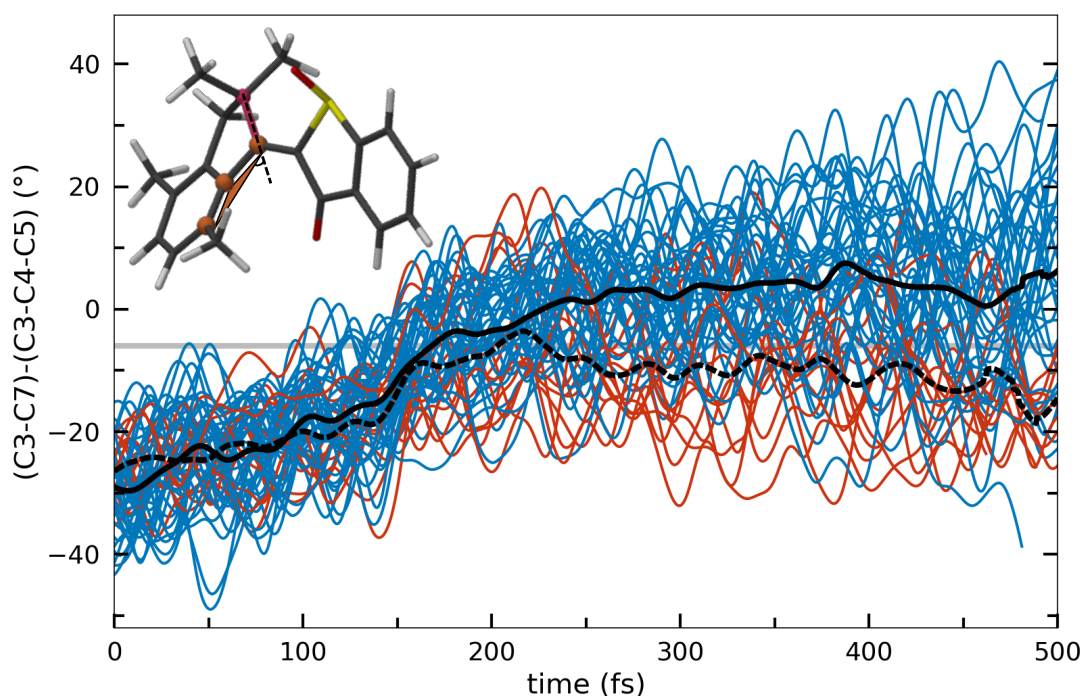


Figure 2.6: Temporal evolution of the angle between the C3-C7 bond and the plane spanned by C3-C4-C5 during the simulation. This internal coordinate defines the ring puckering of the aliphatic carbon atom of the five membered ring of the stilbene part. Trajectories undergoing the $E \rightarrow Z$ isomerization are visualized in blue and trajectories staying in the E configuration are shown in red. The black solid and dashed lines show the averaged angle over all trajectories ending in the Z or E configuration, respectively.

simulation (see appendix fig. C.6).

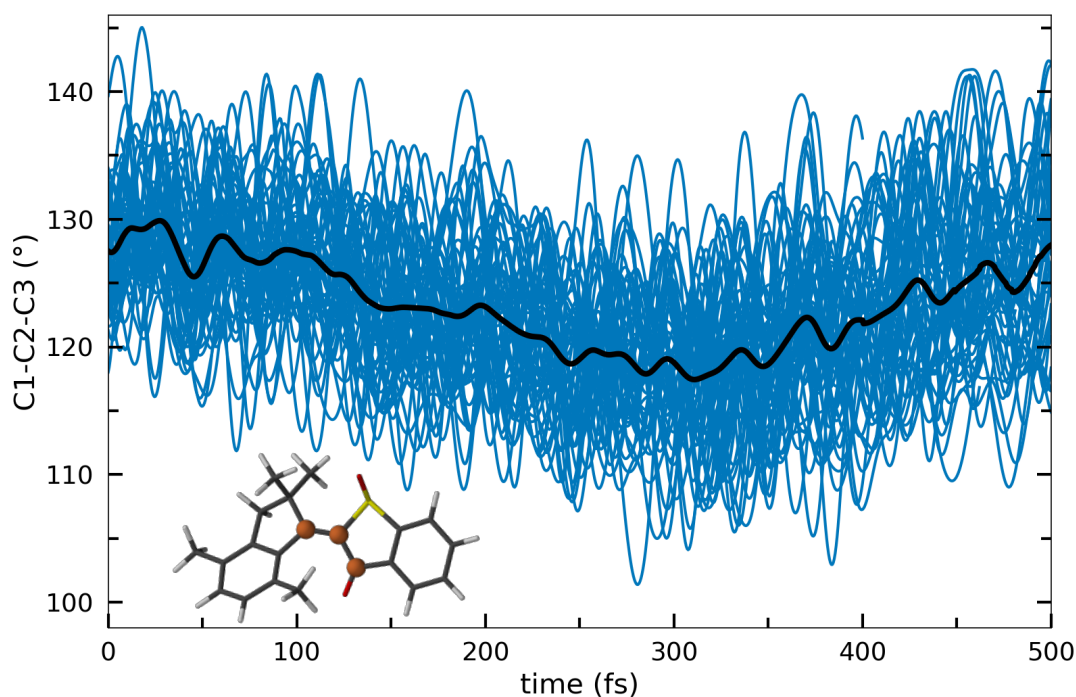


Figure 2.7: Temporal evolution of the angle C1-C2-C3 during the simulation. The black line shows the averaged angle over all trajectories.

In conclusion, the different reaction time of the first photoinduced step of the rotation of the HTI based *motor-1* and *motor-2* can be explained because a barrier of about 1.0 eV on the S_1 surface exists on the direct path from **A-1** to **CoIn₁** while no barrier is observed for *motor-2*. Comparing the electronic structure we conclude that the barrier arises due to the electron rich stilbene part of *motor-1* that leads to a different order of states at the FC point. The hypothetical *motor-3* with the electron poor stilbene part has a similar behavior as *motor-2* and is therefore expected to have a comparable reaction time for the **A** \rightarrow **B** step.

The semi-classical trajectory simulation visualized the first step of the rotation from **A-2** to **B-2** in a full-dimensional picture reproducing well the experimental reaction time and identifying all important motions for a successful isomerization.

As an outlook for the future, we plan to consider the derivative *motor-1* for a dynamics simulation where we hope to reveal differences in important internal coordinates compared to *motor-2*. Further, we want to investigate the slow thermal rotational step **B** \rightarrow **C**. Here, the more stable *Z* configuration is formed via helix inversion. In this step, *motor-2* (990 ns), that was faster in the photochemical step, is a lot slower than *motor-1* (3.0 ns) [44]. The reason for that is the higher sterical hindrance of the methyl groups compared to the more flexible methoxy groups at the stilbene part [43]. For that, we suggest more investigations concerning the substituents at the stilbene part. Substituents with electron withdrawing features accelerate the photoinduced steps and larger groups slow down the thermal helix inversion step because of sterical hindrance. With this considerations, we hope to find a new overall faster molecular motor.

2.2 Dissociation reaction of diphenylmethyl bromide

Depending on the leaving group X different bond cleavage channels are preferred for compounds of the form $\text{Ph}_2\text{CH} - \text{X}$. The cation $\text{Ph}_2\text{CH} - \text{PPh}_3^+$, for example, dissociates clearly preferring heterolytic bond cleavage building the carbo cation Ph_2CH^+ as no charge separation takes place because the molecule already bears a charge [103]. Neutral compounds with halogen leaving groups, in contrast, as e.g. $\text{Ph}_2\text{CH} - \text{Cl}$ and $\text{Ph}_2\text{CH} - \text{Br}$, prefer homolytic bond cleavage building the carbo radical $\text{Ph}_2\text{CH}^\bullet$, because of the essential charge separation in heterolytic bond cleavage [103]. To describe the dissociation reaction of $\text{Ph}_2\text{CH} - \text{Br}$ correctly, a multi-reference method as CASSCF is necessary which is done equivalently to previous calculations with $\text{Ph}_2\text{CH} - \text{Cl}$ [19, 103].

ONIOM approach

For a feasible simulation only one phenyl ring is included in the CASSCF calculations to build the model system $\text{PhCH}_2 - \text{Br}$. With that, a stable active space including the complete π -space of the phenyl ring, the two lone pair orbitals of the bromine atom and the bonding and anti-bonding σ -orbital of the cleaved C-Br bond, can be set up. The second phenyl ring is considered with the Our Own N-Layered Integrated Molecular Orbital and Molecular Mechanics (ONIOM) approach [104, 105] at a low-level of theory. The approximated energy of the real system at the high-level of theory ($E(\text{ONIOM})$) is

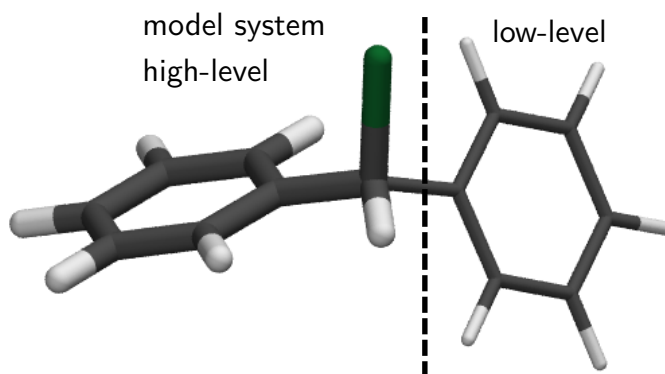


Figure 2.8: ONIOM partitioning of $\text{Ph}_2\text{CH} - \text{Br}$ in the model system for the high-level calculation and the part only included with the low-level of theory.

then calculated by

$$E(\text{ONIOM}) = E(\text{high}, \text{model}) + E(\text{low}, \text{real}) - E(\text{low}, \text{model}). \quad (2.1)$$

The gradient of the energy can be approximated the same way

$$\frac{\partial E(\text{Oniom})}{\partial R} = \frac{\partial E(\text{model}, \text{high})}{\partial R} + \frac{\partial E(\text{real}, \text{low})}{\partial R} - \frac{\partial E(\text{model}, \text{low})}{\partial R}. \quad (2.2)$$

This approach is reasonable because a transfer between the phenyl rings is unlikely as the orbitals of both rings do not overlap. The PES for the quantum dynamics simulation are calculated with DFT (B3LYP) as the low-level method the complete system. In the semi-classical surface hopping simulation HF is used to calculate the real system. The model system $\text{PhCH}_2 - \text{Br}$ is calculated at the same level of theory (CASSCF(12,10)) for both simulations.

Hamiltonian in the reduced coordinate space

In conventional grid-based quantum dynamic (QD) a Gaussian wave packet propagates on ab-initio PES in a reduced reactive coordinate subspace. The terms of the full-dimensional kinetic energy operator in cartesian coordinates ($\hat{T} = -\sum_{\alpha=1}^{3N} \frac{1}{2m_{\alpha}} \nabla_{\alpha}^2$) can be transformed in the reduced (internal) coordinate space by using the Wilson G-matrix formalism [19, 106–108]. The transformed operator \hat{T} is hereby formulated as

$$\hat{T} = -\frac{1}{2} \sum_{k=1}^M \sum_{l=1}^M \mathbf{j}^{-\frac{1}{2}} \frac{\partial}{\partial q_k} \left(\mathbf{j} G_{kl} \frac{\partial}{\partial q_l} \mathbf{j}^{-\frac{1}{2}} \right) \quad (2.3)$$

using the Jacobian determinant $\mathbf{j} = \det |J|$ of the Jacobian matrix with the elements $J_{\alpha k} = \frac{\partial R_{\alpha}}{\partial q_k}$ where R_{α} are the cartesian coordinates and q_k are the M internal coordinates. With the assumption that the position dependency of the Jacobian determinant is neglectable compared to the position dependence of the G-matrix G_{kl} the formulation simplifies to

$$\hat{T} \simeq -\frac{1}{2} \sum_k^M \sum_l^M \frac{\partial}{\partial q_k} G_{kl} \frac{\partial}{\partial q_l}, \quad (2.4)$$

The G-matrix G_{kl} is calculated via its inverse that is easily accessible

$$G_{kl}^{-1} = \sum_{\alpha}^{3N} m_{\alpha} \frac{\partial R_{\alpha}}{\partial q_k} \frac{\partial R_{\alpha}}{\partial q_l} \quad (2.5)$$

using the finite difference method. The geometries are set up with respect to the Eckart conditions [109] to avoid translation and rotation within the system to obtain pure internal geometry changes.

The main effort in QD simulations lies within the setup of suitable reactive coordinates to build the PES to describe the required reaction. For the excited state dissociation of $\text{Ph}_2\text{CH} - \text{Br}$ the same coordinates as for the dissociation of $\text{Ph}_2\text{CH} - \text{Cl}$ are used. The two coordinates are the C – Br distance r and a coordinate describing the planarization of the molecule (d_{py}) which is the second important geometry change during the dissociation. The operator of the kinetic energy in internal coordinates $\hat{T}(r, d_{\text{py}})$ can be setup with the described G-matrix formalism as

$$\hat{T}(r, d_{\text{py}}) = -\frac{1}{2} \left[\frac{\partial}{\partial r} G_{r,r} \frac{\partial}{\partial r} + \frac{\partial}{\partial r} G_{r,d_{\text{py}}} \frac{\partial}{\partial d_{\text{py}}} + \frac{\partial}{\partial d_{\text{py}}} G_{d_{\text{py}},r} \frac{\partial}{\partial r} + \frac{\partial}{\partial d_{\text{py}}} G_{d_{\text{py}},d_{\text{py}}} \frac{\partial}{\partial d_{\text{py}}} \right] \quad (2.6)$$

with the equal kinetic coupling elements $G_{r,d_{\text{py}}}$ and $G_{d_{\text{py}},r}$.

The dynamics is simulated in the diabatic representation. Therefore, the excited states are partly diabaticized in the vicinity around the CoIns using the dipole moments as described in reference [103]. Hereby, the matrix μ^{ad} is formed by the adiabatic dipole moments μ_{ii}^{ad} and transition dipole moments μ_{ij}^{ad} .

$$\mu^{dia} = U^{\dagger} \mu^{ad} U \quad (2.7)$$

Diagonalizing the matrix μ^{ad} yields the transformation matrix U used to calculate the diabatic matrix H^{dia} from the adiabatic energies E_k .

$$H_{ij}^{dia} = \sum_{k=1}^{n_S} U_{ik} E_k U_{kj} \quad (2.8)$$

n_S represents the number of states degenerate at the respective CoIn. For a three-state CoIn $n_S = 3$ and for a two-state CoIn $n_S = 2$, meaning a (3×3) or a (2×2) matrix has to be solved, respectively.

The diagonal elements H_{ii}^{dia} represent the diabatic energies V_i and the off-diagonal elements H_{ij}^{dia} represent the diabatic coupling elements D_{ij} . As population transfer should only take place at the CoIns the couplings are damped offside the vicinity of the CoIns. In the case of $\text{Ph}_2\text{CH} - \text{Br}$ four diabatic states, V_2 , V_3 , V_4 and V_5 , are involved in the diabaticization. Couplings are calculated at two consecutive CoIns, one representing a three-state CoIn (CoIn_1) between V_2 , V_3 and V_4 and the other representing a two-state CoIn (CoIn_2) between V_2 and V_5 . The ground state V_1 needs no diabaticization as in this case the adiabatic and diabatic representation coincides. All further off-diagonal elements are set to zero which also includes the coupling between the degenerate states V_3 and V_4 (both $n_{Br} \Rightarrow \pi^*$ states). Thus, steady population transfer between these states along the complete simulation grid, which is insignificant for the reaction, can be easily avoided with the applied diabaticization. The complete hamiltonian in the diabatic

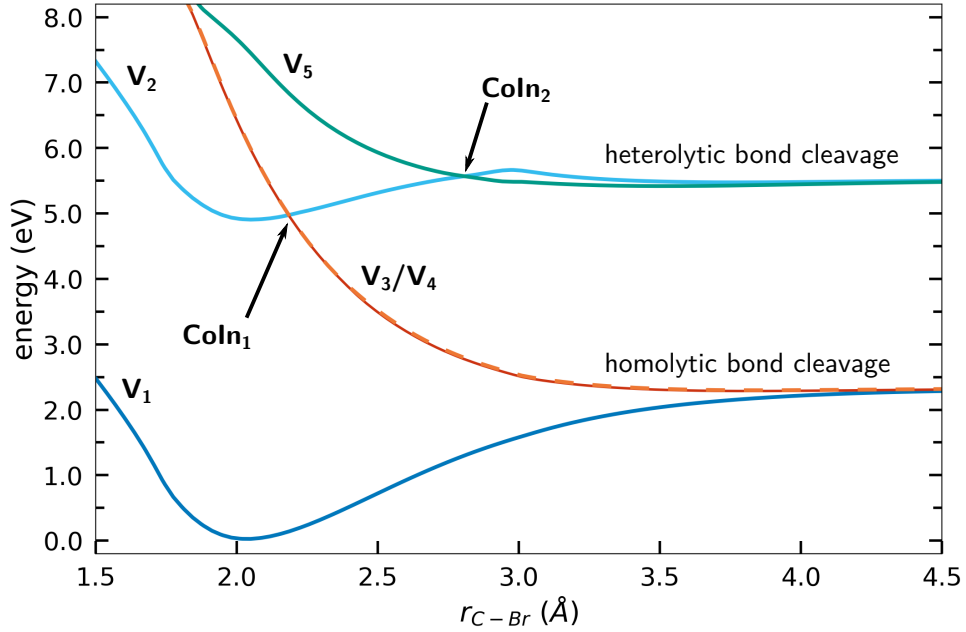


Figure 2.9: Diabatic potential energy surfaces of $\text{Ph}_2\text{CH} - \text{Br}$ of the states included in the dynamics simulation along the C – Br distance r .

description for the simulation is hereby of the form:

$$\hat{H} = \begin{Bmatrix} V_1 & \mu_{12}\epsilon(t) & 0 & 0 & 0 \\ \mu_{12}\epsilon(t) & V_2 & D_{23} & D_{24} & D_{25} \\ 0 & D_{23} & V_3 & 0 & 0 \\ 0 & D_{24} & 0 & V_4 & 0 \\ 0 & D_{25} & 0 & 0 & V_5 \end{Bmatrix} + \hat{T}(\mathbf{r}, \mathbf{d}_{\text{py}}) \quad (2.9)$$

The excitation from the closed shell ground state (V_1) to the S_1 state with $\pi \Rightarrow \pi^*$ character (V_2) is simulated by adding the dipole laser interaction ($\mu_{12}\epsilon(t)$) between these surfaces to the respective off-diagonal elements of the Hamiltonian as perturbation. Here, the adiabatic transition dipole moment μ_{12} between the S_0 and S_1 is used as the excitation only occurs localized in the ground state minimum where the diabatic representation corresponds to the adiabatic one.

The time evolution of the wave packet is obtained by solving the TDSE of the form

$$\Psi(r, R, t + dt) = e^{-i\hat{H}dt}\Psi(r, R, t) \quad (2.10)$$

where the exponential timedependent term $e^{-i\hat{H}t}$ is expanded as a Chebychev series

$$e^{-i\hat{H}dt} \approx \sum_{n=0}^N a_n \varphi_n(-i\hat{H}dt) \quad (2.11)$$

with the expansion coefficients a_n and the complex Chebychev polynomials φ_n [110]. An advantage of the Chebychev propagator, that is slow compared to other propagators, is the high accuracy maintained over a long propagation time, which was necessary to simulate the dissociation of $\text{Ph}_2\text{CH} - \text{Br}$ over more than 1000 fs. The quantum dynamics simulations are performed with the program QDng developed in our group.

The semi-classical dynamics is simulated in the adiabatic representation with an ensemble of independent trajectories moving classically on ab-initio calculated PES. Hereby, the quantum transitions are approximated with the fewest-switches surface hopping algorithm first introduced by Tully[21] and then further developed by Hammes-Schiffer and Tully[22]. The simulation is performed with NewtonX [100, 111].

The main points of the article “Ultrafast non-adiabatic dynamics of excited diphenylmethyl bromide elucidated by quantum dynamics and semi-classical on-the-fly dynamics” are:

- The dissociation dynamics of $\text{Ph}_2\text{CH} - \text{Br}$ with two consecutive CoIns after excitation to the S_1 state is investigated with grid-based wave packet quantum dynamics and semi-classical trajectory surface-hopping. Hereby, the first CoIn, CoIn_1 , leads to homolytic bond cleavage and the second, CoIn_2 , to heterolytic bond cleavage. With both methods, the distinct preference for one product channel (homolytic bond cleavage) and the sequential appearance time of the homolytic and heterolytic bond cleavage products can be explained.
 - The ONIOM approach is applied successfully to $\text{Ph}_2\text{CH} - \text{Br}$ with the model system $\text{PhCH}_2 - \text{Br}$ calculated at CASSCF(12,10) level of theory. Disregard of the second phenyl ring in the high-level calculations is necessary to keep a consistent active space at all calculated points during the dynamics simulations.
 - In the quantum dynamics simulation, the wave packet evolves on five coupled diabatic states with the Chebychev propagator. The PES are calculated with ONIOM(CASSCF:B3LYP) along the two specially adapted coordinates defining the reaction, the C-Br distance r and the planarization distance d_{py} also used for the dissociation of $\text{Ph}_2\text{CH} - \text{Cl}$. For an experimentally comparable product distribution, the wave packet needs an additional momentum towards the respective CoIn to overcome the barrier for the heterolytic bond cleavage existing in the reduced coordinate space. Otherwise, all of the wave packet passes through CoIn_1 with no part passing through CoIn_2 . Nevertheless, the sequential reaction time for both dissociation channels shows the same tendency as the experiment with 50 fs (exp. 100 fs for the homolytic bond cleavage and 120 fs (exp. 200 fs) for the heterolytic channel. The faster reaction time goes along with the simulation in the reduced coordinate space. Specific analysis of the wave packet’s motion revealed that the experimentally observed oscillation in the transient absorption signal can be assigned to a vibration in the S_1 state activated right after the excitation.
 - In the full-dimensional semi-classical trajectory surface-hopping simulation this barrier does not exist and no further activation is required to obtain an experimentally comparable product distribution with 60 % radical pair and 40 % ion pair. The reaction time of 60 fs to 80 fs for the homolytic and 180 fs to 220 fs for the heterolytic bond cleavage channel is in good agreement with the experimental values. A specific analysis of the velocities with an autocorrelation function [112, 113] revealed significant differences in the frequencies activated in both bond cleavage channels. A vibration around 1300 cm^{-1} , assigned to an asymmetric stretch motion at the central carbon atom, is solely appearing in the spectra of the trajectories
-

forming the radical pairs. A second vibration around 1100 cm^{-1} is particularly activated in the trajectories of heterolytic bond cleavage. This vibration is related to a motion of the central carbon atom similar to the coordinate d_{py} describing the pyramidalization.

- In comparison to the highly time-resolved experiment, the quantum dynamics simulation revealed the wave packet features visible in the transient absorption signal and the semi-classical simulation covered the full-dimensionality of the analyzed system.

Following, the article “Ultrafast non-adiabatic dynamics of excited diphenylmethyl bromide elucidated by quantum dynamics and semi-classical on-the-fly dynamics” published in *Physical Chemistry Chemical Physics* is reprinted from *Phys. Chem. Chem. Phys.*, **20**, 22753 (2018) with permission from the PCCP Owner Society.



Cite this: *Phys. Chem. Chem. Phys.*,
2018, 20, 22753

Ultrafast non-adiabatic dynamics of excited diphenylmethyl bromide elucidated by quantum dynamics and semi-classical on-the-fly dynamics†

Franziska Schüppel, Matthias K. Roos and Regina de Vivie-Riedle  *

Carbocations and carboradicals are key intermediates in organic chemistry. Typically UV laser excitation is used to induce homolytical or heterolytical bond cleavage in suitable precursor molecules. Of special interest hereby are diphenylmethyl compounds ($\text{Ph}_2\text{CH-X}$) with $\text{X} = \text{Cl}, \text{Br}$ as a leaving group as they form diphenylmethyl radicals ($\text{Ph}_2\text{CH}^\bullet$) and cations (Ph_2CH^+) within a femtosecond time scale in polar solvents. In this work, we build on our methodology developed for the chlorine case and investigate the photodissociation reaction of $\text{Ph}_2\text{CH-Br}$ by state-of-the-art theoretical methods. On the one hand, we employ specially adapted reactive coordinates for a grid-based wave packet dynamics in reduced dimensionality using the Wilson G-matrix ansatz for the kinetic part of the Hamiltonian. On the other hand, we use full-dimensional semiclassical on-the-fly dynamics with Tully's fewest switches surface hopping routine for comparison. We apply both methods to explain remarkable differences in experimental transient absorption measurements for Cl or Br as the leaving group. The wave packet motion, visible only for the bromine leaving group, can be related to the crucial role of the central carbon atom, which undergoes rehybridization from sp^3 to sp^2 during the photoinduced bond cleavage. Comparable features are the two consecutive conical intersections near the Franck-Condon region controlling the product splitting to $\text{Ph}_2\text{CH}^\bullet/\text{Br}^\bullet$ and $\text{Ph}_2\text{CH}^+/\text{Br}^-$ as well as the difference in delay time for the respective product formation.

Received 22nd May 2018,
Accepted 15th August 2018

DOI: 10.1039/c8cp03257b

rsc.li/pccp

1 Introduction

Carbocations and to a lesser extent carboradicals are important building blocks in organic synthesis.^{1,2} Furthermore, carbocations are used to study the kinetics of reactions with nucleophiles to build reference scales to predict reactivities.^{3,4} The highly reactive species can be prepared by irradiating a suitable precursor molecule with UV light,^{5–7} and in this way initiating a bond cleavage that can occur homolytically or heterolytically. Widely used^{4,7–9} precursors are diphenylmethyl compounds $\text{Ph}_2\text{CH-X}$ with e.g. $\text{X} = \text{Cl}, \text{Br}$ as leaving groups. These compounds are distinguishable by clearly distinct spectra of their photo-products and thus can be easily studied by transient absorption measurements.

In the case of chlorine this was done extensively,^{8–12} lately also with extremely high temporal resolution allowing changes to be resolved in the few femtosecond regime.¹² Delay times of 76 fs for the formation of the radical pair and 124 fs for the

formation of the ion pair were reported.^{11,12} With 95% radical pairs, the product ratio was clearly biased towards the homolytic channel, with only 5% ion pairs. Recently, we could elucidate the initial processes occurring during the ultrafast dissociation of $\text{Ph}_2\text{CH-Cl}$ with theoretical methods.^{12,13} Especially, we discovered the leading role of the chlorine lone pairs. They provide an effective connection between the initial photo-accessible $\pi\pi^*$ state and the radical-pair product channel. The coupling into the lone pair states occurs at a three-state conical intersection (CoIn), the first in a sequence of two CoIns near the Franck-Condon (FC) region. The second CoIn at slightly larger carbon chlorine distance is a two-state CoIn and connects the $\pi\pi^*$ state with the ion-pair product channel. This sequence of CoIns completely defines the product ratio. The delay times were in good agreement with the experimental ones and we could confirm the radical pair as the main product of the initial bond cleavage. Overall, we could successfully explain the reaction process in the first hundreds of femtoseconds.

Bromine, the heavier homologue of chlorine, was also studied experimentally as a leaving group.^{14,15} Here, the dissociation reaction is slower compared to the chlorine case. The reported delay times with respect to the optical excitation are slightly longer for the rise of both product signals. The radical pair is

Department of Chemistry, Ludwig-Maximilians-Universität München,
Butenandstraße 5-13, 81377 Munich, Germany.
E-mail: Regina.de_Vivie@cup.uni-muenchen.de

† Electronic supplementary information (ESI) available. See DOI: 10.1039/c8cp03257b

detected after 100 fs and the ion pair after 200 fs. The product ratio still favors the homolytic channel, but with 70% radical pairs and 30% ion pairs the excess of radicals is not so pronounced. More remarkable is a small-amplitude oscillation superimposed on the rise of the transient absorption signals that was associated with a vibrational mode of the remaining carbon backbone.¹⁴ To the best of our knowledge, there are no theoretical studies on the photodissociation of $\text{Ph}_2\text{CH-Br}$ or this oscillation in particular.

In this work, we investigate the photo-induced bond cleavage of $\text{Ph}_2\text{CH-Br}$ by quantum dynamical and mixed quantum-classical (semi-classical) methods. Specific geometry points that are important for the product splitting such as CoIns are identified and optimized with quantum chemical methods. For the dynamics simulation we apply two different approaches. On the one hand, like in the chlorine case, we employ grid-based wave packet dynamics in reduced dimensionality using the Wilson G-matrix^{16–18} ansatz for the kinetic energy operator. This ansatz allows us to adequately treat arbitrary coordinates in the Hamiltonian, in this case our specially adapted reactive coordinates.¹⁹ With these coordinates, we can take into account the relaxation of the carbon backbone during the bond cleavage without optimizations for each grid point. On the other hand, we use Tully's fewest switches surface hopping routine²⁰ in on-the-fly semi-classical dynamics simulations. Here, due to its full-dimensional nature, we can analyze the motions of the molecule in the complete configuration space using the velocity autocorrelation function to calculate the spectrogram. Both dynamics methods are based on the same electronic structure method. We choose an "Our Own N-Layered Integrated Molecular Orbital and Molecular Mechanics" (ONIOM)^{21–23} quantum chemical description with complete active space self-consistent field (CASSCF) as a high level of theory. The focus of our work is to discuss and explain the differences caused in the photodissociation dynamics by changing the leaving group from chlorine to bromine.

This article is structured as follows: In Section 2, we first introduce the partitioning of the ONIOM layers used in both dynamics simulations, and then discuss details of each of these methods. Section 3.1 deals with optimized minima and CoIns and shows first potential energy surfaces. In Section 3.2, we discuss the results of the quantum dynamical simulations. Section 3.3 concerns the semi-classical dynamical simulations. Section 3.4 discusses the vibrational motions driving the reaction and relates them to the experimental observables. Finally, Section 4 summarizes our findings and concludes this work.

2 Computational details

As shown for the lighter homologue $\text{Ph}_2\text{CH-Cl}$ the π -systems of the phenyl rings are not coupled and can be separated.^{13,24} In $\text{Ph}_2\text{CH-Br}$ they form an angle of 72.5° at the FC point. Since $\text{Ph}_2\text{CH-Br}$ is a rather large molecule to treat at the CASSCF level of theory, the computational effort is reduced by using an ONIOM two-layer ansatz.^{21,22} We do so by employing a program of our own design²³ with interfaces to various

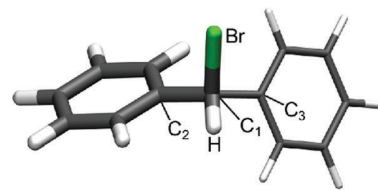


Fig. 1 Geometry of $\text{Ph}_2\text{CH-Br}$ showing the ONIOM partitioning. The thick part shows the model system $\text{PhCH}_2\text{-Br}$ calculated at the high level of theory CAS(12,10). The second phenyl ring is only included for calculations at the low level of theory and replaced by an H atom in the model system.

quantum chemistry program packages. Thus, one phenyl ring is replaced by an H atom for the ONIOM model system forming $\text{PhCH}_2\text{-Br}$ (Fig. 1) treated at the CASSCF level of theory with the program package Molpro2012.^{25,26} The active space (Fig. S10, ESI†) consists of 12 electrons in 10 orbitals, CAS(12,10), and contains all π orbitals of the one phenyl ring, the σ/σ^* orbitals of the $\text{C}_1\text{-Br}$ bond and two lone pair orbitals (n_1 , n_2) of the bromine atom. It is analogous to the active space used for the description of $\text{Ph}_2\text{CH-Cl}$.¹³ Following the argument of uncoupled π -systems, the excitation can be seen as localized on only one phenyl ring and so the constraint low-level state (CLS) approximation²⁷ is used. The complete system is either calculated at the B3LYP level of theory with the program package Gaussian09²⁸ (in the quantum dynamics part) or at the HF level of theory with Molpro2012 (in the semi-classical part). Minima and the two-state CoIn of the model system, $\text{PhCH}_2\text{-Br}$, were optimized at the CAS(12,10) level of theory using the program package Molpro2012. The optimization of the three-state CoIn was done at the same level of theory using the program package Columbus.^{29–32} For all calculations we employed the binning-SVP basis set for the bromine atom and the 6-31G(d) basis set for all other atoms.

2.1 Quantum dynamics

For the quantum dynamical simulation, we reduce the number of coordinates because a full-dimensional simulation on *ab initio* potential energy surfaces (PESs) is not feasible. The photodissociation is described by two specially adapted reactive coordinates¹⁹ that already proved to capture the ultrafast dynamics of the lighter homologue.¹³ The first one is the $\text{C}_1\text{-Br}$ distance r describing the bond cleavage. The second coordinate describes the change of the pyramidalization of the C_1 atom due to rehybridization from sp^3 to sp^2 along the bond cleavage. It is quantified as the distance d_{py} from atom C_1 to the plane spanned by its three neighboring atoms. Both reactive coordinates are shown in Fig. 2.

To include relaxation in the reduced coordinate system, we used the already mentioned concept of specially adapted reactive coordinates¹⁹ that was developed in our group. Significant changes of further internal coordinates during the bond cleavage were considered *via* fit functions derived from a relaxed scan along the $\text{C}_1\text{-Br}$ bond length. Besides the second active coordinate d_{py} , changes along bonds and angles including the central C_1 atom and the relative position between the phenyl

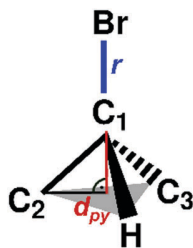


Fig. 2 Reactive coordinates r and d_{py} for the quantum dynamical simulation.

rings emerge as most important. A detailed description of this procedure is reviewed in the ESI.[†]

The Hamiltonian has to be transformed from Cartesian coordinates into the chosen reactive coordinates. The challenging part hereby is the kinetic energy operator $\hat{T}(x,y,z)$ which can be expressed in the reactive coordinates using the Wilson G-Matrix formalism.^{16–19} The transformed operator $\hat{T}(r,d_{py})$ is of the form:

$$\hat{T}(r, d_{py}) = -\frac{\hbar^2}{2} \left[\frac{\partial}{\partial r} G_{rr} \frac{\partial}{\partial r} + \frac{\partial}{\partial r} G_{rd_{py}} \frac{\partial}{\partial d_{py}} + \frac{\partial}{\partial d_{py}} G_{d_{py}r} \frac{\partial}{\partial r} + \frac{\partial}{\partial d_{py}} G_{d_{py}d_{py}} \frac{\partial}{\partial d_{py}} \right],$$

with the diagonal elements G_{rr} , $G_{d_{py}d_{py}}$ and the equal, off-diagonal elements $G_{rd_{py}}$, $G_{d_{py}r}$. The G-Matrix elements are shown in Fig. S3 (ESI[†]).

We used a diabatic description of the potential energy operator for our simulation and included the five lowest singlet states (π^2 , $\pi\pi^*$, $n_1\pi^*$, $n_2\pi^*$ and $\pi\sigma^*$) at the ONIOM(CAS(12,10):B3LYP) level of theory (Fig. S2, ESI[†]). The transformation into the diabatic picture was implemented as described in ref. 13 using the dipole and transition dipole moment. The diabatic coupling matrix elements (DCMEs), necessary to describe population transfer between diabatic states, result from this transformation, as well. The diabatic representation is essential for the quantum dynamics simulation because it allows us to avoid population transfer between the degenerate lone pair states ($n_1\pi^*$ and $n_2\pi^*$). In the diabatic description we can set this coupling to zero and completely eliminate the interaction that is unimportant for the product distribution. Instead, we only include DCMEs (Fig. S4, ESI[†]) in the area of the optimized CoIns between the states of interest.

The wave packet simulation was performed with a program of our own design. For the time propagation we used the Chebychev propagator³³ with a time step of $\Delta t = 10$ a.u. The laser excitation is simulated in the dipole approximation with a Gaussian shaped laser pulse adapted to the experimental parameters (FWHM = 18 fs; $\lambda = 250$ nm; $I_{\max} = 5.63 \times 10^{13}$ W cm⁻²; $t_0 = 0$ fs). More technical details of the simulation are listed in the ESI.[†]

2.2 Semi-classical dynamics

We used our modified version of the program package NewtonX^{34,35} with an interface for Molpro2012^{25,26} implementing the ONIOM

code²³ for the semi-classical dynamics. The five lowest singlet states were considered for the simulation calculated at the ONIOM(CAS(12,10):HF) level of theory. We ran 100 trajectories with different initial conditions generated from a Wigner distribution³⁶ based on a frequency analysis of Ph₂CH–Br in the ground state at the B3LYP level of theory. 69 trajectories reached the end of the selected simulation time and showed C₁–Br bond cleavage. Three trajectories remained in the FC region and did not show any reaction after 250 fs. The other 28 trajectories broke down in the beginning of the simulation in the FC region because the CASSCF calculation did not converge. The 69 reactive trajectories are used as the basis for our analysis which results in a maximum statistical error of less than 12%.³⁷ Investigating a two-pathway mechanism with an experimental distribution of 70%/30% is therefore possible with the given number of trajectories. The Wigner distribution was transferred to the $\pi\pi^*$ state to start the simulation. Transitions between the electronic states were treated according to Tully's fewest switches surface hopping routine.²⁰ A simulation time of 250 fs and a time step of 0.5 fs were applied. The integration of Newton's equations was done with the Velocity Verlet algorithm.

Furthermore, we performed trajectory calculations for the diphenylmethyl radical and cation in the ground state after C₁–Br bond cleavage. This simulation was performed with NewtonX^{34,35} and its interface to Gaussian09.²⁸ To obtain the initial conditions, we used the geometry and velocity at 250 fs of each of the previous trajectories describing the dynamics of the precursor Ph₂CH–Br and discarded the bromine atom. In doing so, we could follow the ground state dynamics of the two fragments (Ph₂CH•/Ph₂CH⁺) at the B3LYP level of theory for a further 1000 fs.

3 Results and discussion

3.1 Potential energy surfaces of Ph₂CH–Br

Within the applied CLS approximation the electronic excitation is restricted to the model system PhCH₂–Br. Optimized geometry points on the PESs that are important during the dissociation are shown in Fig. 3. The closed shell ground state minimum (Fig. 3a) has a C₁–Br bond length r of 2.02 Å and the central carbon atom C₁ is completely sp³ hybridized with a value of $d_{py} = 0.34$ Å. The S₁ minimum with $\pi\pi^*$ character lies close to the FC region (Fig. 3b) with a slightly larger r of 2.06 Å and almost no change in d_{py} (0.32 Å). A three-state CoIn (S₃/S₂/S₁, CoIn₁) between the $\pi\pi^*$ state and the two degenerate $n_1\pi^*/n_2\pi^*$ states (Fig. 3c) is located at $r = 2.21$ Å and $d_{py} = 0.25$ Å. A second CoIn (S₄/S₃, CoIn₂) between the $\pi\pi^*$ state and a state with $\pi\sigma^*$ character is found at $r = 2.80$ Å and $d_{py} = 0.06$ Å. Here, the central C₁ atom is already sp² hybridized (Fig. 3d).

Ground and excited state PESs along the bond cleavage coordinate r and the hybridization coordinate d_{py} are calculated at the ONIOM(CAS(12,10):B3LYP) level of theory. For a first overview, a one-dimensional cut along r for constant $d_{py} = 0.35$ Å is shown in Fig. 4 for the corresponding diabatic PESs. The photodissociation reaction starts with a $\pi\pi^*$ excitation from the ground state to the S₁ state. The excitation energy of 4.85 eV

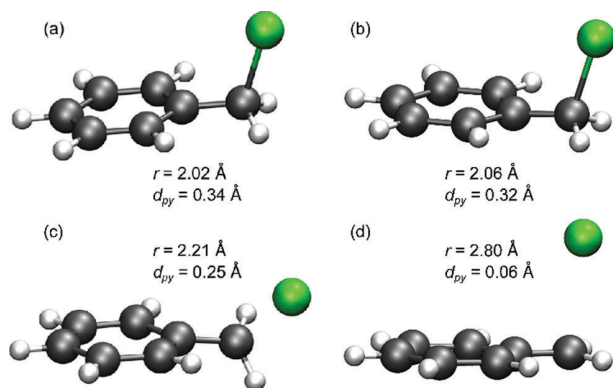


Fig. 3 Optimized geometries at the CAS(12,10) level of theory of the model system $\text{PhCH}_2\text{-Br}$ of (a) the S_0 minimum, (b) the S_1 minimum, (c) the three-state CoIn (CoIn_1) and (d) the two-state CoIn (CoIn_2).

(255 nm) is hereby in good agreement with the experimental value of 4.59 eV (270 nm).¹⁴ Close to the FC region, the two lone pair states ($n_1\pi^*/n_2\pi^*$) cross the $\pi\pi^*$ state (CoIn_1). With larger distance r , the $n_1\pi^*/n_2\pi^*$ states are stabilized and become degenerate to the ground state (π^2), correlating with the homolytic reaction channel leading to radical pairs ($\text{Ph}_2\text{CH}^\bullet/\text{Br}^\bullet$). The second CoIn (CoIn_2) between the $\pi\sigma^*$ and the $\pi\pi^*$ state can be reached *via* a small barrier at a slightly larger $\text{C}_1\text{-Br}$ bond length and leads to heterolytic bond cleavage forming ion pairs ($\text{Ph}_2\text{CH}^+/\text{Br}^-$).

For both homologues, the location of CoIn_1 closer to the FC region than CoIn_2 makes it the decisive factor for the product splitting. Compared to the chlorine case, however, all significant points lie at larger $\text{C}_1\text{-Br}$ distance. This is expected since the bromine atom is larger than the chlorine atom. The main difference shows in the relative position of the CoIn s to the S_1 minimum leading to different barrier heights. Note that the

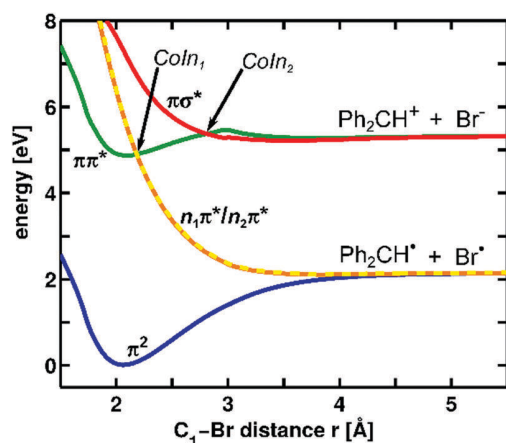


Fig. 4 Diabatic potential energy surfaces of the five lowest singlet states at the ONIOM(CAS(12,10):B3LYP) level of theory along the $\text{C}_1\text{-Br}$ bond length r with constant $d_{\text{py}} = 0.35$ Å. The d_{py} value is chosen to depict the FC point correctly. The reaction starts with an excitation from the ground state (π^2 , blue) to a $\pi\pi^*$ state (green). The $n_1\pi^*/n_2\pi^*$ (yellow/orange dashed) describe the homolytic bond cleavage channel and the $\pi\sigma^*$ state (red) describes the heterolytic bond cleavage channel. For better comparison, the PESs of Ph_2CHCl are shown in Fig. S7 (ESI†).

respective smallest barrier does not lie on the one-dimensional cut for $d_{\text{py}} = 0.35$ Å (Fig. 4). In the bromine case the two lone pair states cross the $\pi\pi^*$ state (CoIn_1) almost at the S_1 minimum resulting in a smaller barrier of only 0.04 eV compared to the barrier of 0.22 eV in the chlorine case. The same tendency is found for the relative position of CoIn_2 . Again the barrier is smaller in the bromine case (0.11 eV) compared to the chlorine case (0.32 eV).¹³ Especially the lower barrier towards CoIn_2 might explain the experimentally found increase in ion pair formation from 5% to 30%.^{11,14,15} We further investigated the influence of triplet states. The respective spin-orbit coupling becomes significant only for the homolytic channel after passing CoIn_1 (see ESI†). Thus intersystem crossing does not influence the dynamics. In contrast to the chlorine case, the S_1 minimum well extends significantly to smaller and larger d_{py} values (Fig. S2b, ESI†), with an ellipsoidal rather than a circular shape in the two-dimensional subspace. The special shape of the minimum well points to a higher coupling probability between the two reactive coordinates and results from a larger $\text{C}_1\text{-Br}$ distance allowing higher flexibility for the phenyl rings.

3.2 Quantum dynamics

The two-dimensional PESs for the five lowest diabatic states (π^2 , $\pi\pi^*$, $n_1\pi^*$, $n_2\pi^*$ and $\pi\sigma^*$) considered in the quantum dynamical simulation are shown in Fig. 5 along both reactive coordinates r and d_{py} . Both conical intersections form each a crossing seam in these two dimensions (Fig. S6, ESI†).

The propagation starts with the first vibrational eigenfunction of the ground state. The wave packet is excited *via* dipole-laser interaction from the ground state to the $\pi\pi^*$ state (Fig. 6, green curve). After successful excitation, the wave packet evolves in the $\pi\pi^*$ state. Population is transferred to the $n_1\pi^*$ and $n_2\pi^*$ states when the wave packet reaches CoIn_1 with a time delay of around 50 fs (orange curve) after excitation. CoIn_2 is reached later with a delay of about 110 fs but only marginal population left in the $\pi\pi^*$ state is transferred to the $\pi\sigma^*$ state (red curve). The homolytic bond cleavage clearly dominates the dissociation. To compare the delay times with the rise in the experimentally observable absorption signals, we must take into account that the products are not

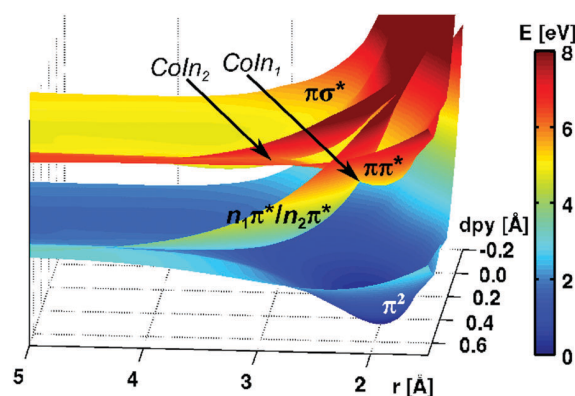


Fig. 5 Two-dimensional diabatic potential energy surfaces of the five lowest singlet states at the ONIOM(CAS(12,10):B3LYP) level of theory along the reactive coordinates r and d_{py} .

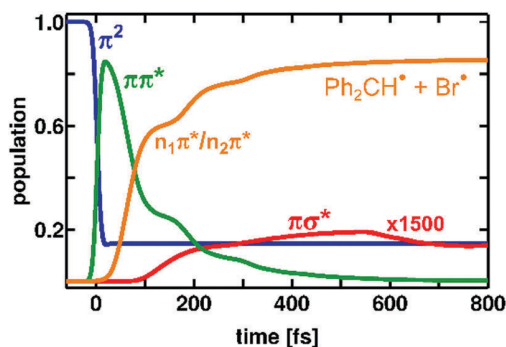


Fig. 6 Population as a function of time. The laser pulse has its maximum at $t = 0$ fs. As the laser pulse occurs, population is transferred from the π^2 state (blue) to the $\pi\pi^*$ state (green). The wave packet reaches CoIn_1 after around 50 fs as the population of the two lone pair states (orange) rises. CoIn_2 is reached later after around 120 fs but almost no population ($\sim 0.1 \times 10^{-3}$) is transferred to the $\pi\sigma^*$ state (red; curve enlarged by a factor of 1500). This means no ion pairs ($\text{Ph}_2\text{CH}^+/\text{Br}^-$) are built in this simulation. The population of the $n_1\pi^*$ and $n_2\pi^*$ states is summed because both lead to the same product.

instantaneously detectable as soon as the wave packet has passed the respective CoIn , but the $\text{C}_1\text{-Br}$ bond has to be broken. By comparing the orbital interaction¹² of the lone pair and the π orbital transforming to the C-Br σ bond, we obtained the threshold of $r = 3.1$ Å for nearly vanishing interaction with the leaving group. Accordingly, we define as the delay time, the point in time when more than 50% of the wave packet after excitation has passed this threshold in its corresponding electronic state. With this definition the delay time for the radical pairs is 110 fs and for the ion pairs 190 fs, which is in good agreement with the experimental results ($\text{Ph}_2\text{CH}^\bullet/\text{Br}^\bullet$: 100 fs; $\text{Ph}_2\text{CH}^+/\text{Br}^-$: 200 fs).^{14,15} For the product distribution, the experimental ratio of 70% radical pairs and 30% ion pairs^{14,15} is not reached, but we also found that the radical pairs are the dominant products. However, in our simulation almost no ion pairs are formed. This means the barrier to CoIn_2 might be overestimated at the ONIOM(CAS(12,10):B3LYP) level of theory in the reduced coordinate space. A correct description of the barrier may be obtained by introducing a third reactive coordinate. As a rather large simulation grid is used, the introduction of a further reactive coordinate is computationally demanding. Therefore, we slightly shifted the initial wave packet by $\Delta r = -0.13$ Å and $\Delta d_{\text{py}} = 0.04$ Å (Fig. S5, ESI†) to overcome the barrier. By this, the resulting product distribution changes to 85% radical pairs ($\text{Ph}_2\text{CH}^\bullet/\text{Br}^\bullet$) and 15% ion pairs ($\text{Ph}_2\text{CH}^+/\text{Br}^-$), which matches better the experimental results. After the laser excitation, the shifted wave packet oscillates more strongly in the $\pi\pi^*$ minimum. Especially the motion along the coordinate d_{py} is enhanced, which corresponds to an activation in this reactive mode. It points to the significance of this motion and related ones to effectively lower the barrier to CoIn_2 when all dimensions are included. With chlorine as the leaving group^{12,13} this was of no concern because the wave packet did not propagate in the direction of the reactive coordinate d_{py} .

In the following, the motion of the wave packet with the original, unmodified starting conditions is discussed for the

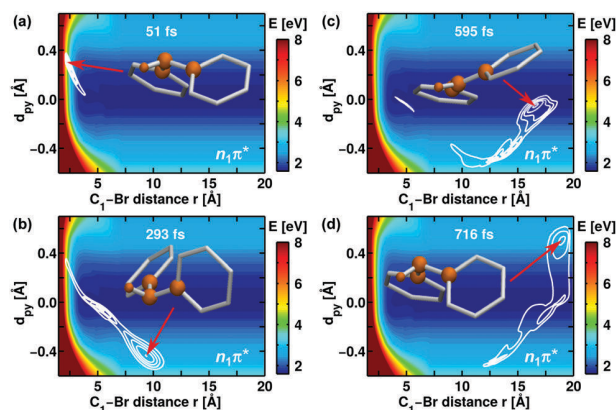


Fig. 7 Wave packet in the $n_1\pi^*$ state at different delay times. (a) The wave packet is transferred to the $n_1\pi^*$ state after around 51 fs. (b) There, it starts immediately leaving the FC region towards smaller d_{py} and larger r values. (c) The wave packet gets decelerated in negative d_{py} as the potential rises and moves back towards $d_{\text{py}} = 0.0$ Å. (d) The wave packet moves further to larger r and d_{py} values reaching the turning point at $d_{\text{py}} \approx 0.5$ Å. For a better overview only the geometry of the carbon backbone without the bromine atom and the hydrogen atoms of the phenyl rings is shown at the location of the maximum of the wave packet in each snapshot.

main product channel, the $n_1\pi^*$ state. Fig. 7 shows snapshots of the wave packet motion together with the geometry of the carbon backbone corresponding to the maximum of the wave packet. During dissociation the wave packet strongly oscillates along d_{py} . The first snapshot (Fig. 7a) shows the wave packet at its first appearance in the $n_1\pi^*$ state after 51 fs where the central carbon atom C_1 is still sp^3 hybridized. The wave packet propagates immediately towards smaller d_{py} and larger r values. At 293 fs (Fig. 7b) the maximum of the wave packet has passed $d_{\text{py}} = 0.0$ Å and has reached the turning point at negative d_{py} values. Now the sp^3 hybridization at the C_1 atom is inverted, after quickly passing the planar sp^2 hybridization. Furthermore, the $\text{C}_1\text{-Br}$ bond can be considered as broken as the wave packet is localized at $r > 3.1$ Å. After 595 fs (Fig. 7c) the wave packet returns to $d_{\text{py}} \approx 0.0$ Å to form again a sp^2 hybridized C_1 atom. The last snapshot at 716 fs (Fig. 7d) shows the wave packet close to the turning point for positive d_{py} values. At $d_{\text{py}} \approx 0.5$ Å the C_1 atom is back in the original sp^3 hybridization. In summary, the wave packet oscillates within the grid between $r = 1.5$ Å and $r = 20.0$ Å from $d_{\text{py}} = 0.0$ Å to $d_{\text{py}} = -0.5$ Å and back in around 500 fs propagation time.

3.3 Semi-classical dynamics

To include all degrees of freedom we performed a full dimensional semi-classical trajectory simulation based on the same electronic structure method. Overall, the 69 trajectories follow the same reaction paths and exhibit the same CoIns as in the quantum dynamics calculation. For the analysis, we separated the trajectories according to their finally populated product channel corresponding either to the radical or ion pair. For each channel, the adiabatic energy is averaged over all respective trajectories, which are 41 for the radical pair and 28 for the ion pair channel (Fig. 8). All states participating in the photoreaction are shown and the leading

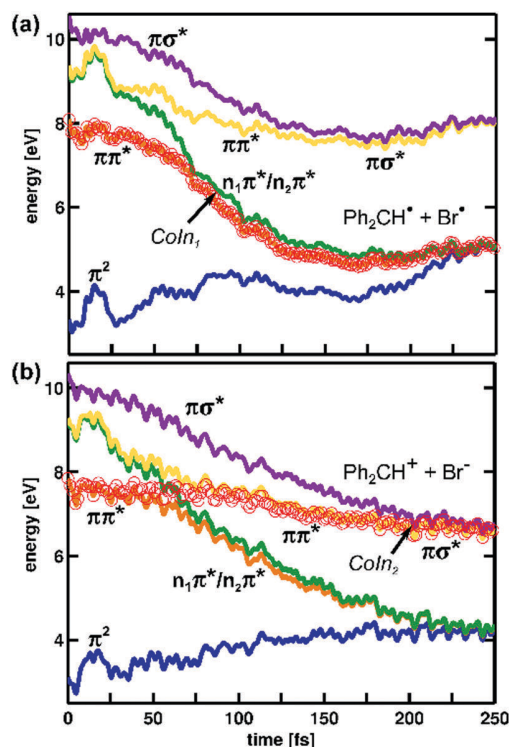


Fig. 8 Averaged adiabatic energies of the five lowest states along the trajectories leading to the homolytic bond cleavage channel (a) and leading to the heterolytic bond cleavage channel (b). The S_0 state is shown in blue, the S_1 in orange, the S_2 in green, the S_3 in yellow and the S_4 in violet. The respective electronic character is also indicated for clarity. The red circles mark the currently occupied state. All energy values are given in reference to the energy of the ground state minimum optimized at the ONIOM(CAS(12,10):HF) level of theory.

configurations are indicated. The currently populated state is marked with red circles. Fig. 8a shows the temporal evolution for the homolytic bond cleavage. The dynamics starts in the S_1 state (orange) which has $\pi\pi^*$ character in the FC region. The system reaches Coln_1 in a time window between 60 and 80 fs. Thereafter the trajectories follow the lone pair states $n_1\pi^*$ and $n_2\pi^*$ (green, orange) towards the lowest dissociation channel $\text{Ph}_2\text{CH}^\bullet + \text{Br}^\bullet$. Fig. 8b shows the temporal evolution of the heterolytic bond cleavage. The first conical intersection Coln_1 has been passed on the $\pi\pi^*$ state and the trajectories reach Coln_2 in a time window between 180 and 220 fs where the transition to the $\pi\sigma^*$ state takes place. This state correlates with the second dissociation channel $\text{Ph}_2\text{CH}^+ + \text{Br}^-$. The product ratio of about 60% homolytic bond cleavage to 40% heterolytic bond cleavage and the appearance time of the products are in good agreement with the experimental results.^{14,15} The good agreement for the product distribution supports our previous assumption in context with the results from quantum dynamics that additional degrees of freedom are important to reach the heterolytic bond cleavage.

3.4 Molecular motions promoting the reaction

Classical nuclear motion. To identify further important molecular degrees of freedom for the reaction we calculated a spectrogram for each product channel using the velocity

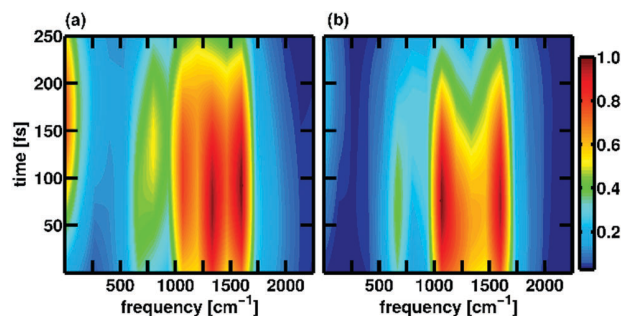


Fig. 9 Spectrogram in the range of 0 to 2500 cm^{-1} for (a) the trajectories leading to the homolytic bond cleavage channel and (b) the trajectories leading to the heterolytic bond cleavage channel. The intensity is normalized to the maximal peak intensity of each spectrogram. The complete spectrograms with the dominant, but non-specific C–H stretch vibrations are shown in Fig. S8 (ESI†).

autocorrelation function (VACF) derived from the semi-classical trajectories.^{38,39} Details of the calculation are explained in the ESI†. As expected C–H stretch vibrations are responsible for the broadest band around 3300 cm^{-1} (Fig. S8, ESI†). These are activated by the Wigner distribution and not specific to one of the product channels. More interesting is the range between 0 and 2500 cm^{-1} (Fig. 9). Both spectrograms show a strong band around 1600 cm^{-1} that can be attributed to normal modes mainly characterized by in-plane C–C–H bending vibrations at the phenyl rings. The weak band around 700 cm^{-1} can be attributed to normal modes mainly characterized by out of plane C–C–H bending vibrations at the phenyl rings. All assigned normal mode vectors are shown in Fig. S11 (ESI†). They are based on the frequency analysis used for the Wigner distribution. Significant differences between both channels are visible in the bands at 1300 cm^{-1} and 1100 cm^{-1} . While the higher frequency band is the strongest for the homolytic channel, it does not appear in the spectrogram of the heterolytic channel. The strongest band there is the lower frequency band that is only weak in the spectrogram of the homolytic channel. The band at 1300 cm^{-1} can be assigned to a normal mode mainly characterized by an asymmetric stretch motion at the carbon center C_1 . Its activation favors the homolytic bond cleavage. The band at 1100 cm^{-1} can be assigned to a normal mode mainly characterized by the pyramidalization at the carbon center C_1 . Its activation leads preferentially to the heterolytic bond cleavage. This finding is in good agreement with the quantum dynamical results discussed before, where an extra activation of the reactive coordinate d_{py} is needed to populate the heterolytic bond cleavage channel. The required activation can be interpreted as a cost for the reduced flexibility in the reactive coordinates compared to the full dimensions. The fast frequencies between 1000 cm^{-1} to 1600 cm^{-1} do not appear in the experiment. A reason might be that the time resolution of 50 fs^{14,15} is not sufficient to resolve those frequencies.

The oscillations observed in the experimental transient absorption signal^{14,15} appear most distinctly after 250 fs. To identify possible mechanisms behind this signature, the simulation time for the trajectories was elongated to the ps regime.

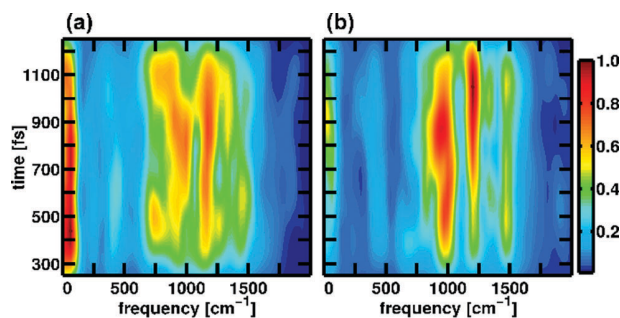


Fig. 10 Spectrogram in the range of 0 to 2000 cm^{-1} of (a) the $\text{Ph}_2\text{CH}^\bullet$ trajectories and (b) the Ph_2CH^+ trajectories. The intensity is normalized to the maximal peak intensity of each spectrogram. For the complete spectrograms, see Fig. S9 (ESI†).

For that, we discarded the bromine atom and continued the propagation for all trajectories after 250 fs where the $\text{C}_1\text{-Br}$ bond can be regarded as broken. Now the calculations can be performed at the B3LYP level of theory only considering the ground state of either $\text{Ph}_2\text{CH}^\bullet$ or Ph_2CH^+ . The corresponding spectrograms for the relevant bands up to 2000 cm^{-1} are shown in Fig. 10. The bands are slightly shifted compared to the short time spectrogram (Fig. 9), which reflects the change of computational method. Overall, both spectra are remarkable similar with a band around 50 cm^{-1} emerging stronger, especially for the homolytic channel. This band can be assigned to a normal mode mainly characterized by a butterfly-like motion of the phenyl rings (Fig. S12, ESI†). In the area of the experimentally reported vibrations at 300 cm^{-1} (110 fs) for $\text{Ph}_2\text{CH}^\bullet$ and 350 cm^{-1} (100 fs) for Ph_2CH^+ only very weak signatures occur. This unexpected finding needs further reflection, therefore the wave packet motion from the QD simulation has to be considered in more detail.

Wave packet motion. The discrepancy between the outcome of the VACF for the trajectory calculations and the experimental signature may be attributed to the presence of an observation window in the experiment. Thus, we adapt the experimental observation window and apply it for the analysis of the wave packet dynamics in the $n_1\pi^*$ state. The observation window is defined as a restricted area on our grid, which reflects the geometric structures for which the experimental signal becomes maximal. $\text{Ph}_2\text{CH}^\bullet$ has the highest absorption when the carbon center is sp^2 hybridized ($d_{\text{py}} = 0.0 \text{ \AA}$).¹² Therefore, the wave packet's motion is visualized by its integral $F(t)$ evaluated at every time step within the restricted area in the $n_1\pi^*$ state (for details see ESI†). These results show pronounced oscillations (Fig. 11b) with strong recurrences with a period of 500 fs and recurrences of decreasing amplitudes with a period of 120 fs.

The slow oscillation can be assigned to the motion of the wave packet's main part in the $n_1\pi^*$ state (see Fig. 7). The fast oscillations are induced by the motion of the wave packet in the $\pi\pi^*$ minimum leading to a stepwise depopulation through CoIn_1 (Fig. 6). To support this statement a second observation window is set along the CoIn_1 seam in the $\pi\pi^*$ state recording the fast oscillations in the S_1 minimum (Fig. 11a). The decrease

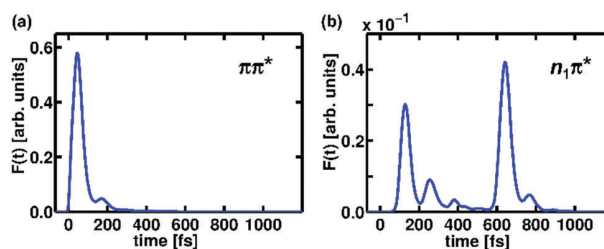


Fig. 11 Time-dependent evaluation of the wave packet's motion as its integral $F(t)$ in the defined restricted area (a) along the CoIn_1 seam in the $\pi\pi^*$ state and (b) along the coordinate r with constant $d_{\text{py}} = 0.0 \text{ \AA}$ in the $n_1\pi^*$ state (for details see ESI†).

in amplitude directly reflects the depopulation of the $\text{S}_1 \pi\pi^*$ state. Their frequency of 280 cm^{-1} matches the experimentally reported frequency of 300 cm^{-1} for $\text{Ph}_2\text{CH}^\bullet$.^{14,15} However, in this area only weak bands occur in the spectrogram (Fig. 10) evaluated from the VACF, so we assume that the measured oscillation contains contributions from several normal modes. These modes are activated during the dissociation reaction and are triggered by the planarization motion of the central carbon atom C_1 .

The slow oscillations cannot be distinguished in the experiment because they have the fast oscillations (Fig. 11b) superimposed on them. To find their corresponding frequencies in the spectrogram we have to take into account that the detection window only records their half cycle. The full period, thus, corresponds to 1000 fs, which means a frequency of 33 cm^{-1} . This frequency is comparable to the band at 50 cm^{-1} in the spectrogram. The difference can be attributed to the reduced coordinate space optimized for the fast part of the dissociation reaction from the FC region through the CoIns . After the bond cleavage, motions of and within the phenyl rings are activated in the full dimensional trajectories. In the QD simulation only the relative motion of the phenyl rings is indirectly considered. The more pronounced amplitude oscillations in the temporal signal of the QD simulation compared to the experimental signal can be explained by the reduced coordinate space, as well. Here, no competing pathways enhance the background signal. The discussed wave packet motion does not occur for chlorine as the leaving group.^{8–12} The differences in the shape of the potential, especially in the FC region, as well as in the mass of the halogen atoms are decisive for this effect. With respect to the experimental observation window, the semi-classical calculations recover only the slow reactive motion of the pyramidalization but not the fast one showing as a frequency of 300 cm^{-1} extracted from the pump-probe experiment. This frequency is attributed to the excited state wavepacket motion crossing the barrier close to the FC-region and can be regarded as a pure quantum effect which cannot be recovered in the semi-classical trajectory calculations.

4 Conclusions

The photodissociation of $\text{Ph}_2\text{CH-Br}$ was studied with quantum chemical, quantum dynamical and semi-classical dynamical methods. Using an effective ONIOM partitioning of the system

and thus reducing the computational effort, we were able to come up with a balanced description of the PESs. Hereby, CAS(12,10) was used as a high-level method. Both in our quantum chemical and semi-classical simulations we could successfully accomplish the passing through two consecutive CoIns. We were able to describe the product splitting into the homolytic and the heterolytic reaction path and explain the different delay times for both product channels as reported in the experiment.^{14,15} In our two-dimensional quantum dynamical simulation, we were able to rely on the framework of specially adapted reactive coordinates. However, it was necessary to further trigger a vibrational mode related to the pyramidalization of the central carbon atom C₁ to enhance the amount of ion pair formation to approach the experimental findings. In the simulated spectra of the full-dimensional semi-classical trajectories, the band of a corresponding mode was a significant indicator for heterolytic dissociation. Therefore, with both our simulations, we could clearly demonstrate the considerable impact of such a mode for the activation of the ion pair channel. The importance of the pyramidalization in general for the dissociation reaction is a huge difference compared to Ph₂CH-Cl where the dynamics in this coordinate is very limited. In Ph₂CH-Br activation of this coordinate explains the difference in the ratio between the homolytic and the heterolytic product channel and leads to a wave packet oscillation accompanying the bond cleavage process observable in the experimental transient absorption signal. Overall, in this work we explained the microscopic details of the photodissociation mechanism of Ph₂CH-Br and successfully pointed out the similarities and contrasts of the photo-induced dissociation reaction of Ph₂CH-Br compared to the case with chlorine as the leaving group.

Conflicts of interest

There are no conflicts of interest to declare.

Acknowledgements

Financial support of this work from the Deutsche Forschungsgemeinschaft through the SFB749 and the excellence cluster 'Munich-Centre for Advanced Photonics' (MAP) is gratefully acknowledged. We thank Chaochen Lu for his contributions to the first calculations.

References

- 1 D. Ravelli, S. Protti and M. Fagnoni, *Chem. Rev.*, 2016, **116**, 9850–9913.
- 2 R. R. Naredla and D. A. Klumpp, *Chem. Rev.*, 2013, **113**, 6905–6948.
- 3 H. Mayr, *Tetrahedron*, 2015, **71**, 5095–5111.
- 4 H. Mayr, J. Ammer, M. Baidya, B. Maji, T. A. Nigst, A. R. Ofial and T. Singer, *J. Am. Chem. Soc.*, 2015, **137**, 2580–2599.
- 5 P. K. Das, *Chem. Rev.*, 1993, **93**, 119–144.
- 6 R. A. McClelland, *Tetrahedron*, 1996, **52**, 6823–6858.
- 7 J. Ammer and H. Mayr, *J. Phys. Org. Chem.*, 2013, **26**, 956–969.
- 8 J. Bartl, S. Steenken, H. Mayr and R. A. McClelland, *J. Am. Chem. Soc.*, 1990, **112**, 6918–6928.
- 9 M. Lipson, A. A. Deniz and K. S. Peters, *Chem. Phys. Lett.*, 1998, **288**, 781–784.
- 10 C. F. Sailer, S. Thallmair, B. P. Fingerhut, C. Nolte, J. Ammer, H. Mayr, I. Pugliesi, R. de Vivie-Riedle and E. Riedle, *Chem-PhysChem*, 2013, **14**, 1423–1437.
- 11 C. F. Sailer, N. Krebs, B. P. Fingerhut, R. de Vivie-Riedle and E. Riedle, *EPJ Web Conf.*, 2013, **41**, 05042.
- 12 E. Riedle, M. K. Roos, S. Thallmair, C. F. Sailer, N. Krebs, B. P. Fingerhut and R. de Vivie-Riedle, *Chem. Phys. Lett.*, 2017, **683**, 128–134.
- 13 S. Thallmair, M. K. Roos and R. de Vivie-Riedle, *Struct. Dyn.*, 2016, **3**, 043205.
- 14 E. Riedle, M. Bradler, M. Wenninger, C. F. Sailer and I. Pugliesi, *Faraday Discuss.*, 2013, **163**, 139.
- 15 C. F. Sailer and E. Riedle, *Pure Appl. Chem.*, 2013, **85**.
- 16 B. Podolsky, *Phys. Rev.*, 1928, **32**, 812–816.
- 17 J. E. B. Wilson, J. C. Decius and P. C. Cross, *Molecular Vibrations: The Theory of Infrared and Raman Vibrational Spectra*, Dover Publ., 1980.
- 18 L. J. Schaad and J. Hu, *J. Mol. Struct. THEOCHEM*, 1989, **185**, 203–215.
- 19 S. Thallmair, M. K. Roos and R. de Vivie-Riedle, *J. Chem. Phys.*, 2016, **144**, 234104.
- 20 J. C. Tully, *J. Chem. Phys.*, 1990, **93**, 1061.
- 21 M. Svensson, S. Humbel, R. D. J. Froese, T. Matsubara, S. Sieber and K. Morokuma, *J. Phys. Chem.*, 1996, **100**, 19357–19363.
- 22 L. W. Chung, W. M. C. Sameera, R. Ramozzi, A. J. Page, M. Hatanaka, G. P. Petrova, T. V. Harris, X. Li, Z. Ke, F. Liu, H.-B. Li, L. Ding and K. Morokuma, *Chem. Rev.*, 2015, **115**, 5678–5796.
- 23 B. P. Fingerhut, S. Oesterling, K. Haiser, K. Heil, A. Glas, W. J. Schreier, W. Zinth, T. Carell and R. de Vivie-Riedle, *J. Chem. Phys.*, 2012, **136**, 204307.
- 24 B. P. Fingerhut, D. Geppert and R. de Vivie-Riedle, *Chem. Phys.*, 2008, **343**, 329–339.
- 25 H. J. Werner, P. J. Knowles, G. Knizia, F. R. Manby, M. Schütz, P. Celani, T. Korona, R. Lindh, A. Mitrushenkov, G. Rauhut, K. R. Shamasundar, T. B. Adler, R. D. Amos, A. Bernhardsson, A. Berning, D. L. Cooper, M. J. O. Deegan, A. J. Dobbyn, F. Eckert, E. Goll, C. Hampel, A. Hesselmann, G. Hetzer, T. Hrenar, G. Jansen, C. Köppl, Y. Liu, A. W. Lloyd, R. A. Mata, A. J. May, S. J. McNicholas, W. Meyer, M. E. Mura, A. Nicklass, D. P. O'Neill, P. Palmieri, D. Peng, K. Pflüger, R. Pitzer, M. Reiher, T. Shiozaki, H. Stoll, A. J. Stone, R. Tarroni, T. Thorsteinsson and M. Wang, *MOLPRO, version 2012.1, a package of ab initio programs*, 2012, see www.molpro.net.
- 26 H.-J. Werner, P. J. Knowles, G. Knizia, F. R. Manby and M. Schütz, *WIREs Comput. Mol. Sci.*, 2012, **2**, 242–253.
- 27 M. J. Bearpark, S. M. Larkin and T. Vreven, *J. Phys. Chem. A*, 2008, **112**, 7286–7295.
- 28 M. J. Frisch, G. W. Trucks, H. B. Schlegel, G. E. Scuseria, M. A. Robb, J. R. Cheeseman, G. Scalmani, V. Barone,

- B. Mennucci, G. A. Petersson, H. Nakatsuji, M. Caricato, X. Li, H. P. Hratchian, A. F. Izmaylov, J. Bloino, G. Zheng, J. L. Sonnenberg, M. Hada, M. Ehara, K. Toyota, R. Fukuda, J. Hasegawa, M. Ishida, T. Nakajima, Y. Honda, O. Kitao, H. Nakai, T. Vreven, J. J. A. Montgomery, J. E. Peralta, F. Ogliaro, M. Bearpark, J. J. Heyd, E. Brothers, K. N. Kudin, V. N. Staroverov, R. Kobayashi, J. Normand, K. Raghavachari, A. Rendell, J. C. Burant, S. S. Iyengar, J. Tomasi, M. Cossi, N. Rega, J. M. Millam, M. Klene, J. E. Knox, J. B. Cross, V. Bakken, C. Adamo, J. Jaramillo, R. Gomperts, R. E. Stratmann, O. Yazyev, A. J. Austin, R. Cammi, C. Pomelli, J. W. Ochterski, R. L. Martin, K. Morokuma, V. G. Zakrzewski, G. A. Voth, P. Salvador, J. J. Dannenberg, S. Dapprich, A. D. Daniels, Ö. Farkas, J. B. Foresman, J. V. Ortiz, J. Cioslowski and D. J. Fox, *Gaussian 09, Revision D.01*, Gaussian, Inc., Wallingford, CT, 2009.
- 29 H. Lischka, R. Shepard, I. Shavitt, R. M. Pitzer, M. Dallos, T. Müller, P. G. Szalay, F. B. Brown, R. Ahlrichs, H. J. Böhm, A. Chang, D. C. Comeau, R. Gdanitz, H. Dachsel, C. Ehrhardt, M. Ernzerhof, P. Höchtl, S. Irle, G. Kedziora, T. Kovar, V. Parasuk, M. J. M. Pepper, P. Scharf, H. Schiffer, M. Schindler, M. Schüler, M. Seth, E. A. Stahlberg, J.-G. Zhao, S. Yabushita, Z. Zhang, M. Barbatti, S. Matsika, M. Schuurmann, D. R. Yarkony, S. R. Brozell, E. V. Beck, J.-P. Blaudeau, M. Ruckebauer, B. Sellner, F. Plasser and J. J. Szymczak, *COLUMBUS, an ab initio electronic structure program, release 7.0*, 2015.
- 30 H. Lischka, T. Müller, P. G. Szalay, I. Shavitt, R. M. Pitzer and R. Shepard, *WIREs Comput. Mol. Sci.*, 2011, **1**, 191–199.
- 31 H. Lischka, R. Shepard, R. M. Pitzer, I. Shavitt, M. Dallos, T. Müller, P. G. Szalay, M. Seth, G. S. Kedziora, S. Yabushita and Z. Zhang, *Phys. Chem. Chem. Phys.*, 2001, **3**, 664–673.
- 32 S. Matsika and D. R. Yarkony, *J. Chem. Phys.*, 2002, **117**, 6907–6910.
- 33 H. Tal-Ezer and R. Kosloff, *J. Chem. Phys.*, 1984, **81**, 3967.
- 34 M. Barbatti, G. Granucci, M. Ruckebauer, F. Plasser, R. Crespo-Otero, J. Pittner, M. Persico and H. Lischka, *NEWXTON-X: a package for Newtonian dynamics close to the crossing seam, version 1.4*, 2014, see www.newtonx.org.
- 35 M. Barbatti, M. Ruckebauer, F. Plasser, J. Pittner, G. Granucci, M. Persico and H. Lischka, *WIREs Comput. Mol. Sci.*, 2013, **4**, 26–33.
- 36 M. Barbatti, A. J. A. Aquino and H. Lischka, *Phys. Chem. Chem. Phys.*, 2010, **12**, 4959.
- 37 R. Crespo-Otero and M. Barbatti, *Chem. Rev.*, 2018, **118**, 7026–7068.
- 38 M. Tamaoki, Y. Yamauchi and H. Nakai, *J. Comput. Chem.*, 2005, **26**, 436–442.
- 39 B. P. Fingerhut, PhD thesis, Ludwigs-Maximilians-Universität, 2010.

CONTROL IN THE VICINITY OF A CONICAL
INTERSECTION

In the previous chapter the role of CoIns for ultrafast reactions was pointed out and also its function as branching point for competing reaction pathways. The next chapter highlights possible control scenarios at CoIns.

Controlling the outcome of chemical reactions is a main goal of chemistry. Commonly this is achieved by varying external parameters as temperature, concentration and solvent or by addition of a catalyst. A further possibility is to control a reaction with light in the form of short laser pulses in the femtosecond regime that can be modulated to achieve coherent interaction with the system [52–54]. Optimal control theory allows to optimize the shape of the laser pulse according to a selected goal, for example the maximal population in a given target state [114–116]. For the nucleobase uracil, for example, which exhibits a double-well potential two pulses were optimized, one trapping the wavepacket in the minimum of the surface and the other accelerating the wavepacket towards the CoIn of the surface [116]. Further, the potential energy surface (PES) can be deformed with strong field laser pulses via the Stark shift [55, 56] to build light-induced conical intersections [57–59]. With this method the absence of a CoIn in a system, as for example in a two-atomic system with an avoided-crossing, is omitted [59]. Likewise, PES can be manipulated by strong coupling to a cavity combined with activation of cavity modes by a laser pulse to induce CoIns [117, 118].

The here used control scheme directly affects the system in the vicinity of the CoIn by forming a superposition between the intersecting states with a short carrier-envelope phase (CEP) stable few cycle laser pulse (fig. 3.1). The CEP defines the phase shift within the envelope function (black line fig. 3.1) determining the waveform of the laser pulse. The phase-dependency of the superposition is defined by this waveform which strongly varies due to the few cycles. The integrity of this scheme has been shown previously, both in theory and experiment [60, 61].

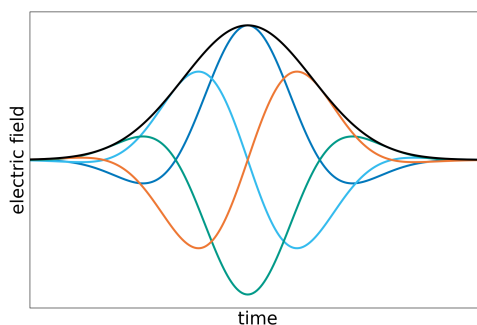


Figure 3.1: Few-cycle laser pulse with varied carrier-envelope phase. The black line shows the envelope function of the laser pulse.

Beside the CEP four more parameters (FWHM, E_{max} , t_0 , ω_0) define the laser pulse which can be expressed as

$$E(t) = E_{max} \cdot e^{-2(\frac{t-t_0}{\sigma})^2} \cdot \cos(\omega_0(t-t_0) + \phi), \quad (3.1)$$

with $\sigma = \text{FWHM}/\sqrt{2\log(2)}$. These parameters are varied in combination with the CEP ϕ and the influence on the control mechanism is investigated. The time-dependent CEP efficiency $\Gamma(t)$ is introduced as quantity of the control effect. It is defined as the difference between the phase-dependent minimal ($a_{min}(t, \phi)$) and maximal ($a_{max}(t, \phi)$) population transfer.

$$\Gamma(t) = a_{max}(t, \phi) - a_{min}(t, \phi) \quad (3.2)$$

The influence of the four parameters on the waveform of the laser pulse is visualized in fig. 3.2. The full-width-half-maximum (FWHM) defines the width of the laser pulse in time and affects the duration of the local deformation of the PES which can lead to an independent population transfer between the states apart from the actual CoIn if the laser pulse is long enough. A change in the maximal electric field strength E_{max} leads to a stronger (or weaker) laser pulse defining the extent of the deformation of the PES which can form light-induced CoIns [57, 59]. The further two parameters, the timing t_0 and the central frequency ω_0 are strongly connected. The laser pulse with the strongest effect is obtained when the frequency ω_0 is aligned to the local energy difference ΔE of the interacting states at time t_0 . In the CEP control scheme, the few-cycle pulse is applied at the time when the wave packet has almost reached the CoIn where $\Delta E = 0$. So when the timing of the laser pulse is optimal and a low central frequency is used forming a 1 – 2 cycle pulse the effect of the CEP control scheme is best.

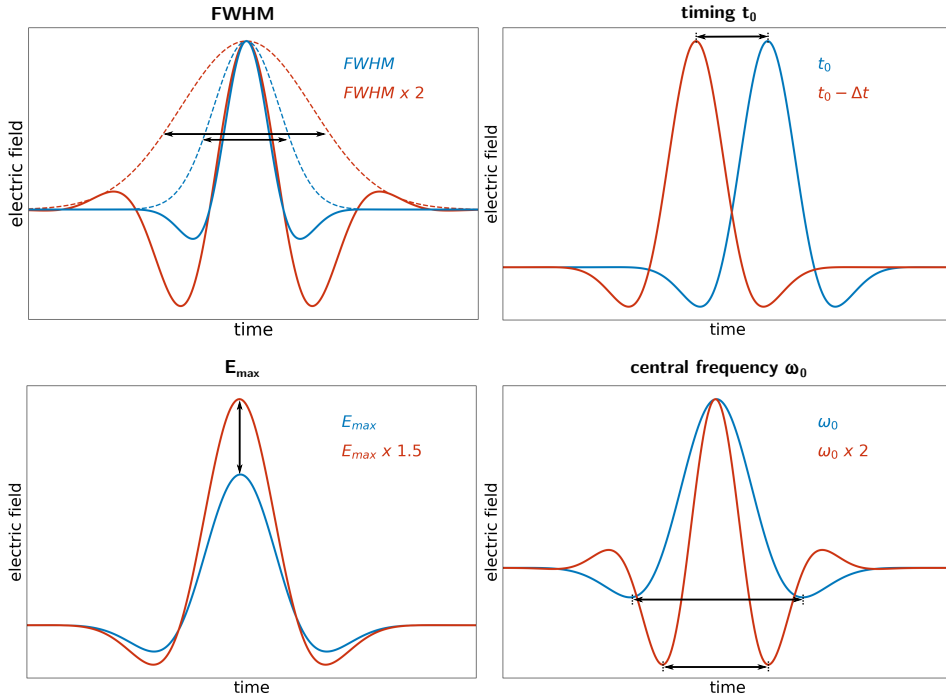


Figure 3.2: Influence of the modification of different pulse parameters (FWHM, E_{max} , t_0 , ω_0) on the electric field of the laser pulse. The black arrows highlight the difference between the original laser pulse (blue line) and the modified laser pulse (red line). The dashed lines show the envelope function of the laser pulse.

In summary, the parameters, FWHM and E_{max} , determine the observable control mechanism. A large field strength and a long duration of the laser pulse lead to the so-called field-only mechanism where the control is only based upon the interaction of

the laser pulse to the system without impact of the CoIn. In contrast, when a low field strength and a short laser pulse is used, the effect of the parameters t_0 and ω_0 appears. These define the amount of possible control in the control scheme purely determined by the interaction between the superposition induced by the CEP and the geometric phase induced by the CoIn. It is called the interference mechanism.

The key points of article “Waveform control of molecular dynamics close to a conical intersection” are:

- The population transfer through a CoIn is controlled by the waveform of a CEP stabilized pulse. The control mechanism is investigated for an analytic model system describing a dissociation and the S_2/S_1 CoIn of the nucleobase uracil.
- The CEP pulse is assumed to be optimally aligned to the molecule. Beside the CEP the laser pulse is varied in the maximal electric field strength (E_{max}), the full-width-half-maximum (FWHM), the central frequency (ω_0) and the timing (t_0). The phase-dependent control efficiency is analyzed according to the change of single parameters and their connection.
- The general features of a possible control are identified via the model system. The interplay between the shape of the transition dipole moment (TDM) and of the non-adiabatic couplings (NACs) is essential. Analysis of different combinations of TDMs and NAC revealed that both have to show the same nodal plane at the CoIn parallel to the wavepacket’s motion towards the CoIn. For a realistic system this means that the direction of motion of the wavepacket is decisive for the possible control efficiency.
- The optimal timing t_0 of the laser pulse is evaluated according to the time window of the wavepacket being located at the CoIn in connection with the optimal central frequency ω_0 . While the CEP efficiency is less sensitive to t_0 of the laser pulse as the wavepacket remains in the vicinity of the CoIn for some time it strongly depends on ω_0 that has to be adjusted to the actual energy gap at time t_0 . The tolerance in the width of the pulse on $\Gamma(t)$ is analyzed and found to be large enough to facilitate possible experimental applications of the investigated control scheme.
- A phase-dependent superposition between the intersecting states is formed in the vicinity of the CoIn due to the pulse interaction. The interference between the phase of the generated superposition and the geometric phase induced by the CoIn is decisive for the control mechanism. With the pure interference mechanism, a phase-dependent population transfer with a periodicity of 2π is obtained. The asymmetric waveform of a few-cycle pulse relevant with a large electric field strength (E_{max}) also induces a CEP dependent population transfer without further interaction. The field-only mechanism shows a periodicity of π . The total CEP efficiency is determined by the interference between both mechanisms.
- The situation of the nucleobase uracil varies in several points compared to the idealistic model system. Uracil is a system with two coupled bounded states with a CoIn seam and a very local TDM along this seam. The wavepacket passes the CoIn several times which leads to a strong time-dependent CEP efficiency that is not converging to a constant value but is still visible after a few cycles. Due to the structure of the CoIn seam the direction of the wavepacket towards the CoIn directly affects $\Gamma(t)$. Therefore, two different starting conditions are chosen. The first (*uracil A*) begins on the S_2 surface at the FC point leading to a delocalized wavepacket at the CoIn and the second (*uracil B*) starts with a shifted gaussian shaped wavepacket leading to a more localized wavepacket passing the CoIn seam.
- The underlying control mechanisms of both cases is analyzed. In *uracil A* the field-only mechanism dominates over the total simulation time. In *uracil B*, in

contrast, both mechanisms are available. The interference mechanism is decisive, when a low electric field strength is used, just like shown for the model system. With large E_{max} the field-only mechanism becomes dominant and the combined mechanism shows a similar behavior as for the model system.

- It is shown that in the non-ideally system uracil the CEP control scheme can be applied successfully, but the pathway towards the CoIn is crucial for the efficiency and the underlying control mechanism.

Hereafter, the article “Waveform control of molecular dynamics close to a conical intersection” published in *The Journal of Chemical Physics* is reprinted from *J. Chem. Phys.*, **153**, 224307 (2020) with the permission of AIP Publishing.

Waveform control of molecular dynamics close to a conical intersection

Cite as: J. Chem. Phys. 153, 224307 (2020); doi: 10.1063/5.0031398

Submitted: 30 September 2020 • Accepted: 24 November 2020 •

Published Online: 14 December 2020



Franziska Schüppel, Thomas Schnappinger, Lena Bäuml, and Regina de Vivie-Riedle^{a)}

AFFILIATIONS

Department of Chemistry, LMU Munich, D-81377 Munich, Germany

^{a)} Author to whom correspondence should be addressed: Regina.de_Vivie@cup.uni-muenchen.de

ABSTRACT

Conical intersections are ubiquitous in chemical systems but, nevertheless, extraordinary points on the molecular potential energy landscape. They provide ultra-fast radiationless relaxation channels, their topography influences the product branching, and they equalize the timescales of the electron and nuclear dynamics. These properties reveal optical control possibilities in the few femtosecond regime. In this theoretical study, we aim to explore control options that rely on the carrier envelope phase of a few-cycle IR pulse. The laser interaction creates an electronic superposition just before the wave packet reaches the conical intersection. The imprinted phase information is varied by the carrier envelope phase to influence the branching ratio after the conical intersection. We test and analyze this scenario in detail for a model system and show to what extent it is possible to transfer this type of control to a realistic system like uracil.

Published under license by AIP Publishing. <https://doi.org/10.1063/5.0031398>

I. INTRODUCTION

Non-adiabatic effects are well-known to influence the dynamics of the photo-relaxation and photo-reaction of molecular systems. These effects are especially pronounced in the vicinity of a conical intersection (CoIn), where the adiabatic separation between nuclear and electronic motion breaks down^{1–3} and the electronic states involved become degenerate. CoIn's open up funnels for radiationless electronic transitions, whose efficiency and branching relation is determined by the shape and size of the non-adiabatic coupling elements (NACs) and the topography in the vicinity. They play a central role in many chemical and biological processes, such as retinal isomerization in vision,^{4,5} DNA photo-protection mechanisms,^{6–9} molecular photo-switches,^{10–12} and molecular motors.^{13–15} As in the entire field of chemistry, the major goal in photo-chemistry is to control the outcome of a reaction. Classical control agents used in chemical synthesis are temperature, solvents, catalysts, pressure, or concentration. Another avenue to obtain control in photo-chemical reactions is to guide the underlying molecular dynamics with specifically designed laser pulses.^{16–18} For this purpose, laser parameters such as the frequency, the phase, and polarization can be optimized. In addition, the waveform of a carrier envelope phase (CEP) stabilized few-cycle laser pulse can be used as a control

parameter. These few-cycle laser pulses can be described via an envelope function $E_0(t)$, the central carrier frequency ω_0 , and a carrier envelope phase ϕ (CEP). This CEP offers the possibility to steer electrons and nuclei.^{19–23} The steering relies on a superposition of two or more electronic or vibrational states with a well-defined phase relationship.

In our theoretical study, we take advantage of the fact that the electron dynamics slows down in the vicinity of CoIn's and approaches the timescale of the nuclear dynamics. For control, we apply a few-cycle IR laser pulse when the system's dynamics approaches a CoIn. The CEP pulse builds up a superposition of the electronic states forming the CoIn, with its phase relationship depending on the CEP. Since this occurs near a CoIn, also a non-trivial phase (called the geometric or Pancharatnam–Berry phase) is introduced.^{1,2,24,25} These two phase terms now lead to an interference process when the CoIn is passed. The interference (constructive or destructive) can be changed by varying the CEP. This process modulates the population transfer via the CoIn toward competing channels. The control of the coupled electron–nuclear dynamics at a CoIn with a laser field is a rich and active field of research, and there are a variety of laser control schemes present in the literature. Both in the experiment and theory, optimal control theory^{26–29} was applied to guide the dynamics of a molecular system via a CoIn toward a

desired target state with shaped laser pulses. Another possibility to obtain control is to modify the potential energy surfaces (PESs) and, thus, the CoIn itself via the Stark shift.^{30,31} The high pulse intensities used in this methodology can create new light-induced CoIn's.^{32–34} The main difference of our applied CEP-control-scheme^{17,35,36} compared to the two mentioned methods is that the control laser is very short and only interacts with the molecular system shortly before the CoIn is reached. The goal is not to control or change the pathway toward the CoIn but to manipulate the phase relationship in the system^{17,35,36} during the transfer.

After introducing the realization of the CEP-control-scheme in our simulations, we want to ascertain to what extent this IR control scheme is possible and determine its boundary conditions. For this, we consider a two-dimensional analytical model system, which is composed of three states. Two of them are connected via a CoIn in a dissociation process. The CEP-control-scheme is applied to modify the ratio between the two competing channels. Since we work with a model, it is possible to change the size and shape of the NACs and the transition dipole moment (TDM) and, thus, to evaluate the necessary molecular conditions for a CEP control. Besides the molecular properties, also the parameters of the few-cycle laser pulse (such as the frequency, the timing, and the strength of the electric field) influence the efficiency of the CEP-control-scheme and have to be optimized. Through a detailed analysis of the CEP dependent population, it is possible to distinguish between the interference process and a process solely due to the component light. Besides the analytic model system, we apply the CEP-control-scheme to a photo-physical active molecule. As an example, we have chosen the nucleobase uracil, where a CoIn enables an ultra-fast few hundred femtosecond relaxation mechanism that prevents harmful chemical modification.^{37,38} In previous studies,^{8,9} we demonstrated that the S_2 – S_1 relaxation dynamics can be accelerated and decelerated by light control. Here, we focus on the control possibilities at the CoIn. The relaxation process occurs step-wise including forth and back crossing through the CoIn, which results in a quite complex situation regarding the geometric phase. Besides this, the TDM between the relevant states is rather weak and localized. Therefore, uracil is a quite challenging system for the CEP-control-scheme.

II. LIGHT-MATTER INTERACTION AND THE CEP EFFICIENCY

Our goal is to influence the population transfer through a CoIn with the waveform of a CEP stabilized few-cycle pulse in the IR and to quantify the controllability. The dynamics of the model system and uracil is simulated on coupled adiabatic PESs (V_{S1} and V_{S2}) by solving the time-dependent Schrödinger equation

$$i\hbar \frac{\partial}{\partial t} \Psi = \hat{H} \Psi, \quad (1)$$

with

$$\hat{H} \Psi = \begin{pmatrix} \hat{T} + V_{S1} & \tau_{12} - \mu_{12} \varepsilon(t) \\ \tau_{12} - \mu_{12} \varepsilon(t) & \hat{T} + V_{S2} \end{pmatrix} \begin{pmatrix} \Psi_1 \\ \Psi_2 \end{pmatrix}. \quad (2)$$

The used Hamiltonian includes the NACs τ_{12} and the transition dipole moments μ_{12} between the first two excited states. This means the light-matter interaction is treated within the dipole approximation and effects such as the Stark shift are taken into account in the dipole-limit.³⁰ For more details, see Sec. I of the [supplementary material](#). The few-cycle pulse has a Gaussian shape and is defined as

$$E(t) = E_{\max} \cdot e^{-2\left(\frac{t-t_0}{\sigma}\right)^2} \cdot \cos(\omega_0(t-t_0) + \phi), \quad (3)$$

with $\sigma = \frac{\text{FWHM}}{\sqrt{2 \log(2)}}$.

We assume an optimal alignment of the transition dipole moment and the electric component of the pulse. There are methods described in the literature,^{39–41} which would, in principle, allow for such an alignment of the molecular system. With the assumed optimal alignment, the maximal possible effect of the CEP-control-scheme for a given laser pulse is determined. Except for the orientation of the electric field, all other laser pulse parameters remain open for optimization to realize a CEP control. Besides the CEP ϕ itself, these are the electric field strength E_{\max} , the central frequency ω_0 , the full width half maximum (FWHM), and the timing of the few-cycle pulse. Time zero t_0 of the pulse, defining the position of the maximum, is selected to match the time when the wave packet approaches the vicinity of the CoIn. The frequency and the time are related to the topography of the CoIn, and the electric field interacts with the TDM of the system. Beyond these parameters, the direct influence of the NACs and the TDM as well as their interplay can be tested in the model system, whereas, for uracil, these values are fixed quantities. The main observable is the time-dependent and phase-dependent population $a(t, \phi)$ of a given target state. As a figure of merit of how efficient the CEP control is, we define the quantity $\Gamma(t)$. The CEP efficiency $\Gamma(t)$ is calculated as the difference of the maximum and the minimum population $a(t, \phi)$ for each time step.

$$\Gamma(t) = \max(a(t, \phi)) - \min(a(t, \phi')). \quad (4)$$

For its maximum value, the population of the target state shows the highest CEP dependence and, consequently, the highest degree of controllability. In a sense, $\Gamma(t)$ is comparable to the asymmetry parameter used in electron recollision and attosecond photoionization experiments.^{23,42–45} Since our model system describes a dissociation process, the wave packet reaches the CoIn region only once and $\Gamma(t)$ remains constant after this event. In this case, we can take this constant value to quantify the controllability of the system for a given laser pulse. It is maximized by varying the parameters relevant to the light-molecule interaction. In cases of non-radiative relaxation without dissociation, the wave packet may cross the CoIn multiple times and $\Gamma(t)$ will not become constant as long as there is an exchange of population between the states. This situation will be discussed for our second example, the nucleobase uracil. In these cases, we aim for a maximum value of $\Gamma(t)$ after the laser pulse.

III. MODEL SYSTEM

The two-dimensional analytical model system is selected as an ideal test system for CEP control at a CoIn. It describes a dissociation process after photo-excitation with two competing pathways. The basic model⁴⁶ is introduced in the diabatic representation and consists of three diabatic electronic states and the corresponding coupling element. Their analytic form can be found in the [supplementary material](#) [Eq. (S3)] together with the relevant parameters in Table S1]. The interference process of the CEP-control-scheme depends on the fact that the wave packet acquires a nontrivial geometric phase when approaching a CoIn. To ensure the correct description, we work in the adiabatic representation. Therefore, we transform from the diabatic to the adiabatic picture. The resulting adiabatic potential energy surfaces (PESs) are shown as a one-dimensional cut along the dissociation coordinate (x -coordinate) together with the CoIn in Fig. 1(a). The transformation depends

on the adiabatic–diabatic transformation angle,^{1,2,47} which is characterized by a phase jump. Either the signed or the absolute value of the transformation angle is taken into account leading to two different pairs of NACs. The two pairs are shown in Fig. 1(b). Details of these two transformations can be found in the [Appendix](#). Using the absolute value leads to model A and the signed value to model B. The differences in the NACs emerge in the number of nodes in the x -element and y -element. The two coordinates x, y are chosen in such a way that the two-dimensional space is identical to the branching space of the CoIn. For the simulations, the first eigenfunction of the S_0 potential is set to the S_2 potential assuming a delta pulse excitation to create a localized wave packet on the excited state surface. In a previous study¹⁷ on the model system, the excitation pulse was explicitly included in the simulation leading to a localized wave packet. With a subsequent applied laser pulse, it was possible to control the population transfer by varying the CEP of the pulse. In this work, we want to focus solely on the effect of the CEP-control-scheme and leave the excitation process out of discussion. For more information regarding the quantum dynamics simulation setup and the free evolution of the population for both models, see Secs. I and II of the [supplementary material](#). The transition dipole moment is chosen arbitrarily with a maximum value of $\sqrt{4.5}$ a.u. Its specific form is discussed later in Sec. III A, and the analytic expressions can be found in the [supplementary material](#) (Table S2).

A. Influence of the TDM and the NACs

Models A and B are combined with TDMs of different shape, as listed in Fig. 2. In this way, we want to find out whether and how the form of the NACs and the TDM as well as their interplay is associated with a possible CEP control. As mentioned, both model systems just differ in the form of the NACs, especially in their nodal structure. Since the x -coordinate is the main direction of motion, the NAC- x elements are decisive for the non-adiabatic coupling efficiency. The origin of the nodal planes in the TDMs is set to the intersection point. More details about the TDMs can be found in the [supplementary material](#) (Table S2). In this simulation series, the following laser pulse parameters are used: $E_{\max} = 0.0082$ GV cm⁻¹, $t_0 = 39$ fs, FWHM = 10 fs, and $\omega_0 = 0.33$ eV (3760 nm). The results are summarized in Fig. 2.

Essential for the control is the interplay of the coupling via the NACs and via the TDM along the direction of the wave packet's motion. In case of model A, the NAC- x element has no nodal structure and CEP control is achieved for a TDM without nodes (case 1). It is also achieved in case 2 although now the TDM has a nodal plane perpendicular to the direction of motion. However, this nodal structure makes no impact as the few-cycle pulse interacts with the wave packet before it has reached the CoIn and, thus, the nodal plane of the TDM is not active. In case 3, the nodal structure of the TDM is in the direction of motion and the interplay with the NAC- x element leads to a cancellation of the CEP-control contributions. In case 4, the nodal structure is the same as in case 3 but without a change in sign. The individual contributions interfere constructively and eventuate in CEP control. In case of model B, the NAC- x element has a nodal plane parallel to the direction of motion and constructive interference in the interplay is only realized when the TDM has the same nodal structure. Thus, for both

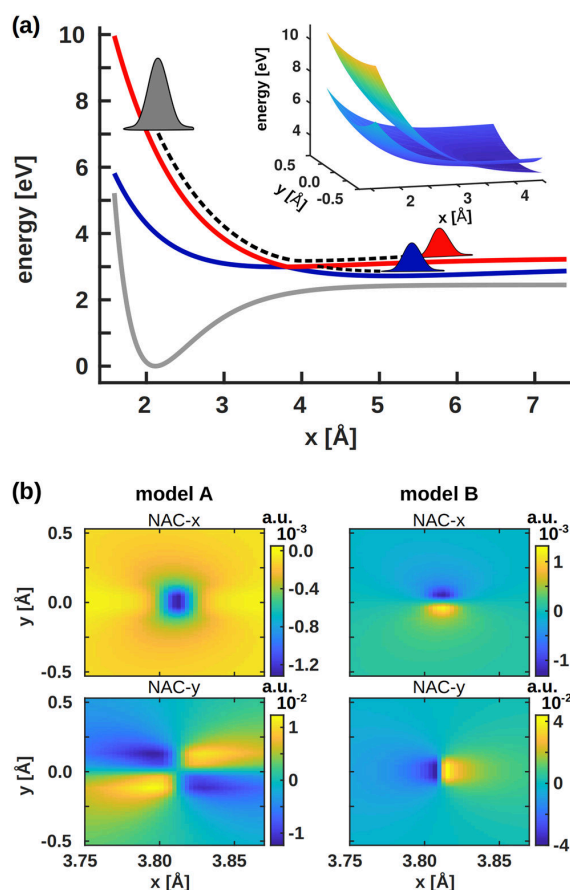


FIG. 1. (a) One-dimensional cut at $y = 0.0$ Å of the 2D adiabatic PES. Gray: S_0 ; blue: S_1 ; red: S_2 . The area of the CoIn is enlarged and shown as an inset. (b) Non-adiabatic coupling elements of model A and model B.

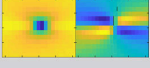
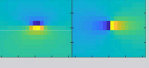
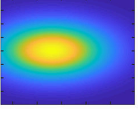
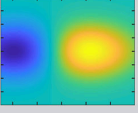
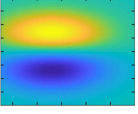
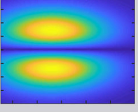
Transition dipole moment		model A	model B
			
1		CEP	no CEP
2		CEP	no CEP
3		no CEP	CEP
4		CEP	no CEP

FIG. 2. CEP-control possibility depending on the form of the NACs and the TDM. TDM-1 and TDM-3 take values from 0 to $\sqrt{4.5}$ a.u. TDM-2 and TDM-4 take values from $-\sqrt{4.5}$ to $\sqrt{4.5}$ a.u. More information of the TDMs can be found in the [supplementary material](#) (Fig. S1 and Table S2).

model systems, a combination with TDMs exists that allows for a CEP control. For the following simulations, we select model **B** because there the full mixing angle is used to calculate the NACs and, therefore, the complete phase relationship is preserved. It was combined with the TDM in case 3, which is showing the same sign change.

B. Correlation of time zero t_0 and central frequency ω_0 of the few-cycle pulse

The optimal control window is determined by the time when the wave packet is at or in the vicinity of the CoIn. This window can be scanned by variation of the pulse parameters, time zero t_0 and the central frequency ω_0 of the few-cycle IR pulse. The variations are performed for model **B**. Ideally, t_0 matches the time window when the wave packet is located at the CoIn [Fig. 3(b), gray area]. For this time, the frequency (ω_0) has to be resonant with the actual energy gap ΔE . The ΔE value is always taken at the maximum of the wave packet [Fig. 3(b), blue line]. Figure 3(a) shows the final CEP efficiency Γ of the target state S_1 in dependence of both variables. One pronounced maximum is found between 30 fs and 45 fs and between 0.2 eV and 0.28 eV. The CEP efficiency is best when t_0 coincides with the arrival time of the wave packet at the CoIn. For comparison,

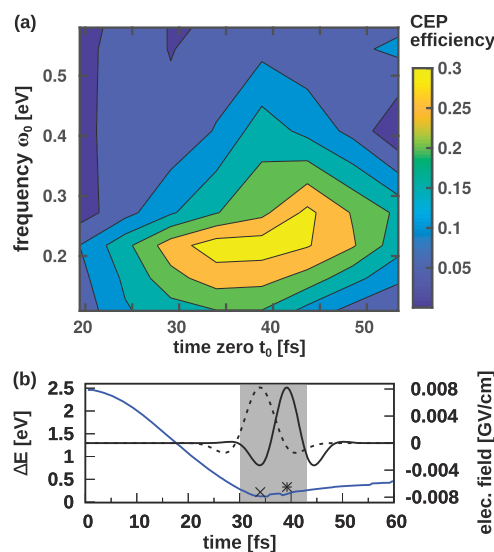


FIG. 3. (a) Two-dimensional CEP-control scheme of model **B** with the laser pulse parameters t_0 and ω_0 . (b) ΔE between S_1 and S_2 at the maximum location of the wave packet (blue), applied laser pulses with a phase shift of $\phi = 0.0\pi$ for the maximum (dashed line), and the time window of the wave packet at the CoIn (gray bar). The cross marks the parameters of the optimal pulse. The subsequently used laser pulse is shown as a solid line, and its parameters are marked with an asterisk.

the free population dynamics without the CEP pulse is shown in Sec. II of the [supplementary material](#). While the central frequency has to match the small energy gap, the CEP efficiency is less sensitive to the timing. The resulting laser pulse is almost a one-cycle pulse and is shown in Fig. 3(b) as a dashed line. Its pulse parameters, $t_0 = 34$ fs and $\omega_0 = 0.22$ eV, are marked with a cross. About 30% CEP efficiency is obtained with that laser pulse. For the following simulations, the parameters $t_0 = 39$ fs and $\omega_0 = 0.33$ eV are used (marked with an asterisk). With 20%, the CEP efficiency is still good and the laser pulse has almost two cycles [Fig. 3(b)].

C. Interference vs field-only mechanism

CEP control based on the cooperative interaction of a few-cycle IR pulse with a CoIn relies on the generation of an electronic superposition with a well-defined phase-relation. The IR pulse induced electronic wave packet interferes with the electronic superposition generated by the non-adiabatic coupling at the CoIn. Their mutual phase relation gives rise to constructive or destructive interference, which can be controlled by varying the CEP. Control via the electron dynamics is possible because here the electron and nuclear dynamics are on the same timescale. The interference pattern modifies the population-transfer through the CoIn and, thus, the branching ratio. This interaction is called the interference mechanism from now on. The degree of modification can solely be controlled by the laser pulse

induced superposition, as the one induced by the CoIn is a given molecular property.

The optimal CEP pulse is just a few-cycle IR pulse, and its shape becomes asymmetric while varying the CEP. Due to this asymmetry, the interaction with the electric field alone, i.e., without contributions from NACs, already creates a CEP dependence of the population. This interaction is called the field-only mechanism from now on. The CEP dependence of both mechanisms enters in the control quantity $\Gamma(t)$. To evaluate their individual contributions, the simulations are done twice once with and once without the NACs included. In this way, it is possible to determine the CEP efficiency $\Gamma(t)$ of the field-only mechanism and compare it with the combined impact. For a detailed understanding of both processes, we varied the parameters of the dipole-laser interaction, i.e., the electric field strength E_{\max} and the size of the TDM. All other laser parameters are kept constant ($t_0 = 39$ fs, FWHM = 10 fs, and $\omega_0 = 0.33$ eV). The variation of the TDM is performed for $E_{\max} = 0.0082$ GV cm $^{-1}$. In the field-free simulation, we observe a population of 67% in the S_1 state after the wave packet passed the CoIn (Fig. S2). Thus, the pure CoIn induced transfer from the S_2 to the S_1 state itself is quite effective. In the following, we discuss the effects of the CEP-control-scheme on the basis of the transferred population to S_1 . The results of the first simulation set are visualized in Fig. 4. For low electric field strengths ($E_{\max} < 0.01$ GV cm $^{-1}$), no CEP efficiency due to the field-only process is observed [orange line, Fig. 4(a)]. Its efficiency increases steadily with field strength even surpassing the combined efficiency (blue line). For the simulations including the NACs, $\Gamma(t)$ is already larger than 0.1 for low field strengths. It reaches a maximum of 0.41 at $E_{\max} = 0.04$ GV cm $^{-1}$ and decreases afterward. At the maximum of the combined efficiency, the field-only contributions are minor with about 5%. This is a clear indication that the interference process dominates for lower field strengths, whereas, for higher field strengths, contributions from the field-only process become important. Both mechanisms may influence the CEP dependent variation of the population. In Fig. 4(b), this variation is shown for different field strengths. The solid lines refer to the simulations including the NACs and the dashed lines to the ones with the laser interaction only. The simulations with low field strength v1 (green lines, $E_{\max} = 0.0041$ GV cm $^{-1}$) and v2 (orange lines, $E_{\max} = 0.0082$ GV cm $^{-1}$) have a mean population transfer of 67% and 65% (averaged over all CEPs), respectively. These transfer rates are almost identical to the field-free case [Fig. 4(b), black dotted line] because the contribution of the field-only process is minimal. The variation of the CEP leads to a change in the mean value by +6% and -7% for v1 and by +11% and -12% for v2. If these values are related to the field-free case, the population can be varied in the range of 13% and 23%, respectively. The CEP dependent population shows a clear sinusoidal behavior with a periodicity of 2π if the NACs are included. This periodicity is typical for an interference process. Without NACs, no CEP dependence is present and the transferred population is constant around zero. In the simulation v3 (violet lines, $E_{\max} = 0.0411$ GV cm $^{-1}$) with maximal $\Gamma(t)$, a mean population transfer of around 51% is observed, which means, in average, the laser pulse is weakening the population transfer via the CoIn. However, at the same time, the CEP-schema modifies the population transfer by +4% and -38% in relation to the field-free case. This is a quite remarkable effect because here it is possible to invert the field-free product distribution by adjusting the CEP. With a larger field strength, simulation v4

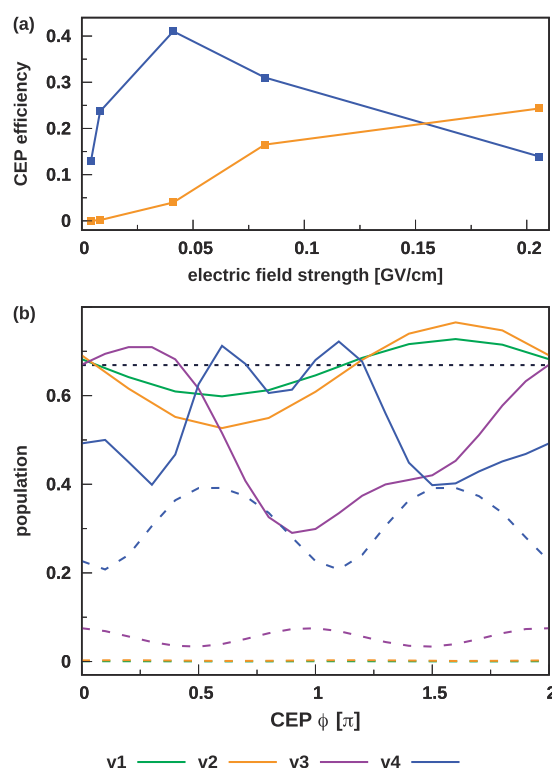


FIG. 4. (a) CEP efficiency with (blue) and without (orange) NACs included for increasing electric field strengths. (b) CEP dependence of the population in the state S_1 at the end of the simulation for selected electric field strengths. In (b), calculations with NACs are shown by solid lines and those without NACs by dashed lines. The field strengths are color coded starting from low (v1) to large (v4) values. The black dotted line shows the population after the CoIn in the S_1 state (67%) of the field-free simulation for comparison.

(blue lines, $E_{\max} = 0.0823$ GV cm $^{-1}$), the variation of the population transfer gets smaller (+5% and -27% in reference to the field-free case). In both simulations (v3 and v4), the transferred population under field-only conditions shows a clear sinusoidal dependence with a periodicity of π . This periodicity reflects the asymmetry in the electric field. Correspondingly, the CEP dependent population with NACs is of a complex sinusoidal form. For v3, the 2π periodicity is still recognizable, whereas v4 already tends more toward the π periodicity. This is an indication that with the increasing field strength, the field-only mechanism gains more and more influence on the overall process. The periodicity of π vs 2π can be used as an indicator whether the interference or field-only mechanism is present and which one is dominating. Our results show that a complex interplay between both mechanisms determines the combined CEP efficiency. It can be increased by increasing the field strength up to a certain limit. Beyond this limit, higher electric field strengths do not improve the combined CEP efficiency [blue line in Fig. 4(a)].

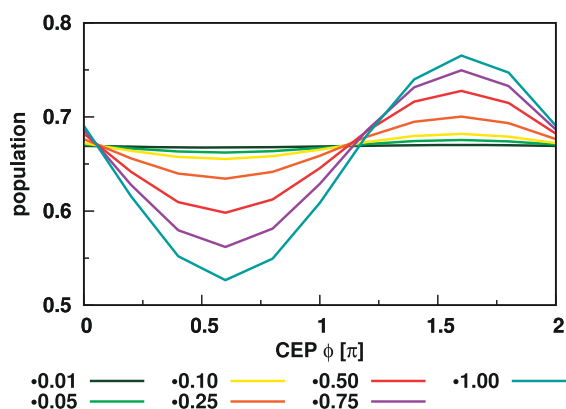


FIG. 5. CEP dependence of the population with different sized TDMs. The maximal TDM value is set to $n\sqrt{4.5}$ a.u., meaning the maximum of the dark green curve is set to $0.01\sqrt{4.5}$ a.u.

For the higher field strengths, we observe an increasing influence of the laser pulse on the field-only simulation, which can be attributed to the temporal asymmetry of the pulse. However, the overall CEP efficiency decreases, see Fig. 4(a). The used field strengths are of a magnitude that is sufficient to shift the PESs via the Stark effect.^{30–34} This can lead to the deformation of the CoIn, which occurs only for a very short timescale due to the duration of the laser pulse (FWHM = 10 fs). So, the expected influence on the population dynamics may not dominate but can partially explain the decreasing CEP efficiency.

In the second set of simulations, we vary the TDM. The maximum of the TDM is set to $n\sqrt{4.5}$ a.u., with $n = 0.01, 0.05, 0.10, 0.25, 0.50, 0.75, 1.00$. The CEP dependent population is shown in Fig. 5.

For a small TDM of around 0.02 a.u., the population shows no CEP dependence (dark green curve). For higher values between 0.11 a.u. and 1.59 a.u., the population shows a clear sinusoidal behavior with a 2π periodicity and an increasing CEP efficiency. The higher TDM enables a better population transfer between the electronic states in the CEP-pulse induced superposition. If their ratio matches the one induced at the CoIn, the best possible CEP control is achieved and the interference process is most efficient. For even larger TDMs, the sinusoidal curves become asymmetric in the height of the amplitudes while the CEP efficiency is still increasing. The periodicity of 2π is conserved, and thus, the mechanism does not change. In molecular systems, the TDM is a fixed quantity and at least a value 0.10 a.u. is required to allow for CEP control. From our results, we can deduce that large TDMs at the CoIn are favorable for the CEP control. Together with the finding in Sec. III A, it becomes clear that both the shape and the size of the TDM are essential quantities for the CEP control.

D. Tolerance on the pulse width

The last tested laser pulse parameter is the pulse width FWHM. The main request is how broad the laser pulse can be to still observe a CEP control. Figure 6 summarizes two simulation series for

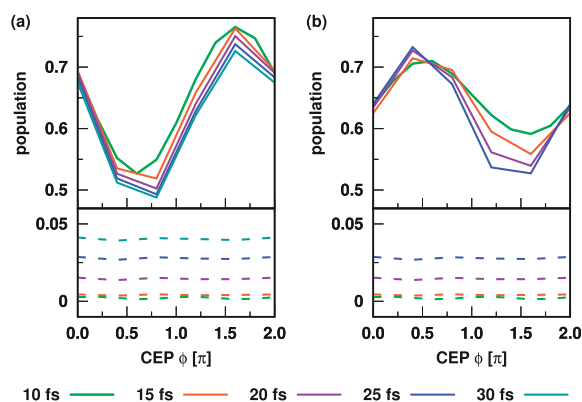


FIG. 6. CEP dependence of the population with pulse widths in the range from 10 fs to 30 fs (color coded). In (a), the laser pulse is applied at $t_0 = 39$ fs and in (b) at $t_0 = 31$ fs. Calculations with NACs are shown by solid lines and those without NACs by dashed lines.

different time zeros where the pulse widths are varied from 10 fs to 30 fs. The solid lines refer to the simulations including the NACs (top), and the dashed lines represent the field-only situation (bottom). The time zero for (a) is $t_0 = 39$ fs, and that for (b) is $t_0 = 31$ fs. The further laser parameters are $E_{\max} = 0.0082$ GV cm⁻¹, for which only the interference process is active, and $\omega_0 = 0.33$ eV.

In the field-only case, the population transfer is constant with the CEP but slightly increases with the pulse length, see Fig. 6 (bottom). With NACs included, the population in the target state follows the sinusoidal form with a periodicity of 2π . We find that a CEP control is possible for laser pulses with a FWHM up to 30 fs, a tolerance that was already indicated in Fig. 3(a) showing the CEP efficiency with respect to the central frequency ω_0 and time zero t_0 . The tolerance in the FWHM of the CEP pulse facilitates experimental realization.

IV. URACIL

Besides the analytic model system, we want to extend our investigations to a more realistic system. We selected the nucleobase uracil, which has an experimentally well studied ultra-fast photo-relaxation channel starting in S_2 and mediated by conical intersections. In previous studies,^{8,9} we demonstrated that the S_2 – S_1 relaxation dynamics can be well described on two-dimensional potential surfaces and offers opportunities for laser control. Here, we focus on the control possibilities at the CoIn. The geometry of uracil is shown as an inset in Fig. 7(a). A seam of CoIn's [Fig. 7(a), black line] enables the ultrafast relaxation mechanism of a few hundred femtoseconds. For the dynamics simulation, we adopted the PES reported by Keefer *et al.*⁸ The system is described fully coherently as no coupling to an external bath is considered. On the timescales relevant to the relaxation process studied, this should be of no major consequence for the reported message. The PESs are spanned by a two-dimensional coordinate space, which properly samples the relaxation pathway in the bright S_2 state [PES shown in Fig. 7(a)]. The S_2 potential energy

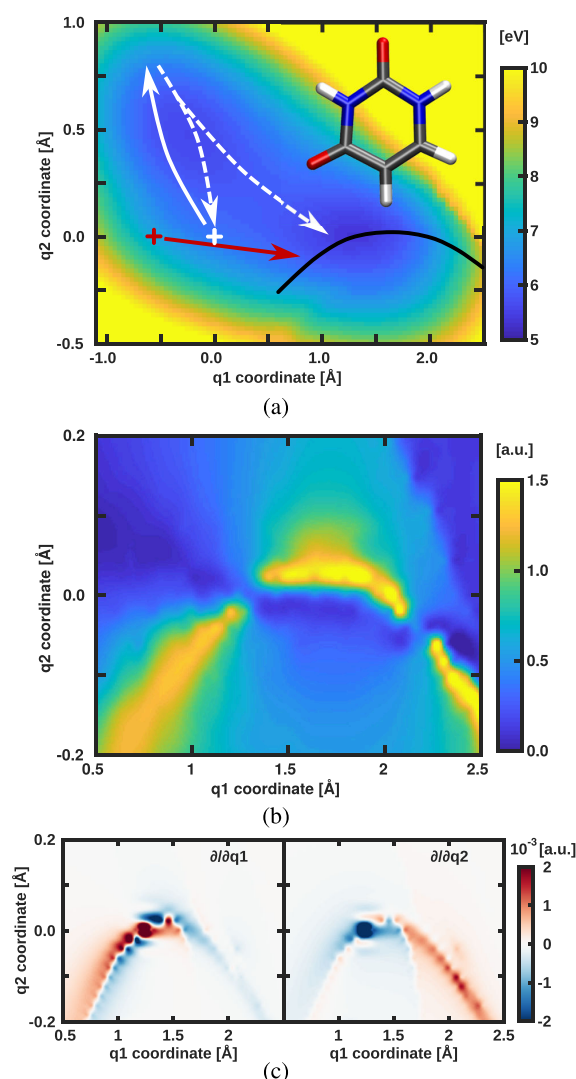


FIG. 7. (a) Potential energy surface of the bright S_2 state of uracil. The conical intersection seam is marked in black, and the evolution of the *uracil A* and the *uracil B* wave packet is sketched in white and red, respectively. The structure of uracil at the Franck-Condon point is shown as an inset. (b) Absolute value of the S_2 - S_1 transition dipole moment at the CoIn. (c) Non-adiabatic coupling elements between S_2 and S_1 at the CoIn, q_1 -element left and q_2 -element right.

surface exhibits a double-well structure with a barrier in between. The left well includes the S_2 minimum, and the right one coincides with the minimum energy CoIn. The absolute value of the TDM between S_2 and S_1 and the non-adiabatic-couplings (NACs) are displayed in Figs. 7(b) and 7(c). Further information about the simulation setup can be found in Sec. I of the [supplementary material](#).

Uracil introduces new aspects compared to the model. Primarily, its dynamics takes place on coupled bound states and is not dissociative, and thus, the wave packet will pass the coupling area several times. In addition, the shape and size of the NACs and the TDM differ from those of the idealized model system. For uracil, not only a single CoIn but parts of the CoIn seam are included, and thus, coupling can occur all along the seam and the behavior of the geometric phase becomes more complex. The absolute value of the TDM is strongly structured and very localized along the seam, but with regard to Sec. III C, in principle, it is large enough to allow for a CEP control. On the other hand, there are regions along the seam where the values of the TDM drop to almost zero. The combination of NACs and TDM in uracil leads to a situation where the control is sensitive to the direction the wave packet hits the seam. Two different starting conditions for the simulations are investigated. For the first, *uracil A*, the dynamics starts on the S_2 state at the Franck-Condon point, assuming a delta pulse excitation. The wave packet motion is indicated in white in Fig. 7(a), its initial oscillation by a solid line, and the subsequent splitting by dashed lines. After the first oscillation period (about 80 fs), the barrier is reached. The parts of the wave packet passing the barrier successively reach the CoIn seam. In the *uracil B* case, a Gaussian shaped wave packet is placed at a position shifted to negative q_1 values with respect to the Franck-Condon point and is marked by the red cross. From here, most of the wave packet directly reaches the CoIn seam in a quite localized way. This relaxation pathway is shown in red in Fig. 7(a). The evolution of the population for both starting conditions can be found in Sec. II of the [supplementary material](#).

A. Optimization of the CEP pulse parameters

First, the optimal control window is determined as in the model system by varying the central frequency ω_0 and the time zero t_0 of the laser pulse. The pulse width is set to 10 fs FWHM for all following studies. The wave packet crosses the seam multiple times so that the CEP efficiency $\Gamma(t)$ will not converge to a constant value. Instead, the end of the laser interaction $t_0 + \text{FWHM}$ is used to record $\Gamma(t)$. As the target state, we refer to the S_2 state. Electric field strengths of 0.15 GV cm^{-1} for *uracil A* and 0.10 GV cm^{-1} for *uracil B* are used. In Fig. 8, the resulting two-dimensional optimization landscapes are shown for *uracil A* (top) and *uracil B* (bottom).

Both landscapes are more complex compared to the model system (Fig. 3). The CEP efficiency of *uracil A*, shown in Fig. 8(a), has four maxima. The largest value of 5% is found for a frequency of 0.2 eV and a t_0 value of 90 fs. Another maximum is located 10 fs earlier for the same frequency. In this time period (80 fs to 90 fs), the first part of the wave packet reaches the vicinity of the CoIn seam. The maxima for later times (100 fs to 110 fs) are shifted toward higher (0.3 eV) and lower (0.1 eV) frequencies and correspond to the subsequent parts of the wave packet. In the following, we will focus on the largest maximum at 0.2 eV and 90 fs. For *uracil B*, shown in Fig. 8(b), only two significant maxima are found. The largest CEP efficiencies form an extended plateau located in the range from 30 fs to 35 fs and from 0.05 eV to 0.20 eV with a global maximum of 30% CEP efficiency at 30 fs and 0.2 eV. A further local maximum is located at a t_0 value of 30 fs and a frequency of 0.3 eV. Again, the time window reflects the time period in which the wave packet reaches the

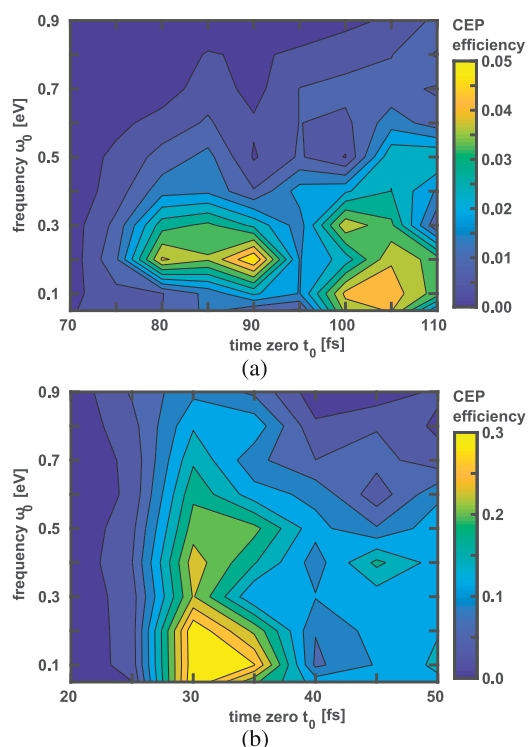


FIG. 8. Two-dimensional optimization landscapes of the CEP efficiency for *uracil A* (a) and *uracil B* (b) determined by varying the central frequency ω_0 of the pulse and its timing classified by the value of its time zero t_0 related to the propagation time of the wave packet.

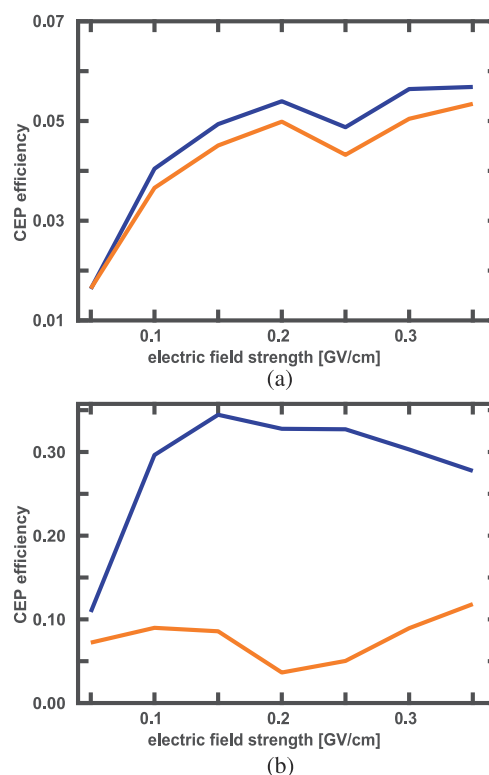


FIG. 9. CEP efficiency determined for increasing electric field strengths with (blue) and without (orange) NACs included for *uracil A* (a) and *uracil B* (b).

vicinity of the CoIn seam for the first time. For this first event, more than 50% of the population is transferred. The maximum efficiency for *uracil B* is nearly six times larger and concentrated on two main peaks, defining an extended time and frequency window. The differences between *A* and *B* are due to the fact that the wave packets approach the CoIn seam along different pathways and thereby experience the NACs and the TDM differently. The *A*-pathway [white lines in Fig. 7(a)] lies between cases 4A and 4B of the model system (Fig. 2) but with a much more localized TDM. This explains the low CEP efficiency confined to small areas. For case *uracil B*, the experienced parts of the NACs and the TDM are similar to those in model case 1A and the TDM near the seam is more extended compared to that in *uracil A*.

The next optimized parameter is the electric field strength. As shown in Sec. III C, this parameter has a strong influence on the CEP induced processes. The CEP efficiency is determined for both starting conditions using the previous optimized values for ω_0 and t_0 in combination with a FWHM of 10 fs. The results of these calculations are visualized in Fig. 9.

For *uracil A* [see Fig. 9(a)], the CEP efficiency with (blue line) and without (orange line) NACs included shows a very similar

response. After an initial increase, the CEP efficiency converges to a value of about 5.5% with a small dip at 0.25 GV cm⁻¹. Overall, the efficiency obtained with NACs is slightly larger. The CEP efficiency of *uracil B*, shown in Fig. 9(b), behaves completely different. When NACs (blue line) are included, the efficiency rises rapidly, reaches a maximum for 0.15 GV cm⁻¹, and decreases slowly afterward. Without NACs (orange line), the efficiency stays on a significant lower level around an average value of 0.1. Obviously, the underlying process leading to the CEP efficiency is different for both cases. For *uracil A*, the simulations with and without NACs show qualitatively and quantitatively a similar behavior, which is an indication that the field-only process dominates. The CEP efficiency of *uracil B* differs strongly whether or not NACs are taken into account. This suggests that now also the interference process is responsible for the CEP efficiency. Just like for the model system, the higher field strengths used are sufficient to shift the PESs and deform the CoIn for a short timescale.

B. Optimal CEP pulses

So far, we restricted our analysis to the CEP efficiency at $t_0 + \text{FWHM}$, shortly after the laser pulse. However, the uracil wave

packet crosses the CoIn seam multiple times, which influences the long-term evolution of the CEP efficiency. We characterize the underlying mechanism following the CEP dependence of the population in time. For *uracil A*, the optimal laser parameters were determined to be $t_0 = 90$ fs, $E_{\max} = 0.2$ GV cm $^{-1}$, and $\omega_0 = 0.2$ eV. The width of the pulse was set to 10 fs. The temporal evolution of the CEP efficiency after t_0 and the CEP dependent population of the target state S_2 at three selected times are shown in Fig. 10.

The CEP efficiency decreases fast already after the maximal field strength of the laser pulse at 90 fs. When the laser pulse is no longer present at approximately 100 fs, the efficiency decreases more slowly. A second large step is observed at 170 fs. A final value of about 3.0% is reached at 200 fs. The field-only CEP efficiency is constant after the laser pulse; its value is plotted as a dashed black line. From 120 fs on, it is higher than the combined effect (blue line). Interestingly, the CEP efficiency survives for the complete simulation

time, although several crossings of the CoIn seam occurred modifying the phase information of the wave packet. In order to analyze the CEP dependence of the population [see Fig. 10(b)], its mean difference is recorded for three selected times marked as vertical lines in Fig. 10(a). The mean difference of the population is chosen for better visualization. The first line at $t_0 + \text{FWHM}$ (100 fs, green) corresponds to the time when the laser pulse is over. The second point (red line) is taken at 150 fs and the third one (yellow line) at the end of the simulation time (197 fs). For all three times, the CEP dependent population shows a sinusoidal oscillation with a periodicity of approximately π , which indicates that, for *uracil A*, the field-only mechanism is the dominating process in the complete simulation time.

The optimal laser parameters for *uracil B* are $t_0 = 30$ fs, $E_{\max} = 0.15$ GV cm $^{-1}$, and $\omega_0 = 0.2$ eV. The temporal evolution of the CEP efficiency starting at t_0 and the CEP dependent population at

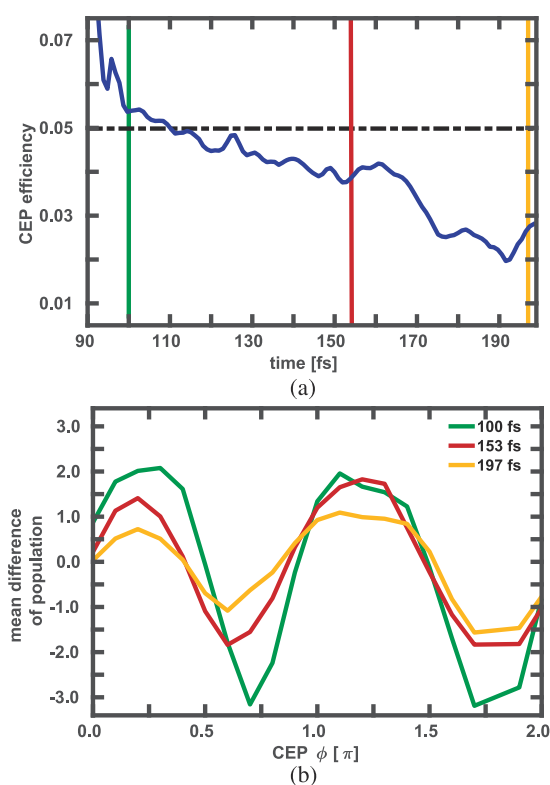


FIG. 10. (a) Temporal evolution of the CEP efficiency for *uracil A* after t_0 using a laser pulse with optimized parameters and a field strength of 0.2 GV cm $^{-1}$. The black dotted line represents the obtained efficiency without NACs included. The blue line denotes the efficiency obtained with the coupling elements included. The vertical colored lines indicate the points in time that are examined more closely. (b) Mean difference of the phase-dependent populations for different points in times obtained including the NACs.

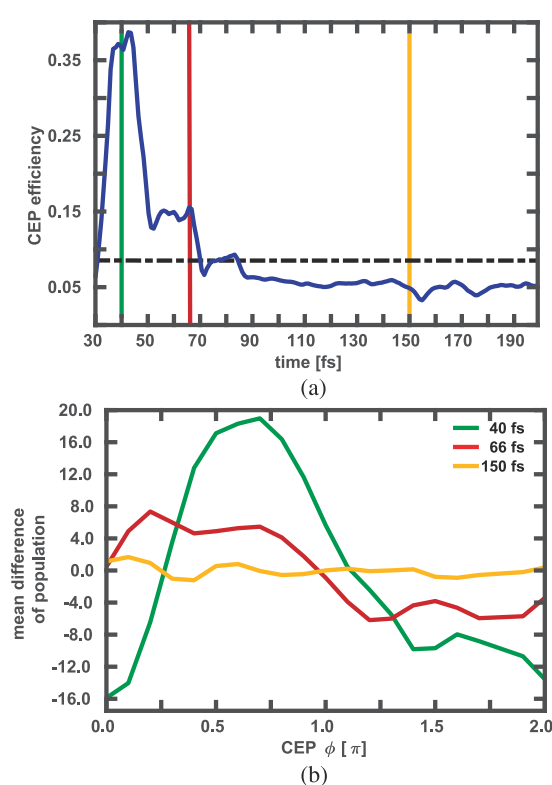


FIG. 11. (a) Temporal evolution of the CEP efficiency for *uracil B* after t_0 using a laser pulse with optimized parameters and a field strength of 0.15 GV cm $^{-1}$. The black dotted line represents the obtained efficiency without NACs included. The blue line denotes the efficiency obtained with the coupling elements included. The vertical colored lines indicate the points in time that are examined more closely. (b) Mean difference of the CEP dependent population for different points in times obtained including the NACs.

three selected times are shown in Fig. 11. Again, the mean difference of the population is plotted.

The higher CEP efficiency for *uracil B* persists for the complete simulation time [Fig. 11(a)]. The main peak occurs between 40 fs and 45 fs, which is 10 fs–15 fs after the field maximum. Thereafter, the efficiency drops in two smaller steps to a value of 6% at 90 fs reflecting the back and forth crossing of the CoIn seam of a still localized wave packet. For the remaining simulation time, the CEP efficiency stays almost constant. The field-only efficiency (black dotted line) is smaller up to 90 fs. Again, the CEP dependence persists for the complete simulation time. The analysis of the CEP dependent population [see Fig. 11(b)] is performed at three points in time, marked as colored lines. Again, the first time at $t_0 + \text{FWHM}$ (40 fs) is taken in the maximum of the efficiency. The second point at 66 fs is at the edge of the second step. The third point is taken at 150 fs in an area where the efficiency stays constant. For the first time (green curve), the CEP dependent population shows a strongly deformed

sinusoidal dependence with no clear periodicity. For the second time (red curve), still some kind of sinusoidal behavior is observed, which is washed out for the third time (yellow curve). This ambiguous periodicity and form are indicators (see Sec. III C) for strong interaction between the interference and the field-only mechanism. To weaken the field-only process, we lower the field strengths to 0.05 GV cm^{-1} (see Fig. S4 in the supplementary material) and 0.025 GV cm^{-1} (see Fig. 12).

In both cases, the achieved CEP efficiency is lower, but its temporal evolution stays qualitatively the same. The CEP dependent population at the same selected points in time now shows a clear sinusoidal form with a periodicity of 2π . This is most distinct for the lowest field strength. These findings confirm our conclusions from the model system (Sec. III C): For low electric field strengths, the dominating mechanism is the interference process that can be identified by the 2π periodicity. Overall, for both starting conditions, the CEP efficiency is surprisingly long-lived and not impaired by the nuclear wave packet motion. Differences are found in magnitude and for the temporal evolution. These are also reflected in the CEP dependent population. Their periodicity classifies the mechanism. In the *uracil A* case, the field-only process dominates, and in *uracil B*, the interference process becomes important. For low field conditions, the 2π periodicity is clearly seen, whereas higher field strengths induce both processes. In general, the field-only process becomes dominant for high field strengths or when the interplay of the NACs and TDM as in *uracil A* does not lead to constructive interference.

V. CONCLUSION

Conical intersections are known to be crucial branching points for excited state reactions. To control the dynamics at these sensitive points, we examined the controllability using the waveform of a CEP stabilized few-cycle pulse in the IR. Performing quantum dynamical simulations on coupled potential energy surfaces, the necessary boundary conditions were defined and appropriate laser pulses were optimized. In the first part, we focused on an analytical model system, describing a dissociation process with two competing pathways connected via a CoIn. Within the model system, we were able to study the mutual influence of the decisive molecular properties, the non-adiabatic coupling elements, and the transition dipole moment. CEP control is only possible if the interplay of these two fundamental quantities allows for constructive interference. For this, their shape along the direction of the wave packet motion is most important. Via optimization of the laser parameters, we could identify two different processes, which both contribute to the overall CEP efficiency. The optimal few-cycle CEP pulse creates a superposition with a well-defined phase-relation just before the CoIn is reached. Together with the geometric phase, this creates an interference when the superposition passes through the CoIn. This interference process modifies the branching ratio after the CoIn. The second process, the field-only mechanism, occurs due to the few-cycle waveform of the IR pulse and is not affected by the NACs. Depending on the molecular system and the chosen laser parameters, both processes can be active, vary in their strength, and even obstruct each other. Assuming ideal conditions for the NACs and TDM, we were able to optimize a laser pulse that leads to a CEP efficiency of 40%, which is almost entirely based on the interference process. This large efficiency is favored by the dissociative character of the model, which leads to a situation where

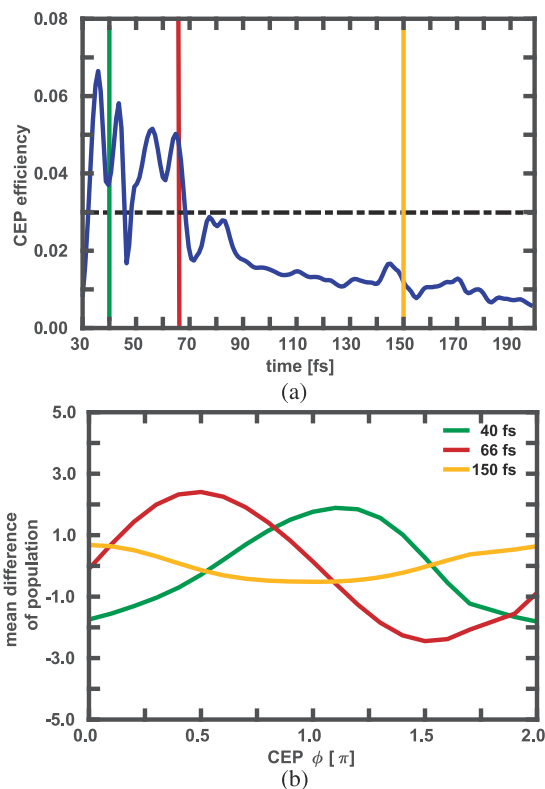


FIG. 12. (a) Temporal evolution of the CEP efficiency for *uracil B* after t_0 using a laser pulse with optimized parameters and a field strength of 0.025 GV cm^{-1} . The black dotted line represents the obtained efficiency without NACs included. The blue line denotes the efficiency obtained with the coupling elements included. The vertical colored lines indicate the points in time that are examined more closely. (b) Mean difference of the CEP dependent population for different points in times obtained including the NACs.

a very localized wave packet passes the CoIn only once. In the second part, we focus on a more realistic molecular system, the nucleobase uracil, whose CoIn's ensure its photostability. We applied the CEP-control scheme to the population dynamics between the S_2 and the S_1 state. As both states are strongly bound, multiple crossings of the CoIn's occur. These molecular boundary conditions are quite challenging for CEP control. Nevertheless, we were able to achieve a short time CEP efficiency between 6% and 37% depending on the two starting conditions. For the first, the excited state wave packet oscillates around the S_2 minimum before parts of it are able to cross the barrier and reach the CoIn. In the second case, the wave packet directly approaches the barrier and, thereafter, the CoIn in a localized form. Besides the overall CEP efficiency, the starting conditions determine also the mechanism. The active parts of the NACs and the TDM for both pathways vary between situations, which enable the interference process or rather prevent it. This finding shows that if a wave packet moves along a suitable pathway toward a CoIn, it is possible to achieve a high degree of CEP control. Some molecular systems may provide these pathways naturally, and for others, such a pathway can be opened by the use of specially shaped laser pulses in the excitation process.⁸ We demonstrated that the control of the branching ratio induced by a CoIn via a CEP pulse is a general concept. The control is most effective for a system where a localized wave packet crosses the CoIn only once and the TDM is extended in this area, but even for a more complex chemical system as uracil situations can be found where a CEP control is realizable. The CEP efficiency is long-lived, which should be favorable for experimental detection. In addition, we showed for the model system that the CEP control tolerates pulse widths up to 30 fs for the IR pulse.

SUPPLEMENTARY MATERIAL

See the [supplementary material](#) for the details of the wave packet simulation setup and the population dynamics without any CEP laser pulse for both the model system and uracil. In addition, the temporal evolution of the CEP efficiency and the CEP dependent population for *uracil B* obtained with the optimized laser parameters and a field strength of 0.05 GV cm^{-1} are shown.

AUTHORS' CONTRIBUTIONS

F.S. and T.S. contributed equally to this work. T.S. and R.d.V.R. initiated the project. F.S. performed the calculations on the model system, and L.B. and T.S. did the simulations for uracil. F.S., T.S., and R.D.V.R. analyzed and interpreted the results. All authors contributed to the final version of the manuscript.

ACKNOWLEDGMENTS

The authors gratefully acknowledge the DFG Normalverfahren and the Munich Center of Advanced Photonics (MAP).

APPENDIX: ADIABATIZATION OF THE MODEL SYSTEM

In this section, the transformation of the diabatic Hamiltonian matrix [Eq. (A1)] of the model system to the adiabatic picture

is described in detail. The model system consists of the three diabatic electronic states V_0 , V_1 , and V_2 and the diabatic coupling element D_{12} ,

$$\hat{H}_{dia} = \begin{pmatrix} \hat{T} + V_0 & 0 & 0 \\ 0 & \hat{T} + V_1 & D_{12} \\ 0 & D_{12} & \hat{T} + V_2 \end{pmatrix}. \quad (\text{A1})$$

The diagonalization^{1,2,48} is done using a unitary transformation matrix U [Eq. (A2)],

$$U = \begin{pmatrix} 1 & 0 & 0 \\ 0 & \cos(\theta) & +\sin(\theta) \\ 0 & -\sin(\theta) & \cos(\theta) \end{pmatrix}. \quad (\text{A2})$$

Here, the angle θ is the adiabatic-diabatic transformation angle (or shortened the mixing angle)^{1,2,47} between the coupled diabatic states V_1 and V_2 . Based on Eq. (A3), this angle θ is defined in a range of $[-0.5\pi, +0.5\pi]$,

$$\theta = \frac{1}{2} \arctan\left(\frac{2D_{12}}{V_2 + V_1}\right). \quad (\text{A3})$$

Following θ along a closed path of nuclear configurations encircling the CoIn, a phase shift of π is observed. This phase shift is called the geometric phase or Pancharatnam-Berry phase^{24,25} and leads to a sign change of adiabatic electronic wavefunctions, if a closed path around the CoIn is followed. Within our two-dimensional model, we can observe the full phase shift of π since we describe the full branching space. For higher dimensional systems, where the chosen sub-space is not identical to the branching space, no clear statement can be made about the phase behavior.⁴⁹ Using the transformation matrix (A2), the adiabatic eigenfunctions can be expressed as a linear combination of the diabatic ones,

$$|\Psi_0^{adi}\rangle = |\Phi_0^{dia}\rangle, \quad (\text{A4})$$

$$|\Psi_1^{adi}\rangle = +\cos(\theta)|\Phi_1^{dia}\rangle + \sin(\theta)|\Phi_2^{dia}\rangle, \quad (\text{A5})$$

$$|\Psi_2^{adi}\rangle = -\sin(\theta)|\Phi_1^{dia}\rangle + \cos(\theta)|\Phi_2^{dia}\rangle. \quad (\text{A6})$$

The corresponding adiabatic states can be calculated from the diabatic states,

$$S_0 = V_0, \quad (\text{A7})$$

$$S_1 = \frac{V_2 + V_1}{2} - \sqrt{\left(\frac{V_2 - V_1}{2}\right)^2 + D_{12}^2}, \quad (\text{A8})$$

$$S_2 = \frac{V_2 + V_1}{2} + \sqrt{\left(\frac{V_2 - V_1}{2}\right)^2 + D_{12}^2}. \quad (\text{A9})$$

The non-adiabatic coupling elements τ_{12} required for the dynamics can be determined as derivatives of the mixing angle θ (A3),^{1,2,50,51}

$$\begin{aligned}\tau_{12} &= \langle \Psi_1^{adi} | \nabla | \Psi_2^{adi} \rangle \nabla + \frac{1}{2} \langle \Psi_1^{adi} | \nabla^2 | \Psi_2^{adi} \rangle \\ &= \nabla \theta \nabla + \frac{1}{2} \nabla^2 \theta.\end{aligned}\quad (\text{A10})$$

Since the $\nabla^2 \theta$ term, which contains the second derivatives, is much smaller than the $\nabla \theta$ term, it can be neglected in first approximation. However, this would lead to a non-Hermitian Hamiltonian operator. To avoid this, the non-Hermitian behavior can be compensated for by using the partition equation (A11).^{49,52} Here, the term $\langle \nabla \Psi_1^{adi} | \nabla \Psi_2^{adi} \rangle$ can be neglected without losing the hermiticity,

$$\langle \nabla \Psi_1^{adi} | \nabla^2 | \Psi_2^{adi} \rangle = \nabla \langle \Psi_1^{adi} | \nabla | \Psi_2^{adi} \rangle - \langle \nabla \Psi_1^{adi} | \nabla \Psi_2^{adi} \rangle. \quad (\text{A11})$$

There are two possible ways to handle the phase shift in θ ,^{50,51} using the absolute value of θ (model A) or using the full value (model B) of it. In both cases, there is a discontinuous point along the closed cycle around the CoIn, but it appears that, at different positions and for model A, the phase shift is neglected. This results in two different coupling pairs with a different number of nodal planes in the resulting elements.

DATA AVAILABILITY

The data that support the findings of this study are available from the corresponding author upon reasonable request.

REFERENCES

- D. R. Yarkony, "Diaboloical conical intersections," *Rev. Mod. Phys.* **68**, 985–1013 (1996).
- M. Baer, "Introduction to the theory of electronic non-adiabatic coupling terms in molecular systems," *Phys. Rep.* **358**, 75–142 (2002).
- M. S. Schuurman and A. Stolow, "Dynamics at conical intersections," *Annu. Rev. Phys. Chem.* **69**, 427–450 (2018).
- R. Send and D. Sundholm, "Stairway to the conical intersection: A computational study of the retinal isomerization," *J. Phys. Chem. A* **111**, 8766–8773 (2007).
- D. Polli, P. Altoè, O. Weingart, K. M. Spillane, C. Manzoni, D. Brida, G. Tomasello, G. Orlandi, P. Kukura, R. A. Mathies, M. Garavelli, and G. Cerullo, "Conical intersection dynamics of the primary photoisomerization event in vision," *Nature* **467**, 440–443 (2010).
- L. Serrano-Andrés and M. Merchán, "Are the five natural DNA/RNA base monomers a good choice from natural selection? A photochemical perspective," *J. Photochem. Photobiol., C* **10**, 21–32 (2009).
- L. Blancafort, "Photochemistry and photophysics at extended seams of conical intersection," *ChemPhysChem* **15**, 3166–3181 (2014).
- D. Keefer, S. Thallmair, S. Matsika, and R. de Vivie-Riedle, "Controlling photorelaxation in uracil with shaped laser pulses: A theoretical assessment," *J. Am. Chem. Soc.* **139**, 5061–5066 (2017).
- S. Reiter, D. Keefer, and R. de Vivie-Riedle, "RNA environment is responsible for decreased photostability of uracil," *J. Am. Chem. Soc.* **140**, 8714–8720 (2018).
- B. L. Feringa, R. A. van Delden, N. Koumura, and E. M. Geertsema, "Chiroptical molecular switches," *Chem. Rev.* **100**, 1789–1816 (2000).
- A. Nenov, T. Cordes, T. T. Herzog, W. Zinth, and R. de Vivie-Riedle, "Molecular driving forces for z/e isomerization mediated by heteroatoms: The example hemithioindigo," *J. Phys. Chem. A* **114**, 13016–13030 (2010).
- B. Maerz, S. Wiedbrauk, S. Oesterling, E. Samoylova, A. Nenov, P. Mayer, R. de Vivie-Riedle, W. Zinth, and H. Dube, "Making fast photoswitches faster—using Hammett analysis to understand the limit of donor–acceptor approaches for faster hemithioindigo photoswitches," *Chem. -Eur. J.* **20**, 13984–13992 (2014).
- S. Kassem, T. van Leeuwen, A. S. Lubbe, M. R. Wilson, B. L. Feringa, and D. A. Leigh, "Artificial molecular motors," *Chem. Soc. Rev.* **46**, 2592–2621 (2017).
- F. F. Graupner, T. T. Herzog, F. Rott, S. Oesterling, R. de Vivie-Riedle, T. Cordes, and W. Zinth, "Photoisomerization of hemithioindigo compounds: Combining solvent- and substituent- effects into an advanced reaction model," *Chem. Phys.* **515**, 614–621 (2018).
- R. Wilcken, M. Schildhauer, F. Rott, L. A. Huber, M. Guentner, S. Thumser, K. Hoffmann, S. Oesterling, R. de Vivie-Riedle, E. Riedle, and H. Dube, "Complete mechanism of hemithioindigo motor rotation," *J. Am. Chem. Soc.* **140**, 5311–5318 (2018).
- T. Brixner and G. Gerber, "Quantum control of gas-phase and liquid-phase femtochemistry," *ChemPhysChem* **4**, 418–438 (2003).
- M. F. Kling, P. von den Hoff, I. Znakovskaya, and R. de Vivie-Riedle, "(Sub-)femtosecond control of molecular reactions via tailoring the electric field of light," *Phys. Chem. Chem. Phys.* **15**, 9448–9467 (2013).
- S. Thallmair, D. Keefer, F. Rott, and R. de Vivie-Riedle, "Simulating the control of molecular reactions via modulated light fields: From gas phase to solution," *J. Phys. B: At., Mol. Opt. Phys.* **50**, 082001 (2017).
- K.-M. Weitzel, "Controlling the electrons provides means for controlling chemistry," *ChemPhysChem* **8**, 213–215 (2007).
- M. F. Kling and M. J. J. Vrakking, "Attosecond electron dynamics," *Annu. Rev. Phys. Chem.* **59**, 463–492 (2008).
- I. Znakovskaya, P. von den Hoff, N. Schirmel, G. Urbasch, S. Zhrebtssov, B. Bergues, R. de Vivie-Riedle, K.-M. Weitzel, and M. F. Kling, "Waveform control of orientation-dependent ionization of DCL in few-cycle laser fields," *Phys. Chem. Chem. Phys.* **13**, 8653–8658 (2011).
- I. Znakovskaya, P. von den Hoff, G. Marcus, S. Zhrebtssov, B. Bergues, X. Gu, Y. Deng, M. J. J. Vrakking, R. Kienberger, F. Krausz, R. de Vivie-Riedle, and M. F. Kling, "Subcycle controlled charge-directed reactivity with few-cycle midinfrared pulses," *Phys. Rev. Lett.* **108**, 063002 (2012).
- A. Alnaser, M. Kübel, R. Siemering, B. Bergues, N. G. Kling, K. Betsch, Y. Deng, J. Schmidt, Z. Alahmed, A. Azzeer, J. Ullrich, I. Ben-Itzhak, R. Moshhammer, U. Kleineberg, F. Krausz, R. de Vivie-Riedle, and M. Kling, "Subfemtosecond steering of hydrocarbon deprotonation through superposition of vibrational modes," *Nat. Commun.* **5**, 3800 (2014).
- H. C. Longuet-Higgins, U. Öpik, M. H. L. Pryce, and R. A. Sack, "Studies of the Jahn-Teller effect. II. The dynamical problem," *Proc. R. Soc. London, Ser. A* **244**, 1–16 (1958).
- M. V. Berry, "Quantal phase factors accompanying adiabatic changes," *Proc. R. Soc. London, Ser. A* **392**, 45–57 (1984).
- J. L. Herek, W. Wohlleben, R. J. Cogdell, D. Zeidler, and M. Motzkus, "Quantum control of energy flow in light harvesting," *Nature* **417**, 533–535 (2002).
- R. Mitrić, M. Hartmann, J. Pittner, and V. Bonačić-Koutecký, "New strategy for optimal control of femtosecond pump-dump processes," *J. Phys. Chem. A* **106**, 10477–10481 (2002).
- D. Geppert, A. Hofmann, and R. de Vivie-Riedle, "Control of a collision complex via a conical intersection," *J. Chem. Phys.* **119**, 5901–5906 (2003).
- M. Abe, Y. Ohtsuki, Y. Fujimura, and W. Domcke, "Optimal control of ultrafast cis-trans photoisomerization of retinal in rhodopsin via a conical intersection," *J. Chem. Phys.* **123**, 144508 (2005).
- D. Townsend, B. J. Sussman, and A. Stolow, "A Stark future for quantum control," *J. Phys. Chem. A* **115**, 357–373 (2011).
- B. Wolter, M. G. Pullen, A.-T. Le, M. Baudisch, K. Doblhoff-Dier, A. Senftleben, M. Hemmer, C. D. Schröter, J. Ullrich, T. Pfeifer, R. Moshhammer, S. Gräfe, O. Vendrell, C. D. Lin, and J. Biegert, "Ultrafast electron diffraction imaging of bond breaking in di-ionized acetylene," *Science* **354**, 308–312 (2016).

- ³²N. Moiseyev, M. Šindelka, and L. S. Cederbaum, "Laser-induced conical intersections in molecular optical lattices," *J. Phys. B: At., Mol. Opt. Phys.* **41**, 221001 (2008).
- ³³G. J. Halász, M. Šindelka, N. Moiseyev, L. S. Cederbaum, and Á. Vibók, "Light-induced conical intersections: Topological phase, wave packet dynamics, and molecular alignment," *J. Phys. Chem. A* **116**, 2636–2643 (2012).
- ³⁴A. Natan, M. R. Ware, V. S. Prabhudesai, U. Lev, B. D. Bruner, O. Heber, and P. H. Bucksbaum, "Observation of quantum interferences via light-induced conical intersections in diatomic molecules," *Phys. Rev. Lett.* **116**, 143004 (2016).
- ³⁵C. Liekhus-Schmaltz, G. A. McCracken, A. Kaldun, J. P. Cryan, and P. H. Bucksbaum, "Coherent control using kinetic energy and the geometric phase of a conical intersection," *J. Chem. Phys.* **145**, 144304 (2016).
- ³⁶C. Arnold, O. Vendrell, R. Welsch, and R. Santra, "Control of nuclear dynamics through conical intersections and electronic coherences," *Phys. Rev. Lett.* **120**, 123001 (2018).
- ³⁷S. Tommasi, M. F. Denissenko, and G. P. Pfeifer, "Sunlight induces pyrimidine dimers preferentially at 5-methylcytosine bases," *Cancer Research* **57**, 4727–4730 (1997).
- ³⁸L. Esposito, A. Banyasz, T. Douki, M. Perron, D. Markovitsi, and R. Improtta, "Effect of C5-methylation of cytosine on the photoreactivity of DNA: A joint experimental and computational study of TCG trinucleotides," *J. Am. Chem. Soc.* **136**, 10838–10841 (2014).
- ³⁹L. Holmegaard, J. H. Nielsen, I. Nevo, H. Stapelfeldt, F. Filsinger, J. Küpper, and G. Meijer, "Laser-induced alignment and orientation of quantum-state-selected large molecules," *Phys. Rev. Lett.* **102**, 023001 (2009).
- ⁴⁰J. L. Hansen, H. Stapelfeldt, D. Dimitrovski, M. Abu-samha, C. P. J. Martiny, and L. B. Madsen, "Time-resolved photoelectron angular distributions from strong-field ionization of rotating naphthalene molecules," *Phys. Rev. Lett.* **106**, 073001 (2011).
- ⁴¹J. L. Hansen, L. Holmegaard, J. H. Nielsen, H. Stapelfeldt, D. Dimitrovski, and L. B. Madsen, "Orientation-dependent ionization yields from strong-field ionization of fixed-in-space linear and asymmetric top molecules," *J. Phys. B: At., Mol. Opt. Phys.* **45**, 015101 (2011).
- ⁴²H. Niikura, F. Légaré, R. Hasbani, M. Y. Ivanov, D. M. Villeneuve, and P. B. Corkum, "Probing molecular dynamics with attosecond resolution using correlated wave packet pairs," *Nature* **421**, 826–829 (2003).
- ⁴³M. F. Kling, J. Rauschenberger, A. J. Verhoef, E. Hasović, T. Uphues, D. B. Milošević, H. G. Muller, and M. J. J. Vrakking, "Imaging of carrier-envelope phase effects in above-threshold ionization with intense few-cycle laser fields," *New J. Phys.* **10**, 025024 (2008).
- ⁴⁴G. Sansone, F. Kelkensberg, J. F. Pérez-Torres, F. Morales, M. F. Kling, W. Siu, O. Ghafur, P. Johnsson, M. Swoboda, E. Benedetti, F. Ferrari, F. Lépine, J. L. Sanz-Vicario, S. Zharebtsov, I. Znakovskaya, A. L'Huillier, M. Y. Ivanov, M. Nisoli, F. Martín, and M. J. J. Vrakking, "Electron localization following attosecond molecular photoionization," *Nature* **465**, 763–766 (2010).
- ⁴⁵S. Kangaparambil, V. Hanus, M. Dörner-Kirchner, P. He, S. Larimian, G. Paulus, A. Baltuška, X. Xie, K. Yamanouchi, F. He, E. Lötstedt, and M. Kitzler-Zeiler, "Generalized phase sensitivity of directional bond breaking in the laser-molecule interaction," *Phys. Rev. Lett.* **125**, 023202 (2020).
- ⁴⁶P. Cattaneo and M. Persico, "Wave packet dynamics in the presence of a conical intersection," *J. Phys. Chem. A* **101**, 3454–3460 (1997).
- ⁴⁷S. Matsika and P. Krause, "Nonadiabatic events and conical intersections," *Annu. Rev. Phys. Chem.* **62**, 621–643 (2011).
- ⁴⁸D. Simah, B. Hartke, and H.-J. Werner, "Photodissociation dynamics of H₂S on new coupled *ab initio* potential energy surfaces," *J. Chem. Phys.* **111**, 4523–4534 (1999).
- ⁴⁹A. Hofmann and R. de Vivie-Riedle, "Adiabatic approach for ultrafast quantum dynamics mediated by simultaneously active conical intersections," *Chem. Phys. Lett.* **346**, 299–304 (2001).
- ⁵⁰A. F. Izmaylov, J. Li, and L. Joubert-Doriol, "Diabatic definition of geometric phase effects," *J. Chem. Theory Comput.* **12**, 5278–5283 (2016).
- ⁵¹I. G. Ryabinkin, L. Joubert-Doriol, and A. F. Izmaylov, "Geometric phase effects in nonadiabatic dynamics near conical intersections," *Acc. Chem. Res.* **50**, 1785–1793 (2017).
- ⁵²W. Domcke and G. Stock, "Theory of ultrafast nonadiabatic excited-state processes and their spectroscopic detection in real time," in *Advances in Chemical Physics* (John Wiley & Sons, 2007), pp. 1–169.

SUMMARY

In this thesis various different applications of theoretical methods to analyze complex organic reactions were used. The first example was the mechanistic study of a ring contraction with triplet oxygen. The following examples involved excited states and their dynamics. First, the TICT formation of a HTI photoswitch was investigated, followed by a dynamics study of a photoinduced rotational step of a molecular motor and a photodissociation reaction. In all these reactions CoIns played a crucial role. Finally, the thesis concluded with the control of a photochemical reaction at a CoIn with a CEP stabilized laser pulse.

In the first part of chapter 1 the reaction of triplet oxygen with a particularly substituted cyclobutene derivative with a conjugated π -system including an aromatic part was investigated. A DFT/CASPT2 approach was found to describe best the oxidative ring contraction forming a cyclopropane ketone (CPK) and the oxidative ring opening reaction forming a diketone (DK). The calculated reaction mechanism explained the different experimental product distributions under thermodynamic and kinetic conditions, respectively. The CPK was identified as the kinetic product as the decisive reaction barrier is lower than the decisive barrier on the DK path. On the other hand, the DK pathway was the preferred one under thermodynamic conditions and when a pure oxygen atmosphere was applied. Further, a stabilized intermediate on the CPK pathway, an epoxide, could also be verified experimentally, supporting the calculated reaction mechanism, as well.

In the second section of chapter 1 the circumstances of the TICT formation of specifically substituted HTI derivatives as a competing pathway beside the $Z \rightarrow E$ double bond isomerization (DBI) isomerization were identified by CASSCF/CASPT2 calculations. It was found out, that the pre-twist of the central C-C single bond, resulting from sterical effects through an ortho-substitution at the stilbene part, are essential for the TICT formation. The TICT state is defined by a single bond twist (SBT) where the two aromatic parts, the thioindigo and the stilbene part, respectively, are almost perpendicular to each other. In polar solvent environments the polar TICT state was found to be the preferred pathway as it is more stabilized than the DBI pathway. In unpolar solvents, in contrast, the TICT state lies higher in energy compared to the minimum leading to the DBI pathway, so that no TICT formation could be observed. The marker bands of the TICT formation apparent in transient IR spectroscopy measurements only in polar solvents were identified by comparison with calculated IR spectra with TDDFT at relevant geometry points. It was found out that a C-O stretch vibration showing a red-shift during the TICT formation is responsible for the outstanding contour of the experimental transient IR spectra. Generally, the analysis of the two pathways in solvent turned out to be challenging as the solvent could only be included via single point calculations. Recently, gradients at the CASSCF level of theory with PCM were formulated by Chenchen Song [119] which will benefit theoretical investigations of such

reactions in the future as the solvent interaction can also be extended to the molecular geometry itself.

The first section of chapter 2 analyzed the dynamics of the first photochemical step of the rotation of an artificial molecular motor based on HTI. Extended benchmark calculations against CASSCF/CASPT2 revealed SF-TDDFT as only feasible method to calculate the dynamics. The reaction mechanism of two derivatives varying only in two substituents at the stilbene part but with significantly different reaction time was calculated. A static comparison of the optimized geometries along the reaction pathway from the *E* isomer via a S_1/S_0 CoIn to the *Z* isomer showed similar relative energies between the points not explaining the different reaction time of 1500 fs (*motor-1*) and 330 fs (*motor-2*), respectively. A linear interpolation between the optimized geometries revealed a barrier of around 1.0 eV for the slower derivative while no barrier exists on the direct path towards the decisive CoIn for the faster derivative. Thus, in the slower motor a fluctuation of additional coordinates in the FC region is necessary to circumvent the barrier on the direct path and to approach the rotational coordinate which explains the significant slower reaction time. With the calculation of a third hypothetical motor with an electron-poor stilbene part also showing no barrier towards the CoIn we concluded that the barrier of *motor-1* arises due to the electron-rich stilbene part changing the electronic character of the S_1 state. The dynamics of the faster derivative, *motor-2*, was simulated with full-dimensional semi-classical trajectories to obtain a qualitative picture of the geometrical motion during the rotation reaction. Beside the obvious dihedral angle defining the *E* → *Z* isomerization further internal coordinates are essential for the rotation. The most important one concerns the ring puckering of the aliphatic carbon atom of the five membered ring from the stilbene part. During the rotation the aliphatic methyl groups are in steric hindrance to the oxygen of the sulfur atom preventing the rotation towards the CoIn. By a planarization motion of the five membered ring the hindrance through the methyl groups is removed and the molecule can continue the rotation along the C-C double bond.

The second part of chapter 2 discussed the dynamics of the photodissociation of $\text{Ph}_2\text{CH} - \text{Br}$ with two competing reaction pathways, the homolytic and heterolytic bond cleavage channel, respectively. Two different dynamics approaches were applied to simulate the excited state reaction, a two-dimensional grid-based wave packet quantum dynamics simulation on ab-initio PES and a full-dimensional ab-initio semi-classical trajectory surface hopping simulation. Both approaches reflected the experimentally observed chronological appearance of the products with first the carboradical and second the carbocation appearing. Further, an experimentally observed fluctuation in the transient absorption signal could be identified as a vibration already triggered in the minimum of the S_1 state right after the excitation. This vibration is defined by a motion of the reactive coordinate describing the planarization of the central carbon atom due to the change in hybridization during the bond cleavage. In comparison to the highly time-resolved experiment, the quantum dynamics simulation revealed the wave packet features visible in the measured signal and the semi-classical simulation covered the full-dimensionality of the analyzed system.

The last chapter discussed the control of a reaction in the vicinity of a CoIn with a few cycle CEP laser pulse on the basis of a dissociative model system and the nucleobase uracil. For the simulation of this control scheme based upon the phase of light, the system has to be treated fully quantum to include the complete description of the geometric phase. The general conditions for an efficient control were identified, namely the direction of motion of the wave packet towards the CoIn. The phase-dependent population transfer through the CoIn was analyzed varying the different laser pulse

parameters (FWHM, t_0 , ω_0 , E_{max}). Hereby, two different control mechanisms were identified where the interaction of both determines the total CEP efficiency. The first is a pure interference mechanism where the phase of the generated superposition by the CEP pulse interferes with the geometric phase induced by the CoIn and leads to a phase-dependent population transfer with a periodicity of 2π . The second, in contrast, the so-called field-only mechanism, is solely determined by the asymmetric waveform of the few cycle pulse with only the laser pulse as coupling magnitude. With this a CEP dependent population transfer with a periodicity of π is obtained. In both systems, both mechanisms were observed and the pulse parameters for the best control efficiency were identified.

Summarized, this thesis exemplifies the diversity and the importance of computational chemistry for the analysis of complex reaction mechanisms ranging from ground state chemistry to light induced excited state dynamics and coherently controlled chemical reactions. Many choices have to be made between the appropriate electronic structure methods to be used, which level of dynamics simulation is optimal and how to include the light interaction when required. With the continuing development of new faster approaches and the increase of available computational resources the level of accuracy and the predictive power of theoretical chemistry will further improve speedily.

SUPPORTING INFORMATION TO CHAPTER 1.1

Active spaces at selected geometry points reprinted from the online available supporting information of article “Oxidative Ring Contraction of Cyclobutenes: General Approach to Cyclopropylketones including Mechanistic Insights”.

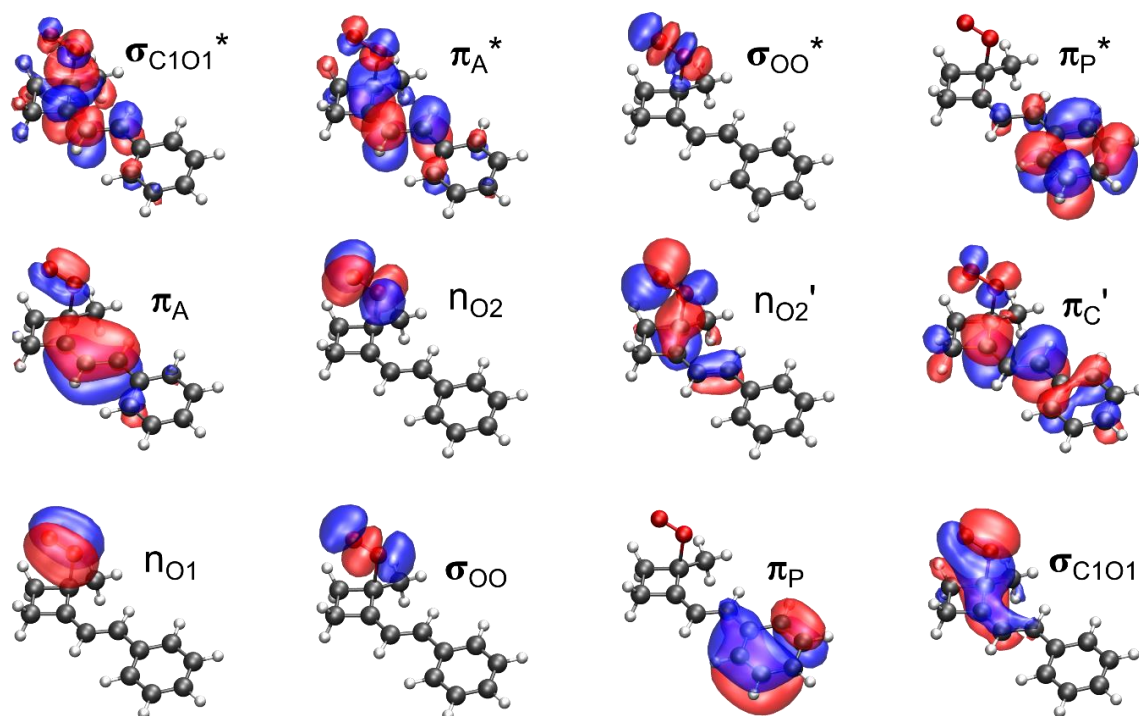


Figure S3. Orbitals of the CASPT2(14,12)/ANO-L-VDZP calculation at the geometry point TS1. The strokes mark the single occupied orbitals of the diradicalic transition state.

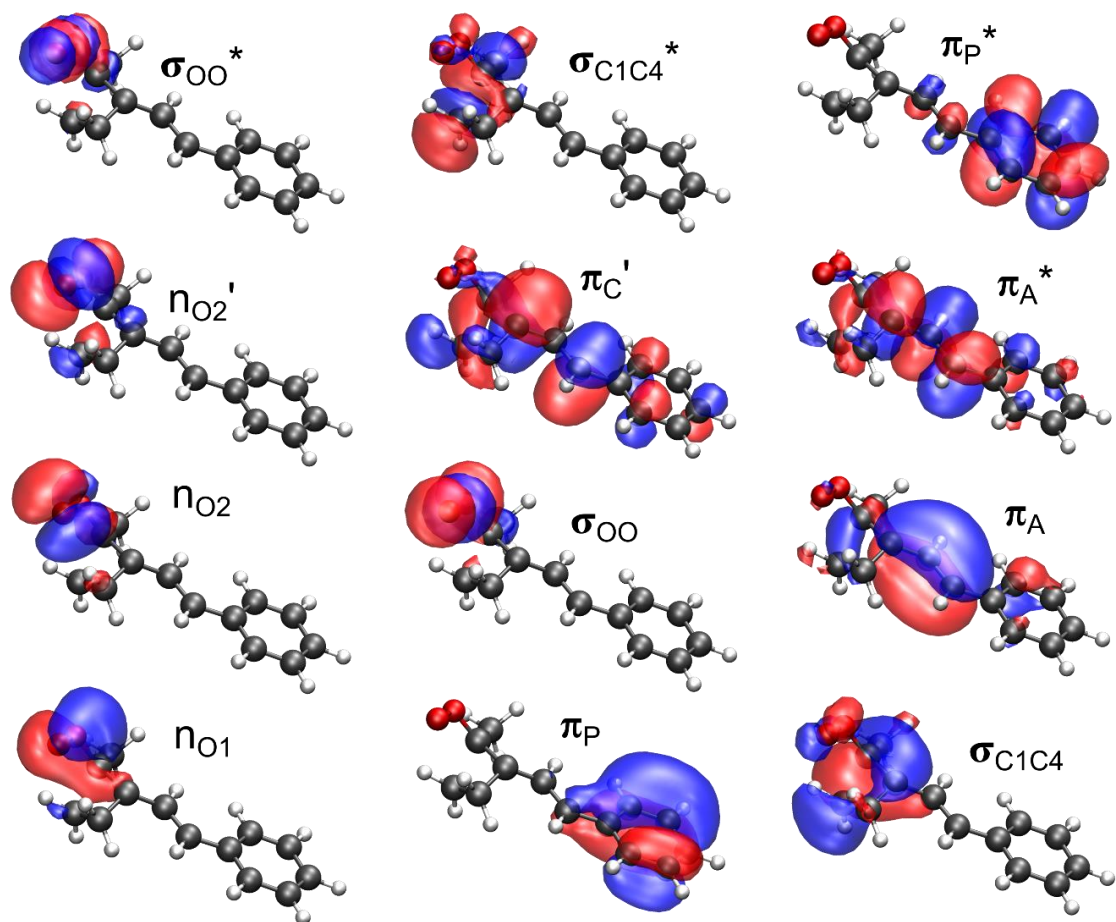


Figure S4. Orbitals of the CASPT2(14,12)/ANO-L-VDZP calculation at the geometry point TSCP1. The strokes mark the single occupied orbitals of the diradicalic transition state.

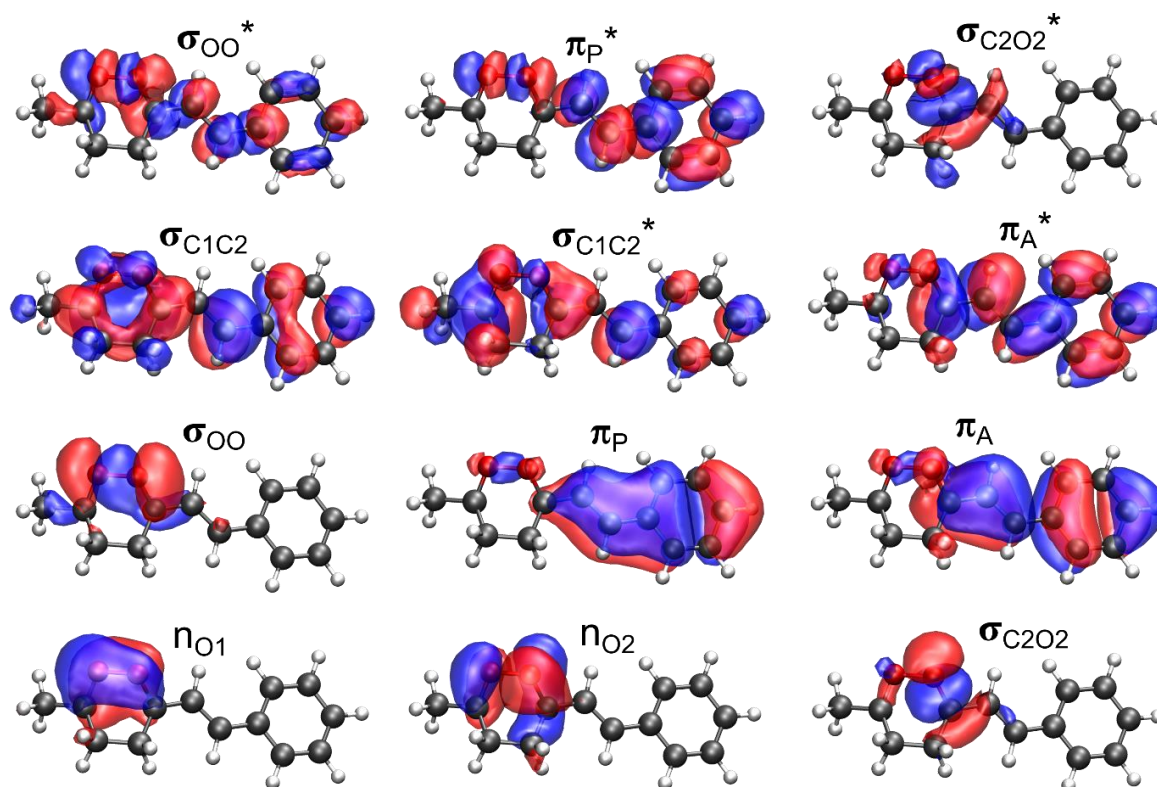


Figure S5. Orbitals of the CASPT2(14,12)/ANO-L-VDZP calculation at the geometry point TSDK2.

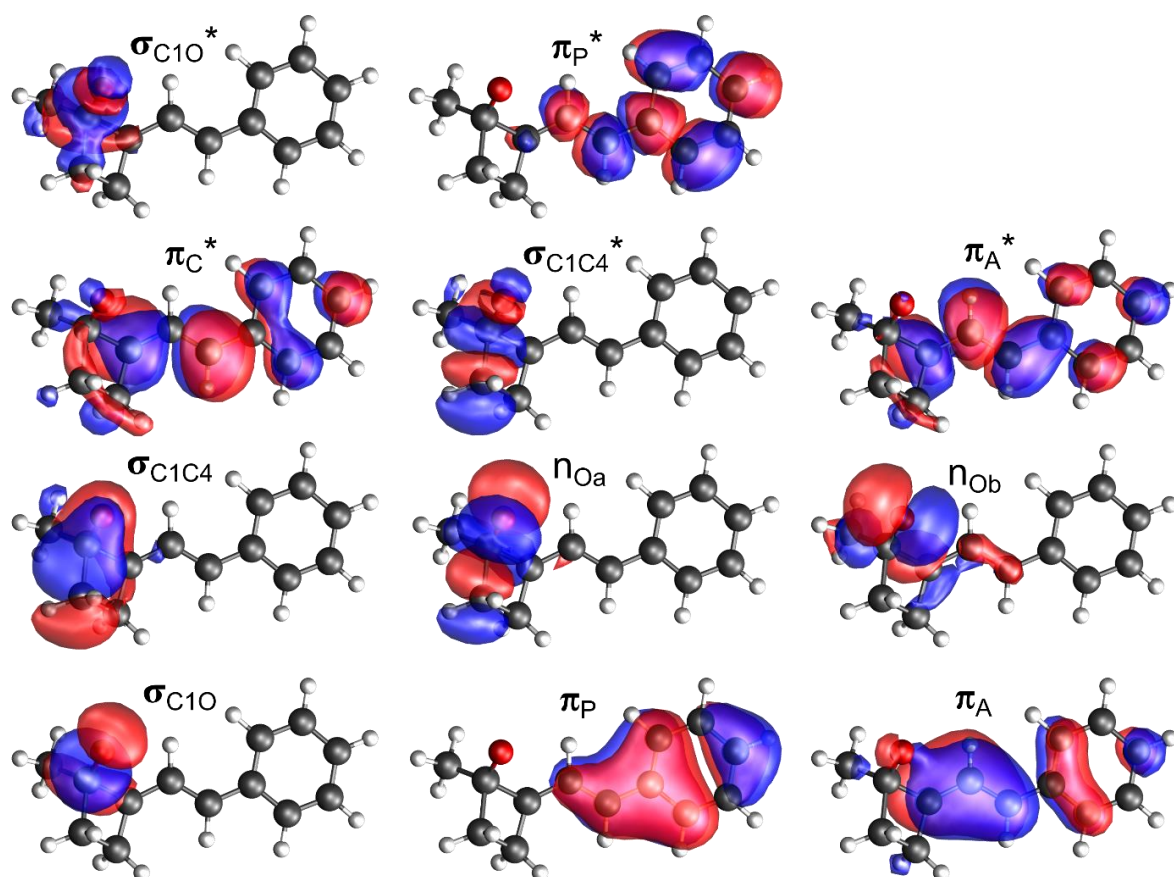


Figure S6. Orbitals of the CASPT2(12,11)/ANO-L-VDPZ calculation at the geometry point TSCP4.

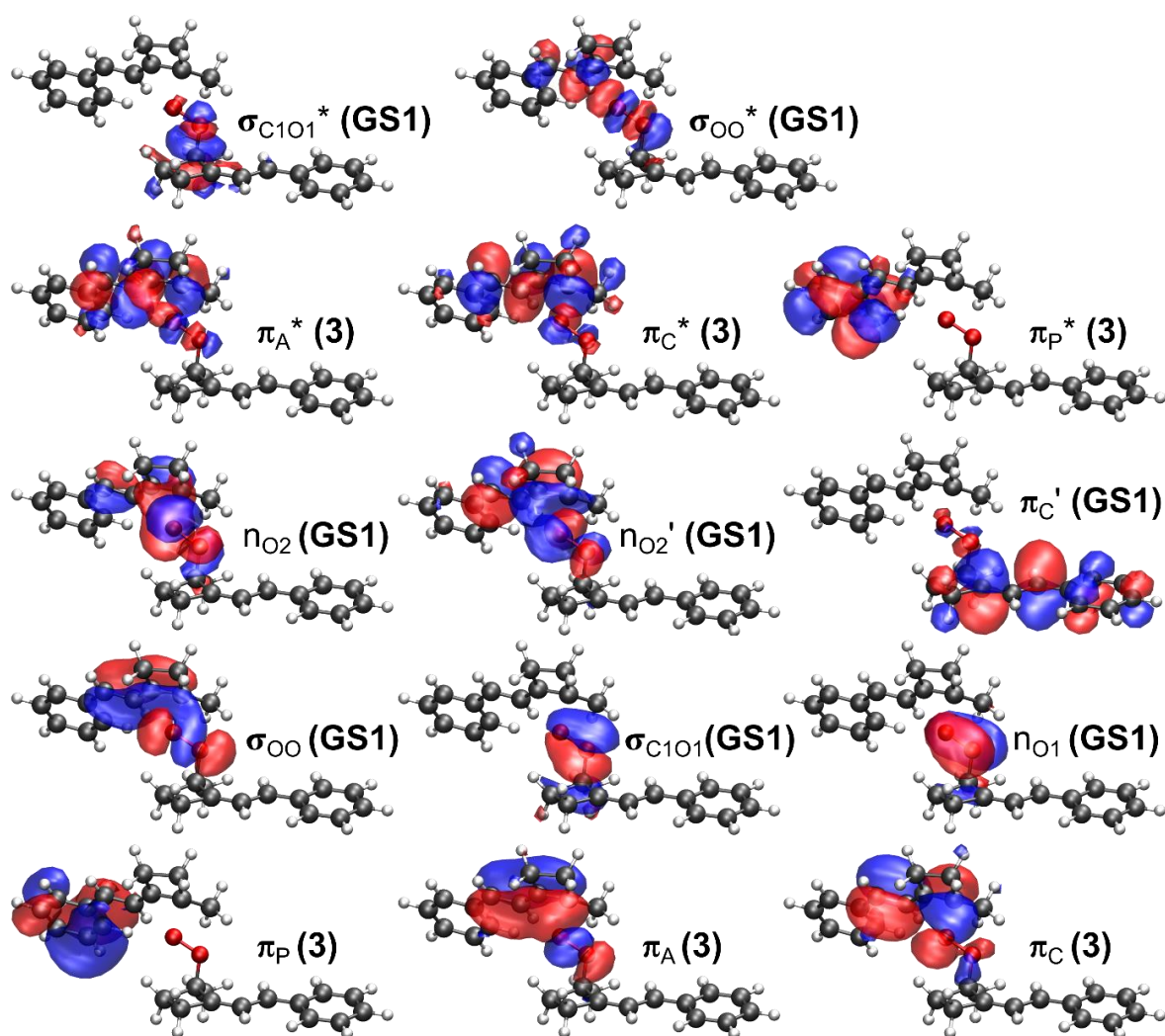


Figure S7. Orbitals of the CASPT2(16,14)/ANO-L-VDZP calculation at the geometry point TSCPX. The strokes mark the single occupied orbitals of the diradicalic transition state.

OPENMOLCAS INPUT-FILES FOR NON-EQUILIBRIUM PCM CALCULATIONS

In the following, all necessary input-files to obtain the singlet vertical excitation and deexcitation energies in solvent environment (here in dichloromethane (DCM)) using PCM with OpenMolcas [80, 81] are listed. The variables **n** and **m** denote hereby the number of electrons and orbitals forming the used active space AS(**n,m**). The number of inactive orbitals is specified as **i** and **x** is the number of calculated states. Please note, that the keyword **cionly** in the &RASSFC blocks specifies, that the orbitals of the wave function in the gas phase are used without optimization. This was necessary for the calculation of HTI derivative **Z-2** because of the strong polarity of the TICT state leading to convergence problems of some states of the CASSCF wave function. Re-optimizations in solvent environment could remove this short coming but unfortunately gradients with PCM are currently not available in OpenMolcas [80, 81].

```
&GATEWAY
COORD= geomtry.xyz
BASIS= ANO-RCC-VDZP
GROUP= NOSYM
RICD
RF-INPUT
      PCM-MODEL
      SOLVENT
      METHYLENECHLORIDE
      CONDUCTOR VERSION
END OF RF-INPUT

>> COPY cas.Joblph JOBOLD

&SEWARD

* Equilibrium Reaction Field for S0
&RASSCF
  EXPert
  JOBlph
  CIONly
  SPIN= 1
  INACTIVE= i
  NACTEL= n 0 0
  RAS2= m
  CIRoot= x x 1
  RFRoot= 1

>> COPY $Project.Joblph JOBOLD

&CASPT2
  IMAG= 0.20
  IPEA= 0.00
  MAXITer= 200
  MULTISTATE= 1 1
  NOMULT
  RFPert
```

Listing B.1: Solvent in equilibrium with S_0 (fig. 1.3 step 1)

```

&GATEWAY
COORD= geom.xyz
BASIS= ANO-RCC-VDZP
GROUP= NOSYM
RICD
RF-INPUT
  PCM-MODEL
  SOLVENT
  METHYLENECHLORIDE
  CONDUCTOR VERSION
END OF RF-INPUT

>> COPY cas.Joblph JOBOLD

&SEWARD

* Equilibrium Reaction Field for S0
&RASSCF
  EXPert
  JOBlph
  CIONly
  SPIN= 1
  INACTIVE= i
  NACTEL= n 0 0
  RAS2= m
  CRoot= s s 1
  RRoot= 1

>> COPY $Project.Joblph JOBOLD

* Non-equilibrium Reaction Field for S1
&RASSCF
  EXPert
  JOBlph
  CIONly
  SPIN= 1
  INACTIVE= i
  NACTEL= n 0 0
  RAS2= m
  CRoot= x x 1
  RRoot= 2
  NONEquilibrium

>> COPY $Project.Joblph JOBOLD

&CASPT2
  IMAG= 0.20
  IPEA= 0.00
  MAXITer= 200
  MULTISTATE= 1 2
  NOMULT
  RFPert

```

Listing B.2: Solvent in non-equilibrium in S_1 with slow part of the solvent response aligned to the S_0 (fig. 1.3 step 2)

```
&GATEWAY
COORD= geomtry.xyz
BASIS= ANO-RCC-VDZP
GROUP= NOSYM
RICD
RF-INPUT
      PCM-MODEL
      SOLVENT
      METHYLENECHLORIDE
      CONDUCTOR VERSION
END OF RF-INPUT

>> COPY cas.Joblph JOBOLD

&SEWARD

* Equilibrium Reaction Field for S1
&RASSCF
  EXPert
  JOBlph
  CIONly
  SPIN= 1
  INACTIVE= i
  NACTEL= n 0 0
  RAS2= m
  CIRoot= x x 1
  RFRoot= 2

>> COPY $Project.Joblph JOBOLD

&CASPT2
  IMAG= 0.20
  IPEA= 0.00
  MAXITer= 200
  MULTISTATE= 1 2
  NOMULT
  RFPert
```

Listing B.3: Solvent in equilibrium with S_1 (fig. 1.3 step 3)

```

&GATEWAY
COORD= geom.xyz
BASIS= ANO-RCC-VDZP
GROUP= NOSYM
RICD
RF-INPUT
  PCM-MODEL
  SOLVENT
  METHYLENECHLORIDE
  CONDUCTOR VERSION
END OF RF-INPUT

>> COPY cas.Joblph JOBOLD

&SEWARD

* Equilibrium Reaction Field for S1
&RASSCF
  EXPert
  JOBlph
  CIONly
  SPIN= 1
  INACTIVE= i
  NACTEL= n 0 0
  RAS2= m
  CRoot= s s 1
  RRoot= 2

>> COPY $Project.Joblph JOBOLD

* Non-equilibrium Reaction Field for S0
&RASSCF
  EXPert
  JOBlph
  CIONly
  SPIN= 1
  INACTIVE= i
  NACTEL= n 0 0
  RAS2= m
  CRoot= s s 1
  RRoot= 1
  NONEquilibrium

>> COPY $Project.Joblph JOBOLD

&CASPT2
  IMAG= 0.20
  IPEA= 0.00
  MAXITer= 200
  MULTISTATE= 1 1
  NOMULT
  RFPErt

```

Listing B.4: Solvent in non-equilibrium in S_0 with slow part of the solvent response aligned to the S_1 (fig. 1.3 step 4)

SUPPORTING INFORMATION TO CHAPTER 2.1

Benchmark

In SF-TDDFT a high-spin reference for the ground state is used, which means for example for the description of singlet states a triplet ground state. The excited states are calculated via spin-flip analog to standard TDDFT [91, 92]. This gives the low-spin ground state (actual ground state) a multi-reference character that is necessary for the description of some subjects, for example S_1/S_0 CoIns. In the following, the method SF-TDDFT is benchmarked against the more accurate methods CASSCF/CASPT2 that are known to describe HTIs well.

The vertical excitation energies for *motor-1* of the benchmark are shown in table C.1. The energies with CASSCF with two different active spaces, namely active space (AS)(12,11) from ref. [45] and the smaller AS(10,9) calculated with Molpro2019 [120, 121] (fig. C.11), are very similar, with the S_1 being a $n \Rightarrow \pi_c^*$ excitation, the S_2 with $\pi_{st} \Rightarrow \pi_c^*$ character and the S_3 describing a $\pi_c \Rightarrow \pi_c^*$ excitation. Correcting the energies obtained with CASSCF with an AS(10,9) by including dynamic electron correlation with CASPT2 [73] leads to a change of the order of states. The $n \Rightarrow \pi_c^*$ state is no longer the first excited state as the energy of the $\pi_{st} \Rightarrow \pi_c^*$ state is stabilized about 1.83 eV whereas the $n \Rightarrow \pi_c^*$ state is only stabilized about 0.69 eV. Thus, both states lie close in energy with only 0.08 eV apart. The excitation energies obtained with SF-TDDFT are comparable to the CASPT2 results. The order of states is equal and the excitation energies are in the same range. The only difference is, that the lone pair orbital (n) describing the S_2 state at the SF-TDDFT level of theory is localized more at the oxygen of the sulfur atom whereas the lone pair orbital included in the AS(10,9) is located at the oxygen of the thioindigo part (compare fig. C.11 and C.10). So summarized the benchmark showed that SF-TDDFT is capable to adequately describe the HTI based *motor-1*.

For comparison the vertical excitation energies for *motor-2* are calculated at the CASSCF and CASPT2 level of theory with an AS(10,9), as well (tab. C.2). The main difference compared to *motor-1* lies in the order of states. The S_1 state retains the $n \Rightarrow \pi_c^*$ character at the CASPT2 and SF-TDDFT level of theory. The character of the S_2 and S_3 state are interchanged with CASPT2 compared to CASSCF and SF-TDDFT. The CASPT2 calculation is performed to verify the character of the S_1 state at the SF-TDDFT level of theory which is succeeded. The order of the higher excited states is not significant as only the dynamic in the S_1 state should be investigated.

Further, the vertical excitation energies of *motor-3* are similar to *motor-2* with the same order of states (table C.3).

Table C.1: Vertical excitation energies at the **A** isomer of *motor-1* (crystal structure[45]).

state	character	CASSCF ^a		CASSCF ^b		CASPT2 ^c		SF-TDDFT ^d	
		ΔE^e	f^f	ΔE^e	f^f	ΔE^e	f^f	ΔE^e	f^f
S ₁	$\pi_{st} \Rightarrow \pi_c^*$	5.40	0.148	5.13	0.094	3.30	0.067	3.52	0.074
S ₂	$n \Rightarrow \pi_c^*$ ^g	3.83	0.001	4.07	0.003	3.38	0.002	3.77	0.037
S ₃	$\pi_c \Rightarrow \pi_c^*$ ^h	5.94	0.507	5.82	0.380	3.85	0.289	4.21	0.511
T ₁	$\pi_c \Rightarrow \pi_c^*$	3.16	–	–	–	–	–	3.07	–

^a CASSCF(12,11)/6-31G* from ref. [45]^b CASSCF(10,9)/6-31G* (AS in fig. C.11)^c CASPT2(10,9)/6-31G* (AS in fig. C.11)^d SF-TDDFT: BHHLYP/6-31G* (relevant orbitals in fig. C.10)^e excitation energy in eV^f oscillator strength^g lone pair orbital in the SF-TDDFT calculation is localized at the sulfur-oxygen.^h excitation from π_c in CASSCF and a more delocalized π_c orbital in SF-TDDFTTable C.2: Vertical excitation energies at the **A** isomer of *motor-2* (optimized geometry with ORCA 5.0).

state	character	CASSCF ^b		CASPT2 ^c		SF-TDDFT ^d	
		ΔE^e	f^f	ΔE^e	f^f	ΔE^e	f^f
S ₁	$n \Rightarrow \pi_c^*$ ^g	3.94	0.002	3.45	0.002	3.74	0.059
S ₂	$\pi_{st} \Rightarrow \pi_c^*$	5.56	0.034	3.94	0.024	4.03	0.040
S ₃	$\pi_c \Rightarrow \pi_c^*$ ^h	5.78	0.522	3.58	0.323	4.16	0.466

^a CASSCF(10,9)/6-31G* (AS in fig. C.13)^b CASPT2(10,9)/6-31G* (AS in fig. C.13)^c SF-TDDFT: BHHLYP/6-31G* (relevant orbitals in fig. C.12)^d excitation energy in eV^e oscillator strength^f lone pair orbital in the SF-TDDFT calculation is localized at the sulfur-oxygen.^h excitation from π_c in CASSCF and a more delocalized π_c orbital in SF-TDDFTTable C.3: Vertical excitation energies of *motor-3* with SF-TDDFT BHHLYP/6-31G* at the optimized geometry with ORCA 5.0

state	ΔE (eV)	$\langle S^2 \rangle$	osc. str.	character	CI-coef
ORCA (UHF reference)					
S ₀	0.00	0.12	–	π^2	-0.9820
T ₁	3.09	2.15	0.00	$\pi_c \Rightarrow \pi_c^*$	-0.5842
S ₁	3.54	0.82	0.03	$n_1 \Rightarrow \pi_c^*$	-0.7358
S ₂	4.04	0.65	0.41	$\pi_{st} \Rightarrow \pi_c^*$	0.6642
S ₃	4.23	1.10	0.02	$\pi_c \Rightarrow \pi_c^*$	-0.6201

Interpolation

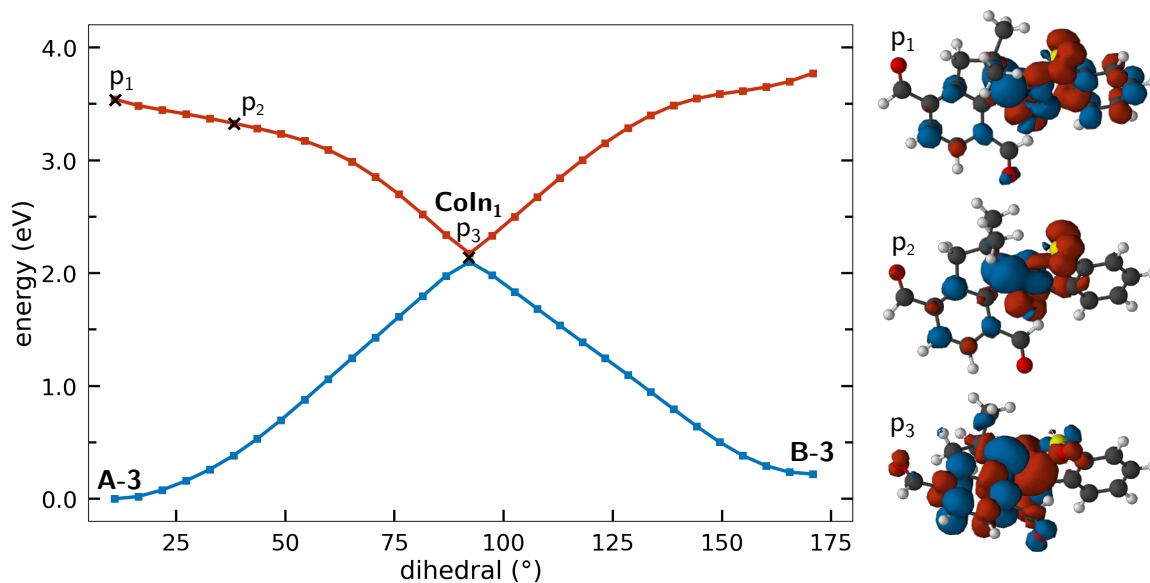


Figure C.1: Linear interpolation of *motor-3* between the isomers **A** and **B** via **Coln₁**. The S₀ is shown in blue and the S₁ in red. The dihedral angle C1-C2-C3-C4 (fig. 2.1) is selected as reaction coordinate. The spin density difference between the S₀ and S₁ state is visualized on the right with an isovalue of ± 0.002 for the selected points p1 to p3.

Table C.4: Vertical excitation energies of *motor-1* at the selected points of the interpolation (fig. 2.3 (a))

state	ΔE (eV)	$\langle S^2 \rangle$	osc. str.	character	CI-coef
p₁ (A-1)					
S ₀	0.00	0.10	–	π^2	-0.9845
T ₁	3.12	2.10	0.00	$\pi_c \Rightarrow \pi_c^*$	-0.5797
S ₁	3.53	0.91	0.07	$\pi_{st} \Rightarrow \pi_c^*$	-0.8559
S ₂	3.83	0.93	0.05	$n_1 \Rightarrow \pi_c^*$	0.7800
S ₃	4.23	0.62	0.49	$\pi_c \Rightarrow \pi_c^*$	0.7324
p₂ (barrier)					
S ₀	2.03	0.13	–	π^2	-0.9403
T ₁	3.81	2.20	0.00	$\pi_c \Rightarrow \pi_c^*$	0.6124
S ₁	4.66	0.45	0.20	$\pi_c \Rightarrow \pi_c^*$	-0.5861
				$n_1 \Rightarrow \pi_c^*$	0.5682
S ₂	4.92	1.10	0.05	$\pi_{st} \Rightarrow \pi_c^*$	-0.8517
S ₃	5.36	0.91	0.27	$\pi_c \Rightarrow \pi_c^*$	-0.6065
p₃ (CoIn₁)					
T ₁	2.08	1.23	–	$\pi_c \Rightarrow \pi_c^*$	0.7514
S ₀	2.11	0.31	–	π^2	-0.9075
S ₁	2.12	1.00	–	$\pi_c \Rightarrow \pi_c^*$	0.9350
S ₂	3.59	1.21	–	$n_1 \Rightarrow \pi_c^*$	-0.5145
				$\pi_c \Rightarrow \pi_c^*$	-0.5136
S ₃	4.21	1.19	–	$\pi_{st} \Rightarrow \pi_c^*$	-0.6777

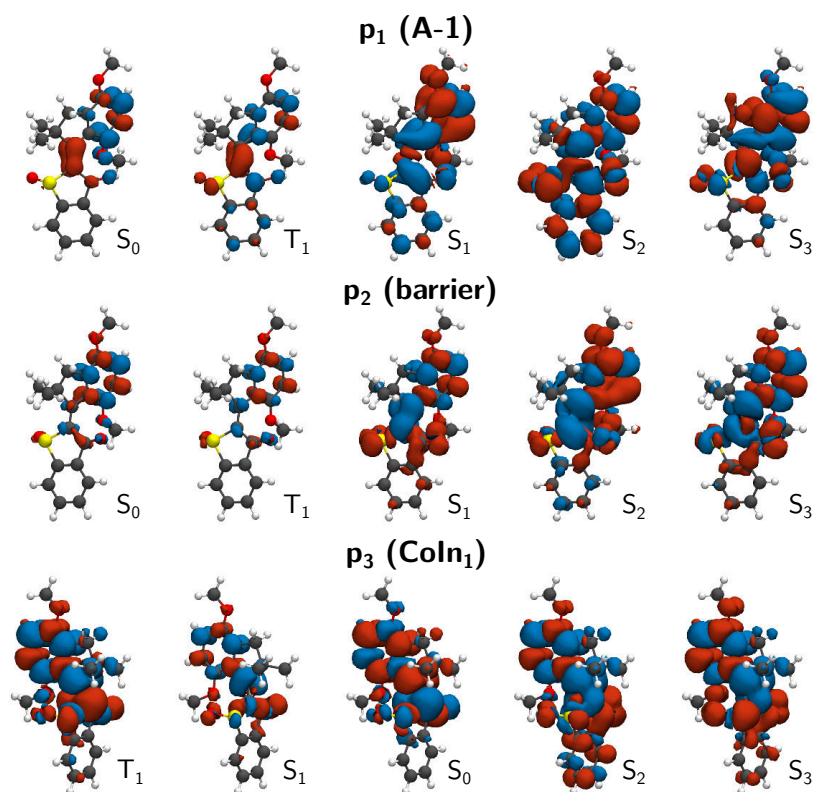
Figure C.2: Spin density of *motor-1* along the interpolation in fig. 2.3 (a)

Table C.5: Vertical excitation energies of *motor-2* at the selected points of the interpolation (fig. 2.3 (b))

state	ΔE (eV)	$\langle S^2 \rangle$	osc. str.	character	CI-coef
p₁ (A-2)					
S ₀	0.00	0.11	–	π^2	0.9658
T ₁	3.17	2.15	0.00	$\pi_c \Rightarrow \pi_c^*$	0.6009
S ₁	3.74	0.84	0.06	$n_1 \Rightarrow \pi_c^*$	0.6078
S ₂	4.03	1.06	0.04	$\pi_{st} \Rightarrow \pi_c^*$	-0.9021
S ₃	4.16	0.64	0.47	$\pi_c \Rightarrow \pi_c^*$	0.7607
p₂ (barrier)					
S ₀	0.46	0.12	–	π^2	0.9142
T ₁	2.68	2.17	0.00	$\pi_c \Rightarrow \pi_c^*$	-0.5920
S ₁	3.48	0.57	0.13	$n_1 \Rightarrow \pi_c^*$	-0.6012
				$\pi_c \Rightarrow \pi_c^*$	-0.5362
S ₂	4.07	0.80	0.36	$\pi_c \Rightarrow \pi_c^*$	-0.7040
S ₃	4.18	1.09	0.04	$\pi_{st} \Rightarrow \pi_c^*$	0.9363
p₃ (CoIn₁)					
T ₁	2.03	1.22	–	$\pi_c \Rightarrow \pi_c^*$	-0.7293
S ₀	2.08	0.38	–	π^2	-0.8882
S ₁	2.08	0.94	–	$\pi_c \Rightarrow \pi_c^*$	0.9342
S ₂	3.57	1.22	–	$n_1 \Rightarrow \pi_c^*$	-0.6154
S ₃	4.27	1.23	–	$\pi_c \Rightarrow \pi_c^*$	-0.4926

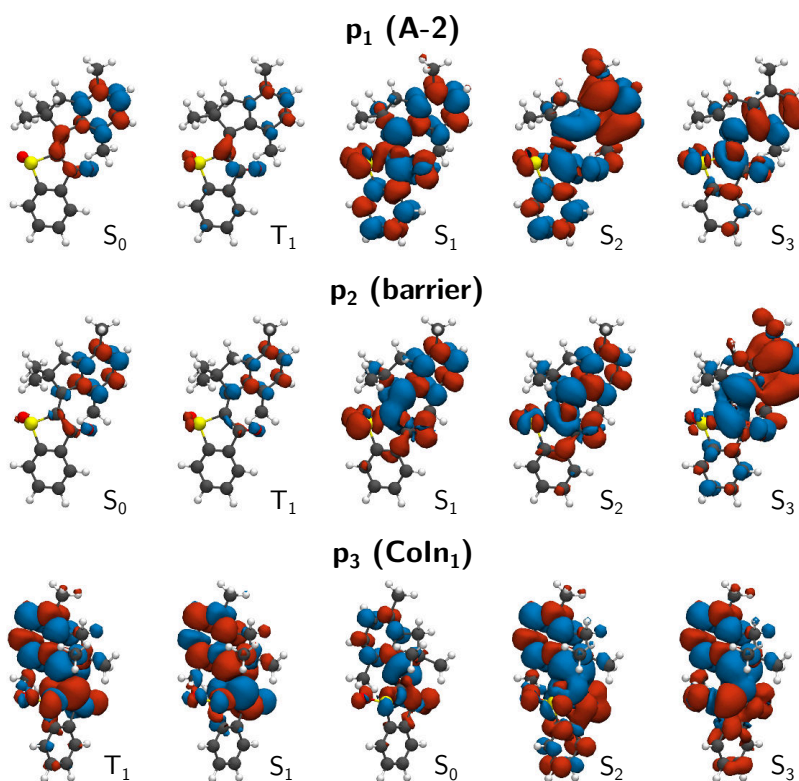
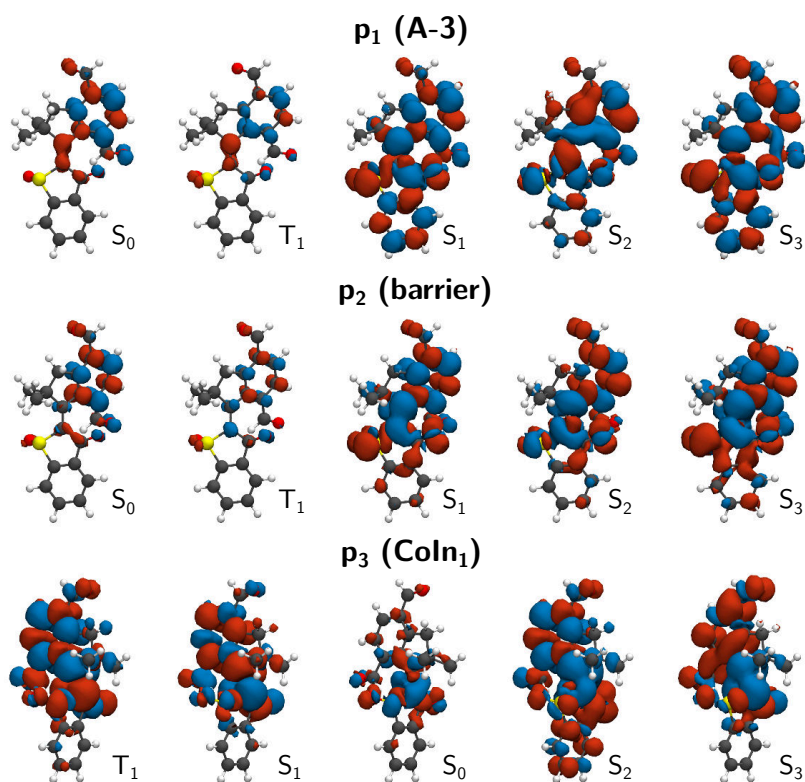


Figure C.3: Spin density of *motor-2* along the interpolation in fig. 2.3 (b)

Table C.6: Vertical excitation energies of *motor-3* along the interpolation in fig. C.1

state	ΔE (eV)	$\langle S^2 \rangle$	osc. str.	character	CI-coef
p₁ (A-3)					
S ₀	0.00	0.12	–	π^2	0.9820
T ₁	3.09	2.15	0.00	$\pi_c \Rightarrow \pi_c^*$	-0.5842
S ₁	3.54	0.82	0.03	$n_1 \Rightarrow \pi_c^*$	-0.7358
S ₂	4.04	0.65	0.42	$\pi_{st} \Rightarrow \pi_c^*$	-0.6642
				$\pi_c \Rightarrow \pi_c^*$	-0.5431
S ₃	4.23	1.10	0.02	$\pi_c \Rightarrow \pi_c^*$	-0.62011
p₂ (barrier)					
S ₀	0.38	0.13	–	π^2	-0.9588
T ₁	2.61	2.20	0.00	$\pi_c \Rightarrow \pi_c^*$	0.5641
S ₁	3.33	0.67	0.08	$n_1 \Rightarrow \pi_c^*$	-0.6510
				$\pi_c \Rightarrow \pi_c^*$	0.4945
S ₂	3.95	0.80	0.32	$\pi_{st} \Rightarrow \pi_c^*$	0.5572
				$\pi_c \Rightarrow \pi_c^*$	0.5087
S ₃	4.14	1.16	0.04	$n_2 \Rightarrow \pi_c^*$	-0.4892
				$\pi_c \Rightarrow \pi_c^*$	0.4869
p₃ (CoIn₁)					
T ₁	2.10	1.25	–	$\pi_c \Rightarrow \pi_c^*$	-0.7463
S ₀	2.17	1.00	–	π^2	-0.8624
S ₁	2.17	0.40	–	$\pi_c \Rightarrow \pi_c^*$	-0.9025
S ₂	3.54	1.20	–	$\pi_c \Rightarrow \pi_c^*$	-0.5515
				$n_1 \Rightarrow \pi_c^*$	0.4112
S ₃	4.10	1.20	–	$\pi_c \Rightarrow \pi_1^*$	0.7351

Figure C.4: Spin density of *motor-3* at the selected points of the interpolation (fig. C.1)

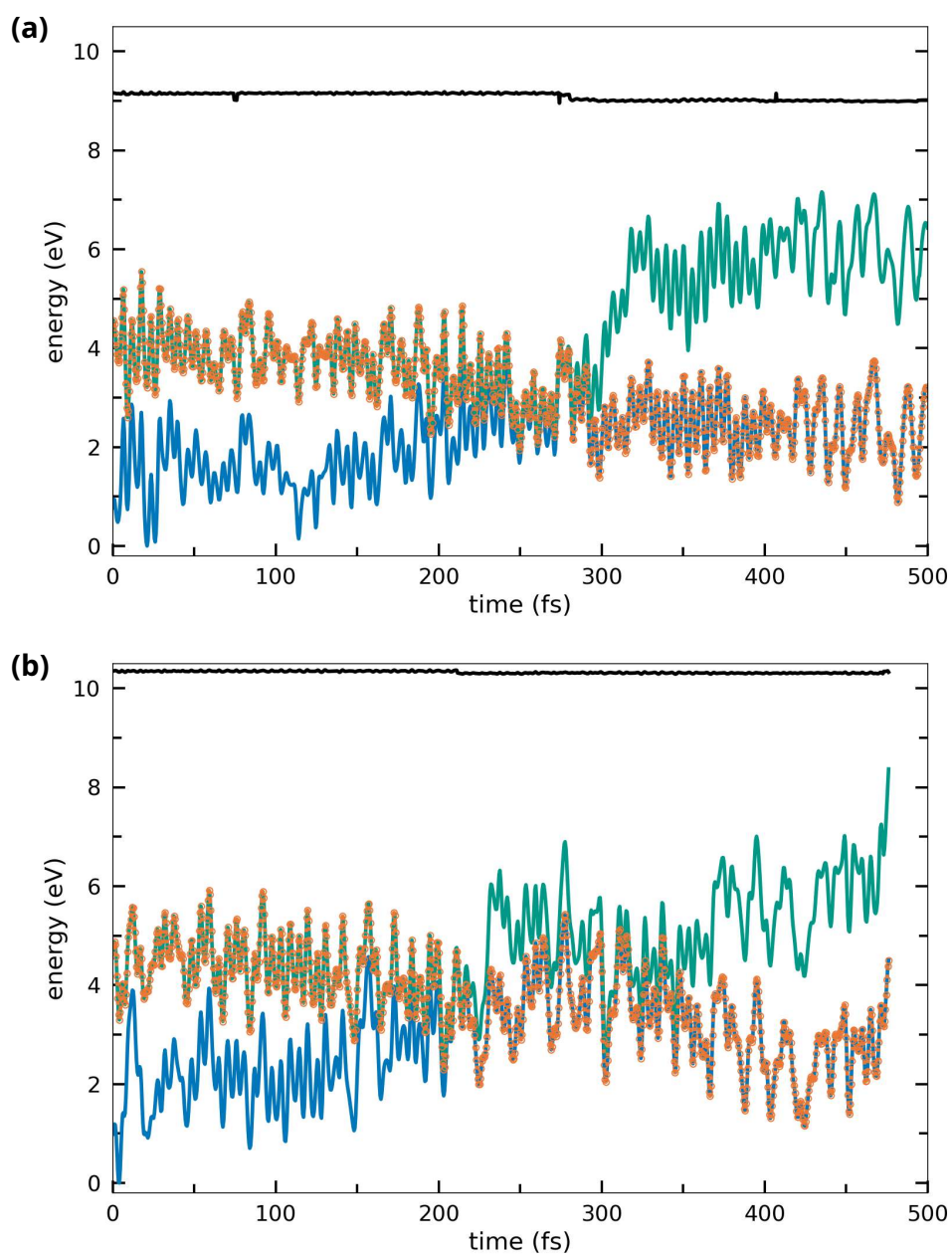
On-the-fly dynamic

Figure C.5: Potential energy surfaces for a typical trajectory ending in the *Z* isomer (a) and a typical trajectory returning to the *E* isomer (b). The currently occupied state is marked with orange circles.

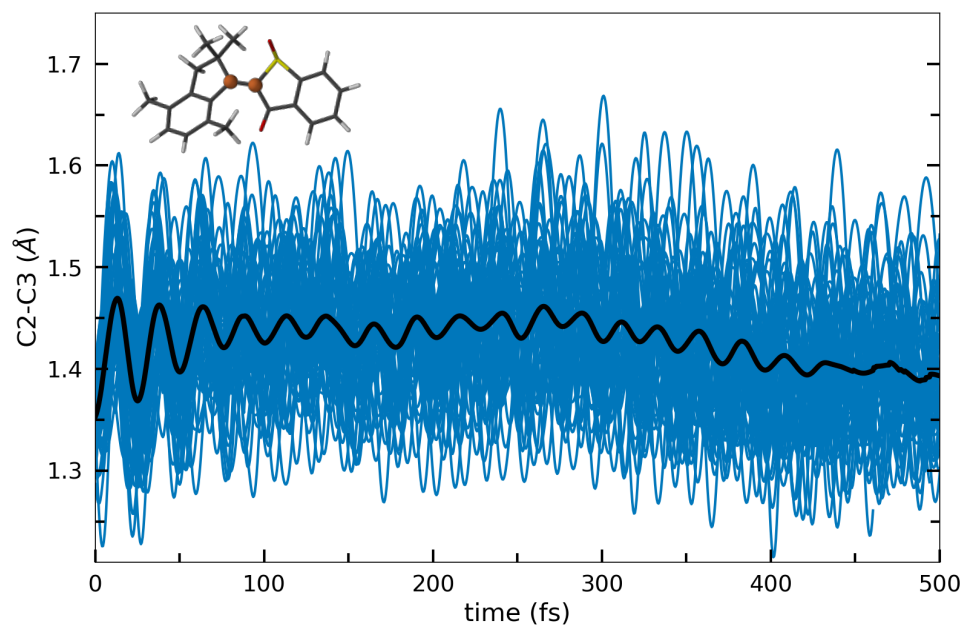


Figure C.6: Evolution of the C2-C3 bond length during the simulation. The black line shows the averaged bond length over all trajectories.

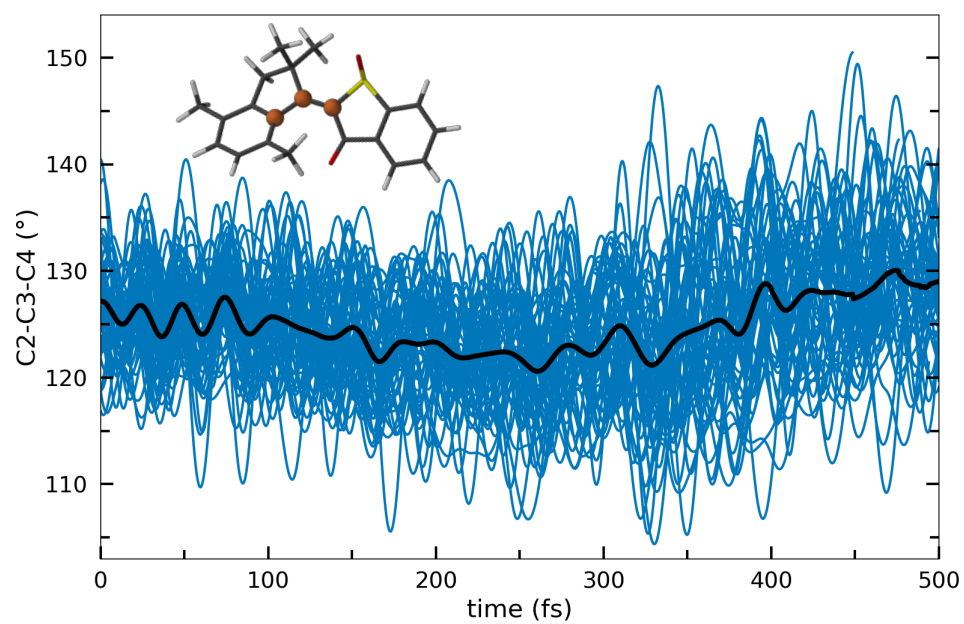


Figure C.7: Evolution of the C2-C3-C4 angle during the simulation. The black line shows the averaged angle over all trajectories.

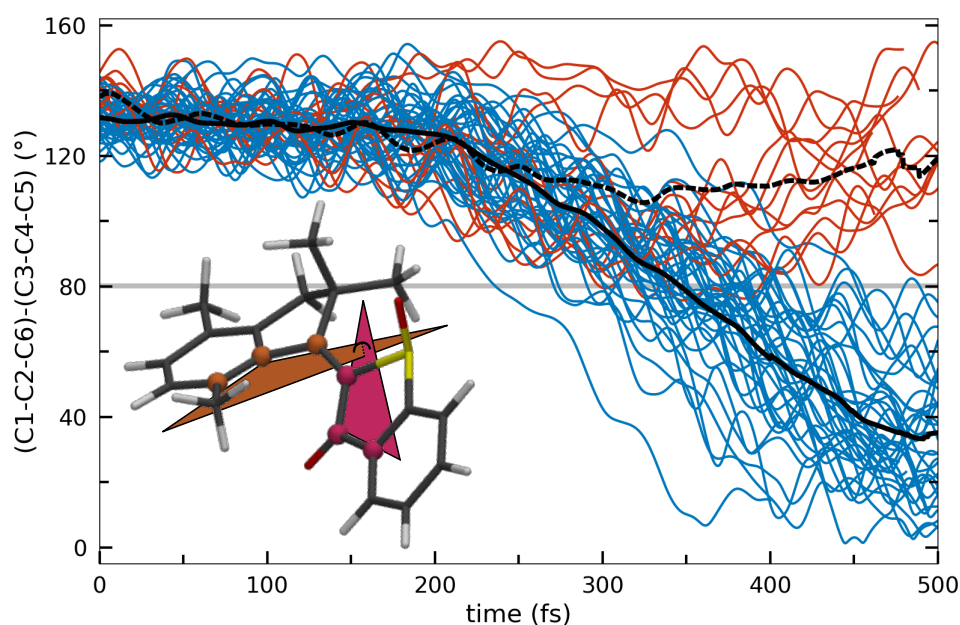


Figure C.8: Evolution of the angle between the thioindigo and stilbene part defined as the angle between the planes spanned by C1-C2-C6 and C3-C4-C5 during the simulation. Trajectories undergoing the $E \rightarrow Z$ isomerization are visualized in blue and trajectories staying in the E isomer are shown in red. The black solid and dashed lines show the averaged angle over all trajectories ending in the Z or E configuration, respectively.

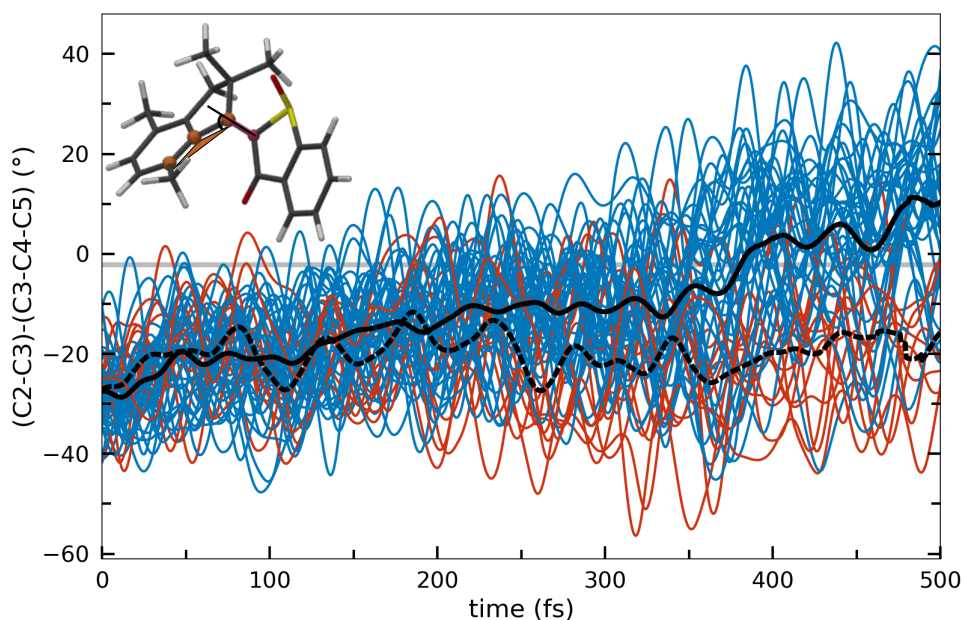


Figure C.9: Evolution of the angle between the C2-C3 bond and the plane spanned by C3-C4-C5 during the simulation. Trajectories undergoing the $E \rightarrow Z$ isomerization are visualized in blue and trajectories staying in the E isomer are shown in red. The black solid and dashed lines show the averaged angle over all trajectories ending in the Z or E configuration, respectively.

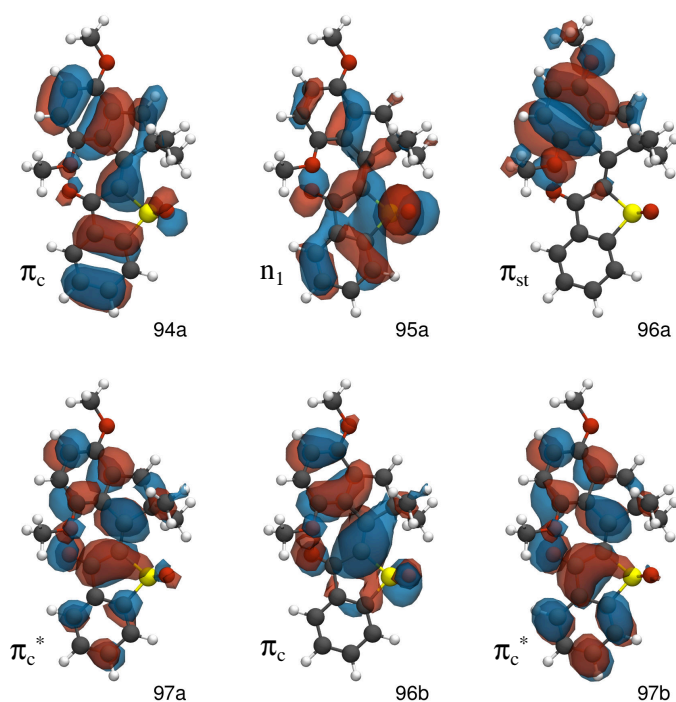
Important orbitals belonging to the benchmark

Figure C.10: Relevant orbitals of *motor-1* of the SF-TDDFT calculation with UHF reference (ORCA 5.0).

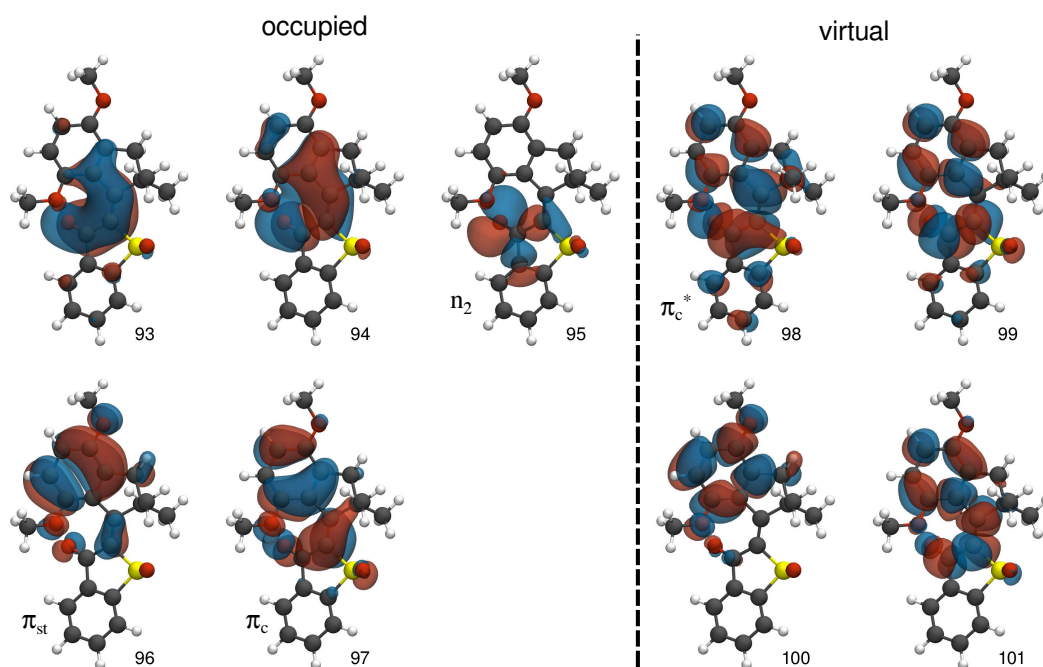


Figure C.11: Active space of *motor-1* of the CAS(10,9) calculation with Molpro2019 [120, 121].

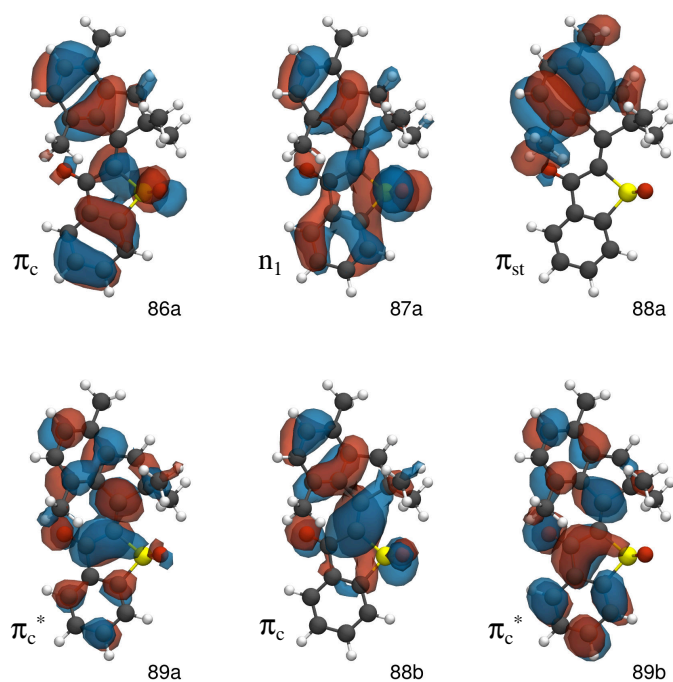


Figure C.12: Relevant orbitals of *motor-2* of the SF-TDDFT calculation with UHF reference (ORCA 5.0).

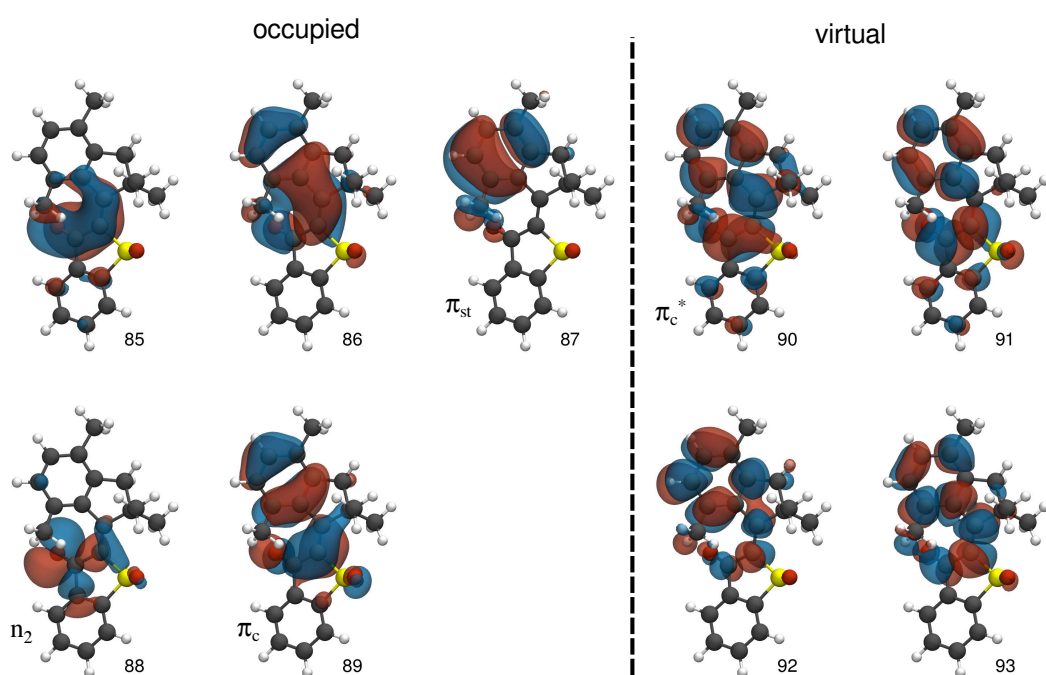


Figure C.13: Active space of *motor-2* of the CAS(10,9) calculation with Molpro2019 [120, 121].

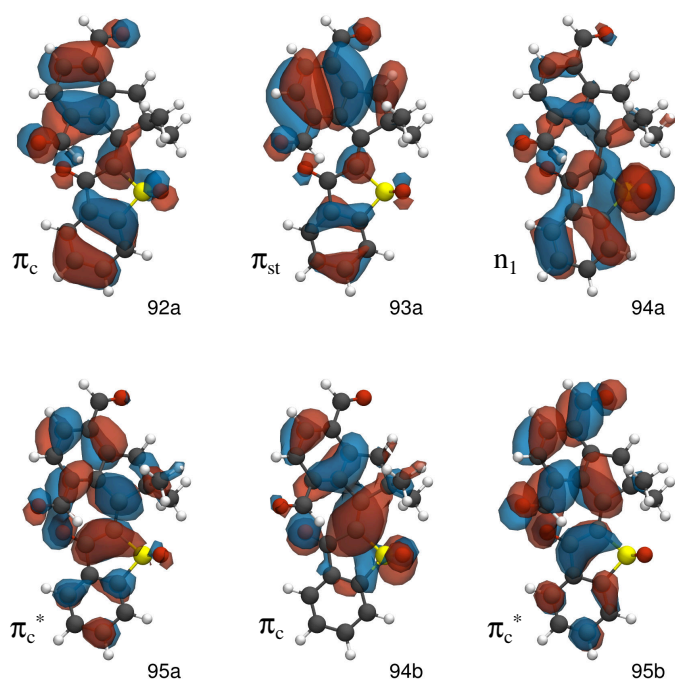


Figure C.14: Relevant orbitals of *motor-3* of the SF-TDDFT calculation with UHF reference (ORCA 5.0).

Optimized Geometries
Table C.7: *motor-1 A-1*

C	-3.428827	-0.406639	-0.130080
O	-0.870731	1.738377	-1.249228
O	0.369386	2.055123	1.083248
C	-4.772264	-0.598610	0.133283
C	-3.796475	1.885722	-0.745248
C	-5.143727	1.709805	-0.485417
C	-5.625642	0.479709	-0.040859
C	-2.937586	0.814686	-0.546282
C	-1.469059	0.836748	-0.717939
C	-0.895452	-0.451274	-0.243572
C	0.396332	-0.729704	-0.014714
C	1.059511	-2.112117	0.109705
C	3.870670	1.648878	0.091542
C	3.882713	0.306169	-0.265196
C	2.684106	-0.384086	-0.243563
C	2.455232	-1.834324	-0.510027
C	1.496613	1.570561	0.549492
C	2.696292	2.264735	0.508263
C	1.206743	-2.470647	1.596420
C	1.487863	0.242971	0.083344
C	0.257942	3.436133	1.308922
C	0.392042	-3.269730	-0.627151
H	4.777783	2.227018	0.084492
H	2.740988	3.289196	0.830779
H	-0.763014	3.605579	1.625415
H	0.934284	3.766144	2.095526
H	0.452390	3.995153	0.397195
H	2.439189	-2.036083	-1.581309
H	3.227668	-2.464610	-0.077589
H	1.743534	-3.412564	1.693193
H	1.762703	-1.707497	2.134672
H	0.227943	-2.577997	2.052113
H	-0.478912	-3.644101	-0.101426
H	0.109669	-2.996297	-1.640875
H	1.102471	-4.091858	-0.692103
H	-3.399623	2.828014	-1.084049
H	-5.829684	2.529362	-0.623400
H	-6.677322	0.363588	0.164204
H	-5.139476	-1.553322	0.471345
S	-2.194453	-1.694516	-0.081523
O	-2.171657	-2.322892	1.276783
O	4.983970	-0.395988	-0.626474
C	6.219648	0.265327	-0.646921
H	6.486498	0.645060	0.338476
H	6.952075	-0.470129	-0.955023
H	6.219748	1.089425	-1.359047

Table C.8: *motor-1* **CoIn₁**

C	3.260220	-0.086604	0.554887
O	1.433918	1.154257	-2.223544
O	-0.046938	-1.983886	-0.464570
C	4.452859	-0.575028	1.051895
C	4.222132	0.267818	-1.617462
C	5.426194	-0.214776	-1.131152
C	5.538409	-0.640060	0.189483
C	3.134152	0.319854	-0.761906
C	1.763886	0.753217	-1.122639
C	0.883552	0.633760	0.024943
C	-0.532352	0.835699	0.022813
C	-1.215001	2.165282	0.305031
C	-3.714129	-1.801001	-0.363658
C	-3.901483	-0.435121	-0.203497
C	-2.785380	0.372411	-0.109431
C	-2.718627	1.855611	0.065299
C	-1.313080	-1.554051	-0.365809
C	-2.435210	-2.351271	-0.442964
C	-0.981891	2.574891	1.767999
C	-1.499842	-0.171107	-0.173574
C	0.241385	-3.324885	-0.153637
C	-0.704441	3.271291	-0.622735
H	-4.558131	-2.463723	-0.434222
H	-2.337696	-3.414486	-0.575068
H	1.317851	-3.388071	-0.072657
H	-0.205076	-3.602851	0.796968
H	-0.105904	-3.995004	-0.938163
H	-3.083137	2.359028	-0.829921
H	-3.345205	2.198142	0.885757
H	-1.491412	3.513557	1.978021
H	-1.363276	1.819635	2.450891
H	0.076360	2.714401	1.973788
H	0.346797	3.479283	-0.440917
H	-0.808866	2.988409	-1.665585
H	-1.263618	4.189269	-0.450201
H	4.109515	0.590134	-2.639023
H	6.284530	-0.267493	-1.780580
H	6.480359	-1.021273	0.548511
H	4.535414	-0.901837	2.075268
S	1.772627	0.156588	1.522460
O	1.297910	-1.142928	2.087185
O	-5.106505	0.182247	-0.121841
C	-6.263841	-0.600354	-0.229134
H	-6.323801	-1.337404	0.570617
H	-7.100403	0.082120	-0.146775
H	-6.312408	-1.111859	-1.189584

Table C.9: *motor-1 B-1*

C	3.094932	0.580252	-0.647308
O	2.109349	-1.977480	1.555502
O	-0.759660	2.266362	0.835474
C	4.088360	1.144349	-1.422423
C	4.497469	-1.295174	-0.093291
C	5.494174	-0.749338	-0.885173
C	5.289451	0.458692	-1.545295
C	3.293747	-0.618226	0.010915
C	2.105380	-1.063506	0.767887
C	0.943581	-0.205279	0.409675
C	-0.337117	-0.612693	0.330327
C	-0.830222	-2.079832	0.401216
C	-4.058096	1.262707	-0.395662
C	-3.848062	-0.095033	-0.586087
C	-2.588095	-0.608422	-0.323676
C	-2.162211	-2.031351	-0.391566
C	-1.774002	1.567525	0.324098
C	-3.033164	2.081372	0.067683
C	0.067069	-3.138068	-0.241706
C	-1.536592	0.200585	0.082670
C	-0.891365	3.637100	1.117133
C	-1.112291	-2.440713	1.865849
H	-5.021801	1.702853	-0.581943
H	-3.238749	3.122112	0.241996
H	0.086494	3.943633	1.458809
H	-1.164427	4.195397	0.223699
H	-1.638547	3.802204	1.891037
H	-2.906068	-2.708810	0.019249
H	-2.000918	-2.332103	-1.426761
H	-0.523481	-4.038645	-0.399513
H	0.428171	-2.809019	-1.214344
H	0.914041	-3.400642	0.374806
H	-0.193654	-2.413284	2.440468
H	-1.826407	-1.751276	2.310340
H	-1.530963	-3.443875	1.923085
H	4.634413	-2.224629	0.433738
H	6.437022	-1.260140	-0.991221
H	6.077393	0.871982	-2.153557
H	3.941925	2.092993	-1.912089
S	1.549229	1.394612	-0.215984
O	1.958251	2.358730	0.853332
O	-4.785986	-0.980529	-1.000861
C	-6.084362	-0.510426	-1.242956
H	-6.665862	-1.370258	-1.550621
H	-6.527344	-0.080613	-0.345554
H	-6.097702	0.233104	-2.038800

Table C.10: *motor-2 A-2*

C	-3.458597	-0.444500	-0.158944
O	-0.903946	1.698667	-1.298966
C	-4.801683	-0.639466	0.102569
C	-3.843555	1.816690	-0.873570
C	-5.191077	1.637078	-0.617456
C	-5.664012	0.421909	-0.124813
C	-2.976563	0.762954	-0.623788
C	-1.506564	0.797447	-0.769870
C	-0.921376	-0.463426	-0.247138
C	0.378930	-0.726113	-0.014725
C	1.033309	-2.109140	0.119844
C	3.890978	1.585397	0.050731
C	3.882794	0.256223	-0.352873
C	2.663180	-0.396204	-0.303097
C	2.399632	-1.844235	-0.561099
C	1.514186	1.564013	0.565893
C	2.745828	2.204455	0.525935
C	1.235666	-2.432197	1.608951
C	1.477781	0.250869	0.070484
C	0.344556	-3.288970	-0.560068
H	4.818991	2.135886	0.037059
H	2.815259	3.213960	0.899414
H	2.325950	-2.049358	-1.630194
H	3.177213	-2.493962	-0.164634
H	1.771840	-3.374066	1.708872
H	1.811861	-1.658716	2.109276
H	0.273512	-2.527308	2.101961
H	-0.502623	-3.655220	0.008398
H	0.022989	-3.046951	-1.569910
H	1.058615	-4.107719	-0.628674
H	-3.453302	2.749276	-1.245037
H	-5.883927	2.443107	-0.794120
H	-6.715959	0.304025	0.077601
H	-5.162066	-1.582065	0.479601
S	-2.210008	-1.713147	-0.045599
O	-2.187921	-2.283198	1.337364
C	0.361712	2.269641	1.215317
H	-0.151379	2.914900	0.509506
H	-0.367768	1.570226	1.612190
H	0.722718	2.881142	2.037918
C	5.136661	-0.447254	-0.786950
H	5.391955	-1.262787	-0.111639
H	5.031264	-0.877858	-1.780912
H	5.979666	0.236858	-0.809630

Table C.11: *motor-2 CoIn₁*

C	3.350475	0.018295	0.502292
O	1.402508	1.178771	-2.225843
C	4.573604	-0.425074	0.967715
C	4.243306	0.398185	-1.699270
C	5.475480	-0.036575	-1.243424
C	5.635749	-0.452921	0.075953
C	3.176409	0.414868	-0.814124
C	1.784950	0.778241	-1.145000
C	0.894804	0.565909	0.006329
C	-0.531556	0.741171	0.027571
C	-1.165484	2.091226	0.344279
C	-3.853576	-1.724786	-0.439242
C	-3.969034	-0.351352	-0.284092
C	-2.797268	0.367406	-0.141610
C	-2.645914	1.855286	-0.040254
C	-1.431520	-1.642862	-0.327124
C	-2.612623	-2.345283	-0.465894
C	-1.064530	2.377781	1.852998
C	-1.537055	-0.252486	-0.145774
C	-0.552090	3.254607	-0.434211
H	-4.744766	-2.322119	-0.551104
H	-2.567177	-3.415136	-0.598103
H	-2.861395	2.313605	-1.007346
H	-3.326713	2.310156	0.677111
H	-1.561948	3.316307	2.094373
H	-1.532283	1.583876	2.429437
H	-0.028177	2.461897	2.172631
H	0.479439	3.434537	-0.136069
H	-0.561133	3.059755	-1.502246
H	-1.108946	4.169915	-0.241606
H	4.092590	0.707468	-2.719985
H	6.317836	-0.061177	-1.914553
H	6.599672	-0.799479	0.410401
H	4.694665	-0.747039	1.988448
S	1.889448	0.243644	1.512001
O	1.509156	-1.023168	2.203229
C	-5.307485	0.331071	-0.286244
H	-5.481324	0.874440	0.641346
H	-5.384891	1.053762	-1.097319
H	-6.112803	-0.387654	-0.405204
C	-0.108263	-2.346026	-0.368156
H	0.506658	-1.987536	-1.194677
H	0.451867	-2.201410	0.554300
H	-0.246191	-3.413858	-0.511917

Table C.12: *motor-2 B-2*

C	3.058419	0.486237	-0.831011
O	2.237559	-1.875891	1.646758
C	3.990603	0.997495	-1.712960
C	4.522818	-1.318859	-0.219557
C	5.457736	-0.826499	-1.115745
C	5.192783	0.320517	-1.856315
C	3.317656	-0.651936	-0.092383
C	2.187246	-1.044999	0.786588
C	0.990899	-0.213088	0.432526
C	-0.291018	-0.615050	0.460280
C	-0.789362	-2.069389	0.550494
C	-3.940917	1.236655	-0.527130
C	-3.697296	-0.108284	-0.778825
C	-2.467174	-0.599282	-0.374279
C	-1.997538	-2.016274	-0.423289
C	-1.782403	1.539188	0.556776
C	-3.022498	2.022061	0.148851
C	0.152256	-3.180271	0.092394
C	-1.488682	0.213089	0.207205
C	-1.265245	-2.353342	1.981162
H	-4.886371	1.666282	-0.820545
H	-3.286912	3.037551	0.398645
H	-2.769270	-2.728447	-0.137829
H	-1.670846	-2.288910	-1.427718
H	-0.443970	-4.069063	-0.106259
H	0.663069	-2.916310	-0.831697
H	0.893616	-3.433777	0.836008
H	-0.424630	-2.310249	2.666583
H	-2.015300	-1.636348	2.304186
H	-1.701063	-3.348984	2.034072
H	4.711510	-2.199052	0.371555
H	6.400853	-1.332785	-1.239266
H	5.933265	0.692343	-2.545293
H	3.794473	1.899342	-2.269114
S	1.522689	1.311174	-0.393645
O	1.929662	2.404379	0.541927
C	-4.722895	-0.992010	-1.429101
H	-4.334264	-1.458471	-2.332549
H	-5.036001	-1.795717	-0.764311
H	-5.608514	-0.426225	-1.702233
C	-0.928933	2.410781	1.435181
H	-0.241654	1.830478	2.039479
H	-0.324058	3.115243	0.875511
H	-1.571557	2.979523	2.102300

Table C.13: *motor-3 A-3*

C	-3.463383	-0.438603	-0.196670
O	-0.858294	1.803001	-0.991720
C	-4.818917	-0.649138	-0.029249
C	-3.817035	1.858217	-0.816480
C	-5.176435	1.660990	-0.657264
C	-5.671057	0.419989	-0.258970
C	-2.962110	0.792947	-0.570976
C	-1.490257	0.847087	-0.614286
C	-0.922878	-0.459749	-0.173350
C	0.372229	-0.749690	0.042796
C	1.018394	-2.136367	0.162272
C	3.882171	1.605475	-0.054440
C	3.855129	0.259423	-0.407706
C	2.655296	-0.437547	-0.292482
C	2.391904	-1.890279	-0.510710
C	1.552320	1.544658	0.552236
C	2.754515	2.228698	0.447243
C	1.207967	-2.467451	1.652417
C	1.488513	0.215319	0.107687
C	0.321671	-3.307042	-0.525642
H	4.806597	2.155610	-0.138402
H	2.787405	3.247971	0.790620
H	2.339818	-2.113597	-1.575853
H	3.173602	-2.521941	-0.103428
H	1.737231	-3.412795	1.749354
H	1.787710	-1.702753	2.162971
H	0.242372	-2.558548	2.139612
H	-0.532204	-3.667441	0.036239
H	0.010570	-3.060103	-1.537411
H	1.030044	-4.130392	-0.591430
H	-3.408636	2.811434	-1.106959
H	-5.861771	2.472994	-0.834536
H	-6.732911	0.288275	-0.130935
H	-5.198304	-1.609470	0.277658
S	-2.220581	-1.711114	-0.054995
O	-2.247734	-2.302307	1.317822
C	0.449312	2.222643	1.280936
H	-0.377789	1.582603	1.601037
O	0.488112	3.380880	1.593353
C	5.095429	-0.379680	-0.879493
H	5.972012	0.284922	-0.898688
O	5.191126	-1.525623	-1.230870

Table C.14: *motor-3 CoIn₁*

C	3.302267	0.006065	0.563147
O	1.385991	1.103225	-2.217321
C	4.523862	-0.401572	1.059332
C	4.223884	0.409571	-1.614930
C	5.459491	0.007362	-1.131350
C	5.607083	-0.401380	0.190143
C	3.141017	0.394836	-0.753606
C	1.739902	0.737960	-1.111135
C	0.895790	0.564592	0.047251
C	-0.513056	0.760439	0.079255
C	-1.145961	2.109145	0.356125
C	-3.836915	-1.696969	-0.530559
C	-3.945013	-0.334070	-0.271990
C	-2.784199	0.401108	-0.079164
C	-2.655893	1.863496	0.177782
C	-1.430737	-1.609568	-0.404432
C	-2.603263	-2.317830	-0.601271
C	-0.829654	2.543632	1.797912
C	-1.519582	-0.221946	-0.136863
C	-0.617766	3.168658	-0.620699
H	-4.734308	-2.276755	-0.681228
H	-2.525139	-3.370592	-0.807981
H	-3.065540	2.428984	-0.656601
H	-3.238946	2.164180	1.043856
H	-1.305697	3.500879	1.996437
H	-1.202442	1.822605	2.521530
H	0.238863	2.658699	1.948907
H	0.444760	3.334138	-0.476949
H	-0.769750	2.869980	-1.652758
H	-1.138399	4.107341	-0.444923
H	4.085004	0.718173	-2.637304
H	6.315200	0.003476	-1.786231
H	6.572734	-0.721797	0.545052
H	4.632423	-0.719103	2.083148
S	1.797044	0.127638	1.527042
O	1.389207	-1.224612	2.018870
C	-0.162717	-2.392286	-0.500572
H	0.755247	-1.903566	-0.190115
O	-0.165234	-3.530437	-0.887147
C	-5.285077	0.280214	-0.218660
H	-6.116542	-0.421499	-0.379346
O	-5.497879	1.445814	-0.019636

Table C.15: *motor-3 B-3*

C	3.086906	0.492525	-0.922711
O	2.236195	-2.022340	1.394855
C	4.070251	1.122484	-1.660151
C	4.636745	-1.172641	-0.142452
C	5.627933	-0.560583	-0.889967
C	5.346777	0.578757	-1.639422
C	3.360193	-0.633641	-0.170020
C	2.190375	-1.145345	0.569464
C	0.977565	-0.373879	0.193156
C	-0.304507	-0.758272	0.357507
C	-0.854899	-2.177315	0.558077
C	-3.870561	1.300271	-0.547332
C	-3.725797	-0.075852	-0.711560
C	-2.527219	-0.668044	-0.328787
C	-2.151563	-2.112442	-0.300297
C	-1.673504	1.471384	0.434609
C	-2.878144	2.051529	0.051107
C	-0.001432	-3.338203	0.054224
C	-1.472403	0.112024	0.148092
C	-1.200259	-2.388414	2.038690
H	-4.794955	1.772178	-0.842859
H	-3.027615	3.092353	0.279498
H	-2.943245	-2.738496	0.097165
H	-1.953553	-2.474921	-1.308075
H	-0.635596	-4.219132	-0.022143
H	0.397884	-3.135228	-0.937455
H	0.819403	-3.567441	0.717870
H	-0.295921	-2.360560	2.638434
H	-1.885019	-1.627405	2.405104
H	-1.672169	-3.359272	2.171292
H	4.832633	-2.046372	0.456106
H	6.627016	-0.963621	-0.890163
H	6.132244	1.047716	-2.208839
H	3.857312	2.014182	-2.225858
S	1.400242	1.090540	-0.795701
O	1.440142	2.369201	-0.021603
C	-0.806362	2.280930	1.349335
H	0.026516	1.759572	1.819116
O	-1.086917	3.410235	1.639854
C	-4.847626	-0.853721	-1.266327
H	-5.738522	-0.258154	-1.514794
O	-4.835286	-2.041236	-1.453860

MODIFICATIONS OF THE PROGRAM CODE IN GAMESS AND NEWTONX

Changes in the program code of cioverlap

The direct calculation of nonadiabatic coupling elements is not (yet) available for SF-TDDFT in the GAMESS code. Thus, time-derivative couplings are calculated with the Hammes-Schiffer and Tully model [22, 102] by the finite-difference approximation via

$$\sigma_{ji}(t) \approx \frac{1}{2\Delta t} \left[\left\langle \phi_j \left(t - \frac{\Delta t}{2} \right) \middle| \phi_i \left(t + \frac{\Delta t}{2} \right) \right\rangle - \left\langle \phi_j \left(t + \frac{\Delta t}{2} \right) \middle| \phi_i \left(t - \frac{\Delta t}{2} \right) \right\rangle \right]. \quad (\text{D.1})$$

Thus, only the overlaps between CI wavefunctions ϕ_i, ϕ_j at different time steps are necessary.

In NewtonX this is realized with the external program cioverlap by Jiri Pittner [102]. Here, the linear-response terms from a TDDFT calculation are used to build the CIS-like Casida wavefunction. A CIS-like slaterdeterminant is setup containing all possible permutations of single-excitations. In standard TDDFT this includes $\alpha_{occ} \rightarrow \alpha_{virt}$ and $\beta_{occ} \rightarrow \beta_{virt}$ excitations. In SF-TDDFT less permutations are available as only $\alpha_{occ} \rightarrow \beta_{virt}$ excitations are allowed. The program code is extended for the spin-flip case with an restricted open-shell Hartree-Fock (ROHF) reference, meaning the eigenvalues for the α and β orbitals are equal.

In **cioverlap.cc** the lines checking the size of the slaterfile are commented because it does not match the standard size. It concerns the lines after

```
"int r = read( slaterfile ,&dummy,1);".
```

The modifications in the source code of **cis_slatergen.cc** and **cis_casida.cc** are summarized in the listings D.1 and D.2, respectively.

```

void do_cis_casida(bool uhf, bool spnflp,
int ncore, int (&nocc)[2], int (&nvirt)[2], bool orthonormalize, bool
do_casida, int inactive_occ, int inactive_virt)
{
...
cout << "Is this Spinflip run? " << spnflp << endl;
...

//now generate all possible excitations
...
if(uhf)
...
else if(spnflp) //alpha to beta excitations
{
for(int iocc=1; iocc<nocc[0]; ++iocc)
for(int ivirt=nocc[1]+1; ivirt<=nocc[1]+nvirt[1]; ++ivirt)
{
int spin=nocc[0]>nocc[1]?-1:1;
int pos = 2*shiftcore + 2*iocc-2;
tmp[pos] = spin * (ivirt + numcore);
tmp.put(slaterfile,false); //alpha to beta excitation
tmp[pos] = -spin * (iocc + numcore); //restore vacuum
}
//Last Spinflip
for(int ivirt=nocc[1]+1; ivirt<=nocc[1]+nvirt[1]; ++ivirt)
{
int spin=nocc[0]>nocc[1]?-1:1;
int pos = 2*shiftcore+nocc[0]+nocc[1]-1;
tmp[pos] = spin * (ivirt + numcore);
tmp.put(slaterfile,false); //alpha to beta excitation
}
}
else //rhf
...

if(spnflp)
{
cout << "Number of determinats generated =
" << 1+nocc[0]*nvirt[1] << endl;
}
else
...

bool spnflp=0; \\ default value for spnflp
...

if(argc>1 && !strcmp(argv[1],"-S"))
{
spnflp=1;
argc-=1; argv+=1;
}
...

do_cis_slater(uhf, spnflp, ncore, nocc, nvirt, inactive_occ, inactive_virt,
include_occ, number_occ);

```

Listing D.1: Extension of the code in **cis_slatergen.cc** for spin-flip calculations

```

void do_cis_casida(bool uhf, bool spnflp,
int ncore, int (&nocc)[2], int (&nvirt)[2], bool orthonormalize, bool
do_casida, int inactive_occ, int inactive_virt)
{
...
cout << "Is this Spinflip run? " << spnflp << endl;
...

//create eivecfile header
int ndets;
if(!spnflp) ndets = 1+nocc_eff[0]*nvirt_eff[0]+nocc_eff[1]*nvirt_eff[1];
else ndets = 1+nocc_eff[0]*nvirt_eff[1];
...

//optional casida's adjustment of the coefficients

if(uhf)
...
else if(spnflp) //spinflip: alpha to beta exc.
{
//must be same order of loops as in cis_slatergen case so that
coefficients correspond to determinants
int ithru=0;
for(int iocc=0; iocc<nocc[0]; ++iocc) //alpha spin
for(int ivirt=0; ivirt<nvirt[1]; ++ivirt) //beta spin
{
cis_coefs(i,ithru++) = tddft_coefs(i,0)(iocc+inactive_occ,ivirt)
*(do_casida?
sqrt( (orbener[0][ivirt+ncore+nocc[1]]
- orbener[0][iocc+ncore+inactive_occ]) /
(energies[i+1] - energies[0]))
:1.);
}
}
else //rhf
...

bool spnflp=0; // default value for spnflp
...

if(argc>1 && !strcmp(argv[1],"-S")) {spnflp=1;}
--argc;++argv; // "-S" option calls spin-flip
...

int ncore, nocc[2], nvirt[2];
cin >> ncore >> nocc[0] >> nvirt[0];
if(uhf||spnflp) cin >> nocc[1] >> nvirt[1]; // read nocc(beta) and nvirt
(beta)
else {nocc[1]=nocc[0]; nvirt[1]=nvirt[0];}

do_cis_casida(uhf, spnflp, ncore, nocc, nvirt, orthonormalize, do_casida,
inactive_occ, inactive_virt);
}

```

Listing D.2: Extension of the code in **cis_casida.cc** for spin-flip calculations

Changes in the program code of GAMESS

Several changes in the GAMESS code were necessary to perform the SF-TDDFT trajectory calculations with NewtonX. The modifications are described for each source file of the GAMESS code.

sfdft.src

In the standard version of the program GAMESS[101] no option is implemented to print out the CI-vectors of SF-TDDFT calculations necessary for the setup of the Casida wavefunction. Here, the CI-vectors can only be printed out for a SF-CIS (spin-flip configuration interaction singles) calculation. The print command is written after an IF-statement asking for the keyword to print the CI-vectors and if the spin-flip calculation is a SF-CIS calculation `IF(SOME .AND. SFTYPE.EQ.SFCIS)THEN`.

In the modified GAMESS version for NewtonX the IF-statement is commented that the CI-vectors are always printed for spin-flip calculations. The print command can be found after the comment `----- PUNCH CIS VECTORS TO .DAT FILE -----`.

inputa.src

Further, in the standard GAMESS version the maximal number of iterations `maxit` in the SCF routine is limited to 200. In the SF-TDDFT calculations the SCF routine tends to need more iterations for convergence so the limit for `maxit` is removed by commenting the IF-statement `IF(MAXIT.LE.0 .OR. MAXIT.GT.200)THEN`.

dclib.src and **mthlib.src**

For the calculation of the overlap between the Casida wavefunctions the one-electron integrals of the overlapping geometries are necessary. For that a two-molecule calculation with the geometries of the timesteps t and $t - 1$ is needed. Here, the atoms are overlapping and the geometry control of the program GAMESS prohibits a calculation. Therefore, the section controlling the input-geometry is commented. In the source file **dclib.src** this concerns the lines 1689–1695 (`IF(CROWD)THEN` and following). In the source file **mthlib.src** the lines 801–815 (`IF(CROWD)THEN` and following) are commented.

gamess.src

The following modification also concerns the calculation of the one-electron integrals. The `RUNTYPE` keyword `PROP` is modified to only execute the routine calculating the one-electron integrals (`ONEINT`). This gives, especially for large molecules, a significant speed-up in the calculation time. The modification is in line 1072 and following (`IF(RUNTYP.EQ.PROP)THEN`).

BIBLIOGRAPHY

- [1] W. Domcke and A. L. Sobolewski, “Molecular mechanisms of the photostability of life”, *Physical Chemistry Chemical Physics* **12**, 4897 (2010).
- [2] J. M. Pecourt, J. Peon, and B. Kohler, “DNA Excited-State Dynamics: Ultrafast Internal Conversion and Vibrational Cooling in a Series of Nucleosides”, *Journal of the American Chemical Society* **123**, 10370 (2001).
- [3] J. Peon and A. H. Zewail, “DNA/RNA nucleotides and nucleosides: direct measurement of excited-state lifetimes by femtosecond fluorescence up-conversion”, *Chemical Physics Letters* **348**, 255 (2001).
- [4] R. Send and D. Sundholm, “Stairway to the Conical Intersection: A Computational Study of the Retinal Isomerization”, *Journal of Physical Chemistry A* **111**, 8766 (2007).
- [5] D. Polli, P. Altoè, O. Weingart, K. M. Spillane, C. Manzoni, D. Brida, G. Tomasello, G. Orlandi, P. Kukura, R. A. Mathies, M. Garavelli, and G. Cerullo, “Conical intersection dynamics of the primary photoisomerization event in vision”, *Nature* **467**, 440 (2010).
- [6] M. Maiuri, M. Garavelli, and G. Cerullo, “Ultrafast Spectroscopy: State of the Art and Open Challenges”, *Journal of the American Chemical Society* **142**, 3 (2020).
- [7] A. H. Zewail, “Femtochemistry: Atomic-Scale Dynamics of the Chemical Bond”, *Journal of Physical Chemistry A* **104**, 5660 (2000).
- [8] G. A. Worth and L. S. Cederbaum, “BEYOND BORN-OPPENHEIMER: Molecular Dynamics Through a Conical Intersection”, *Annual Review of Physical Chemistry* **55**, 127 (2004).
- [9] B. F. E. Curchod and T. J. Martínez, “Ab Initio Nonadiabatic Quantum Molecular Dynamics”, *Chemical Reviews*, 10.1021/acs.chemrev.7b00423 (2018).
- [10] R. Crespo-Otero and M. Barbatti, “Recent Advances and Perspectives on Nonadiabatic Mixed Quantum-Classical Dynamics”, *Chemical Reviews* **118**, PMID: 29767966, 7026 (2018).
- [11] G. J. Cheng, X. Zhang, L. W. Chung, L. Xu, and Y. D. Wu, “Computational organic chemistry: Bridging theory and experiment in establishing the mechanisms of chemical reactions”, *Journal of the American Chemical Society* **137**, 1706 (2015).
- [12] L. González, D. Escudero, and L. Serrano-Andrés, “Progress and Challenges in the Calculation of Electronic Excited States”, *ChemPhysChem* **13**, 28 (2012).
- [13] M. Pastore, E. Mosconi, F. D. Angelis, and M. Grätzel, “A Computational Investigation of Organic Dyes for Dye-Sensitized Solar Cells: Benchmark, Strategies, and Open Issues”, *Journal of Physical Chemistry C* **114**, 7205 (2010).

- [14] A. Dreuw, “Quantum Chemical Methods for the Investigation of Photoinitiated Processes in Biological Systems: Theory and Applications”, *ChemPhysChem* **7**, 2259 (2006).
 - [15] M. S. Schuurman and A. Stolow, “Dynamics at Conical Intersections”, *Annual Review of Physical Chemistry*, **16** (2018).
 - [16] D. R. Yarkony, “Nonadiabatic Quantum Chemistry—Past, Present, and Future”, *Chemical Reviews* **112**, 481 (2012).
 - [17] S. A. Mewes, F. Plasser, A. Krylov, and A. Dreuw, “Benchmarking Excited-State Calculations Using Exciton Properties”, *Journal of Chemical Theory and Computation* **14**, 710 (2018).
 - [18] A. D. Laurent and D. Jacquemin, “TD-DFT benchmarks: A review”, *International Journal of Quantum Chemistry* **113**, 2019 (2013).
 - [19] S. Thallmair, M. K. Roos, and R. de Vivie-Riedle, “Design of specially adapted reactive coordinates to economically compute potential and kinetic energy operators including geometry relaxation”, *Journal of Chemical Physics* **144**, 234104 (2016).
 - [20] M. Barbatti, R. Shepard, and H. Lischka, *Computational and Methodological Elements for Nonadiabatic Trajectory Dynamics Simulations of Molecules*, edited by W. Domcke, D. R. Yarkony, and H. Köppel, 2011.
 - [21] J. C. Tully, “Molecular dynamics with electronic transitions”, *Journal of Chemical Physics* **93**, 1061 (1990).
 - [22] S. Hammes-Schiffer and J. C. Tully, “Proton transfer in solution: Molecular dynamics with quantum transitions”, *The Journal of Chemical Physics* **101**, 4657 (1994).
 - [23] I. C. Merritt, D. Jacquemin, and M. Vacher, “cis → trans photoisomerisation of azobenzene: a fresh theoretical look”, *Physical Chemistry Chemical Physics* **23**, 19155 (2021).
 - [24] T. Schnappinger, M. Marazzi, S. Mai, A. Monari, L. González, and R. D. Vivie-Riedle, “Intersystem Crossing as a Key Component of the Nonadiabatic Relaxation Dynamics of Bithiophene and Terthiophene”, *Journal of Chemical Theory and Computation* **14**, 4530 (2018).
 - [25] M. Barbatti, A. J. A. Aquino, and H. Lischka, “The UV absorption of nucleobases: semi-classical ab initio spectra simulations”, *Physical Chemistry Chemical Physics* **12**, 4959 (2010).
 - [26] J. S. Baskin, L. Bañares, S. Pedersen, and A. H. Zewail, “Femtosecond Real-Time Probing of Reactions. 20. Dynamics of Twisting, Alignment, and IVR in the trans-Stilbene Isomerization Reaction”, *Journal of Physical Chemistry* **100**, 11920 (1996).
 - [27] M. Quick, A. L. Dobryakov, M. Gerecke, C. Richter, F. Berndt, I. N. Ioffe, A. A. Granovsky, R. Mahrwald, N. P. Ernsting, and S. A. Kovalenko, “Photoisomerization Dynamics and Pathways of trans- and cis-Azobenzene in Solution from Broadband Femtosecond Spectroscopies and Calculations”, *Journal of Physical Chemistry B* **118**, 8756 (2014).
 - [28] S. J. Wezenberg and B. L. Feringa, “Photocontrol of Anion Binding Affinity to a Bis-urea Receptor Derived from Stiff-Stilbene”, *Organic Letters* **19**, 324 (2017).
 - [29] A. Goulet-Hanssens, F. Eisenreich, and S. Hecht, “Enlightening Materials with Photoswitches”, *Advanced Materials* **32**, 1905966 (2020).
 - [30] M.-M. Russew and S. Hecht, “Photoswitches: From Molecules to Materials”, *Advanced Materials* **22**, 3348 (2010).
-

-
- [31] K. Matsubara, M. Watanabe, and Y. Takeoka, "A Thermally Adjustable Multicolor Photochromic Hydrogel", *Angewandte Chemie International Edition* **46**, 1688 (2007).
- [32] W. A. Velema, W. Szymanski, and B. L. Feringa, "Photopharmacology: Beyond proof of principle", *Journal of the American Chemical Society* **136**, 2178 (2014).
- [33] B. L. Feringa, "The Art of Building Small: From Molecular Switches to Motors (Nobel Lecture)", *Angewandte Chemie International Edition* **56**, 11060 (2017).
- [34] A. Nenov, T. Cordes, T. T. Herzog, W. Zinth, and R. de Vivie-Riedle, "Molecular Driving Forces for Z/E Isomerization Mediated by Heteroatoms: The Example Hemithioindigo", *Journal of Physical Chemistry A* **114**, 13016 (2010).
- [35] B. Maerz, S. Wiedbrauk, S. Oesterling, E. Samoylova, A. Nenov, P. Mayer, R. de Vivie-Riedle, W. Zinth, and H. Dube, "Making Fast Photoswitches Faster-Using Hammett Analysis to Understand the Limit of Donor-Acceptor Approaches for Faster Hemithioindigo Photoswitches", *Chemistry - A European Journal* **20**, 13984 (2014).
- [36] F. F. Graupner, T. T. Herzog, F. Rott, S. Oesterling, R. de Vivie-Riedle, T. Cordes, and W. Zinth, "Photoisomerization of hemithioindigo compounds: Combining solvent- and substituent- effects into an advanced reaction model", *Chemical Physics* **515**, 614 (2018).
- [37] S. Wiedbrauk, B. Maerz, E. Samoylova, A. Reiner, F. Trommer, P. Mayer, W. Zinth, and H. Dube, "Twisted Hemithioindigo Photoswitches: Solvent Polarity Determines the Type of Light-Induced Rotations", *Journal of the American Chemical Society* **138**, 12219 (2016).
- [38] S. Wiedbrauk, B. Maerz, E. Samoylova, P. Mayer, W. Zinth, and H. Dube, "Ingredients to TICT Formation in Donor Substituted Hemithioindigo", *Journal of Physical Chemistry Letters* **8**, 1585 (2017).
- [39] J. P. Abrahams, A. G. W. Leslie, R. Lutter, and J. E. Walker, "Structure at 2.8 Å resolution of F1-ATPase from bovine heart mitochondria", *Nature* **370**, 621 (1994).
- [40] P. D. Boyer, "Catalytic site forms and controls in ATP synthase catalysis", *Biochimica et Biophysica Acta (BBA) - Bioenergetics* **1458**, 252 (2000).
- [41] J. P. Sauvage, "From Chemical Topology to Molecular Machines (Nobel Lecture)", *Angewandte Chemie International Edition* **56**, 11080 (2017).
- [42] J. F. Stoddart, "Mechanically Interlocked Molecules (MIMs)—Molecular Shuttles, Switches, and Machines (Nobel Lecture)", *Angewandte Chemie International Edition* **56**, 11094 (2017).
- [43] L. A. Huber, S. Thumser, K. Grill, D. Voßiek, N. N. Bach, P. Mayer, and H. Dube, "Steric Effects on the Thermal Processes of Hemithioindigo Based Molecular Motor Rotation", *Chemistry – A European Journal* **27**, 10758 (2021).
- [44] R. Wilcken, L. Huber, K. Grill, M. Guentner, M. Schildhauer, S. Thumser, E. Riedle, and H. Dube, "Tuning the Ground and Excited State Dynamics of Hemithioindigo Molecular Motors by Changing Substituents", *Chemistry - A European Journal* **26**, 13507 (2020).
- [45] R. Wilcken, M. Schildhauer, F. Rott, L. A. Huber, M. Guentner, S. Thumser, K. Hoffmann, S. Oesterling, R. D. Vivie-Riedle, E. Riedle, and H. Dube, "Complete Mechanism of Hemithioindigo Motor Rotation", *Journal of the American Chemical Society* **140**, 5311 (2018).
- [46] N. Koumura, R. W. J. Zijlstra, R. A. van Delden, N. Harada, and B. L. Feringa, "Light-driven monodirectional molecular rotor", *Nature* **401**, 152 (1999).
-

- [47] S. Kassem, T. van Leeuwen, A. S. Lubbe, M. R. Wilson, B. L. Feringa, and D. A. Leigh, "Artificial molecular motors", *Chemical Society Reviews* **46**, 2592 (2017).
 - [48] D. R. S. Pooler, A. S. Lubbe, S. Crespi, and B. L. Feringa, "Designing light-driven rotary molecular motors", *Chemical Science*, 10.1039/D1SC04781G (2021).
 - [49] J. Ammer and H. Mayr, "Photogeneration of carbocations: applications in physical organic chemistry and the design of suitable precursors", *Journal of Physical Organic Chemistry* **26**, 956 (2013).
 - [50] R. R. Naredla and D. A. Klumpp, "Contemporary carbocation chemistry: Applications in organic synthesis", *Chemical Reviews* **113**, 6905 (2013).
 - [51] D. Ravelli, S. Protti, and M. Fagnoni, "Carbon-Carbon Bond Forming Reactions via Photogenerated Intermediates", *Chemical Reviews* **116**, 9850 (2016).
 - [52] S. Thallmair, D. Keefer, F. Rott, and R. de Vivie-Riedle, "Simulating the control of molecular reactions via modulated light fields: from gas phase to solution", *Journal of Physics B: Atomic, Molecular and Optical Physics* **50**, 82001 (2017).
 - [53] P. Nuernberger, G. Vogt, T. Brixner, and G. Gerber, "Femtosecond quantum control of molecular dynamics in the condensed phase", *Physical Chemistry Chemical Physics* **9**, 2470 (2007).
 - [54] T. Brixner and G. Gerber, "Quantum control of gas-phase and liquid-phase femtochemistry", *ChemPhysChem* **4**, 418 (2003).
 - [55] D. Townsend, B. J. Sussman, and A. Stolow, "A Stark future for quantum control", *Journal of Physical Chemistry A* **115**, 357 (2011).
 - [56] G. W. Richings and G. A. Worth, "Non-resonant dynamic stark control at a conical intersection: The photodissociation of ammonia", *Journal of Physical Chemistry A* **116**, 11228 (2012).
 - [57] G. J. Halász, M. Šindelka, N. Moiseyev, L. S. Cederbaum, and Á. Vibók, "Light-Induced Conical Intersections: Topological Phase, Wave Packet Dynamics, and Molecular Alignment", *Journal of Physical Chemistry A* **116**, 2636 (2011).
 - [58] J. Kim, H. Tao, J. L. White, V. S. Petrović, T. J. Martinez, and P. H. Bucksbaum, "Control of 1,3-Cyclohexadiene Photoisomerization Using Light-Induced Conical Intersections", *Journal of Physical Chemistry A* **116**, 2758 (2011).
 - [59] A. Natan, M. R. Ware, V. S. Prabhudesai, U. Lev, B. D. Bruner, O. Heber, and P. H. Bucksbaum, "Observation of Quantum Interferences via Light-Induced Conical Intersections in Diatomic Molecules", *Physical Review Letters* **116**, 143004 (2016).
 - [60] M. F. Kling, P. V. D. Hoff, I. Znakovskaya, and R. D. Vivie-Riedle, "(Sub-)femtosecond control of molecular reactions via tailoring the electric field of light", *Physical Chemistry Chemical Physics* **15**, 9448 (2013).
 - [61] I. Znakovskaya, P. von den Hoff, N. Schirmel, G. Urbasch, S. Zhrebtssov, B. Bergues, R. de Vivie-Riedle, K.-M. Weitzel, and M. F. Kling, "Waveform control of orientation-dependent ionization of DCl in few-cycle laser fields", *Physical Chemistry Chemical Physics* **13**, 8653 (2011).
 - [62] K. N. Houk, M. N. Paddon-Row, N. G. Rondan, Y. D. Wu, F. K. Brown, D. C. Spellmeyer, J. T. Metz, Y. Li, and R. J. Loncharich, "Theory and Modeling of Stereoselective Organic Reactions", *Science* **231**, 1108 (1986).
 - [63] Y. Liang, S. Liu, Y. Xia, Y. Li, and Z. X. Yu, "Mechanism, Regioselectivity, and the Kinetics of Phosphine-Catalyzed [3+2] Cycloaddition Reactions of Allenates and Electron-Deficient Alkenes", *Chemistry – A European Journal* **14**, 4361 (2008).
-

-
- [64] P. MacKey, A. Turlik, K. Ando, M. E. Light, K. N. Houk, and G. P. McGlacken, "Stereoselective Installation of Five Contiguous Stereogenic Centers in a Double Aldol-Tishchenko Cascade and Evaluation of the Key Transition State through DFT Calculation", *Organic Letters* **23**, 6372 (2021).
- [65] Y. H. Lam, M. N. Grayson, M. C. Holland, A. Simon, and K. N. Houk, "Theory and Modeling of Asymmetric Catalytic Reactions", *Accounts of Chemical Research* **49**, 750 (2016).
- [66] M. Wanko, M. Garavelli, F. Bernardi, T. A. Niehaus, T. Frauenheim, and M. Elstner, "A global investigation of excited state surfaces within time-dependent density-functional response theory", *The Journal of Chemical Physics* **120**, 1674 (2004).
- [67] A. Dreuw and M. Head-Gordon, "Failure of Time-Dependent Density Functional Theory for Long-Range Charge-Transfer Excited States: The Zincbacteriochlorin-Bacteriochlorin and Bacteriochlorophyll-Spheroidene Complexes", *Journal of the American Chemical Society* **126**, 4007 (2004).
- [68] Z. L. Cai, K. Sendt, and J. R. Reimers, "Failure of density-functional theory and time-dependent density-functional theory for large extended π systems", *The Journal of Chemical Physics* **117**, 5543 (2002).
- [69] A. Dreuw and M. Head-Gordon, "Single-Reference ab Initio Methods for the Calculation of Excited States of Large Molecules", *Chemical Reviews* **105**, 4009 (2005).
- [70] H. Lebel, J. F. Marcoux, C. Molinaro, and A. B. Charette, "Stereoselective cyclopropanation reactions", *Chemical Reviews* **103**, 977 (2003).
- [71] F. Cuccu, L. Serusi, A. Luridiana, F. Secci, P. Caboni, D. J. Aitken, and A. Frongia, "Tandem Wittig Reaction-Ring Contraction of Cyclobutanes: A Route to Functionalized Cyclopropanecarbaldehydes", *Organic Letters* **21**, 7755 (2019).
- [72] M. Mato, A. Franchino, C. García-Morales, and A. M. Echavarren, "Gold-Catalyzed Synthesis of Small Rings", *Chemical Reviews* **121**, 8613 (2021).
- [73] K. Andersson, P. Å. Malmqvist, B. O. Roos, A. J. Sadlej, and K. Wolinski, "Second-order perturbation theory with a CASSCF reference function", *Journal of Physical Chemistry* **94**, 5483 (1990).
- [74] A. Toniolo, C. Ciminelli, M. Persico, and T. J. Martínez, "Simulation of the photodynamics of azobenzene on its first excited state: Comparison of full multiple spawning and surface hopping treatments", *The Journal of Chemical Physics* **123**, 234308 (2005).
- [75] M. Pederzoli, J. Pittner, M. Barbatti, and H. Lischka, "Nonadiabatic Molecular Dynamics Study of the cis-trans Photoisomerization of Azobenzene Excited to the S1 State", *Journal of Physical Chemistry A* **115**, 11136 (2011).
- [76] J. Tomasi, B. Mennucci, and R. Cammi, "Quantum mechanical continuum solvation models", *Chemical Reviews* **105**, 2999 (2005).
- [77] M. Cossi and V. Barone, "Separation between fast and slow polarizations in continuum solvation models", *Journal of Physical Chemistry A* **104**, 10614 (2000).
- [78] R. Cammi, S. Corni, B. Mennucci, and J. Tomasi, "Electronic excitation energies of molecules in solution: State specific and linear response methods for nonequilibrium continuum solvation models", *Journal of Chemical Physics* **122**, 104513 (2005).
- [79] M. Cossi and V. Barone, "Solvent effect on vertical electronic transitions by the polarizable continuum model", *Journal of Chemical Physics* **112**, 2427 (2000).
-

- [80] I. F. Galván, M. Vacher, A. Alavi, C. Angeli, F. Aquilante, J. Autschbach, J. J. Bao, S. I. Bokarev, N. A. Bogdanov, R. K. Carlson, L. F. Chibotaru, J. Creutzberg, N. Dattani, M. G. Delcey, S. S. Dong, A. Dreuw, L. Freitag, L. M. Frutos, L. Gagliardi, F. Gendron, A. Giussani, L. González, G. Grell, M. Guo, C. E. Hoyer, M. Johansson, S. Keller, S. Knecht, G. Kovačević, E. Källman, G. L. Manni, M. Lundberg, Y. Ma, S. Mai, J. P. Malhado, P. Å. Malmqvist, P. Marquetand, S. A. Mewes, J. Norell, M. Olivucci, M. Oppel, Q. M. Phung, K. Pierloot, F. Plasser, M. Reiher, A. M. Sand, I. Schapiro, P. Sharma, C. J. Stein, L. K. Sørensen, D. G. Truhlar, M. Ugandi, L. Ungur, A. Valentini, S. Vancoillie, V. Veryazov, O. Weser, T. A. Wesolowski, P.-O. Widmark, S. Wouters, A. Zech, J. P. Zobel, and R. Lindh, "OpenMolcas: From Source Code to Insight", *Journal of Chemical Theory and Computation* **15**, 5925 (2019).
- [81] F. Aquilante, J. Autschbach, A. Baiardi, S. Battaglia, V. A. Borin, L. F. Chibotaru, I. Conti, L. D. Vico, M. Delcey, I. F. Galván, N. Ferré, L. Freitag, M. Garavelli, X. Gong, S. Knecht, E. D. Larsson, R. Lindh, M. Lundberg, P. Å. Malmqvist, A. Nenov, J. Norell, M. Odelius, M. Olivucci, T. B. Pedersen, L. Pedraza-González, Q. M. Phung, K. Pierloot, M. Reiher, I. Schapiro, J. Segarra-Martí, F. Segatta, L. Seijo, S. Sen, D. C. Sergentu, C. J. Stein, L. Ungur, M. Vacher, A. Valentini, and V. Veryazov, "Modern quantum chemistry with [open]molcas", *Journal of Chemical Physics* **152**, 214117 (2020).
- [82] K. Stallhofer, M. Nuber, F. Schüppel, S. Thumser, H. Iglev, R. D. Vivie-Riedle, W. Zinth, and H. Dube, "Electronic and Geometric Characterization of TICT Formation in Hemithioindigo Photoswitches by Picosecond Infrared Spectroscopy", *Journal of Physical Chemistry A* **125**, 4390 (2021).
- [83] E. S. Kryachko and D. R. Yarkony, "Diabatic Bases and Molecular Properties", *International Journal of Quantum Chemistry* **76**, 235243 (2000).
- [84] V. B. Delchev, A. L. Sobolewski, and W. Domcke, "Comparison of the non-radiative decay mechanisms of 4-pyrimidinone and uracil: an ab initio study", *Physical Chemistry Chemical Physics* **12**, 5007 (2010).
- [85] S. F. Altavilla, J. Segarra-Martí, A. Nenov, I. Conti, I. Rivalta, and M. Garavelli, "Deciphering the photochemical mechanisms describing the UV-induced processes occurring in solvated guanine monophosphate", *Frontiers in Chemistry* **3**, 29 (2015).
- [86] S. B. Nielsen and T. I. Sølling, "Are Conical Intersections Responsible for the Ultrafast Processes of Adenine, Protonated Adenine, and the Corresponding Nucleosides?", *ChemPhysChem* **6**, 1276 (2005).
- [87] A. Nikiforov, J. A. Gamez, W. Thiel, and M. Filatov, "Computational Design of a Family of Light-Driven Rotary Molecular Motors with Improved Quantum Efficiency", *Journal of Physical Chemistry Letters* **7**, 105 (2016).
- [88] A. Kazaryan, Z. Lan, L. V. Schäfer, W. Thiel, and M. Filatov, "Surface hopping excited-state dynamics study of the photoisomerization of a light-driven fluorene molecular rotary motor", *Journal of Chemical Theory and Computation* **7**, 2189 (2011).
- [89] A. Kazaryan, J. C. Kistemaker, L. V. Schäfer, W. R. Browne, B. L. Feringa, and M. Filatov, "Understanding the dynamics behind the photoisomerization of a light-driven fluorene molecular rotary motor", *Journal of Physical Chemistry A* **114**, 5058 (2010).
- [90] J. Wen, S. Mai, and L. González, "Non-Adiabatic Dynamics Simulations of a Light-Driven Molecular Motor in Solution", *ChemRxiv. Cambridge: Cambridge Open Engage*; 2021; This content is a preprint and has not been peer-reviewed. (2021).
-

-
- [91] Y. Shao, M. Head-Gordon, and A. I. Krylov, "The spin-flip approach within time-dependent density functional theory: Theory and applications to diradicals", *The Journal of Chemical Physics* **118**, 4807 (2003).
- [92] Y. A. Bernard, Y. Shao, and A. I. Krylov, "General formulation of spin-flip time-dependent density functional theory using non-collinear kernels: Theory, implementation, and benchmarks", *Journal of Chemical Physics* **136**, 204103 (2012).
- [93] D. Casanova and A. I. Krylov, "Spin-flip methods in quantum chemistry", *Physical Chemistry Chemical Physics* **22**, 4326 (2020).
- [94] L. Yue, Y. Liu, and C. Zhu, "Performance of TDDFT with and without spin-flip in trajectory surface hopping dynamics: cis-trans azobenzene photoisomerization", *Physical Chemistry Chemical Physics* **20**, 24123 (2018).
- [95] F. Neese, "Software update: The ORCA program system—Version 5.0", *Wiley Interdisciplinary Reviews: Computational Molecular Science*, e1606 (2022).
- [96] F. Neese, F. Wennmohs, U. Becker, and C. Riplinger, "The ORCA quantum chemistry program package", *The Journal of Chemical Physics* **152**, 224108 (2020).
- [97] F. Neese, "Software update: the ORCA program system, version 4.0", *Wiley Interdisciplinary Reviews: Computational Molecular Science* **8**, e1327 (2018).
- [98] F. Neese, "The ORCA program system", *Wiley Interdisciplinary Reviews: Computational Molecular Science* **2**, 73 (2012).
- [99] M. Persico, H. Lischka, M. Barbatti, G. Granucci, M. Ruckebauer, F. Plasser, R. Crespo-Otero, and J. Pittner, *NEWTON-X: a package for Newtonian dynamics close to the crossing seam (v2.2)*. Available via the Internet at www.newtonx.org, 2018.
- [100] M. Barbatti, M. Ruckebauer, F. Plasser, J. Pittner, G. Granucci, M. Persico, and H. Lischka, "Newton-X: a surface-hopping program for nonadiabatic molecular dynamics", *Wiley Interdisciplinary Reviews: Computational Molecular Science* **4**, 26 (2014).
- [101] G. M. J. Barca, C. Bertoni, L. Carrington, D. Datta, N. De Silva, J. E. Deustua, D. G. Fedorov, J. R. Gour, A. O. Gunina, E. Guidez, T. Harville, S. Irle, J. Ivanic, K. Kowalski, S. S. Leang, H. Li, W. Li, J. J. Lutz, I. Magoulas, J. Mato, V. Mironov, H. Nakata, B. Q. Pham, P. Piecuch, D. Poole, S. R. Pruitt, A. P. Rendell, L. B. Roskop, K. Ruedenberg, T. Sattasathuchana, M. W. Schmidt, J. Shen, L. Slipchenko, M. Sosonkina, V. Sundriyal, A. Tiwari, J. L. Galvez Vallejo, B. Westheimer, M. Wloch, P. Xu, F. Zahariev, and M. S. Gordon, "Recent developments in the general atomic and molecular electronic structure system", en, *The Journal of Chemical Physics* **152**, Version 2020 R2, 154102 (2020).
- [102] J. Pittner, H. Lischka, and M. Barbatti, "Optimization of mixed quantum-classical dynamics: Time-derivative coupling terms and selected couplings", *Chemical Physics* **356**, 147 (2009).
- [103] S. Thallmair, M. K. Roos, and R. de Vivie-Riedle, "Molecular features in complex environment: Cooperative team players during excited state bond cleavage", *Structural Dynamics* **3**, 43205 (2016).
- [104] M. Svensson, S. Humbel, R. D. J. Froese, T. Matsubara, S. Sieber, and K. Morokuma, "ONIOM: A Multilayered Integrated MO + MM Method for Geometry Optimizations and Single Point Energy Predictions. A Test for Diels-Alder Reactions and Pt(P(t-Bu)₃)₂ + H₂ Oxidative Addition", *Journal of Physical Chemistry* **100**, 19357 (1996).
-

- [105] L. W. Chung, W. M. C. Sameera, R. Ramozzi, A. J. Page, M. Hatanaka, G. P. Petrova, T. V. Harris, X. Li, Z. Ke, F. Liu, H.-B. Li, L. Ding, and K. Morokuma, "The ONIOM Method and Its Applications", *Chemical Reviews* **115**, PMID: 25853797, 5678 (2015).
 - [106] E. B. Wilson, J. C. Decius, and P. C. Cross, *Molecular Vibrations: The Theory of Infrared and Raman Vibrational Spectra*, unabridged and corrected republication of the work originally published in 1955 (Dover Publ., 1980).
 - [107] L. J. Schaad and J. Hu, "The schrödinger equation in generalized coordinates", *Journal of Molecular Structure: THEOCHEM* **185**, 203 (1989).
 - [108] B. Podolsky, "Quantum-Mechanically Correct Form of Hamiltonian Function for Conservative Systems", *Physical Review* **32**, 812 (1928).
 - [109] C. Eckart, "Some Studies Concerning Rotating Axes and Polyatomic Molecules", *Physical Review* **47**, 552 (1935).
 - [110] H. Tal-Ezer and R. Kosloff, "An accurate and efficient scheme for propagating the time dependent Schrödinger equation", *Journal of Chemical Physics* **81**, 3967 (1984).
 - [111] M. Persico, H. Lischka, M. Barbatti, G. Granucci, M. Ruckebauer, F. Plasser, R. Crespo-Otero, and J. Pittner, *NEWTON-X: a package for Newtonian dynamics close to the crossing seam, version 1.4, 2014, see www.newtonx.org*.
 - [112] B. P. Fingerhut, "Optimale Photochemische Energiekonversion und Umgebungseffekte in Reaktiver Moleküldynamik." (Ludwig-Maximilians-Universität München, 2010).
 - [113] M. Tamaoki, Y. Yamauchi, and H. Nakai, "Short-time Fourier transform analysis of ab initio molecular dynamics simulation: Collision reaction between CN and C₄H₆", *Journal of Computational Chemistry* **26**, 436 (2005).
 - [114] P. von den Hoff, S. Thallmair, M. Kowalewski, R. Siemering, and R. de Vivie-Riedle, "Optimal control theory – closing the gap between theory and experiment", *Physical Chemistry Chemical Physics* **14**, 14460 (2012).
 - [115] M. Abe, Y. Ohtsuki, Y. Fujimura, and W. Domcke, "Optimal control of ultrafast cis-trans photoisomerization of retinal in rhodopsin via a conical intersection", *The Journal of Chemical Physics* **123**, 144508 (2005).
 - [116] D. Keefer, S. Thallmair, S. Matsika, and R. de Vivie-Riedle, "Controlling Photorelaxation in Uracil with Shaped Laser Pulses: A Theoretical Assessment", *Journal of the American Chemical Society* **139**, 5061 (2017).
 - [117] M. Kowalewski, K. Bennett, and S. Mukamel, "Non-adiabatic dynamics of molecules in optical cavities", *The Journal of Chemical Physics* **144**, 054309 (2016).
 - [118] M. Kowalewski, K. Bennett, and S. Mukamel, "Cavity Femtochemistry: Manipulating Nonadiabatic Dynamics at Avoided Crossings", *Journal of Physical Chemistry Letters* **7**, 2050 (2016).
 - [119] C. Song, "State-averaged CASSCF with polarizable continuum model for studying photoreactions in solvents: Energies, analytical nuclear gradients, and non-adiabatic couplings", *The Journal of Chemical Physics* **156**, 104102 (2022).
 - [120] H.-J. Werner, P. J. Knowles, G. Knizia, F. R. Manby, and M. Schütz, "Molpro: a general-purpose quantum chemistry program package", *WIREs Comput Mol Sci* **2**, 242 (2012).
-

- [121] H.-J. Werner, P. J. K. and G. Knizia, F. R. Manby, M. Schütz, P. Celani, W. Györffy, D. Kats, T. Korona, R. Lindh, A. Mitrushenkov, G. Rauhut, K. R. Shamasundar, T. B. Adler, R. D. Amos, S. J. Bennie, A. Bernhardsson, A. Berning, D. L. Cooper, M. J. O. Deegan, A. J. Dobbyn, F. Eckert, E. Goll, C. Hampel, A. Hesselmann, G. Hetzer, T. Hrenar, G. Jansen, C. Köppl, S. J. R. Lee, Y. Liu, A. W. Lloyd, Q. Ma, R. A. Mata, A. J. May, S. J. McNicholas, W. Meyer, T. F. Miller III, M. E. Mura, A. Nicklass, D. P. O'Neill, P. Palmieri, D. Peng, K. Pflüger, R. Pitzer, M. Reiher, T. Shiozaki, H. Stoll, A. J. Stone, R. Tarroni, T. Thorsteinsson, M. Wang, and M. Welborn, *MOLPRO, version 2019.1, a package of ab initio programs*, see <https://www.molpro.net>, Stuttgart, Germany.
-

LIST OF ABBREVIATIONS

AS	active space
ATP	adenosine triphosphate
CASPT2	complete active space perturbation theory to the second order
CASSCF	complete active space self-consistent field
CEP	carrier-envelope phase
CoIn	conical intersection
CPK	cyclopropane ketone
CT	charge transfer
DBI	double bond isomerization
DCM	dichloromethane
DFT	density functional theory
DK	diketone
FC	Franck-Condon
FWHM	full-width-half-maximum
HTI	hemithioindigo-stilbene
IR	infrared
NAC	non-adiabatic coupling
ONIOM	Our Own N-Layered Integrated Molecular Orbital and Molecular Mechanics
PCM	polarized continuum model
PES	potential energy surface
QD	quantum dynamic
SBT	single bond twist
SCF	self-consistent field
SF-TDDFT	spin-flip time-dependent density functional theory
TDDFT	time-dependent density functional theory
TDM	transition dipole moment
TICT	twisted intramolecular charge transfer

DANKSAGUNG

An dieser Stelle möchte ich mich noch bei allen bedanken, die mich in der Zeit meiner Promotion unterstützt haben.

Zuerst gilt mein Dank meiner Doktormutter Frau Prof. Dr. Regina de Vivie-Riedle, die es mir ermöglicht hat in ihrer Gruppe zu promovieren und mir interessante Themen zum Forschen zur Auswahl gestellt hat. Besonders hervorzuheben ist hierbei die Freiheit, die sie mir bei meiner Arbeit gelassen hat, aber gleichzeitig jederzeit unterstützend mit ergiebigen Diskussionen und guten Vorschlägen zur Verfügung stand und dadurch meine Forschung maßgeblich voran gebracht hat.

Ich möchte meinen Kollegen (aktuelle und ehemalige), Thomas, Matthias, Martin, Flo, Sebastian, Lena, Ferdinand, Daniel, Sven, Julius und Robert, für das angenehme Arbeitsklima danken, ohne das es mir nicht so leicht gefallen wäre immer Spaß an der Arbeit zu finden. Die regelmäßigen Diskussionen in der Kaffeeküche haben stets für Abwechslung gesorgt und oft neue Ideen hervorgebracht.

Mein Dank gilt auch allen meinen Kooperationspartnern für die gute und ertragreiche Zusammenarbeit.

Besonders bedanken möchte ich mich bei Thomas für das geduldige Korrekturlesen, das die Arbeit auf ein höheres Level gebracht hat, und Flo für das Bereitstellen einer funktionierenden Latex-Vorlage, das mir viel Zeit und Nerven erspart hat.

Außerdem danke ich meiner Freundin Mandy, die mich mit ihrer Liebe und Zuversicht immer wieder motiviert hat.